EXPLOITING THE THIAMIN BIOSYNTHESIS OF *STAPHYLOCOCCUS AUREUS* TOWARDS PRO-DRUG DISCOVERY

DISSERTATION

zur Erlangung des akademischen Grades eines Doktors der
Naturwissenschaften (Dr. rer. nat.) im

Fachbereich Chemie

der Universität Hamburg

vorgelegt von

JULIA DREBES

aus Hamburg, Deutschland

Hamburg, September 2012

Die vorliegende Arbeit wurde im Zeitraum von Oktober 2009 bis September 2012 in der Arbeitsgruppe von Prof. Ch. Betzel im Laboratorium für Strukturbiologie von Infektion und Entzündung am Institut für Biochemie und Molekularbiologie des Fachbereichs Chemie der Universität Hamburg und am Bernhard-Nocht-Institut für Tropenmedizin, durchgeführt.

1. Gutachter: **Prof. Ch. Betzel**
2. Gutachter: **Prof. P. Heisig**

Tag der Disputation: 2. November 2012

Für mich

Table of contents

I. List of abbreviations

ATP	adenosine triphosphate
ABC	ATP-binding cassette
ADP	adenosine diphosphate
AHT	anhydrotetracycline
Amp	ampicillin
APS	ammonium persulphate
ATP	adenosine triphosphate
ATTP	adenosine thiamin triphosphate
ATTP	adenosine thiamin triphosphate
BSA	bovine serum albumin
Cam	chloramphenicol
***Ca*MRSA**	community acquired MRSA
CD	circular dichroism
Clp	caseinolytic proteins
CoA	coenzyme A
DLS	dynamic light scattering
DTT	dithiotreitol
EDTA	ethylenediaminetetraacetic acid
EMA	European Medicines Agency
ETA	extrafoliative toxin A
ETB	extrafoliative toxin A
FAD	adenine dinucleotide
FDA	US Food and Drug Administration
FPLC	fast protein liquid chromatography
HABA	hydroxyl-azophenyl-benzoic acid
***Ha*MRSA**	hospital acquired MRSA
***hca*MRSA**	hospital acquired community onset MRSA
HMBC	heteronuclear multiple bond correlation
HMP	4-amino-5-hydroxymethylpyrimidine
IPTG	β-d-thiogalactopyranoside

k_{cat}	turnover number
K_M	Michaelis-Menten constant
*La*MRSA	livestock *associated* MRSA
MRSA	methicillin-resistant *Staphylococcus aureus*
MW	molecular weight
NMR	nuclear magnetic resonance
NOE	nuclear Overhauser effect
NOESY	nuclear Overhauser enhancement spectroscopy
OD	optical density
ORFs	open reading frames
PBP2a	penicillin binding protein 2a
PBS	phosphate buffered saline
PCR	polymerase chain reaction
PK	pantothenate kinase
PMN	polymorphonuclear leukocytes
PMSF	phenylmethylsulfonylfluoride
PTPP	pyrithiamin pyrophosphate
PTSAgs	pyrogenic toxin superantigens
PVL	Panton-Valentine leukocidin
Rg	radius of gyration
ROS	Reactive oxygen species
RT	room temperature
SAXS	small angle X-ray scattering
SDS	sodiumdodecylsulfate
Spl A/ B	serine protease-like proteins A/ B
SSCmec	staphylococcal cassette chromosome mec
STD	saturation transfer difference
Tbpa	thiamin binding protein
TEMED	*N,N,N′,N′*-Tetramethylethan-1,2-diamine
TenA	thiaminase type II
TEV	tabacco etch virus
THF	tetrahydrofolate
THI elements	thiamin pyrophosphate riboswitches
ThiD	4-amino-5-hydroxymethylpyrimidine kinase

ThiE	thiamin phosphate synthase
ThiM	5-(2-hydroxyethyl)-4-methylthiazole kinase
THZ	5-(2-hydroxyethyl)-4-methylthiazole
TLC	thin layer chromatography
TMP	thiamin monophosphate
TPK	thiamin pyrophosphokinase
TPP	thiamin pyrophosphate
TSST-1	toxic shock syndrome toxin-1
TTP	thiamin triphosphate
$\mathbf{V_{max}}$	maximum rate attainable
VRE	vancomycin resistent enterococci
WT	wildtype

1 INTRODUCTION

1.1 Hospital acquired infections with MRSA: an introduction

Infections with the methicillin-resistant *Staphylococcus aureus* (MRSA) are a major burden in disease control. Therapeutic options are restricted and the number of effective new drugs is also limited [1]. Strains originating from different reservoirs show different resistance patterns [2], but statistics are not divided into *community acquired* MRSA (*Ca*MRSA) and *hospital acquired* MRSA (*Ha*MRSA) infections. That complicates specific antibiotic interventions. Mortality rates for Europe differ from 25,000 deaths per year in 29 countries [3], but other sources state up to 40,000 deaths in Germany alone [4].

Resistance emerges very fast, and therefore, novel approaches and strategies to treat staphylococcal infections are urgently needed. Classical antibiotic targets seem to be still the first choice, but an effective drug has not been found to date. A so far rarely investigated class of antibiotics are pro-drugs that have to be activated by the bacterium. Bioinformatics tools, combining active site parameters to analyse the druggability of proteins could show that proteins involved in vitamin biosyntheses are scored within the highest category as druggable [5].

1.2 General information on *Staphylococcus aureus*

Staphylococcus aureus is a commensal gram-positive bacterium, which colonises the nasal mucosa of humans. 20 % of the population is colonised permanently, whereas up to 60 % are colonised transiently [6]. *S. aureus* can breach the initial colonisation site at the anterior nares and can lead to severe infections [7, 8]. As long as the immune system is not affected, *S. aureus* persists in the body without clinical symptoms. In contrast, it has been estimated that 19-25 % of colonised individuals develop an infection with MRSA [9]. For immuno-compromised individuals, *S. aureus* colonisation leads to life threatening conditions [10].

Infection with MRSA, can cause symptoms from skin lesions up to serious conditions like endocarditis, pneumonia and meningitis [11]. The major problem in *S. aureus* infection control is the occurrence of multi-drug resistant strains. Ten years after introducing penicillin in the 1940s, already 50 % of *S. aureus* isolates were already found to be resistant [12, 13]. This was the consequence of antibiotic misuse for decades by treatment of non-bacterial infections with antibiotics or inadequate compliance with the regulations for drug ingestion [3].

In the 1950s a penicillin resistant *S. aureus* clone occurred, that was responsible for most hospital outbreaks in maternity units in the USA and UK [14]. In order to treat this problem, semisynthetic approaches were developed and methicillin was introduced as a drug [15, 16]. Its efficacy was limited, as only seven years later multi-drug resistance (MDR) was reported in Switzerland, France, Denmark, England, Australia and India [17-22]. After *S. aureus* turned unresponsive to methicillin and other antibiotics, the multi-drug resistant pathogen was termed MRSA.

Based on resistance patterns, MRSA is divided into *Ca*MRSA, *Ha*MRSA, *hospital acquired community onset* MRSA (*hca*MRSA) and *livestock associated* MRSA (*La*MRSA) [2].

*Ca*MRSA strains have been reported to occur among facility staff and intravenous drug users [23, 24] and express different methicillin-resistance cassettes. Panton-Valentine leukocidin (PVL) virulence factor expression is more abundant in these strains [25]. When colonisation is acquired during a short-term hospital stay and symptoms arise after the patient´s discharge, *S. aureus* strains are termed *hca*MRSA strains. A poorly investigated group is *La*MRSA, which can be obtained after having contact with livestock breeding. *Ha*MRSA has been reported to be more active in biofilm formation, adhesion and invasion of the host cell [26].

In the US, the *Ca*MRSA frequency in outpatients has increased sevenfold from 1999-2006 in comparison to inpatients, which assigns a major role to outpatients as reservoir for *Ca*MRSA. However, *Ca*MRSA strains are not replacing *Ha*MRSA strains, but complicating MRSA treatment [27].

Among the emerging multi-drug resistant pathogens grouped by Rice as ESKAPE organisms (*Enterococcus faecium, Staphylococcus aureus, Klebsiella pneumonia, Acinetobacter baumannii, Pseudomonas aeruginosa* and *Enterobacter* species) [28], MRSA has been reported to be the most common pathogen in ventilator associated pneumonia (VAP), respiratory tract infections and second rank in surgical site infections (SSI) [29]. It has been the second leading cause for nosocomial bacteraemia, pneumonia and cardiovascular infections in the US [30-32].

1.2.1 Resistance mechanisms and MRSA prevalence in Europe

Antibiotic resistance is encoded on plasmids which can be exchanged by horizontal transfer among strains and species, but even among different genera, which makes resistance spread control a very complex issue [33-35].

The colonisation with MRSA increases the likeliness to be infected with another multi-drug resistant organism (MDO). It was shown that *S. aureus* resistant to clindamycin is highly unresponsive to structurally related erythromycin (97.2 %) and vice versa (58.3 %). The same applies for fusidic acid resistant strains, when tested for clindamycin/erythromycin resistance (34.5/33.2 %) in comparison to susceptible strains (13.1/12.8 %) [36].

The intrinsic methicillin resistance is encoded on the *mecA* gene. Its gene product is the modified penicillin binding protein 2a (PBP2a) which lacks affinity to beta-lactam antibiotics. It is part of the staphylococcal cassette chromosome mec (SSCmec) [37]. PBP2a is a transpeptidase which can take over cell wall biosynthesis blocked by beta-lactam antibiotics [38].

As methicillin resistance is highly prevalent in *S. epidermidis* and horizontal resistance transfer could also be shown between *S. epidermidis* and *S. aureus* during antibiotic treatment, *S. epidermidis* was the suggested reservoir for SSCmec [37].
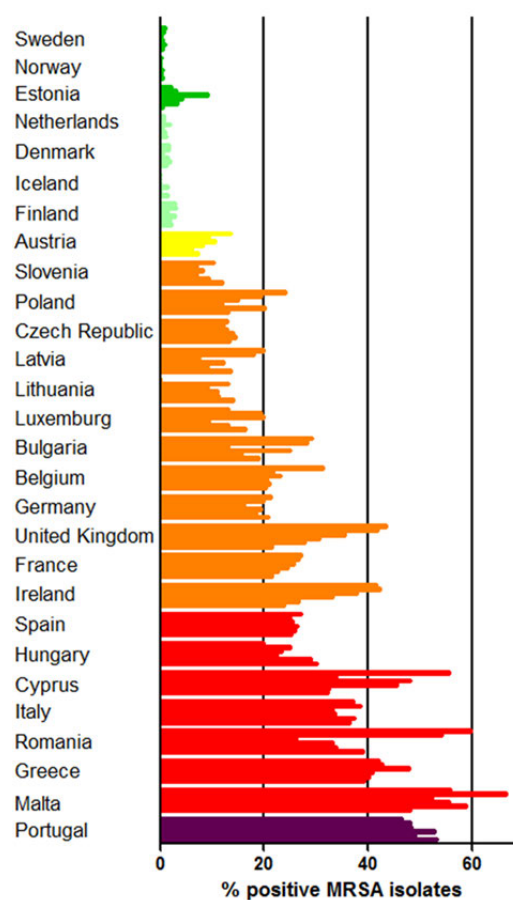
Figure 1: Overview of MRSA positive isolates in Europe from 2005 to 2010 [39] sorted by numbers of positive isolates from 2010 increasing from top to bottom. Green indicates an oxacillin resistance of <1 %, light green <5 %, yellow <10 %, orange <25 %, red <50 % and purple >50 % in 2010. Figure was generated with GraphPad Prism 5 version 5.01 for Windows (GraphPad Software, La Jolla California USA, www.graphpad.com).

Average methicillin resistance data for Europe are consistent with the data known for the US, whereas the resistance rate in southern Europe is still higher than 50 %. Only Scandinavia, Estonia and the Netherlands remain at low drug resistance levels, but even there drug resistance is increasing [37, 39]. Over the past years Germany, Spain and Belgium were stable with an incidence of approximately 20 % for positive oxacillin resistance. Although the UK and Ireland were able to decrease resistance rates by approximately 50 %, they still exceed 20 %. The highest frequencies were found in Malta and Portugal with more than 50 % [39] (see Figure 1). Even higher levels are observed in other parts of the world like Taiwan, Hong-Kong, Singapore, Japan, much of South America and Middle East as well as in Africa [37, 40-42].

1.2.2 MRSA treatment

As seen before, antibiotic resistance is a serious problem in *S. aureus* infection treatment. Although new drugs have been approved, their targets remain invariable in comparison to existing antibiotics. The classical targets like cell wall synthesis, protein biosynthesis and gyrase inhibitors are still in focus of the drug development process.

Despite the existence of some new antibiotics (daptomycin, linezolid and tigecycline) adding to the classic antibiotics (trimethoprim/ sulfamethoxazole, clindamycin), the glycopeptide antibiotic vancomycin remains the first-line drug for MRSA treatment.

Glycopeptide antibiotics inhibit crosslinking of the bacterial cell wall by interference with a terminal L-aa-D-alanyl-D-alanine group as a part of murein [43]. Thus, important components like N-acetylglucosamin and N-acetylmuramic acid cannot be integrated into the cell wall. Unfortunately, vancomycin resistance is increasing among MRSA due to resistance transfer between MRSA and vancomycin resistant enterococci (VRE) [44].

The semi-synthetic glycopeptide dalbavancin carries additional sugars and a C-terminal dimethyl-aminopropyl group. These modifications enhance activity also against vancomycin resistant staphylococci and VRE [45-48]. It has been approved in the US by the Food and Drug Administration (FDA) in 2007, but Pfizer withdrew the global market application for additional phase-III trials in 2008 (http://www.drugs.com/history/dalbavancin.html; accessed: August 22, 2012). Also the glycopeptide oritavancin carries additional side chains which can on the one hand interfere with the bacterial cell wall synthesis and on the other hand disrupt cell

membrane potential. This would make oritavancin an additional drug to treat vancomycin resistant bacteria [49]. In 2008, global market application was withdrawn by the FDA (http://www.drugs.com/history/oritavancin.html; accessed: August 22, 2012).

Telavancin shares this twofold mode of action as seen for oritavancin [50] and is FDA approved since 2009 (http://www.drugs.com/history/vibativ.html; accessed: August 22, 2012) and also approved by the European Medicine Agency (EMA) since 2011 [51].

The lipophilic glycopeptide daptomycin disrupts cell membrane potential and is used to treat bacteraemia, endocarditis [52] and complicated tissue infection [53], but not pneumonia [54].

Ceftaroline belongs to the antibiotic class of cephalosporins, a class of β-lactam antibiotics. It shows increased stability against β-lactamases compared to first generation cephalosporins [55]. It is FDA approved for complicated skin and skin structure infections and community acquired pneumonia (http://www.accessdata.fda.gov/scripts/cder/drugsatfda/index.cfm?fuseaction=Search .DrugDetails; Accessed: August 22, 2012) and still under EMA revision [56].

Linezolid is an oxazolidinone compound and interacts with the 50S ribosomal subunit, but it has notable side effects like bone marrow suppression, lactic acidosis, peripheral and optic neuropathy and serotonin syndrome [57]. These results limit the applicability for MRSA bacteraemia [58].

Retapamulin, a pleuromutilin, is used to treat bacterial skin infections such as impetigo and interacts with the 50S ribosomal subunit by a different mechanism than quinolones and β-lactams as it exhibits antimicrobial activity against clinical isolates carrying resistance determinants to these classes of protein synthesis inhibitors [59].

Clindamycin and the group of tetracycline derivatives act bacteriostatic by inhibiting the protein biosynthesis via interference with the 30S and 50S ribosomal subunits respectively.

Trimethoprim/ sulfamethoxazole, clindamycin and the tetracyclines are presently used to treat *Ca*MRSA skin and soft tissue infection [60], whereas vancomycin showed better results regarding the duration of bacteraemia, sterilisation of wound culture and reduction of fever [61].

Trimethoprim/ sulfmethoxazole inhibit the folate biosynthesis which results in purine starvation, but it may be less effective in the presence of pus from which *S. aureus* is

able to salvage thymidine [62]. Recently it was shown, that an upcoming resistance for combinatorial therapy with cotrimoxazole is occurring [63].

Rifampicin is an effective drug, but it has notable side-effects like teratogenicity [64, 65]. Therefore, the application is limited to combinatorial therapy. However, an inhibition of PVL production has been demonstrated [66].

Lysostaphin is a bacteriocin with lytic activity against staphylococci [67]. It was shown that lysostaphin is able to eradicate susceptible *S. aureus* and *S. epidermidis* biofilms [68]. In a rabbit model it could show effectiveness against keratitis [69], but it is not yet in clinical use.

To prevent antibiotic resistance, the treatment with narrow-spectrum antibiotics is desirable, but not always feasible. In the case of sepsis, the evidence of MRSA can be determined in blood culture tests. In case of internal infections like pneumonia or endocarditis data from a retrograde colonisation tests could help to identify the pathogen [70]. However, under these conditions no proof of pathogen is possible and physicians have to rely on antibiotics with additional anti-gram negative activity. Antibiotics should be selected based on local epidemiology, but if the pathogen is unknown, a broad-spectrum approach has to be applied [71]. Penicillins can also be combined with β-lactamase inhibitors like tazobactam [72, 73].

Resistance against tigecycline is not widely distributed [63], but it has limited effectiveness against gram-negative *Pseudomonas aeruginosa* [74], and is not reliable if the pathogen is not identified.

1.3 The vitamin B1 biosynthesis of *S. aureus* as potential drug target

1.3.1 Vitamin B1: an overview

Vitamins have been discovered many centuries ago. However, modern classification was of course not applied and composition of plant and animal-extracts could not be further investigated. In these times the role of vitamins was associated with medication of deficiency diseases.

One of these diseases, first described by the Dutch physician Jacobus Bonitus in 1630, is the vitamin B1 deficiency beriberi [75]. Vitamin B1 is also called thiamin (formerly aneurin) and has been considered as the anti-beriberi factor in a study carried out by the Dutch physician Christiaan Eijkman towards the end of 19th century. He found a connection between beriberi and the diet of polished rice and discovered that chicken develop polyneuritis, which is similar to human beriberi when

given polished rice as main food. This effect could be reversed by feeding the thiamin rich silver skin [76]. Almost forty years later Eijkman was awarded the Nobel Prize in Medicine together with the British biochemist and physician Frederick Gowland Hopkins for their contribution in the field of vitamins [77].

Structure and synthesis of thiamin were published in 1936 by Robert R. Williams and Adolf Windaus [78]. Before that time, beriberi was endemic in East Asia, were rice consumption increased the beriberi risk. The peak was reached in 1923 with nearly 28,000 deaths in Japan [79] and a rank among the 15 most common causes of death at that time [80].

By the time Williams and Windaus elucidated the thiamin structure, Rudolph Peters linked thiamin to pyruvate metabolism [81]. In the late 1950s Ronald Breslow determined the ylid formation in thiamin at C2 position, which is essential for thiamin catalysed reactions [82].

1.3.2 Thiamin as a prosthetic group in enzymatic reactions

Thiamin consists of a thiazole- and a pyrimidine ring linked by a methylene bridge (see Figure 2). Within the living cell, the thiamin has to be converted into its biologically activated form thiamin pyrophosphate (TPP) to act as prosthetic group of enzymes.
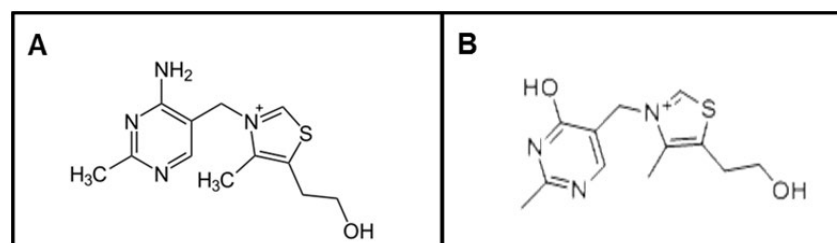
Figure 2: **Thiamin (A) and its antagonist oxythiamin (B). Figures were generated through Accelrys draw 4.0 (Accelrys Software Inc., USA).**

In TPP catalysed reactions, the thiazolium ring is deprotonated at C2 position and a reactive carbanion is formed which is stabilised by 3d orbitals of neighbouring sulphur (ylid-group) [83]. It was shown that thiamin derivatives having an oxazolium or imidazolium ring, are less reactive than the thiazolium compound, as in the absence of 3d orbitals the transition state cannot be stabilised [82, 84, 85]. Also, turnover of decarboxylation is more than 1,000 times faster for α-mercaptocarboxylic acids than for their oxygen containing counterparts [86-88]. Additionally, oxazolium

compounds underwent ring opening, which explains the lack of activity [89]. Higher electronegativity of oxygen in comparison to sulphur also favours hydrolysis even if 3d orbitals would be present [83].

The ylid reacts with the carbonyl carbon of α-ketoacids (2-oxoacids) to form the thiamin bound acetaldehyde intermediate in addition to CO_2 elimination, which can be seen in decarboxylation of pyruvate by the pyruvate-dehydrogenase complex (see Figure 3). Thiamin that is methylated at C2 position showed no biological activity [90]. The thiamin antagonist oxythiamin (see Figure 2 B) binds in its pyrophosphorylated form to the active site of the pyruvate dehydrogenase. It is able to form the C2-adduct, but the aldehyde is not released [91].
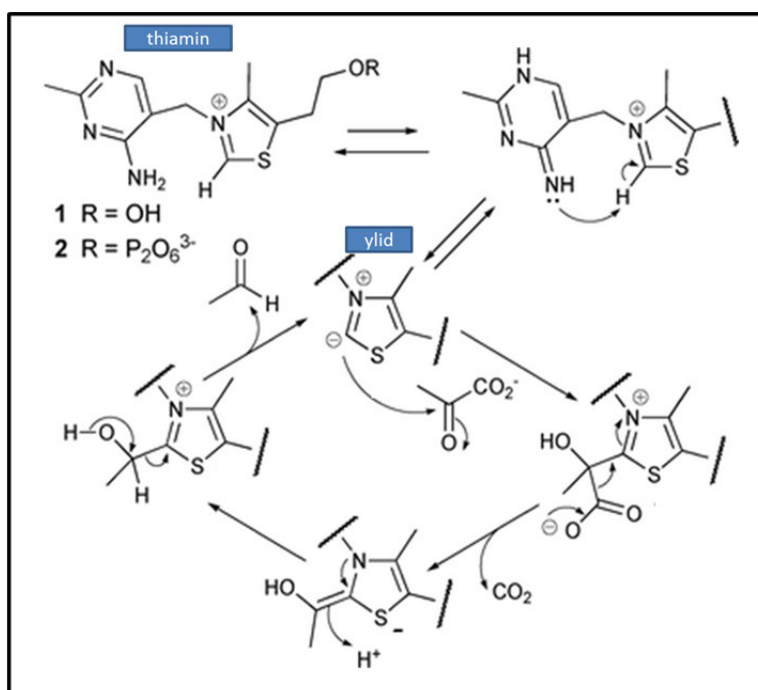
Figure 3: Thiamin catalysing pyruvate decarboxylation. Thiamin is bound as a prosthetic group to the pyruvate-dehydrogenase complex, where it is able to form the reactive ylid-group. The carbanion performs a nucleophilic addition to the carbonyl group of pyruvate to yield a thiamin bound acetaldehyde intermediate. Acetaldehyde is released after CO_2 elimination. Figure modified from [92].

1.3.3 Role of vitamin B1 in humans and bacteria

In animal tissue, thiamin is most abundant in the enzyme bound form. In the free state it can form thiamin monophosphate (TMP), thiamin pyrophosphosphate (TPP) and thiamin triphosphate (TTP) [79]. It has also been considered, that thiamin plays a role in nerve excitation and is released during this process [93].

In bacteria, an accumulation of TTP was observed during amino acid starvation. This could account for a signalling pathway, initiated trough extreme nutritional situations.

Also, a new adenosine thiamin triphosphate (ATTP) compound was identified during amino acid starvation. It might act as signal molecule to highlight carbon starvation and a low energy state [94].

In most thiamin-catalysed reactions, the holoenzyme catalyses the cleavage of a 2-oxoacid and subsequently transfers one of the cleavage products to an acceptor in the presence of divalent Mg^{2+}. Reactions can be divided into oxidative decarboxylation and transketolations. From the first class of reaction the conversion of i) pyruvate to acetyl- coenzyme A (CoA), ii) 2-oxoglutarate to succinyl-CoA and iii) branched chain 2-oxoacids to corresponding acyl-CoAs is carried out. This assigns special importance towards thiamin as a cofactor in essential reactions of the carbohydrate and amino acid- metabolism. TPP is bound as a lipoic acid to a lysine residue and catalyses reactions which link the glycolysis with the citric acid cycle [79]. The 2-oxoglutarate dehydrogenase complex converts 2-oxoglutarate to succinyl-CoA in the citric acid cycle and the branched chain 2-oxoacid dehydrogenase is a multienzyme complex within the inner mitochondrial membrane that degrades the branched-chain amino acids valine, isoleucine and leucine after transamination [79].

The second class of thiamin containing enzymes are transketolases. They catalyse non-oxidative decarboxylations and form aldehydes. They link glycolysis with the pentose phosphate pathway and transfer a keto-group from xylulose-5-phosphate to ribulose-5-phosphate to yield glyceraldehyde 3-phosphate [95].

Due to the central role of thiamin dependent enzymes in amino acid and carbohydrate metabolism, thiamin deficiency diseases or mutations in genes encoding for thiamin dependent enzymes, lead to severe neurological impairment in humans.

During thiamin deprivation, mammals develop polyneuritis, which is related to hypomotility, tremors, ataxia and convulsions due to pathophysiological changes in the central nervous system, in which thiamin is relevant for nervous stimulation [96].

Alcoholism is the most common cause of thiamin deficiency. The diet-related decreased TPP and transketolase levels affect the enzymes of the oxidative metabolism [97, 98] [79].

1.3.4 Vitamin B1 biosynthesis, transport and regulation in *S. aureus*

Thiamin can be synthesised *de novo* by most bacteria, fungi and plants [99, 100]. Some bacteria form exclusively the pyrimidine or only the thiazole part, depending on the compound they are able to synthesise.

In a few bacteria, thiamin ATP-binding cassette (ABC) transporters were found, but in *S. aureus* only a precursor of the pyrimidine portion is thought to be transported via the microbial membrane. The *E. coli* thiamin binding protein (TbpA) binds not only to thiamin itself but also to its mono and pyrophosphorylated forms [101]. The analysis of THI elements (thiamin-pyrophosphate riboswitches) revealed the presence of the *ykoE-ykoD-ykoC* genes encoding for a two transmembrane components (YkoE and YkoC) and an ATPase component (YkoD) predicted to actively transport the pyrimidine moiety of thiamin via the microbial membrane. These genes co-occur with the biosynthetic genes regulated by a THI element [102].
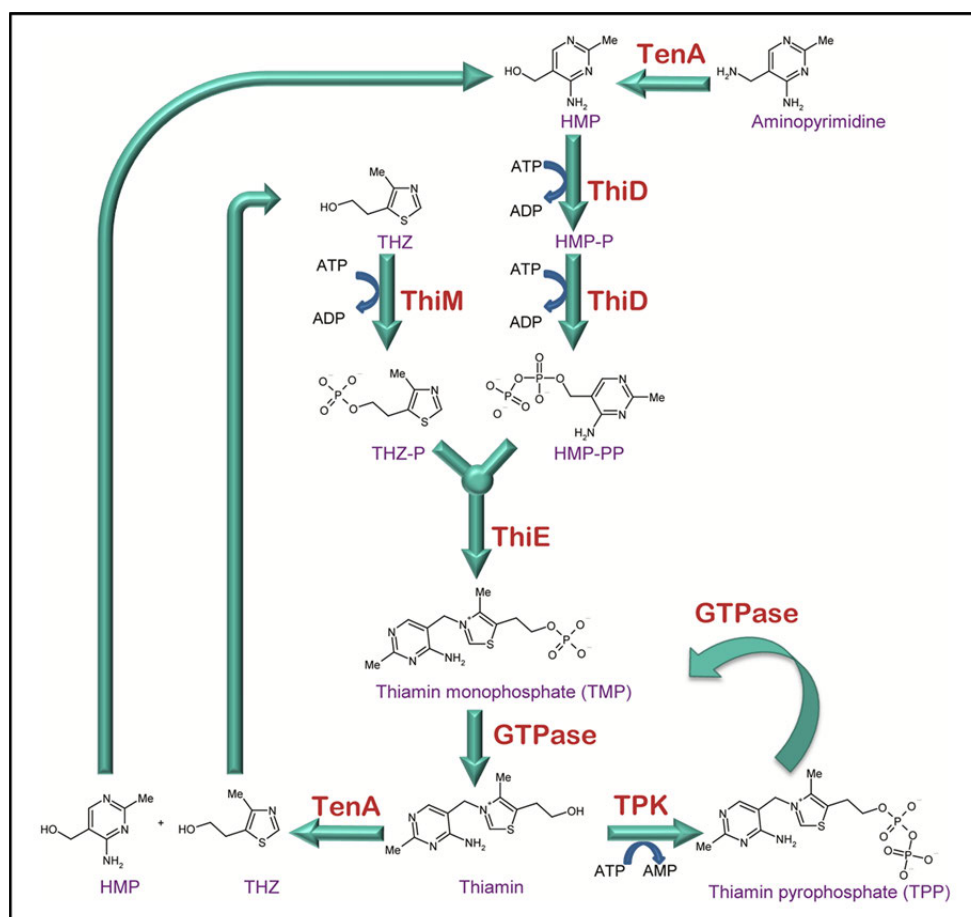
Figure 4: Thiamin biosynthesis in *S. aureus*. TenA deaminates aminopyrimidine to HMP, which is subsequently phosphorylated in two iterative steps by ThiD. ThiM phosphorylates THZ and ThiE links THZ-P and HMP-PP to TMP. A GTPase dephosphorylates this intermediate to yield thiamin. Thiamin can either be pyrophosphorylated by TPK or cleaved by TenA depending on TPP levels. Enzymes are highlighted in red, intermediate names in purple. Modified after [103].

In *Staphylococcus aureus,* the thiazole and the pyrimidine moiety of thiamin are synthesised independently and then linked in a further step. Proteins Involved in biosynthesis are organised in two operons. The first operon encodes for a thiaminase type II (TenA, EC 3.5.99.2), 4-amino-5-hydroxymethylpyrimidine kinase (ThiD, EC 2.7.1.49), 5-(2-hydroxyethyl)-4-methylthiazole kinase (ThiM, EC 2.7.1.50) and thiamin phosphate synthase (ThiE, EC 2.5.1.3). A phosphatase, an epimerase and the thiamin pyrophosphokinase (TPK, EC 2.7.6.2) are encoded separately on a further operon.

During biosynthesis 5-(2-hydroxyethyl)-4-methylthiazole (THZ) is phosphorylated by ThiM such as 4-amino-5-hydroxymethylpyrimidine (HMP) is pyrophosphorylated in a two-step mechanism by ThiD. THZ and HMP derivatives are linked by ThiE yielding thiamin monophosphate (TMP), which is subsequently dephosphorylated by a GTPase [103]. The direct phosphorylation of TMP in *S. aureus* is not possible due to the lack of the TMP kinase ThiL (EC 2.7.4.16) existing in yeast and some bacteria [99, 104].

In *S. aureus,* thiamin can be pyrophosphorylated by TPK thereby turning thiamin into its active form TPP. However, if TPP is not required thiamin is recycled through cleavage. The latter is performed by TenA which either cleaves thiamin (but not its phosphate esters) into its thiazole and pyrimidine portions or converts aminopyrimidine to hydroxypyrimidine. The deamination reaction is 100 times faster than the hydrolysis of thiamin [94]. In *Saccharomyces cerevisiae* TenA and ThiD are fused into one protein [102]. The chromosomal clustering of TenA with the biosynthetic enzymes, which can also be seen in *B. subtilis,* is consistent with the finding that TenA rather deaminates HMP precursors than degrades thiamin [105, 106]. It was also proposed that TenA plays an important role in HMP salvage from base-degraded forms of thiamin from soil [105].

In *Bacillus thiaminolyticus*, a pathogen toxic to the host due to its thiamin cleavage activity, a thiaminase I (TenI) with structural similarity to TbpA has been identified. This suggest a common ancestor, but low sequence identity indicates evolutionary divergence [107]. TenI is less widely distributed than TenA and is usually found in clusters with other thiamin biosynthetic proteins or salvage genes. It shows sequence similarity to ThiE, particularly in the active site region, which suggests that it is able to bind TMP [108].

Thiamin biosynthesis is regulated by riboswitches. They consist of a TPP sensing non-coding mRNA element, which, after binding to TPP, undergoes a conformational change. For that reason, high TPP concentrations prevent protein biosynthesis through blocking the ribosomal binding site [109, 110]. This regulation was shown for *tenA-thiM-thiD-thiE* operon as 28 % of TPP binds to the 5′-UTR of this gene cluster, but regulation by TPP of *gtpase-epi-tpk* operon is limited due to poor TPP binding capacity [103]. In *B. subtilis,* this gene cluster is not regulated by thiamin or HMP, but slightly repressed by THZ [111].

Additionally to transcriptional regulation, a GTPase that is encoded on the *gtpase-epi-tpk* operon also accepts TPP as a substrate too which implies further regulation on translational level [103].

1.4 Suicide-drugs to treat staphylococcal diseases

As seen in chapter 1.2.2, MRSA treatment is limited and there is an urgent need to develop new antibiotics. Current medications still use classical targets and novel approaches are only rarely found. Despite emerging resistance, the FDA approval of new drugs was decreased by 75 % from 1983 to 2007 [1] and only a few attempts have been made to discover pro-drugs, a class of antibiotics that have to be activated by a bacterial compartment.

The use of protein 3D information for structure based drug discovery has been applied successfully in former studies [112]. A new approach for antibiotic development is a special class of pro-drugs combining two features: they interfere with a bacterial pathway, absent in the human host, but instead of inhibiting this pathway, they are metabolised by the bacterium. The product of this process, the suicide-drug, poisons then specifically co-factor dependent enzymes (see Figure 5). This was already approved for the malaria parasite *Plasmodium falciparum*. The compound is trapped after uptake within the cell and the toxic co-factor poisons PLP dependent enzymes [113]. This approach targeting the thiamin biosynthesis in *S. aureus* will be addressed in this work.

This means that classic approaches can be combined in a new way. Unique pathways have to be screened and analysed. Additionally, uptake mechanisms have to be taken into account. Instead of inhibiting the targeted pathway, the toxic product poisons a wide variety of co-factor dependent enzymes (see Figure 5).
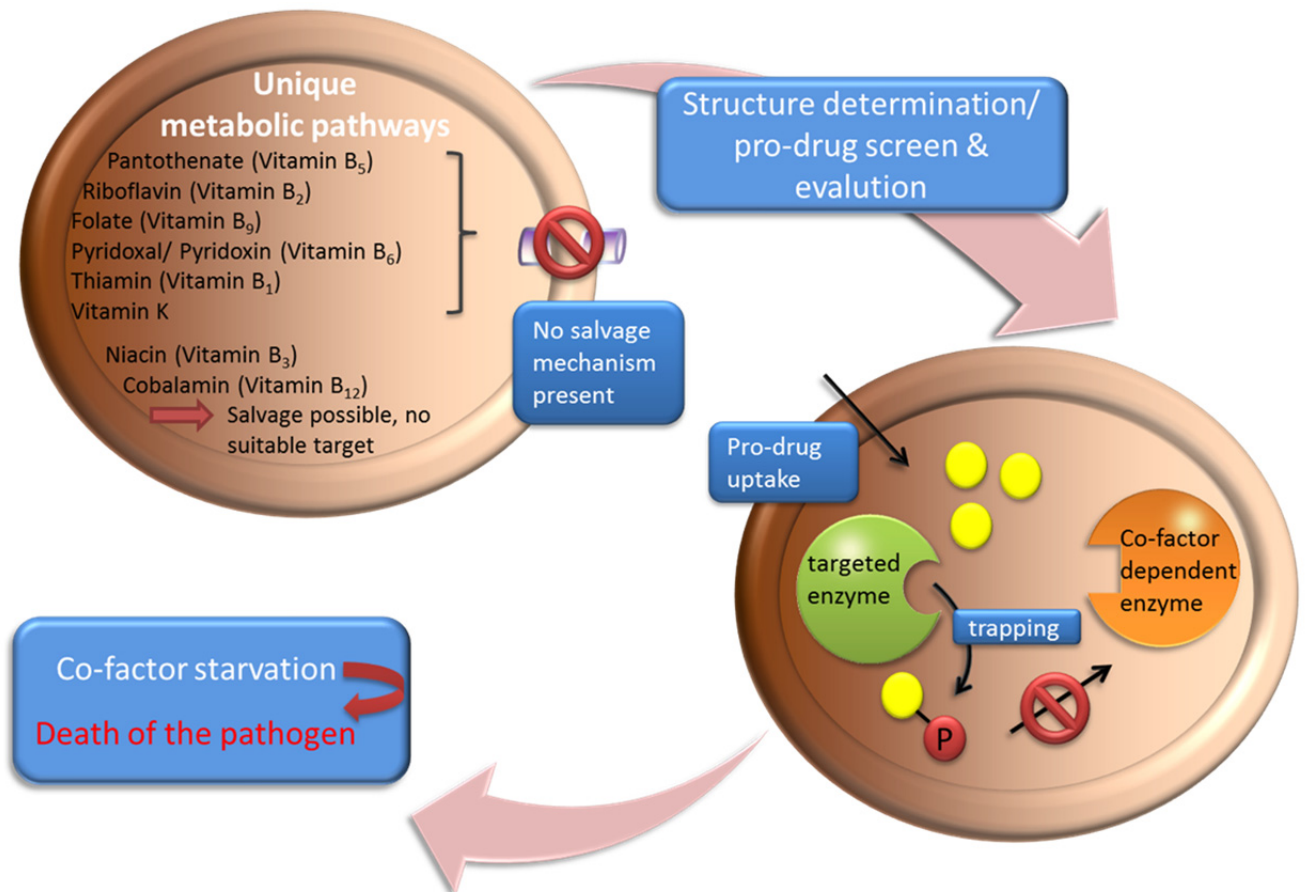
Figure 5: Principle of suicide-drug inhibition addressed in this work targeting the thiamin biosynthesis in *S. aureus*. **Metabolic pathways that are unique to the bacterium are targeted by the pro-drug. Instead of inhibition of the targeted enzyme, the pro-drug is metabolised by the pathogen and this modified co-factor poisons co-factor dependent enzymes, resulting in the pathogen´s death.**

2 AIM OF THIS WORK

Staphylococcus aureus is a commensal bacterium that colonises 20 % of the population permanently and up to 60 % transiently [6]. Infections with the methicillin resistant form MRSA are a major concern in nosocomial disease control, as resistance against one class of antibiotics is often associated with the phenomenon of multi-drug resistance. In Germany alone 40,000 patients die per year as a result of hospital infections, mainly by its most famous representative MRSA [4]. This necessitates the discovery and characterisation of novel antibiotics interfering with pathways specific to the bacterium.

One of these pathways is the thiamin biosynthesis in *S. aureus*, which is absent in humans as their needs are covered by dietary uptake. This is important to prevent side-effects and allows to specifically targeting the bacterium.

The thiamin biosynthesis pathway has been characterised biochemically, but structural information of the involved enzymes was absent so far.

In the course of this thesis, 3D-structures of involved enzymes should be analysed in order to obtain a detailed insight into active site architecture. Subsequently, the information should be used for structure-based pro-drug discovery. The main emphasis should lie on the analysis of ThiM as one of the first enzymes participating in thiamin synthesis. With the active site information, putative substrate analogues should be identified and characterised in terms of activity alone and in comparison to the natural substrate. The ideal substrate analogue (pro-drug) would be metabolised by the bacterium and would yield an inactive thiamin, which poisons thiamin dependent enzymes. Thus, a drug would be developed which primarily interferes with the thiamin biosynthesis, but as a consequence would disrupt all thiamin dependent processes in the bacterium.

Also, structural information of other involved enzymes like TPK should be obtained to optimise the potential pro-drug.

Another topic that should be addressed in this work is the relationship of oligomeric state and its biological function by taking the example of the thiaminase II TenA. Structural data should be obtained and based on this, interface residues should be selected for *site directed* mutagenesis. Different TenA species should be compared regarding their activity and stability in order to analyse the influence of oligomerisation.

3   MATERIAL AND METHODS

3.1   Instrumentation and Chemicals

3.1.1   Instrumentation

Beamlines   <u>X13, consortium beamline, HASYLAB/DESY, Hamburg, Germany</u>

Synchrotron source: bending magnet

Wavelength: 0.81 Å

Focal spot: 2 mm x 0.4 mm

Detector: MARCCD 165 mm

<u>X33, SAXS beamline, EMBL, HASYLAB/DESY, Hamburg, Germany</u>

Synchrotron source: DORIS bending magnet

Wavelength: 1.5 Å

Focal spot: 2 mm x 0.6 mm

Detectors Photon counting Pilatus 1M-W pixel detector; Photon counting Pilatus 300K-W pixel detector; Mar345 image plate (345 mm^2)

<u>A1 beamline, CHESS, Ithaca, USA</u>

Synchrotron source: bending magnet 49 pole wiggler

Wavelength: 0.987 Å

Focal spot: 1 mm x 0.2 mm

Detector: ADSC Quantum-210

<u>F1 beamline, CHESS, Ithaca, USA</u>

Synchrotron source: bending magnet 24 pole wiggler

Wavelength: 0.918 Å

Focal spot: 1 mm x 0.2 mm

Detector: ADSC Quantum-270

Centrifuges

Centrifuge 5804R (Eppendorf, Germany)

Centrifuge 5415R (Eppendorf, Germany)

Centrifuge 5424 (Eppendorf, Germany)

Centrifuge 5415C (Eppendorf, Germany)

Centrikon T-1065 (Kontron, Germany)

Optima TL Ultracentrifuge (Beckman Coulter, USA)

Avanti J-26 XP (Beckman Coulter, USA)

Megafuge 1.0 R (Heraeus, UK)

PCR machines   UNO II (Biometra, Germany)

TProfessional (Biometra, Germany)

Spectrophotometer	UVIKOM-Spectrophotometer 932 (Bio-Tek Kontron Instruments, Germany)
Water baths and Incubators	GFL 1092 (GFL, Germany)
	GFL 1002 (GFL, Germany)
	GFL 3033 (GFL, Germany)
	Memmert Incubator (Memmert, Germany)
Thermoblock	Thermostat 3401 (Eppendorf, Germany)
Crystallization robots	Honeybee 961 (Genomic Solutions, USA)
DLS instrumentation	SpectroSIZE 300 (Nabitec, Germany)
Imaging	CrystalScore (Diversified Scientific Inc., USA)
	Microscope SZX12 with camera DP10 (both Olympus, Japan)
Crystal plate incubator	RUMED 3001 (Rubarth, Germany) incubators
Microbalance	Sartorius CP224S-OCE (Sartorius, Germany)
pH Meter	Five Easy FE20 (Mettler-Toledo, Switzerland)
	pH 211 (Hanna Instruments, USA)
FPLC machine	ÄKTA Purifier P-901 (GE Healthcare, UK)
CD-Spectrometer/polarimeter	J-815 (Jasco, UK)
Photospectrometry	Nanodrop 2000c (ThermoScientific, Peqlab, Germany)
Pipetting robots	Lissy (Zinsser, Germany)
SDS-PAGE	EV734 Power Supply (Consort, Belgium)

	Hoefer Mighty Small II SE 250 electrophoresis chamber (Hoefer, USA)
Western Blot	Semi Dry Blotter Unit 20 x 20 cm (Roth, Germany)
Agarose Gels	Horizon 11.14 (Biometra, Germany)
	PowerPac Basic (Bio Rad, USA)
UV-light source	CrystalLIGHT 100 (Nabitec, Germany)
UV Transilluminator	Phero-lum 285 (Biotech Fischer, Germany)
Tube Rotators	Roller mixer SRT6D (Stuart, UK)
	Rotator SB3 (Stuart, UK)
Microwave	MR-6450 (Hitachi, Japan)
Scanner	Canon9950S (Canon, USA)
Beta/ Gamma Counter	LS 5000 CE (Beckman Coulter, USA)
NMR Spectrometer	DRX 700 MHz (Bruker BioSpin, USA)

3.1.2 Bacterial strains and plasmids

3.1.2.1 <u>Bacterial strains</u>

E. coli DH5α (Stratagene, USA)

E. coli XL10 Gold (Stratagene, USA)

E. coli BLR (DE3) (Stratagene, USA)

3.1.2.2 <u>Plasmids</u>

pASK-IBA3 (IBA, Germany)

pRK793 (NEB, USA)

3.1.3 Primer

Table 1: Primer sequences used for cloning and *site directed* mutagenesis in 5′→3′ direction. Mutation sites are underlined for mutagenesis primers.

Primer for cloning	
SaTPK-S	5′-GCGCGCGGTCTCCAATGCATATAAATTTATTATGTTC-3′
SaTPK-TEV-His-Stop-AS	GCGCGCGGTCTCAGCGCTTTAATGATGATGATGATGATGGCCCTGAAAATAAAGATTCTCATTTAAATCTGTACTTCTAATTTGC-3′
SaThiM-S	5′-GCGCGCGGTCTCGAATGAATTATCTAAATAACATACGTATTG-3′
SaThiM-TEV-His-Stop-AS	5′-GCGCGCGCGCGCGGTCTCAGCGCTTTAATGATGATGATGATGATGGCCCTGAAAATAAAGATTCTCTTCCACCTCTTGAATGCGAATCCG-3′
SaThiE-His-TEV-S	5′-GCGCGCGGTCTCGAATGCATCATCATCATCATCATGGTGAAAATTTATATTTTCAAGGTTTTAACCAATCGTATCTAAATGTG-3′
SaThie-Stop-AS	5′-GCGCGCGGTCTCAGCGCTTTAATTATTAAAAAAATCTTTGAATCGA-3′
SaTenA-S	5′-GCGCGCGGTCTCGAATGGAATTTTCACAAAAATTGTACCAAGC-3′
SaTenA-TEV-His-Stop-AS	5′-GCGCGCGGTCTCAGCGCTTTAATGATGATGATGATGATGGCCCTGAAAATAAAGATTCTCATCATTTACTTTTCCTCCAAATTCCC-3′
SaThiD-His-TEV-S	5′-GCGCGCGGTCTCGAATGCATCATCATCATCATCATGGTGAAAAATTATATTTTCAAGGTATTAAACCTAAAATAGCATTAACC-3′
SaThiD-Stop-AS	5′-GCGCGCGGTCTCAGCGCTTTATTTAGATAATTCATCGTCTAATCCC
SaGTPase-S	5′-GCGCGCGGTCTCGAATGAAGACAGGTCGAATAGTGAAATC-3′
SaGTPase-TEV-His-Stop-AS	5′-GCCCGCGGTCTCAGCGCTTTAATGATGATGATGATGATGGCCCTGAAAATAAAGATTCTCATATCTAACCTTTCTATTTGAAATTTC-3′
Mutagenesis Primer	
SaTenA-K49S-S	5′-CAAGCTGATGCAGCTTATTTA<u>AGT</u>GAATTTACAAACTTATATGC-3′
SaTenA-K49S-AS	5′-GCATATAAGTTTGTAAATT<u>CAC</u>TTAAATAAGCTGCATCAGCTTG-3′
SaTenA-E76A-S	5′-CGTAAAATTTTTAGTAGAGCAAATA<u>GCA</u>TTTATGGTTGAAGGTGAAG-3′
SaTenA-E76A-AS	5′-CTTCACCTTCAACCATAAA<u>TGC</u>TATTTGCTCTACTAAAAATTTTACG-3′
SaTenA-D111A-S	5′-GTTTGGCCTCCAAGTGGC<u>GCC</u>CATTACATAAAACATATGTATTTCAA-3′
SaTenA-D111A-AS	5′-TTGAAATACATATGTTTTATGTAATG<u>GGC</u>GCCACTTGGAGGCCAAAC-3′
SaTenA-D111-K115A-S	5′-CGCTTGGAAATACATATG<u>TGC</u>TATGTAATG<u>GGC</u>GCCACTTGGAGGCCAAAC-3′
SaTenA-D111A-K115A-AS	5′-GTTTGGCCTCCAAGTGGC<u>GCC</u>CATTACATA<u>GCA</u>CATATGTATTTCCAAGCG-3′

3.1.4 Buffers and solutions

If not specified, pH was adjusted with HCl or NaOH.

General buffers

Buffer W   100 mM tris/HCl, 150mM NaCl, pH 8, autoclaved

1 x TBE buffer	90 mM tris, 90 mM borate, 2 mM EDTA, pH 8.0 autoclaved
1 x PBS	10 mM Na_2HPO_4, 1.8 mM KH_2PO_4, 2.6 mM KCl, 136.9 mM NaCl, pH 7.4, autoclaved

E. coli cell culture

LB-medium/ agar	1.0 % Bacto-Tryptone, 0.5 % Bacto-Yeast-Extract, 1.0 % NaCl in dH_2O, autoclaved For LB-agar: 1.5 % agar-agar in LB-medium
Selective antibiotic	50 mg/ml ampicillin in 50 % ethanol (abs.); stock solution 25 mg/ml chloramphenicol in 50 % ethanol (abs.); stock solution
Anhydrotetracycline	2 mg/ml in DMF; stock solution
IPTG	1 M in dH_2O; stock solution

Protein purification

Protease inhibitor	0.1 M PMSF in isopropanol
His-lysisbuffer	Buffer W with 10 mM imidazole (imidazole addition after autoclaving)
His-washingbuffer	Buffer W with 20 mM imidazole (imidazole addition after autoclaving)
His-elutionbuffer	Buffer W with 250 mM imidazole (imidazole addition after autoclaving)
Strep-elutionbuffer	2.5 mM desthiobiotin (buffer E, IBA, Germany) in buffer W
TEV storage buffer	20 % glycerol, 5 mM DTT in buffer W

Agarosegel electrophoresis

Loading dye   0.05 % bromophenol blue, 0.25 % xylene cyanol, 1 mM
                           EDTA, 50 % glycerol

Ethidium bromide   10 mg/ml in dH_2O

Competent cells

100 mM $CaCl_2$, autoclaved

100 mM $CaCl_2$, 10 % glycerol, (glycerol addition after autoclaving)

SDS PAGE

1 x running buffer   192 M glycine, 25 mM tris, 0.1 % SDS in H_2O

6 x sample buffer   2 % SDS (w/v), 50 mM tris, pH 6.8, 10 % glycine (w/v),
                           0.02 % bromophenol blue (w/v), 0.05 % β-
                           mercaptoethanol (v/v)

APS   10 % in dH_2O

Stacking gel buffer   0.5 M Tris/HCl, pH 6.9

Separating gel buffer   1.5 M Tris/HCl, pH 8.9

SDS buffer   10 % (w/v) in dH_2O

Staining solution   45 % methanol (v/v), 10 % glacial acetic acid (v/v), 0.1 %
                           in dH_2O

Destaining solution   20 % ethanol (v/v), 10 % glacial acetic acid (v/v) in dH_2O

Western Blot

Ponceau S   0.2 % Ponceau S (w/v) in 5 % acetic acid (v/v)

22

Transfer buffer	25 mM tris, 192 mM glycine, 20 % methanol (v/v)

Circular dichroism

Protein buffer	50 mM KH_2PO_4, pH 7.5 (pH adjusted with potassium hydroxide)

Activity tests

KH_2PO_4 buffer	1 M in dH_2O, pH 7.5 (pH adjusted with potassium hydroxide); stock solution
ATP	10 mM in dH_2O; stock solution
$MgCl_2$	10 mM in dH_2O; stock solution
THZ	4 mM in dH_2O; stock solution
^{14}C-ATP	10 µCi in dH_2O; stock solution
^{33}P-ATP	7.5 µCi/ml dH_2O; stock solution
Eluent 1	1 M LiCl in dH_2O
Eluent 2	0.1 M LiCl, 0.1 M formic acid in dH_2O

Ni-NTA agarose regeneration

SDS buffer	2 % (w/v) in dH_2O
EDTA buffer	100 mM, pH 8.0 in dH_2O
$NiSO_4$ buffer	100 mM in dH_2O
Regeneration buffer	6 M guanidine chloride, 0.1 M acetic acid

Ethanol buffers	25, 50, 75 % ethanol (den.) in dH_2O

Strep-tactin sepharose regeneration

Regeneration buffer	1 mM HABA in buffer W

Protein quantification

Bradford reagent	0.01 % Coomassie Brilliant Blue G-250 (w/v), 4.7 % ethanol (w/v), 8.5 % (v/v) H_3PO_4

NMR buffer

50 mM tris-*d11*-D_2O, 150 mM NaCl, pH 8 (pH adjusted with DCl)

Crystallisation

For crystallisation, only ethanol (abs.) was used.

3.2   Molecular biology methods

3.2.1   Polymerase chain reaction (PCR)

PCR was used for DNA fragment amplification using *Taq*-polymerase containing PCR supermix (Invitrogen, USA). The reactions were carried out in a Biometra Uno II thermocycler (Biometra, Germany) and the mix was applied according to the manufacturer´s protocol.

For a typical reaction, primers (Sigma, Germany) were diluted to a final concentration of 30 pM and 1 µl of each primer, 1 µl (approximately 100 ng) template and 47 µl PCR supermix were mixed in a PCR tube. The first step in the amplification reaction was denaturation for 5 min at 95 °C followed by 30 cycles of denaturation for 45 s at 95 °C, annealing for 1 min at 48 °C (based on the oligonucleotide annealing temperature, determined by the supplier) and elongation for 1 min at 72 °C (this step was modified based on the number of basepairs to be amplified, as *Taq*-polymerase is able to amplify 1,000 basepairs per minute). When reaction was carried out overnight, samples were stored at 4 °C within the PCR machine. To examine the success of the PCR 5 µl were applied to a 1 % agarose gel (see chapter 3.2.5).

3.2.2 Removal of template-DNA from a PCR reaction

After PCR, the template-deoxyribonucleic acid (DNA) has to be removed from the mixture. This reaction is carried out by *DpnI* restriction endonuclease (NEB, USA). It specifically cuts methylated and hemi-methylated DNA with the motif GA-(CH$_3$)-TC.

For digestion, 1 µl (20 U) of *DpnI* was added to 45-50 µl of the PCR reaction and incubated for 1-2 h at 37 °C. After that, the DNA was purified using the PureLink PCR purification Kit (Invitrogen, USA) (see chapter 3.2.4)

3.2.3 *Site directed* Mutagenesis PCR

Site directed mutagenesis is a technique to specifically insert mutations to a plasmid. The mutation is incorporated using mutagenesis primers, containing the desired mutation. For this type of PCR reaction the *Pfu*-polymerase (Promega, USA) was used, due to its proof-reading function.

Typically, the reaction mix contained 1 µl of each mutagenesis primer diluted to 30 pM, 1 µl of template DNA (approximately 10 ng), 5 µl 10x buffer (Promega, USA), 5 µl dNTP mix and 36 µl dH$_2$O. The program that was used started with denaturation for 5 min at 95 °C and was followed by 16 cycles of denaturation for 30 s at 95 °C, annealing for 1 min at 55 °C and elongation for 8 min at 68 °C as in this type of reaction the whole plasmid had to be amplified.

DpnI digestion (see chapter 3.2.2) was indispensable after *site directed* mutagenesis PCR to assure that only mutated plasmid was transformed into competent cells.

3.2.4 DNA purification

To purify PCR products from salts and DNA-fragments resulted from *DpnI* digest, the PureLink PCR purification kit was used according to the manufacturer´s specifications. Instead of elution buffer, 50 µl dH$_2$O were used to elute the DNA.

3.2.5 Agarose gelelectrophoresis

Agarose electrophoresis is a technique to separate DNA fragments based on their size. Negatively charged DNA is attracted by the anode and moves through an agarose gel depending on agarose concentration, size and conformation of the fragment and applied power.

Typically, 1 g of agarose was heated in 100 ml 1x TBE buffer. The solution was cooled to 50 °C and 5 µl ethidium bromide solution (Sigma, USA) were added to visualise DNA fragments with UV-light.

Samples were mixed with 5x loading buffer containing glycerol to increase density of the solution. To run the gel, 100 V were applied to the agarose gel apparatus. The result was documented with a photo under UV-light.

3.2.6 Restriction enzyme digestion

Restriction enzyme digestion was used to either prepare DNA fragments for latter ligation into a plasmid or to control the success of the ligation.

In the cloning procedure, all fragments were ligated into IBA-3 (IBA, Germany) vectors, containing a *BsaI* (NEB, USA) restriction site. PCR product and vector were digested according to manufacturer's protocol for 2 h at 37 °C. The PCR product and vector were purified (see chapter 3.2.4) separately and eluted in 30 µl dH_2O.

To verify success of cloning, 0.5 µg of DNA preparation after transformation in *E. coli* were digested with relevant restriction endonucleases, typically *XbaI* and *HindIII* (both NEB, USA) and visualised in an agarose gel.

3.2.7 Ligation

To ligate PCR fragments and vector DNA, 1-2 µl linearised vector were mixed with 15-16 µl of *BsaI* digested PCR fragment and in a final volume of 20 µl and incubated with 2 µl of T4-DNA-ligase and 1 µl ligase buffer (both NEB, USA) at 14 °C overnight.

3.2.8 Preparation of chemically competent cells with $CaCl_2$

A single *E. coli* colony or a glycerol stock (200 µl) were used to inoculate 100 ml Luria Bertani (LB)-medium and incubated at 37 °C overnight. The overnight culture was diluted 1:50 in LB-medium (10 ml of overnight culture were added to 500 ml LB-medium) and grown at 37 °C to an optical density at 600 nm (OD_{600}) of 0.6-0.8.

Reaching this OD_{600}, the solution was cooled on ice for 10 min and centrifuged at 4 °C and 4,000 rpm for 10 min.

The supernatant was discarded and cells resuspended in a sterile solution containing 0.1 M $CaCl_2$ and incubated for 15 min on ice.

This suspension was again centrifuged at 4 °C and 4,000 rpm for 10 min and the supernatant was discarded. The cells were resuspended in 5 ml cold 0.1 M $CaCl_2$/ 10 % glycerol containing buffer. Aliquots of 200 µl were shock frozen in liquid nitrogen and stored at -80 °C.

3.2.9 Transformation of plasmids into *E. coli* cells

An aliquot of chemically competent cells was thawed on ice and incubated with 100 ng of plasmid DNA for 10 min on ice. A water bath (GFL, Germany) was pre-heated to 42 °C and cell-DNA mixture was incubated for 1 min at 42 °C. Subsequently the sample was cooled on ice for 1 min and 1 ml of sterile LB-medium was added. The suspension was then incubated for 30 min at 37 °C. After that, it was centrifuged at room temperature (RT) for 30 s and supernatant was decanted. Cells were resuspended with residual LB-medium and plated in a sterile environment. Plates contained 1.5 % agar-agar and the respective antibiotic for selection.

After incubation overnight at 37 °C, colonies were picked and further analysed. For subsequent DNA isolation, competent *E. coli* XL10-Gold or DH5α cells, for expression BLR (DE3) cells were used for transformation.

3.2.10 Isolation and purification of plasmids

A single *E. coli* colony was used to inoculate 3 ml of antibiotic containing LB-medium and incubated at 37 °C overnight. Plasmids were isolated with the peqGOLD plasmid Miniprep Kit I (peqlab, Germany) according to the manufacturer´s protocol.

3.2.11 DNA-sequencing

To investigate success of cloning or mutation insertion, plasmid DNA was sequenced by SeqLab by extended hotshot sequencing. Samples were prepared mixing 6 µl of DNA with 1 µl of sequencing forward or reverse primer.

3.3   Biochemical methods

3.3.1 Recombinant expression of proteins

For recombinant expression, the plasmid encoding for the target protein under control of a *tet*-promoter was transformed into *E. coli* BLR (DE3) expression cells. A single colony or 10 µl of a glycerol-stock (see chapter 3.3.3) were used to inoculate an overnight culture containing 50 µg/ml ampicillin, which was incubated at 37 °C. This overnight culture was diluted 1:50 in medium with the same antibiotic

concentration and incubated at 37 °C until the OD_{600} reached 0.5 and induced with anhydrotetracycline (AHT) (IBA, Germany) to a final concentration of 2 ng/ml.

After 4 h of expression, culture was centrifuged at 8,000 x g for 10 min. Cells were resuspended in 30 ml buffer W in case of Strep-tag protein expression or 30 ml His-lysisbuffer in case of His-tag expression and stored at -20 °C.

3.3.2 Tabacco etch virus (TEV) protease expression

A glycerol stock from TEV-protease mutant S219V overproducing BL21 (DE3)-RIL cells was obtained from NASSER YOUSEF. TEV protease was encoded on pRK793 plasmid under *lac*-operon control. An overnight culture was grown at 37 °C in LB-medium with addition of 25 µg/ml chloramphenicol (Cam) (Sigma, USA) and 50 µg/ml ampicillin (Amp) (Roth, Germany).

The overnight culture was diluted 1:50 in the same medium as used for the overnight culture and grown until OD_{600} reached 0.6. For induction, 1 mM β-*d*-thiogalactopyranoside (IPTG) (Roth, Germany) was used and culture was centrifuged after 37 °C of expression for 10 min at 8,000 x g and cells were resuspended in glycerol containing buffer for storage at -20 °C.

3.3.3 Preparation of glycerol stocks

For glycerol stock preparation, respective plasmids were transformed into *E. coli* BLR (DE3) expression cells and plated on LB-Amp agar. An overnight culture was inoculated with a single colony and incubated at 37 °C. 600 µl of overnight culture were mixed thoroughly with 800 µl of glycerol and stored at -80 °C.

3.3.4 Cell disruption for protein purification

A bacterial pellet was thawed at RT. After that, a spatula tip of lysozyme powder was added and suspension incubated at RT for 10 min. The cells were mixed with the protease inhibitor phenylmethylsulfonylfluoride (PMSF) (Sigma, USA) to a final concentration of 100 µM and transferred to a glass beaker. Sonification was carried out with a Branson sonifier 250 (Emerson Electric Co, USA) for 10 min at 40 kHz output frequency. The lysate was centrifuged at 50,000 x g at 4 °C for 50 min. Cell debris was pelleted and the supernatant was used for further experiments.

3.3.5 Purification of His-tagged proteins

After cell disruption and centrifugation (see chapter 3.3.4), the supernatant was incubated at 4 °C with previously equilibrated Ni-NTA agarose (Qiagen, Germany) with washing buffer for 30 min under rotation.

For washing, matrix was pelleted at 800 rpm, for 1 min, at 4 °C and incubated for 20 min with His-washing buffer at 4 °C. In a second washing step, matrix was transferred to an empty column and protein was eluted with 5 ml His-elution buffer, reusing 3x the same buffer. At the end, 1-2 ml of fresh elution buffer depending on matrix volume were added to the matrix and protein dialysed against 2 l of the respective imidazole-free buffer overnight at 4 °C.

3.3.6 Purification of TEV protease

TEV protease was fused to a 6x His- tag and was sonified and purified like described for His- tagged proteins in chapters 3.3.4 and 3.3.5. Due to TEV instability against oxidation, elution buffer was immediately removed in a centrifugal filter device (Millipore, USA) and exchanged by TEV protease storage buffer containing 20 % glycerol and 5 mM dithiotreitol (DTT) (Biomol, Germany). TEV protease was stored at -80 °C.

3.3.7 Regeneration of Ni-NTA agarose

Ni-NTA agarose was washed with 5 column volumes (CVs) of water and after that with 3 CVs of 2 % sodiumdodecylsulfate (SDS) solution. An ethanol (Roth, Germany) gradient from 25 % (1 CV per washing step) to 100 % (5 CVs) and back to 25 % was applied. To remove ethanol, the resin was washed with 1 CV of water.

To complex Ni^{2+} ions, the matrix was incubated with 5 CVs of 100 mM ethylenediaminetetraacetic acid (EDTA), pH 8 (Biomol, Germany) containing buffer and subsequently washed with 2 CVs of water. Agarose was recharged with 2 CVs of 100 mM $NiSO_4$ (AppliChem, Germany) containing buffer for 30 min, washed with 2 CVs of water, 2 CVs of regeneration buffer and 1 CV of water. For subsequent use, it was equilibrated with protein buffer or stored as a 50 % suspension in 30 % ethanol at 4 °C.

3.3.8 Purification of Strep-tagged proteins

For purification, 1 ml of Strep-tactin resin (IBA, Germany) was applied to an empty column and equilibrated with 1 CV of buffer W. Cell lysate from sonified and centrifuged cell pellet was applied to the column and the matrix was washed with 2 CVs of buffer W. Protein was eluted 3x, reusing 2.5 mM desthiobiotin (IBA, Germany) containing buffer W in 2 ml and then again with 1 ml of fresh elution buffer. The protein was dialysed against 2 l of the respective desthiobiotin-free buffer.

Strep-tactin matrix was regenerated with 1 CV buffer W containing 1 mM hydroxyl-azophenyl-benzoic acid (HABA) (IBA, Germany) and washed with 3 CVs of buffer W. For subsequent use the resin was equilibrated with buffer W or stored at 4 °C in a 50 % suspension with 30 % ethanol.

3.3.9 Protein quantification

3.3.9.1 Bradford assay [114]

For protein quantification, 2 µl of protein solution were mixed with 1 ml of Bradford reagent in a cuvette (LLG, labware) and absorption at 595 nm (A_{595}) was measured in a Bio-TEK Uvikom photometer (Kontron AG, Switzerland). Protein concentration was calculated with a previously established standard curve. A_{595} of increasing bovine serum albumin (BSA) (Roth, Germany) concentrations in Bradford reagent were plotted against BSA concentration. For protein quantification, A_{595} of the measured sample was divided by the slope of the standard curve.

3.3.9.2 Protein quantification with the Nanodrop 2000c

More accurately than with the Bradford assay, protein concentration was determined with the Nanodrop 2000c (ThermoScientific, Peqlab, Germany). 2 µl of protein buffer were pipetted to the sensor, the lever arm was brought down and measurement was blanked. For concentration determination, procedure was repeated with 2 µl of protein solution. Measurements were carried out in duplicates.

Values for molar extinction coefficient (ε) and molecular weight were entered and protein concentration was displayed by the software, calculated on the basis of Lambert-Beer-law:

$$A_{280} = \varepsilon * b * c$$

A_{280}= absorption at 280 nm

ε= molar extinction coefficient [M^{-1} cm^{-1}]

b= path length [cm]

c= protein concentration [mg/ml]

3.3.10 SDS-polyacrylamide gelelectrophoresis (SDS- PAGE)

SDS-PAGE is a technique to separate proteins by their size and shape. Usually, a 12.5 % polyacrylamide separating gel with a 4 % polyacrylamide stacking gel was used to analyse proteins with a size in the range of 20-30 kDa. Samples were mixed with 5x SDS-sample buffer and denatured at 95 °C for 10 min.

Cooled and centrifuged samples were applied to the gel, that was inserted into an electrophoresis cell (Hoefer Inc, USA), supplied with SDS running buffer. Gel run was carried out at 35 mA per gel.

For 12.5 % polyacrylamide gel the following chemicals were pipetted:

	4 %stacking gel	12.5 % separating gel
stacking/ separating gel buffer	1 ml	1.5 ml
bidest water	2.59 ml	2.6 ml
40 % acrylamide	400 µl	1.9 ml
10 % SDS	40 µl	60 µl
10 % ammonium persulphate (APS)	20 µl	25 µl
N,N,N',N'-Tetramethylethan-1,2-diamin (TEMED)	5 µl	5µl

3.3.11 Coomassie staining of SDS-Gels

For coomassie staining, stacking gel was removed and separating gel was incubated in coomassie staining solution for at least 2 h. To visualise only protein bands, the gel was incubated for 4 h with destaining solution and stored in water. Results were documented by scanning of the gel.

3.3.12 Westernblot

Previously separated proteins (see chapter 3.3.10) were blotted to a nitrocellulose membrane (Whatman, Germany) in a Roth semi-dry blotting apparatus (Roth, Germany) for 1 h at 35 mA per gel. Membrane was stained with Ponceau S (Roth, Germany) staining solution until protein bands became visible. Stained membrane

was photocopied for documentation and rinsed with phosphate buffered saline (PBS) to remove staining solution.

Membrane was blocked at 4 °C overnight or for 1 h at RT with 3 % BSA (w/v) in PBS and washed with 1x PBS containing 0.3 % Tween 20 (w/v) (Roth, Germany) and incubated with His-probe antibody (ThermoScientific, USA) diluted 1:5,000 in 1x PBS containing 1 % BSA (w/v) and 0.03 % Tween 20 (w/v) overnight at 4 °C or for 1 h at RT.

The blot was rinsed 3 times with PBS containing 0.3 % Tween 20 (w/v) and incubated with 1 ml of chemiluminescence detection kit solution mix for 5 min in the dark. After removal of residual solution the membrane was transferred to a developing cassette and a western blot film was exposed for 0.5-5 min and developed, depending on signal strength.

3.3.13 TEV protease digestion and purification of TEV cleaved proteins

TEV protease was used to remove His- tags of proteins when cleavage site was cloned in front of the His-tag. Protein solution dialysed against an imidazole-free buffer, was mixed with 5 mM DTT and TEV protease was added in a 1:100 ratio from purified aliquots at -80 °C. Digestion was carried out at 4 °C overnight.

The next day, the mixture of TEV protease and protein for His- tag removal were incubated with previously equilibrated Ni-NTA resin (buffer W for equilibration) for 30 min. Flow through contained cleaved protein; the protease and cleaved His-tags where bound to Ni-NTA matrix.

3.3.14 Fast protein liquid chromatography (FPLC) (ÄKTA system)

To analyse proteins under non-reducing conditions, 1 mg of protein was applied to a superdex 200 (S-200) (GE-Healthcare) gelfiltration column. The FPLC ÄKTA purifier system (GE Healthcare, UK) was previously rinsed with water and protein buffer and the column equilibrated respectively. The run was initiated by the software and A_{280} detection unit was turned on. Peak fractions, showing high A_{280} were pooled and analysed on SDS gels.

Protein size was determined with a calibration run according to the manufacturer´s protocol and calibration curve was used to determine the molecular weight from retention volume.

3.3.15 Dynamic light scattering (DLS)

DLS was applied to analyse the dispersity of a solution. In preparation to crystallisation trials, previously purified and dialysed samples were centrifuged at 100,000 x g at 4 °C for 50 min and 9 µl were transferred to an optical cuvette. Buffer conditions and measurement parameters were specified in the software.

3.3.16 Circular dichroism (CD)

CD is a standard technique to determine secondary structure elements in proteins. The CD machine (Jasco, UK) was started according to supplier´s procedure.

Protein samples were dialysed against salt-free or low-salt phosphate buffer and centrifuged for 50 min at 4 °C and 100,000 x g. Final concentration for CD measurement was 0.1 mg/ml. Typically, a wavelength scan from 190 nm-260 nm was carried out. Result was displayed by the software (Jasco, UK) as CD signal [mdeg] against wavelength and was automatically converted by the software to molar ellipticity (Θ*1000 [deg cm^2 dmol^{-1}]).

From standard curves determined by Yang *et al.* [115] secondary structure elements were determined. Typical curves for α-helical folding show minima at 208 and 220 nm and a maximum at 192 nm (see black curve Figure 6), proteins with mainly β-sheet folding show a minimum at 215 nm and a maximum at 195 nm (see red curve Figure 6), whereas turn structures show a single maximum at 200 nm in the CD spectra (see green curve Figure 6). Random coil structures lead to a minimum between 190 and 200 nm and a maximum at 220 nm (see yellow curve Figure 6). All these values are not absolute values, but landmarks for CD spectra analyses.
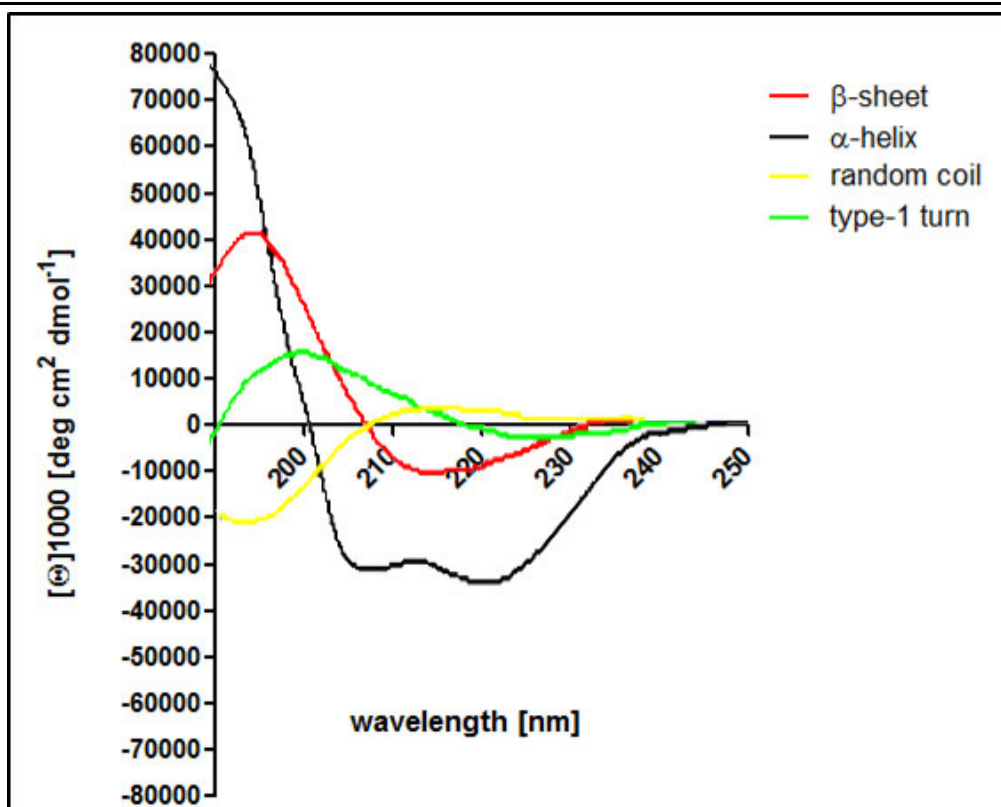
Figure 6: Standard curves for CD measurements determined by Yang *et al* [115]. The CD signal for β-sheets is depicted in red, for α-helices in black, for random coil in yellow and for turn structures (type-1) in green. Figure has been generated with GraphPad Prism 5 version 5.01 for Windows (GraphPad Software, La Jolla California USA, www.graphpad.com).

3.3.17 Activity tests

3.3.17.1 ThiM activity test

To determine the linear region of ThiM activity, ThiM assay was performed with 4 amounts, namely 0.125 µg, 0.250 µg, 0.500 µg and 1.000 µg ThiM per reaction tube. All reactions were carried out in duplicates from three separate preparations of the protein from separate expressions. THZ phosphorylation was monitored, by adenosine triphosphate (ATP) adenosine diphosphate (ADP) conversion with ^{14}C-ATP (Hartmann Analytik, Germany). All reactions were incubated for 15 and 30 min respectively with saturation of THZ (MP Biomedicals, Germany) (400 µM). A typical reaction contained: 50 mM potassium phosphate buffer (pH 7.5), 10 mM MgCl$_2$, 0.5 mM ATP (Sigma, USA), 50 nCi ^{14}C-ATP and 400 µM THZ. For zero value ThiM was replaced by dH$_2$O and all blanks contained 1 µg ThiM inactivated for 2 min at 95 °C.

Reactions were pipetted on ice and incubated at 37 °C for 15 min or 30 min respectively and subsequently inactivated for 2 min at 95 °C.

After centrifugation, samples were spotted onto a polyethylenimine-modified (PEI) cellulose thin layer chromatography (TLC) plates (Merck, Germany) in two iterative steps using 5 µl respectively while drying the TLC plate with a hair dryer. For visualisation of ATP and ADP (Sigma, USA) spots, 2 µl of 5 mM ATP and ADP solutions respectively were spotted onto the TLC plate.

Chambers were filled with 100 ml of a 1 M LiCl solution and plates were inserted until the solvent front had reached the top leaving down 4 cm approximately. After that, plates were dried and ATP and ADP spots visualised under UV-light. Encircled spots were cut and transferred to scintillation vials. The radioactivity was quantified in a LS5000 CE (BeckmanCoulter, USA) counter.

The ATP-ADP conversion was calculated and the non-linear regression curves from 15 min incubation and 30 min incubation time were compared. For further ThiM investigations, the amount of ThiM in the linear part of the curve, where conversion doubled comparing 15 and 30 min was applied.

3.3.17.2 Competitive ThiM assay

To compare whether substrate analogues or THZ is the preferred substrate for ThiM, and to investigate if putative substrate analogues are accepted, a competitive assay has been carried out. In comparison to the preliminary test (see chapter 3.3.17.1), ^{33}P-ATP has been used to directly see phosphorylated product on the TLC plate. Samples had the same composition as seen in chapter 3.3.17.1, but instead of ^{14}C-ATP, 75 nCi ^{33}P-ATP and 0.315 µg ThiM per reaction has been used. For substrate analogue testing, 400 µM of the respective compound have been applied, for competitive samples 400 µM of compound and 400 µM of THZ. Samples were incubated for 30 min at 37 °C and inactivated for 2 min at 95 °C. All reactions were carried out in duplicates from 3 separate preparations of the protein from separate expressions. For zero value ThiM was replaced by dH_2O and all blank contained 1 µg ThiM inactivated for 2 min at 95 °C.

After centrifugation samples were spotted onto PEI-cellulose TLC plates in two iterative steps using 5 µl respectively while drying the TLC plate with a hair dryer.

Chambers were filled with 100 ml of a 0.1 M LiCl and 0.1 M formic acid solution and plates were inserted until the solvent front had reached the top leaving down 4 cm approximately. After that, plates were dried, transferred to cassettes and exposed to X-ray sensitive films (X-ray Retina, Germany) at -80 °C for 2 d. Developed film was

used to localise ^{33}P-ATP and phosphorylated product spots on the TLC plate. Radioactivity was quantified in a LS5000 CE (BeckmanCoulter, USA) counter.

3.3.17.3 K_M determination for ThiM compounds

K_M was determined, applying increasing substrate concentrations at constant enzyme concentration. Reactions were carried as described in chapter 3.3.17.2 for separate compound testing using ^{33}P-ATP as radioactively labelled reagent. Compound concentrations ranged from 0-4 mM, ATP concentration was 4 mM for all reactions.

3.3.17.4 K_i determination for a selected ThiM compound

K_i was determined, applying increasing THZ concentrations (0-800 µM) at constant enzyme concentration at three different inhibitor concentrations. Inhibitor concentrations were 10 µM, 50 µM and 250 µM. Reactions were carried as described in chapter 3.3.17.2 for separate compound testing, using ^{33}P-ATP as radioactively labelled reagent. ATP concentration was 1 mM for all reactions.

3.3.17.5   TenA K_M determination for wildtype (WT) and D111A-K115A mutant

TenA activity was measured in a combined test in which the formation of thiazole was detected in a subsequent radioactive ThiM assay.

75 µg TenA WT or mutant were applied in a 50 µl reaction, containing 100mM tris (pH 7.5) and concentrations of 0.05-20 mM thiamin (Sigma, USA) were tested. All reactions were carried out in duplicates from 3 separate preparations of the protein from separate expressions. For zero value, TenA WT or mutant were replaced by dH$_2$O and the blank contained 75 µg TenA WT or mutant respectively inactivated for 2 min at 95 °C.

Reactions were pipetted on ice and after short centrifugation, incubated at 37 °C for 30 min. Subsequently, tubes were cooled on ice and ThiM assay was carried out as described in chapter 3.3.17.2.

TenA reaction was added to 1 mM MgCl$_2$, 20 mM ATP, 75 nCi ^{33}P-ATP and incubated for 2 h at 37 °C. Positive control for ThiM activity test was a reaction as described in chapter 3.3.17.2, containing 400 µM THZ.

Detection was carried out as in chapter 3.3.17.2.

3.3.18 TenA stability assay

To assess stability of WT and mutant TenA, 200 µg of both protein species were digested at RT for 52 h with proteases from the Floppy Choppy Kit (Jena Bioscience, Germany) according to the manufacturer´s protocol using 1:100 and 1:1,000 dilutions of the proteases. During digestion 5 µl samples were taken and subsequently incubated at 95 °C for 10 min with SDS-PAGE sample buffer to prevent further digestion. Before analysis on an SDS-gel, samples were stored at 4 °C. Gels were stained with coomassie and scanned.

3.4 Methods to analyse the 3D structure

3.4.1 Crystallisation and data collection

3.4.1.1 <u>Sample preparation for protein crystallisation</u>

Proteins were purified and the His-tag were cleaved in order to minimise additional flexible regions within the protein. Tag-cleavage was performed for TPK. Initial protein concentration was assessed by Pre-Crystallization Test (Hampton Research, USA) according to the manufacturer´s protocol.

After protein purification, samples were concentrated and centrifuged in an ultra-centrifuge at 70,000-100,000 x g for 50 min. Dispersity was monitored by DLS measurements and samples were concentrated in to their final concentration.

Screening to obtain initial crystallisation conditions was usually carried out applying the pipetting robot Honeybee 961 (Genomic solutions, UK). Protein and precipitant solutions were transferred to 96 well *Nextal Qia1* plates (Qiagen, Germany). Usually, the commercially available screens *JCSG+*, *Classic, Cryos and ComPAS* (all Qiagen, Germany) were used. 300 nl of protein solution were mixed with 300 nl of the respective precipitant solution in one well. The reservoir was filled with 55 µl of precipitant solution. The plates were sealed and stored at 20 °C. If no initial condition could be obtained or further optimised, the *Morpheus, MacroSol, Stura Footprint, PACT* (all Molecular Dimensions, UK) and *AmSO4 Suite* (Qiagen, Germany), for co-crystallisation conditions of ThiM *Wizard Screens I-IV* (Emerald BioSystems, USA) and *Crystal Screen I* and *II* (Hampton Research, USA) were applied additionally. The plates were monitored every three days to identify crystallisation hits.

3.4.1.2 Optimisation of initial crystallisation conditions

If an initial crystallisation condition was obtained, this condition was optimised by varying the precipitant concentration around the condition found in the initial screen. In case of polyethylene glycols (PEGs) as precipitant, concentration was increased and decreased by 2 % increments, in case of salts in 200 mM increments.

Conditions were optimised in CPL-130 plates (JenaBioscience, Germany) applying hanging drop vapour diffusion, consisting of 1-2 µl protein solution and 1-2 µl precipitant solution and the reservoir filled with 500 µl of precipitant solution. Conditions also were optimised in 48-well MRC sitting drop plates (Molecular Dimensions, UK). Droplets were made of 2 µl protein solution and 2 µl precipitant solution, the reservoir was filled with 50 µl of precipitant. 48-well MRC sitting drop plates (Molecular Dimensions, UK) were also used to optimise conditions with self-designed screens. Droplets were pipetted by the Honeybee 961 (Genomic Solutions, USA) pipetting robot with 55 µl of reservoir solution and droplets in the upper well consisting of 0.5 µl protein solution and 0.5 precipitant solution and in the lower well consisting of 0.5 µl protein solution and 0.7 precipitant solution. Temperature was also varied and plates were either stored at 4 °C or 20 °C in a vibration free incubator (Rubarth, Germany) or at 14 °C in in an air conditioned laboratory.

An initial condition provides several opportunities to optimise it. Usually, hanging and sitting drop variations have been applied, but also crystallisation under oil or seeding techniques have been considered.

For crystallisation under oil, a Terazaki plate (Nunc, Denmark) was previously treated with paraffin oil (Applichem, Germany) to fill all wells with oil. Under the microscope, 1 µl of protein and 1 µl of precipitant were pipetted into the well.

Microseeding is a powerful tool to bypass spontaneous nucleation and to optimise crystal quality. A seedstock was prepared with a crystal in stabilising solution in a tube with a glass ball according to the supplier´s protocol (Jena BioScience, Germany). Seedstock was either diluted 1:10- 1:10,000 with protein solution containing half of the protein concentration at which the crushed crystal was obtained or used to draw streaklines with cat whiskers within droplets containing 2 µl precipitant and 2 µl protein solution (half concentrated in comparison to initial crystallisation condition).

3.4.1.3 Precipitation of ThiM with magnesium formate

ThiM was concentrated to A_{280} of 8, assessed by NanoDrop (peqlab, Germany) and incubated with an equal volume of 0.5 M magnesium formate overnight at 4 °C. After that, it was centrifuged at 16,000 x g for 1 h at 4 °C.

3.4.1.4 Sample preparation for the Shenzou8 space project

ThiM was purified via Ni-NTA resin and dialysed overnight against buffer W. The next day, ThiM was concentrated to an A_{280} of approximately 8 and precipitated with an equal volume of 0.5 M magnesium formate overnight. After that, it was centrifuged at 20,000 x g for 30 min and showed stable monodispersity for several days and used for counter diffusion experiments.

The capillaries for microgravity environment were prepared by RAPHAEL EBERLE and DOMINIK OBERTHÜR. After return of the space shuttle, the micro crystals were prepared from agarose with microtools (Mitegen, USA) and transferred to an 1.5 ml microcentrifuge tube with a glass bead (Jena BioScience, Germany) and a seedstock was prepared according to the manufacturer´s protocol.

A ThiM solution with a concentration of 10 mg/ml was precipitated overnight at 4 °C with an equal volume of 0.5 M magnesium formate. For crystallisation, it was concentrated to a final concentration of 9.8 mg/ml and 1 µl of protein solution was mixed with 1 µl of precipitant containing 20 % PEG 3,350 and 7 % isopropanol on a siliconised cover slide. Previously the wells of a 24-well CPL-130 plate (JenaBioscience, Germany) for hanging drop vapour diffusion were filled with 500 µl of precipitant solution. A streak seeding tool (Hampton Research, USA) was immersed in the microseed stock and a streakline was drawn through eight drops before dipping the tool again into the seedstock. From this crystal, again a microseedstock was prepared. In 48-well MRC sitting drop plates (Molecular Dimensions, UK) for sitting drop vapour diffusion, two rows of the precipitants with different PEG 3,350 concentrations were prepared by filling 50 µl of precipitant (18, 20 and 22 % PEG 3,350, 0.2 M magnesium formate and 5 % isopropanol) into the reservoirs. In contrast to the first seeding experiment, ThiM was purified, dialysed overnight against buffer W and directly used at 10 mg/ml concentration after centrifugation (100,000 x g, 4 °C for 50 min). 2 µl of precipitant and 2 µl of protein solution were prepared and a streakline was drawn within six droplets before dipping again into the microseedstock.

3.4.1.5 Evaluation of protein crystals

To differentiate between protein and salt crystals, droplets containing crystals were monitored with the CrystalScore (Diversified Scientific Inc, USA) according to the manufacturer´s specifications.

3.4.1.6 Data collection applying synchrotron radiation

Consortium beamline X13 (Hasylab/DESY, Germany), X11 (Hasylab/EMBL, Germany), A1 (CHESS, USA) and F1 (CHESS, USA) were used to further characterise obtained crystals and to collect datasets. Cryo-protection was assessed by exposing the loop, containing droplet solution, to liquid nitrogen stream. If ice appeared, glycerol was added to crystallisation droplet or crystals were directly transferred to a cryo-protectant solution and incubated for approximately 1 min. Crystals were mounted with nylon loops or Micromount (Mitegen, USA) loops and flash frozen in liquid nitrogen. If diffraction image showed ice rings but an intact crystal, simulated annealing was applied by blocking and subsequently releasing the liquid nitrogen stream.

In case of intergrown crystals, they were separated with microtools (Mitegen, USA).

At the consortium beamline X13, measurement was conducted by the programs *DNA* [116] and *BEST* [117, 118], at CHESS beamlines the *ADX* software package was used.

3.4.1.7 Data processing and model building

Data was processed with *iMOSFLM* [119], *XDS* [120] or *HKL2000/ Denzo* [121]. For scaling, either *SCALA* [122] or *SCALEPACK* [121] was used. For further data analysis and refinement programs from the *CCP4* [123] or *PHENIX* [124] suite were applied. Model building was carried out with *COOT* [125].

3.4.2 Small angle X-ray scattering (SAXS)

For SAXS measurements, at least three dilutions of the protein in the range from 1-10 mg/ml, typically 1, 2, 5 and 7 mg/ml were prepared and centrifuged at 100,000 x g for 50 min at 4 °C. DLS measurements were applied to monitor the dispersity of the solution. Only monodisperse solutions were used for SAXS measurement at P33 beamline (Hasylab/EMBL, Germany) with a detector distance of 2.7 m and a wavelength of 1.5 Å. The range of momentum transfer $0.01 < s < 0.6$ Å^{-1} was covered ($s = 4\pi \sin\theta/\lambda$, where 2θ is the scattering angle). The data were normalised to the

intensity of the transmitted beam and radially averaged; the scattering of the buffer was subtracted and the difference curves were scaled according to the protein concentration. The low angle data were extrapolated to infinite dilution to yield the final composite scattering curves.

The Guinier approximation [126] was used to evaluate the forward scattering I(0) and the radius of gyration (R_g), assuming that at very small angles (s < 1.3/Rg) the intensity is represented as I(s) = I(0) exp(-(sRg)2/3). The indirect transform package *GNOM* [127] was used to compute R_g from the entire scattering pattern, the pairwise distribution function p(r) and the size of the particle $D_{max.}$

Initial data processing was carried out with the program *PRIMUS* [128] from the *Atsas* suite.

The programs *DAMMIN* [129] and *DAMMIF* [130] were used from the Atsas online server for *ab initio* modelling, *DAMAVER* [131] to merge *ab initio* pdb data.

CRYSOL [132] and *SASREF* [133] served for comparison of *ab initio* shapes with crystallographic data.

3.4.3 Nuclear magnetic resonance (NMR)

For NMR measurements, protein sample buffer was exchanged in a centrifugal filter device (Millipore, USA) against deuterium oxide buffered with 50 mM tris-d_{11} (Euroisotope Laboratories, France), pH 8 and containing 150 mM sodium chloride. Compounds were dissolved in the same deuterated buffer.

NMR spectra were acquired at 300 K with a Bruker Avance 700 MHz NMR spectrometer equipped with a TXI cryoprobe incorporating z-gradient. Samples (160 µl in 3 mm sample tubes) contained 5 mM ligand and 40 µM protein. Data processing was carried out with *TOPSPIN* 3.1 (Bruker, USA).

STD-NMR is used to characterise the binding epitopes of ligands based on the nuclear Overhauser effect (NOE) [134]. The saturation of the protein was transferred to the bound ligand and was detected in solution after leaving the active site of the protein.

Saturation difference (STD) NMR spectra were acquired using a Bruker standard sequence (stddiff.3) incorporating a spin-lock filter of 10 ms duration to suppress residual protein resonances. On resonance irradiation was applied at 0 ppm and off resonance irradiation at 40 ppm. Saturation was achieved by a cascade of 40

Gaussian pulses with duration of 50 ms (field strength 100 Hz) to give a total saturation time of 2 s. STD spectra and reference spectra were acquired with 32,768 data points and a total of 32 transients. FIDs were multiplied with an exponential function (line broadening 1.0 Hz) before Fourier transformation. All ligands were assigned using ^{1}H-^{1}H nuclear overhauser correlation (NOESY) and ^{1}H-^{13}C heteronuclear multiple bond correlation (HMBC) spectra.

To determine the size of STD effects, resonances in the STD spectrum were integrated with respect to the reference spectrum. Therefore, an STD effect of 100 % results if the resonances in both spectra show the same intensity.

For epitope mapping, all STD effects of one ligand were normalised to the resonance that gives rise to the largest STD effect in the molecule (100 %).

Inversion recovery experiments for determination of longitudinal relaxation constants were performed with $\tau = 0.01 - 20$ s and with an interscan delay of 20 s.

4 RESULTS

4.1 Cloning, expression and purification of thiamin synthesising enzymes in *S. aureus*

The open reading frames (ORFs) of ThiM, ThiD, ThiE, GTPase and TPK were amplified from Strep-tagged constructs by PCR. The reverse primer encoded for a 6 x His-tag and a TEV protease cleavage site in front of the tag and a stop codon after the tag to prevent Strep-tag translation during the expression. Fragments and the empty vector pASK-IBA3 were digested with *BsaI* and ligated. After transformation of these plasmids into *E. coli* XL10-Gold or DH5α cells, plasmid DNA was isolated and sequenced. The C-terminal tagged constructs were transformed into *E. coli* BLR (DE3) expression cells and a test-expression with 1 l LB-medium containing the selective antibiotic ampicillin (Amp) was carried out. Cells were lysed and protein purified with Ni-NTA matrix. During purification, 5 µl of lysate, supernatant and pellet after centrifugation at 50,000 x g, and 5 µl of washing fractions and eluate were taken and subsequently incubated with SDS-sample buffer at 95 °C for 10 min. These fractions were analysed by SDS-PAGE.
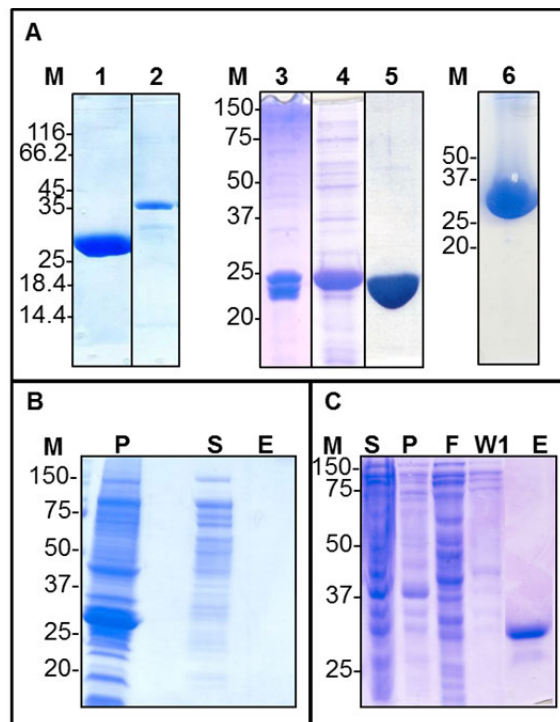
Figure 7: Test expression and purification of *S. aureus* thiamin synthesising enzymes with 6x His-tag and TEV protease cleavage site and analysis by SDS-PAGE. The gel was stained with coomassie. A: M=marker (molecular weight in kDa), 1= TenA (C-terminal tag), 2=GTPase (C-terminal tag), 3= ThiE(C-terminal tag), 4= ThiE (N-terminal tag), 5= TPK (C-terminal tag), 6= ThiM (C-terminal tag); B: Purification of C-terminal tagged ThiD, P= pellet, S= supernatant, E= elution; C: Purification of N-terminal tagged ThiD, S= supernatant, P= pellet, F= flow through, W1= washing fraction 1, E= elution

TenA, TPK and ThiM elution fractions were pure after affinity chromatography (see Figure 7 A, lane 1, 5 and 6). Sequence based molecular weight (MW) predictions for monomeric proteins were TenA= 28,454 Da, TPK= 25,589 Da and ThiM= 29,744 Da which matches with the molecular masses seen by SDS-PAGE analysis. The predicted MW for GTPase was 33,881 Da, but the main elution band is slightly larger than 35 kDa. Additionally, impurities at approximately 33 kDa were seen (see Figure 7 A, lane 2). When ThiE was expressed with a C-terminal His-tag the protein eluted in a double band of about 25 kDa. The predicted MW was 23,398 Da. This size could also be seen in the SDS gel. When expressed with an N-terminal tag only the main elution band was present, but purity was not optimal (see Figure 7 A, lanes 3 and 4). ThiD was insoluble with a C-terminal tag. A band with the predicted size of 30,242 Da was identified in the pellet fraction, but not anymore in the supernatant or elution fraction (see Figure 7 B). When expressed with an N-terminal tag, ThiD was soluble and was purified, but residual impurities smaller than 30 kDa have been observed (see Figure 7 C). All predictions were calculated by the programme *ProtParam* [135] on the ExPASy webpage.

4.2 Structure analysis of TenA

4.2.1 TenA crystallisation

Initial crystallisation screens have been carried out by MARKUS PERBANDT and AFSHAN BEGUM. TenA with a Strep-tag was purified via Strep-tactin matrix and dialysed against 100 mM tris/HCl (pH 8) and 10 % glycerol containing buffer overnight. Dispersity of the protein solution was assessed by DLS: 9 µl were filled into an optical cuvette for DLS measurement and radius distribution was displayed as a heatmap (see Figure 8 A).
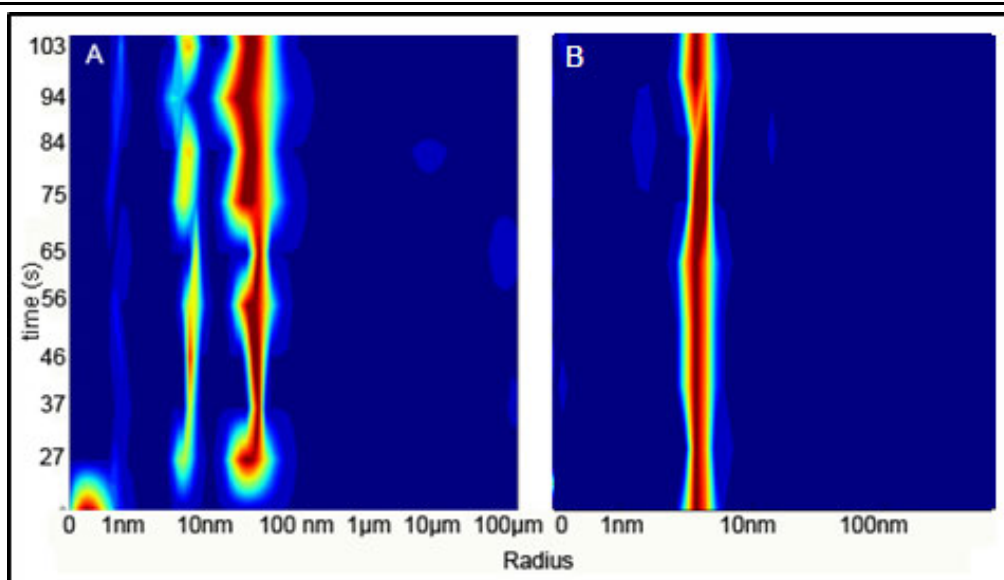
Figure 8: DLS heatmaps of TenA-Strep fusion protein. A: Radius distribution after centrifugation at 20,000x g; B: Radius distribution after centrifugation at 70,000 x g. The colours of the heatmap indicate the relative intensity of the particle, with blue being zero and dark red being maximum.

For initial crystallisation condition search, a TenA solution was centrifuged at 20,000 x g and 4 °C for 1 h. For crystallisation, the protein solution was concentrated to a concentration of 10 mg/ml using a centrifugal filter device with a MW cut-off of 3,000 Da (Millipore, USA). In total, 384 conditions were tested applying the *Cryos*, *Classics*, *JCSG+* and *ComPAS* screening suites (all Qiagen, Germany). 300 nl of the protein solution were mixed with 300 nl of the precipitant solution by the pipetting robot Honeybee 961 (Genomic Solutions, USA) in 96-well sitting drop plates (NeXtal QIA1 µplates, Qiagen, Germany). The reservoir was filled with 55 µl of precipitant solution. After 5 d at 20 °C, initial crystals grew in three conditions (see Figure 9 A-C).

These conditions were optimised varying PEG and salt conditions around the initial concentration in 24-well hanging drop CPL-130 plates (JenaBioscience, Germany) by mixing 2 µl of previously clarified (70,000 x g, 4 °C, 50 min) protein solution and 2 µl of the respective precipitant solution. Centrifugation at 70,000 x g removed larger aggregates and a monodisperse solution with a main radius of 4.1 ± 0.1 nm corresponding to a MW of approximately 83 kDa was applied for crystallisation (see Figure 8 B).

Varying the PEG 4,000 concentration of condition H6 of the *Classics* suite (Qiagen, Germany) (0.2 M sodium acetate, 0.1 M Tris/ HCl pH 8.5, 32 % PEG 4,000) from 24

to 34 %, X-ray suitable crystals grew in the presence of 26 % PEG 4,000 after 7 d to the following dimensions: 0.1 x 0.1 x 0.4 mm [136] (see Figure 9 D).
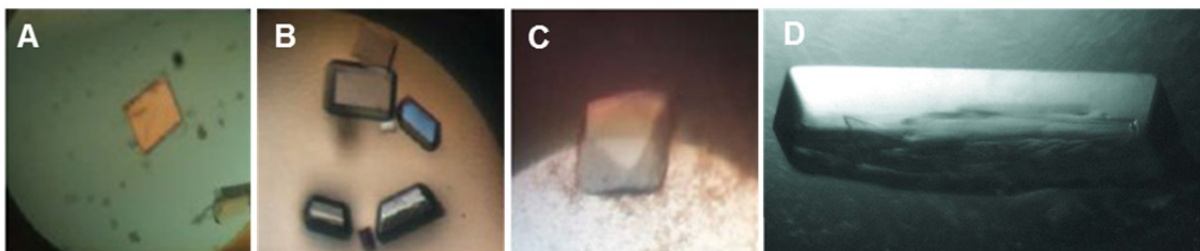
Figure 9: TenA crystals in the screen for initial crystallisation conditions appearing after 5 d. A: Classic suite H6 (0.2 M sodium acetate, 0.1 M Tris/ HCl pH 8.5, 32 % PEG 4,000); B: *ComPAS* suite F12 (0.2 M tri-sodium citrate, 0.5 M ammonium dihydrogen phosphate); C: *JCSG+* suite D10 (0.2 M calcium acetate, 0.1 M sodium cacodylate pH 6.5, 40 % PEG 400); D: optimised crystal from A (0.2 M sodium acetate, 0.1 M Tris/ HCl pH 8.5, 26 % PEG 4,000 (w/v)).

4.2.2 TenA X-ray diffraction data collection analysis

Prior to data collection, a crystal was transferred to cryo protectant (precipitant containing 10 % glycerol), soaked for 20 s and flash frozen in liquid nitrogen. Diffraction was recorded to 2.69 Å at the consortium beamline X13 (Hasylab/DESY, Germany).

Table 2: Data collection and refinement statistics for TenA

Data collection statistics[a]:

Beamline	Consortium Beamline X13, HASYLAB/DESY
Temperature [K]	100
Wavelength [Å]	0.81
Space group	$P2_12_12_1$
Unit cell parameters: a, b, c [Å]	103.27, 104.06, 109.45
Resolution range	30-2.69
Measured reflections	424031
Unique reflections	33445
Completeness [%]	95.0 (95.3)
Multiplicity	5.2 (5.0)
Average I/σ(I)	23.0 (3.3)
R_{merge}[b]	4.2 (48.8)

Refinement statistics:

Resolution range	30-2.69 (2.83-2.76)
R_{work}/ R_{free} [%]	21.31/ 25.88 (33.08/ 41.08)
Asymmetric unit content	
Protein atoms	7461
Water molecules	81
Rms bond-length deviation [Å]	0.01
Rms bond angle deviation [°]	1.2
Mean *B* factor [Å2]	58.45

Ramachandran plot analysis:

Most favoured regions [%]	97.9
Allowed regions [%]	2.1
Generously allowed regions [%]	0

[a]Values in parentheses are for the highest resolution shell.

[b]R_{merge}: $\sum_{hkl} \sum_i | I_i (hkl) - \langle I (hkl) \rangle | / \sum_{hkl}\sum_i I_i (hkl)$, where $\langle I (hkl) \rangle$ is the mean intensity of the observations $I_i (hkl)$ of reflection hkl.

Data were indexed with the *HKL-2000* [121] suite and scaled with *Scalepack* [121] in the orthorhombic space group $P2_12_12_1$ in a resolution range from 30-2.69 Å with an

overall R_{merge} of 4.2 %. A Matthews´ coefficient [137] of 2.85 Å^3 Da^{-1} with a corresponding solvent content of approximately 56 % indicated four molecules in the asymmetric unit.

NCBI/BLAST [138] search revealed the highest sequence identity for TenA from *S. epidermidis* (pdb entry: 3NO6, 58 % sequence identity). A homology model with *Se*TenA was built with the homology modelling server *HOMER* [139] (see Figure 10).
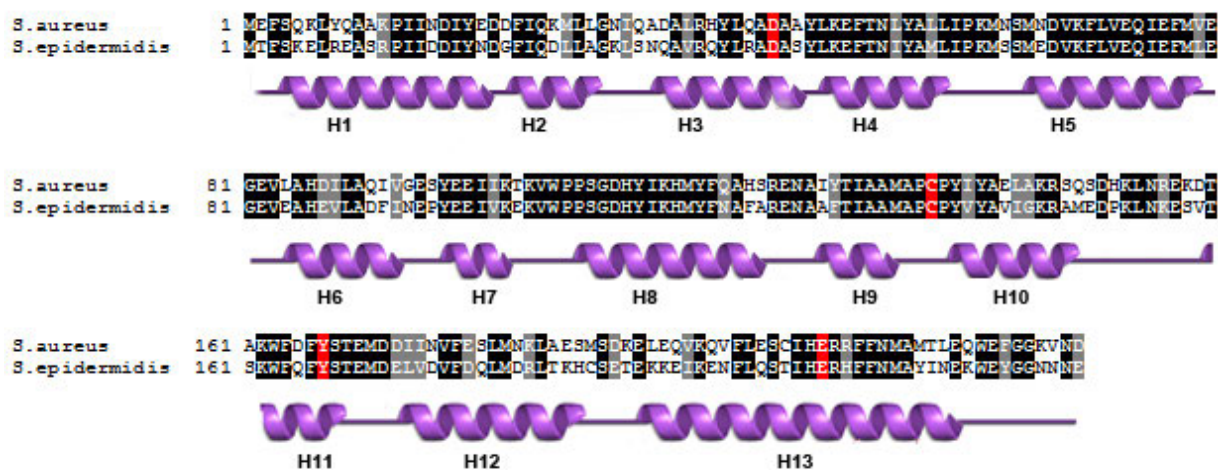
Figure 10: Sequence alignment for TenA derived from *S. aureus* and *S. epidermidis*. Alignment was carried out with *Clustal W* [140] and *BOXSHADE* [141]. Identical residues are shown in black, similar residues in grey and active site residues in red. Secondary structure elements are marked below in a purple ribbon representation. H= α-helix. Figure was modified with [136]. Secondary structure elements are based on the solved crystal structure seen in Figure 11. Ribbon representation was generated with *PDBsum* [142].

Molecular replacement was carried out with *MOLREP* [143]. The best solution was obtained with a correlation coefficient of 51.8 % and an R-factor of 45.8 % for data in the resolution range from 15–3.5 Å. Model building was carried out with *COOT* [125] and refinement with *Refmac5* from the *CCP4* [123] suite and *REFINE* from the *PHENIX* suite [124]. The starting model was refined to final R: 21.3 % and R_{free}: 25.9 %.
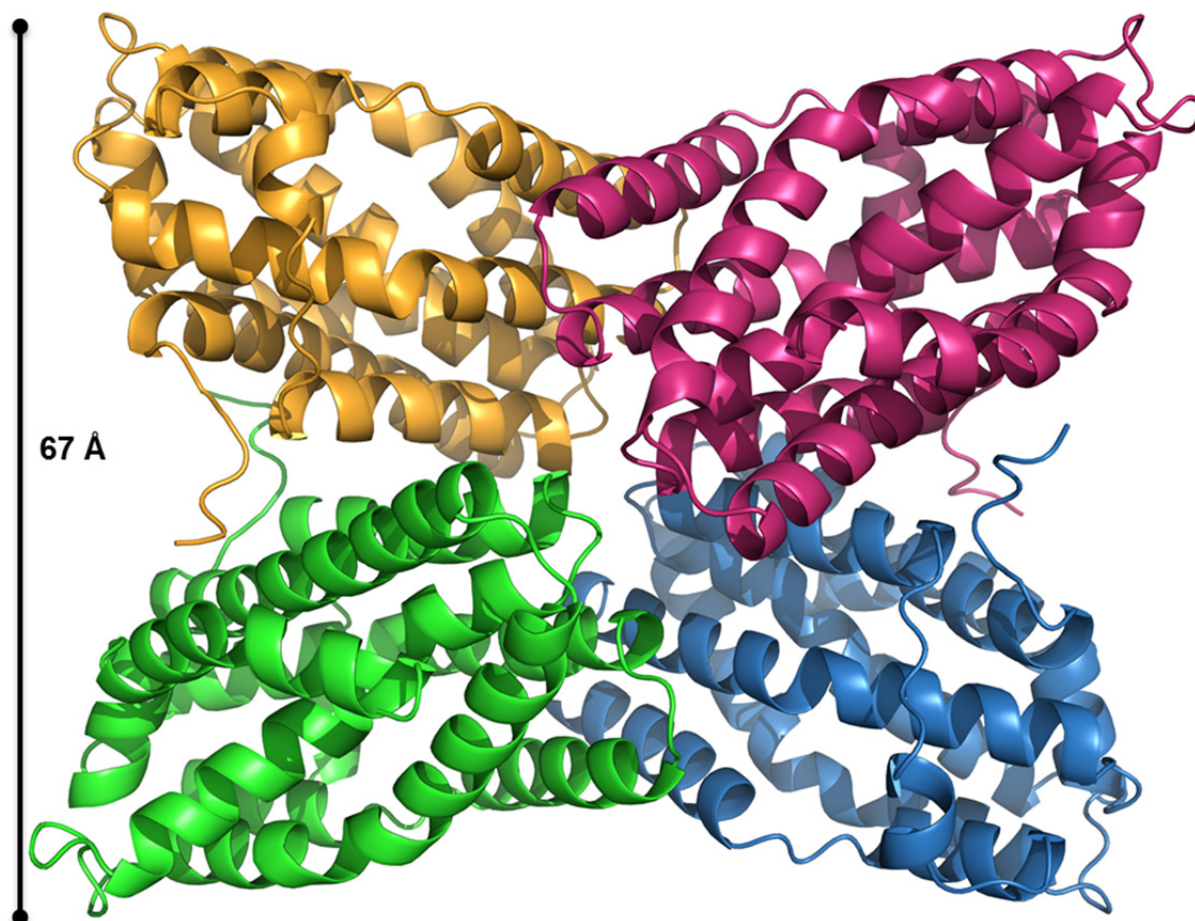
Figure 11: Ribbon representation of the *Sa*TenA structure, which was solved to 2.69 Å resolution. The structure comprises four identical monomers, indicated by four different colours. Figure was obtained using PyMOL (PyMOL Molecular Graphics System, Version 1.3, Schrödinger, LLC.).

The structure comprises four monomers building a tetramer with four independent active sites and with a total surface of approximately 38,000 $Å^2$ (calculated with *AREAMOL* from the *CCP4* [123] suite). Every monomer contains 13 α-helices accounting for approximately 76 % α-helix content [144] (see Figure 11). These helices are forming a channel for ligand binding (see Figure 13).
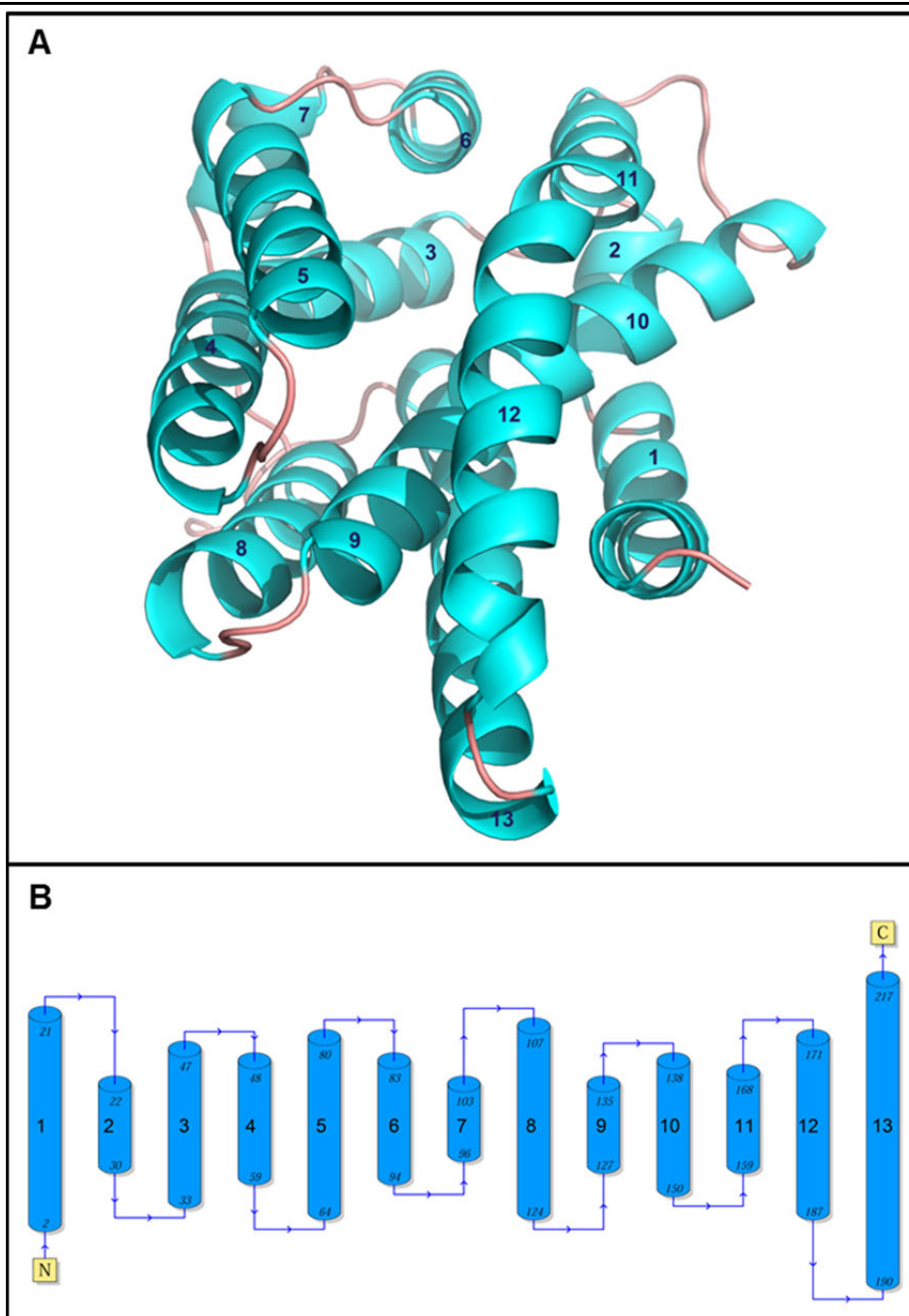
Figure 12: Topology and ribbon drawing of the subunit structure of TenA. A: In the ribbon drawing the α-helices are depicted as light blue coils and loops are depicted in pale red. Numbers in dark blue designate the α-helices numbered from the N- to the C-terminus. Figure was obtained using PyMOL (PyMOL Molecular Graphics System, Version 1.3, Schrödinger, LLC.); B: Topology diagram. The α-helices are represented by light blue cylinders, the connecting loops in dark blue. The smaller numbers indicate the beginning and ending residue number of each secondary structural element. The figure was prepared with *PDBsum* [142].

As no complex data were recorded, the active site of TenA was identified by superimposition with TenA from *Bacillus subtilis* which was co-crystallised with hydroxymethylpyrimidine [106] (pdb entry: 1YAK) (see Figure 13).
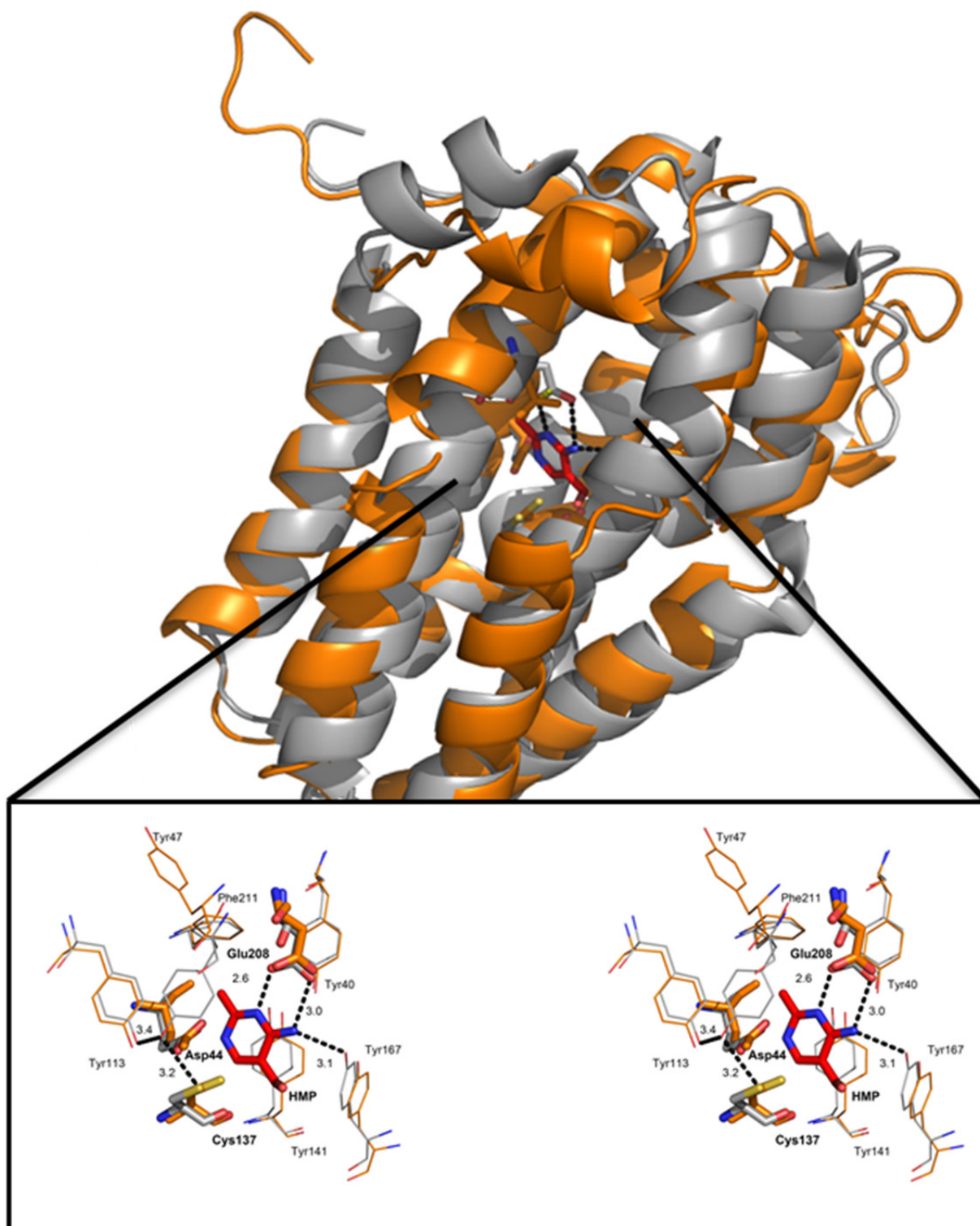
Figure 13: Superimposition model in ribbon representation of *Sa*TenA and *Bs*TenA co-crystallised with HMP (pdb entry: 1YAK) and stereo diagram (wall-eye) of the active site in stick/lines representation. On the top, one monomer of *Sa*TenA is superimposed with a monomer from *Bs*TenA, the structure of *Bs*TenA is displayed in grey, *Sa*TenA in orange, the active site residues are highlighted by sticks representation, the ligand HMP is displayed in red. On the bottom in the stereo diagram (wall-eye), the key interactions of TenA with HMP are shown. *Sa*TenA residues are coloured in orange, *Bs*TenA residues in grey, HMP in red. The catalytic residues are displayed as sticks, other active side residues as lines with oxygen atoms in red, carbon in the respective chain colour, nitrogen in blue, and sulphur in yellow. Labels indicate the respective *Sa*TenA residues, hydrogen bonds are represented as dashed lines and numbers show the hydrogen bond length.

4.2.3 TenA SAXS structure

To verify that TenA is tetrameric in solution and the oligomeric state seen in the crystal is not a crystallographic artefact, SAXS measurements at beamline X33 (Hasylab/EMBL, Germany) were carried out. TenA was purified and centrifuged at 100,000 x g, for 50 min, at 4 °C. Dispersity was monitored by DLS. Four different solutions were prepared in the concentration range of 1.2-7.2 mg/ml. Dialysis buffer was used as reference for the measurements. To monitor the radiation damage, eight successive exposures for 15 s of protein solutions were compared and no significant changes were observed.

The MW of (84±8 kDa was estimated from forward scattering and suggests that the sample is tetrameric in solution. An experimental R_g of 32 ± 1 Å and D_{max} of 100 ± 10 Å suggested an oblate structure. The smaller angles (up to s = 0.18 Å^{-1}) were fitted (χ= 1.4) with a 69 × 69 × 38 Å rectangular prism. *DAMMIN* [129] was used to calculate the *ab initio* structure employing the range of scattering vectors up to s = 0.25 Å^{-1} and imposition of P222 symmetry. A model out of a dozen reconstructions merged with *DAMAVER* [131] fits the experimental data with χ = 1.1 and the obtained model is in good agreement with the crystal structure (see Figure 14). The scattering from the high resolution crystal structure was calculated with the program *CRYSOL* [132]. The crystal structure yields a good fit (χ = 0.9) to the experimental data (see Figure 14).
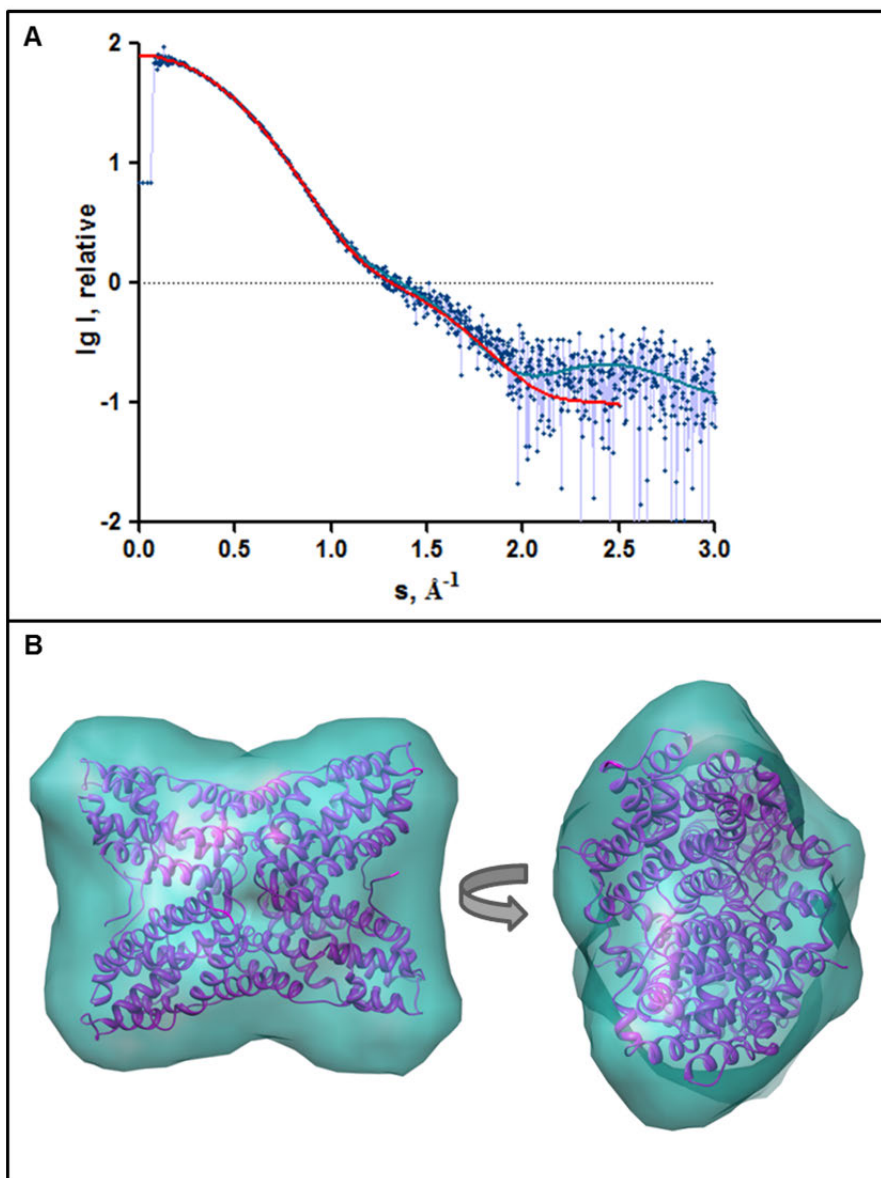
Figure 14: Processed solution scattering pattern and *ab initio* shape from TenA. A: Experimental data is displayed in blue with the *CRYSOL* [132] fit based on the crystal structure in light blue and the *ab initio* model fit in red. B: Front and side view of tetrameric TenA *ab initio* shape in turquoise in superimposition with the crystal structure in a purple ribbon representation. Figure was generated with CHIMERA [145].

4.3 Mutagenic studies of TenA

4.3.1 *Site directed* mutagenesis of TenA

To study the relationship between oligomeric states, the activities as well as the effect on stability, TenA mutants were generated by *site directed* mutagenesis to destabilise the tetramer in order to gain a soluble monomeric protein. Interfaces were analysed by the *PDBsum* server [142] and the respective contacts in the A-B and C-D interfaces are shown in Table 3.

Table 3: Interface contacts for tetrameric TenA based on calculations with the *PDBsum* server [142]. Whereas A-B≈ C-D and A-C≈ B-D. For every interface the buried surface and the number of involved residues is shown. The contacts between the monomers were made through hydrogen bonds and non-bonded contacts.

Chains	No. of interface residues	Interface area (Å^2)	No. of hydrogen bonds	No. of non-bonded contacts
A-B	21:21	1072:1075	2	105
C-D	21:22	1091:1075	6	112
B-C	12:13	782:748	1	29
A-D	12:11	765:759	1	35
B-D	3:3	136:136	4	25
A-C	3:3	129:135	4	26

Within the tetramer, two contacts per interface where selected for mutagenic analysis. Within the B-C and A-D interfaces the mutations E76A, K49S and within the A-B and C-D interfaces D111A and K115A were selected respectively. The aim was to disrupt mainly the formation of hydrogen bonds between the respective monomers. In Figure 15 it was shown that the selected mutations affect five non-bonded contacts and two hydrogen bonds at the A-B interface, five hydrogen bonds at the C-D interface, four non-bonded contacts and one hydrogen bond at the A-D interface and B-C interface. Corresponding genes were expressed, the derived proteins purified and applied to an S-200 gelfiltration column. As D111 and K115 are in very short distance to each other, these two amino acids were mutated in double. For single mutant generation, WT construct was used as template in a PCR reaction. To generate the mutant D111A-K115A-E76A-K49S, the construct encoding for the D111A-K115A double mutant was used to insert the E76A mutant. With the triple mutated plasmid, *site directed* mutagenesis using the mutation primer K49S was carried out (for primers see Table 1).
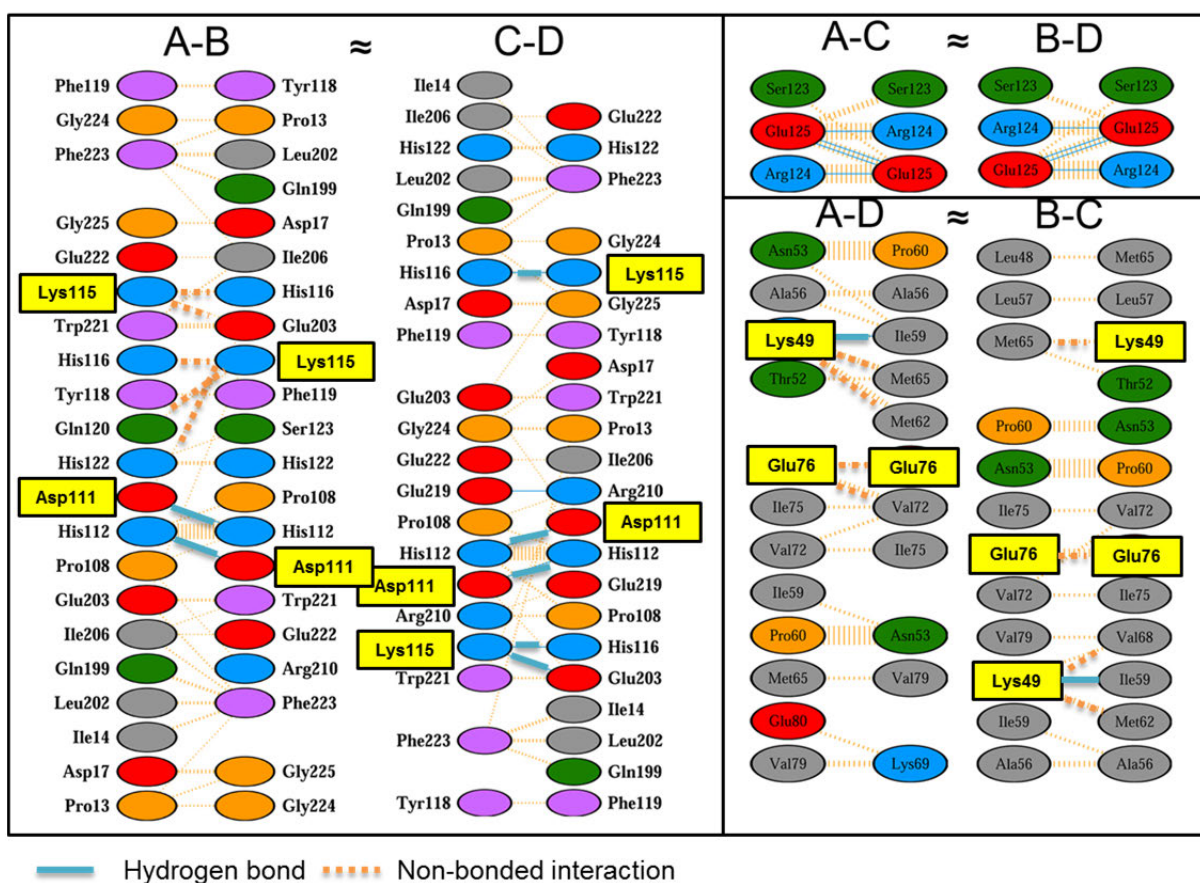
Figure 15: Schematic of non-covalent interactions within the TenA tetramer, analysed with *PDBsum* [142]. On the top of every column the respective interface is indicated with the letters for the amino acid chains. Based on symmetry: A-B≈ C-D and A-C≈ B-D. Amino acids are depicted as ovals, whereas positive residues (H,K,R) are depicted in blue, negative residues (D,E) in red, neutral residues (S,T,N,Q) in green, aliphatic residues (A,V,L,I,M) in grey; aromatic residues (F,Y,W) in purple and P and G in orange. Residues selected for mutation are encircled with a yellow box. Interactions are highlighted with a dashed orange line for non-bonded interactions and a light blue line for hydrogen bond interaction.

It was shown, that the D111A-K115A double mutant already had the effect to monomerise the protein. The D111A single mutant revealed a residual tetrameric conformation of TenA, whereas the E76A mutation had no effect on oligomerisation compared to the WT. Mutation of all 4 selected amino acids led to a mix of oligomeric states in solution (see Figure 16). For further characterisation only the D111A-K115A double mutant was analysed as this double mutation already led to the monomeric form. A detailed view of the interactions which led to the monomeric form is exemplarily depicted for the A-B interface in Figure 17.
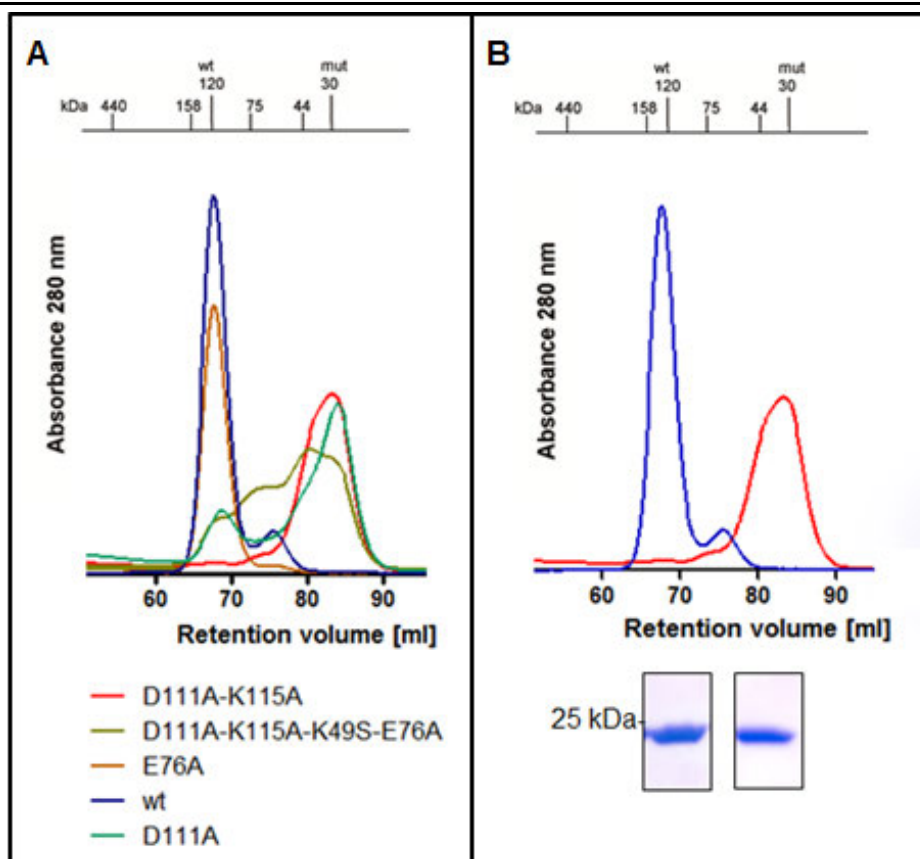
Figure 16: Gelfiltration profile for TenA WT and mutants. A: All TenA species were compared applying them to a gelfiltration column and the absorbance at 280 nm was plotted against the respective retention volume. WT=blue, D111A-K115A= red, D111A= turquoise, E76A= brown, D111A-K115A-E76A-K49S= navy green; B: Gelfiltration chromatogram of TenA species that were used for further characterisation including coomassie stained peak fractions applied to an SDS gel. Figure was generated with GraphPad Prism 5 version 5.01 for Windows (GraphPad Software, La Jolla California USA, www.graphpad.com).
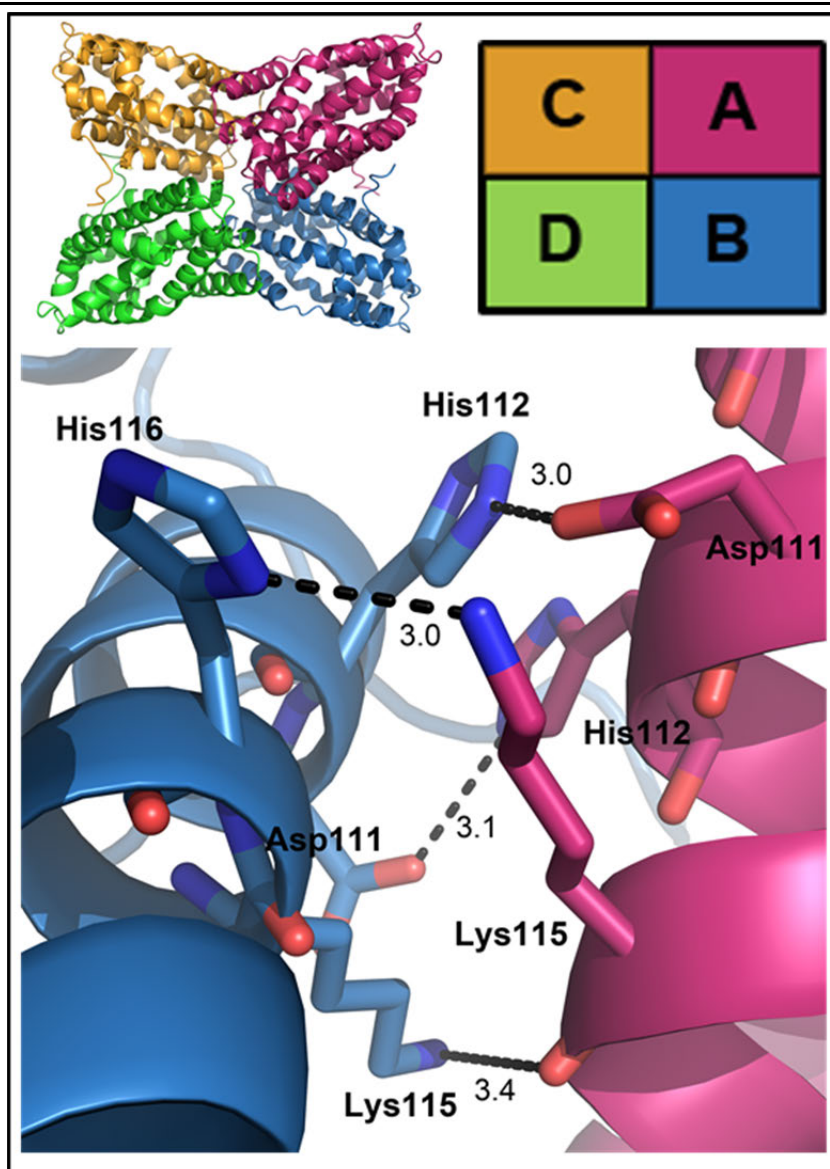
Figure 17: Detailed view of D111 and K115 mutation site and its interactions between monomers A and B. The ribbon representation on the upper left refers to the TenA crystal structure solved to 2.69 Å (see Figure 11) comprising four identical monomers indicated by different colours. The schematic on the upper right side connects the crystal structure colour code with the designation of the four amino acid chains. On the bottom, the residues at the A-B interface are displayed as sticks, with oxygen atoms in red, carbon in the respective chain colour and nitrogen in blue. Labels indicate the respective *Sa*TenA residues, hydrogen bonds are represented as dashed lines and numbers show the hydrogen bond length. The figure was generated with PyMOL (PyMOL Molecular Graphics System, Version 1.3, Schrödinger, LLC.).

Before testing stability and activity, CD measurements have been carried out to ensure, that both species were folded in the same way. The wavelength scan from 190 to 260 nm showed no major differences between the curves. As already seen in the crystal structure the predominant secondary structure element is α-helix as assessed from standard curves (see Figure 6) with minima at 208 and 222 nm and maxima at 192 nm for mutant and 195 nm for the WT (see Figure 18).
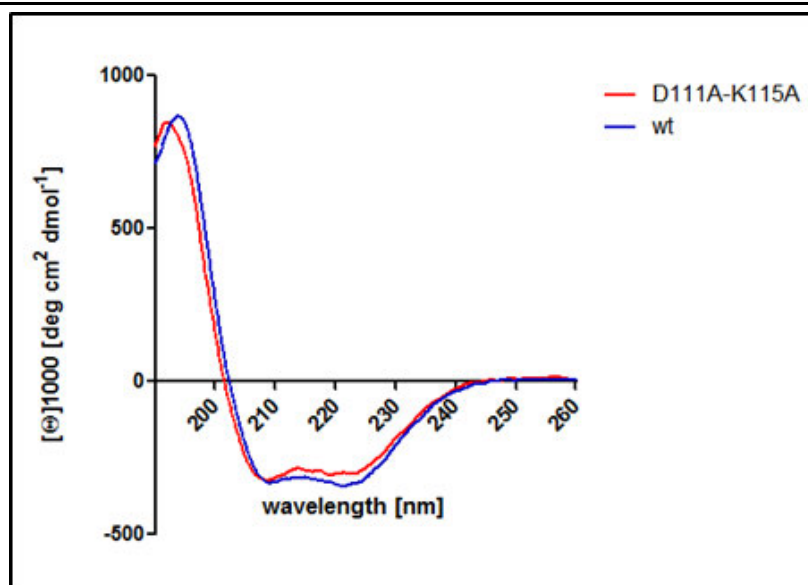
Figure 18: CD measurement of TenA WT and D111A-K115A mutant solutions. Mutant curve is displayed in red, the WT in blue. Figure was generated with GraphPad Prism 5 version 5.01 for Windows (GraphPad Software, La Jolla California USA, www.graphpad.com).

During mutagenic studies, it was observed that solubility of the double mutant D111A- K115A was decreased in comparison to the WT. The WT could be concentrated up to 30 mg/ml, but the mutant precipitated when the concentration reached approximately 2-3 mg/ml. With the PBEQ solver [146, 147] the electrostatic potential and solvation energy was calculated for both protein species by solving the Poisson-Boltzmann equation. The electrostatic free energy (ΔG^{elec}) for the tetramer is -27,678 kcal/mol and for the monomer -4,936 kcal/mol. A $\Delta\Delta G^{elec}$ of 22,742 kcal/mol indicates a significant stability increase for the complex in solution.

A monodisperse solution could not be prepared due to concentration dependent aggregation. Therefore SAXS and DLS analyses were not suitable to further characterise the TenA double mutant. However, the concentrations used for gelfiltration, activity tests and CD spectroscopy were in the range from 0.1-1.5 mg/ml. At this concentration gelfiltration showed a clear peak for monomeric protein (see Figure 16 B).

Analysis of surface residues in the monomer and tetramer with the *PROTORP* server [148] revealed that in the tetramer the distribution of polar, non-polar and charged residues is approximately the same, whereas the monomerisation leads to an increase of solvent exposed non-polar residues. The loss of tetramerisation led to an exposure of more than 60 % non-polar amino acids to the solvent. This can also be seen in the surface representation (see Figure 19).
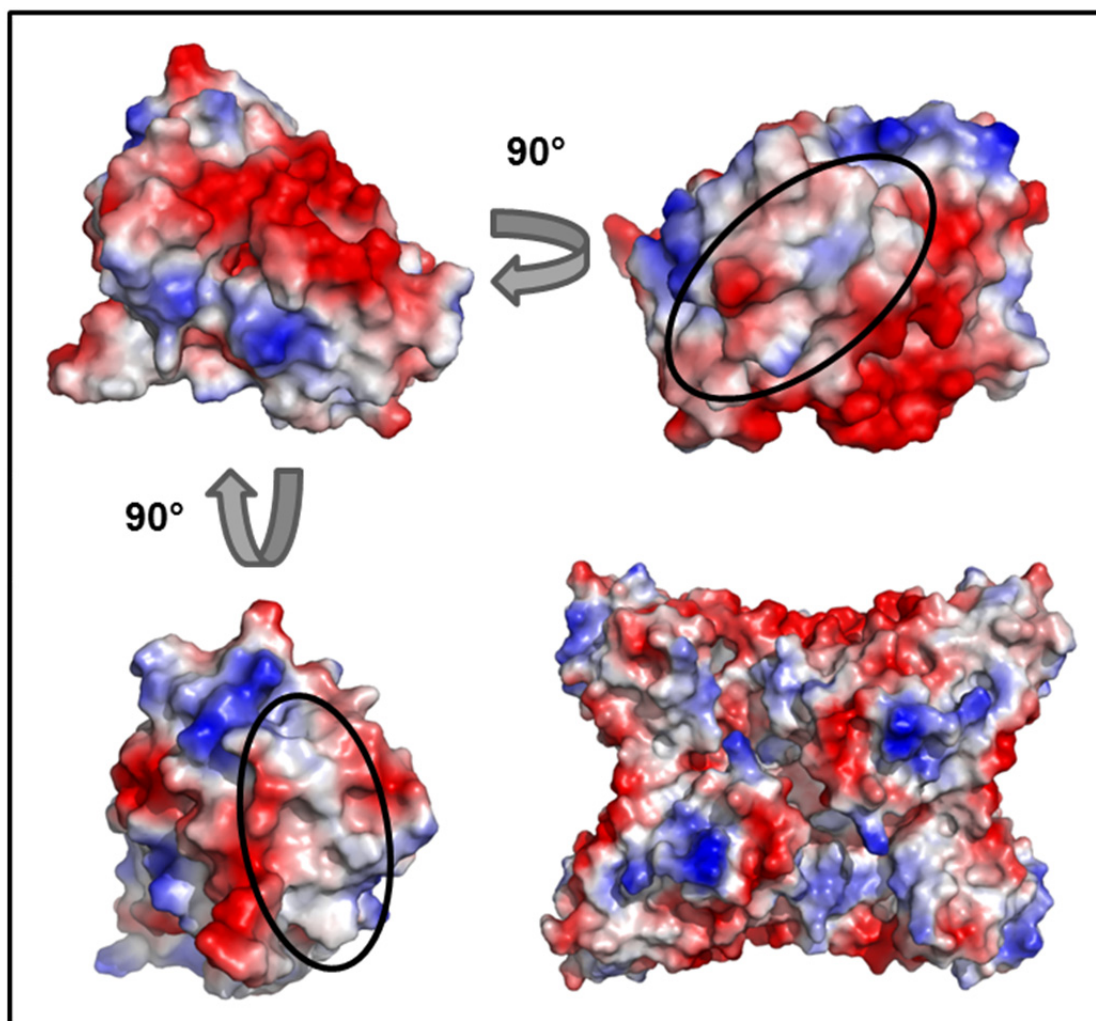
Figure 19: Surface charge representation for TenA. Positive charge is marked in red, negative charge in blue and uncharged residues in grey. Previously buried surfaces are encircled. On the upper left side A-C interface and on the lower left side A-B interface is shown. The encircled contain mainly hydrophobic residues, which led to the significantly reduced solubility of the monomer when compared to the tetramer. Figure was generated with PyMOL (PyMOL Molecular Graphics System, Version 1.3, Schrödinger, LLC.).

4.3.2   Activity assays for TenA WT and the D111A-K115A mutant

To analyse the effect of monomerisation on activity, a comparison of kinetic parameters has been carried out for the cleavage of thiamin by TenA. Conversion of thiamin was plotted against substrate concentration in a Michaelis-Menten diagram (see Figure 20).
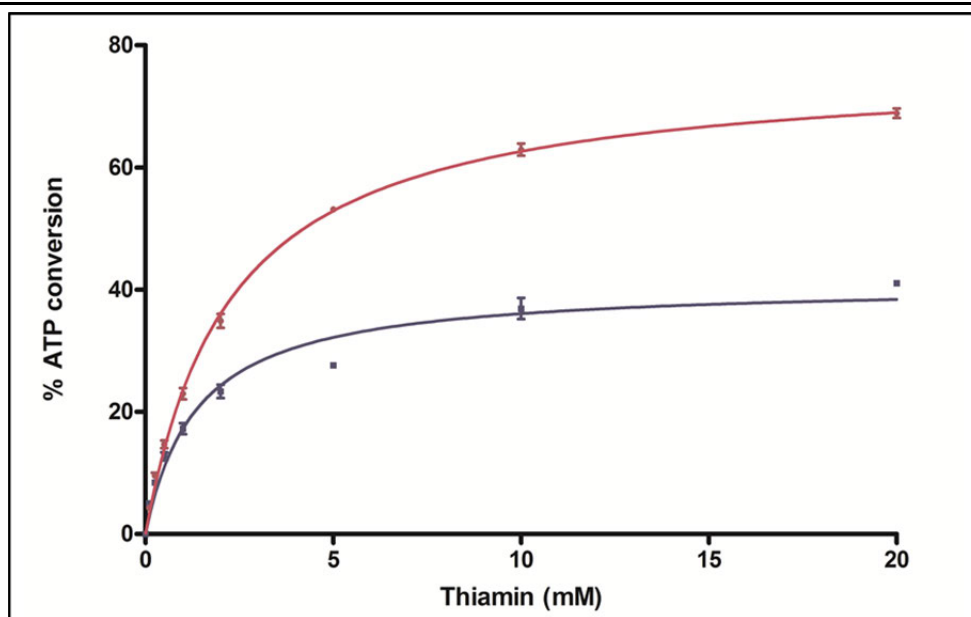
Figure 20: Michaelis-Menten diagram for TenA WT and D111A-K115A mutant activity. Purple line represents the mutant, the blue line the WT. Analysis was carried out in duplicates from three individual protein preparations. ATP-conversion was measured with ^{33}P-ATP in the ThiM assay. ATP conversion was equated with THZ phosphorylation. This was then equated with thiamin cleavage into HMP and THZ, derived from the TenA assay. Error bars indicate standard error of the mean (SEM). Figure has been generated with GraphPad Prism 5 version 5.01 for Windows (GraphPad Software, La Jolla California USA, www.graphpad.com).

Michaelis-Menten kinetics is a model in which the reaction rate *v* is related to substrate concentration *[S]*. The formula is given by:

$$v = \frac{V_{max}\,[S]}{K_M + \,[S]}$$

V_{max}= maximum rate attainable

K_M= Michaelis-Menten constant, [S] at half maximum rate

From the non-linear regression curves the maximum rate V_{max} and also the substrate concentration at half maximal rate K_M was determined. The mutant revealed a V_{max}-value and also K_M-value, which are both approximately double of the WT protein. Additionally, the turnover number was calculated using the following equation:

$$\mathrm{k}_{cat} = \frac{V_{max}}{[E]} = turnover\ number$$

k_{cat}= turnover number

[E]= enzyme concentration

Specific activity of the WT is slightly smaller than for the mutant, but in the same range, the same accounts for the turnover number k_{cat} and the efficiency k_{cat}/K_M (see Table 4).

Table 4: Kinetic parameters of the tetrameric TenA WT and monomeric TenA D111A-K115A mutant.

	K_M (mM)	Specific Activity (mU/mg)	k_{cat} (ms^{-1})	k_{cat}/K_M (M^{-1} s^{-1})
TenA D111A-K115A	2.25 ± 0.17	15.31 ± 0.24	6.8 ± 0.11	3.04 ± 0.05
TenA WT	1.40 ± 0.19	9.12 ± 0.16	4.07 ± 0.07	2.92 ± 0.05

4.3.3 TenA stability test

To further identify differences between the tetrameric and monomeric protein, CD measurements were carried out. TenA WT and D111A-K115A mutant protein was purified and dialysed against salt-free phosphate buffer. 0.1 mg/ml dilutions of both protein species were prepared and monitored during 15 d by CD spectroscopy. One set of samples was stored at RT and the other 4 °C.
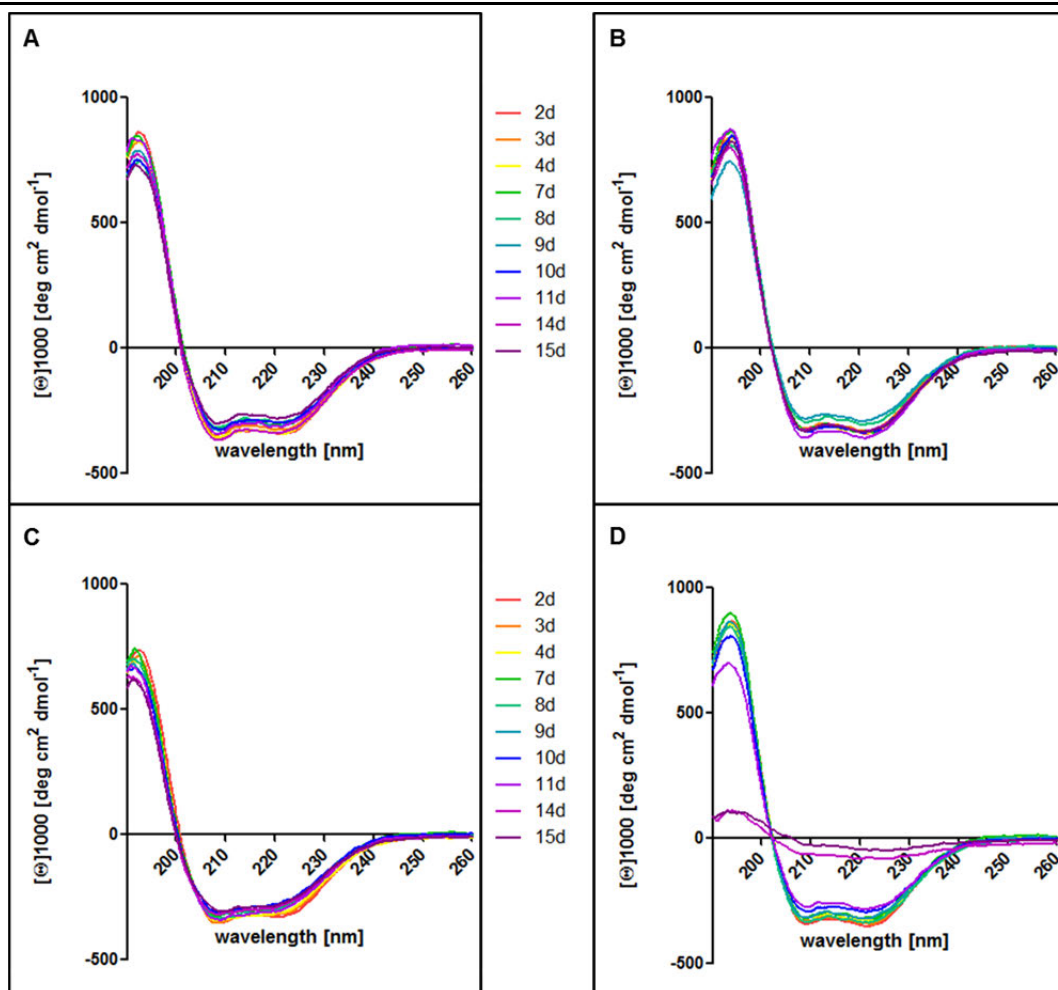
Figure 21: TenA stability monitored by CD spectroscopy. D111A-K115A mutant stored at 4 °C (A), and at RT (C) and the respective WT protein measurements at 4 °C (B) and RT (D) for 15 d. Measurements were performed from the same stock every one to three days at a concentration of 0.1 mg/ml. Figure was generated with GraphPad Prism 5 version 5.01 for Windows (GraphPad Software, La Jolla California USA, www.graphpad.com).

It was observed that the curve shapes do not differ between WT and mutant as it was already shown at the beginning of mutagenic studies (see Figure 18). Both solutions show mainly α-helical folding, whereas the respective maxima and minima values differ due to differences in concentration. No difference have been observed between the two proteins after storage at 4 °C for 15 d (see Figure 21 A and B), however the WT protein stored at RT unfolded after 11 d due to a contamination in comparison to the mutant (see Figure 21 C and D) .

As no significant difference were observed between the two proteins, a protease stability test was carried out. 200 µg of TenA WT and TenA D111A-K115A respectively were digested with the serine proteases subtilisin and trypsin (Floppy Choppy Kit, Jena BioScience, Germany) at a ratio of 1:1000 for 52 h. During digestion, 5 µg samples were taken, incubated with SDS-sample buffer and

subsequently applied to a 12.5 % SDS-gel. The gel was stained with a coomassie brilliant blue solution for further evaluation (see Figure 22).
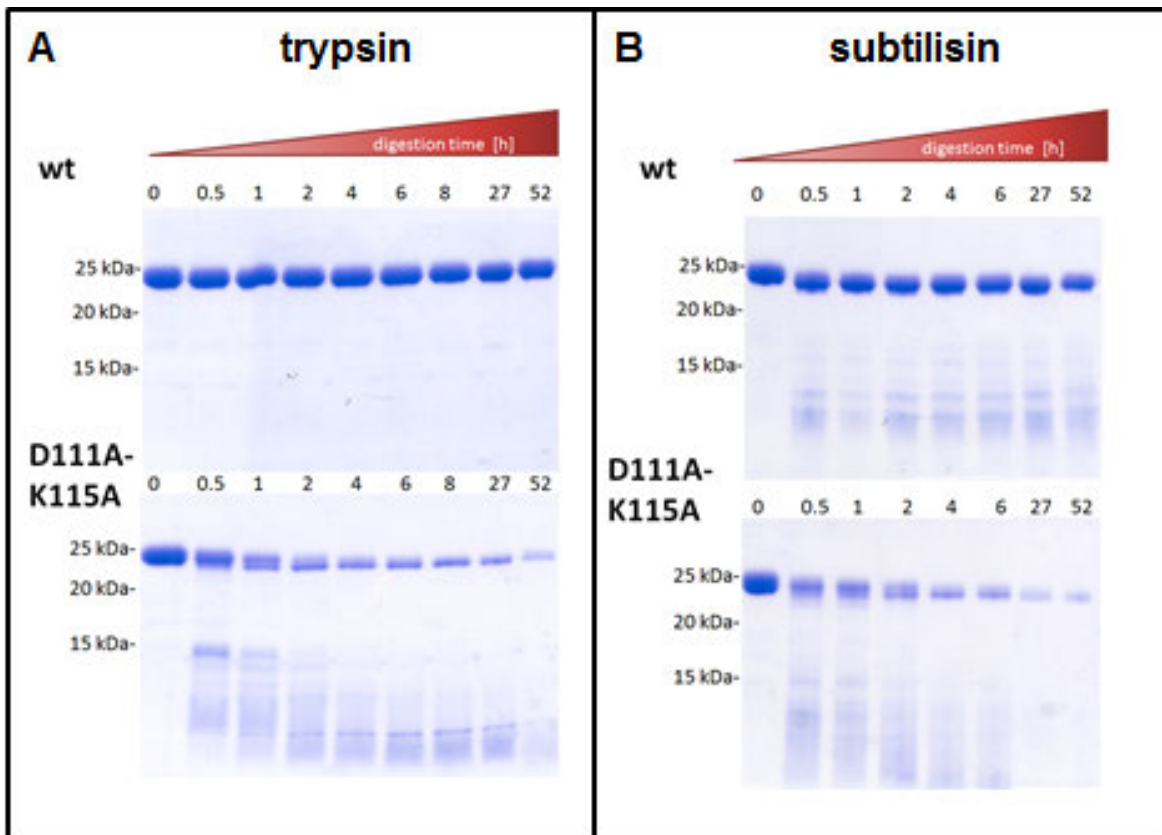
Figure 22: Trypsin (A) and subtilisin (B) digest of TenA WT (upper gels) and D111A-K115A mutant (lower gels). Proteases were added 1:1,000 to the protein sample and incubated at RT for 52 h. Numbers on the left side of the gels show marker band size, numbers on the top of the gels indicate incubation time. Samples were subsequently incubated at 95 °C °C with SDS-sample buffer and stored at 4 °C until they were applied to an SDS gel. Undigested protein served as control. The SDS-gel was stained with coomassie.

The WT protein is not affected by trypsin digestion and remains stable during the whole time course of digestion. After 52 h no degradation bands of the WT protein were observed. In contrast, the mutant is partially digested after 0.5 h and undigested protein with a size of 25 kDa almost disappeared after 52 h (see Figure 22 A).

Also during subtilisin digestion a difference between both protein species was observed. In contrast to trypsin digestion the WT protein is also digested, but not in the same extent as the mutant. After 52 h, undigested WT protein was only slightly reduced, whereas mutant protein was almost completely digested (see Figure 22 B)

4.4 Structure of ThiM

4.4.1 ThiM crystallisation

A ThiM preparation as a Strep-tag fusion protein was used to identify initial crystallisation conditions. The protein was purified with a Strep-tactin matrix and dialysed against desthiobiotin-free buffer W. The solution was concentrated to a concentration of 10 mg/ml and centrifuged at 20,000 x g, at 4 °C for 1 h. Dispersity was monitored by DLS (see Figure 23 A).
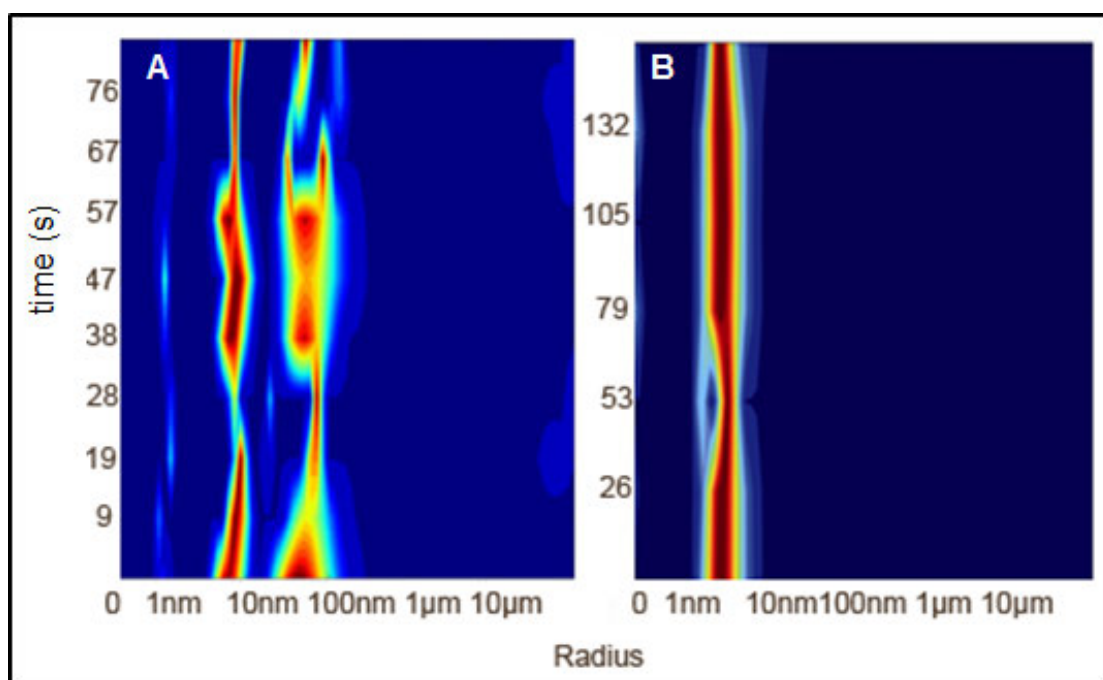
Figure 23: DLS measurement of ThiM solution with Strep-tag (A) centrifuged at 20,000 x g and with His-tag centrifuged at 100,000 x g (B) at a concentration of 20 mg/ml. The colours of the heatmap indicate the relative intensity of the particle, with blue being zero and dark red being maximum. The particle size was plotted against the time of the measurement.

For initial crystallisation in total 384 conditions were tested applying the *Cryos*, *Classics*, *JCSG+* and *ComPAS* screening suites (all Qiagen, Germany). 300 nl of protein solution were mixed with 300 nl of precipitant solution using the pipetting robot Honeybee 961 (Genomic Solutions, USA) in 96-well sitting drop plates (NeXtal QIA1 µplates, Qiagen, Germany). The reservoir was filled with 55 µl of precipitant solution. After 6 d at 20 °C, initial crystals grew at five conditions (see Figure 24 A-F).
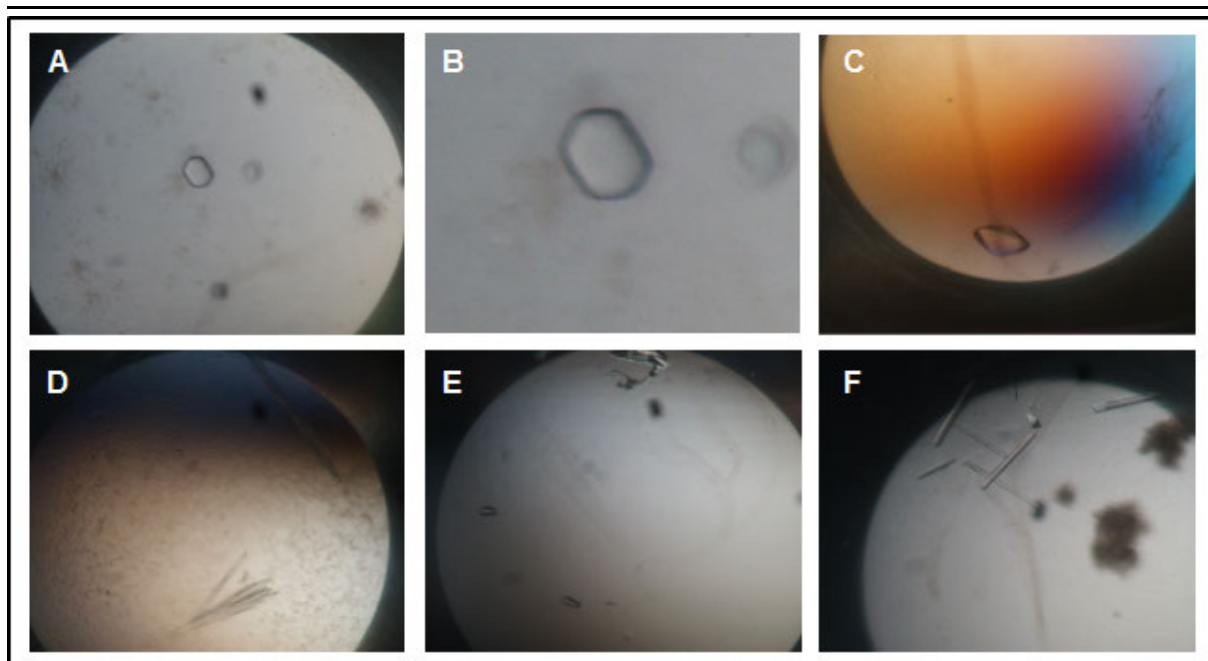
Figure 24: ThiM crystals grown after 6 d at a concentration of 20 mg/ml obtained by the vapour diffusion technique in NeXtal QIA1 μplates (Qiagen, Germany). A: *JCSG+* **suite A5 (20 % PEG 3,350, 0.2 M magnesium formate); B: Detailed view of crystal observed in A. C: Classic suite F8 (20 % PEG 8,000, 0.2 M magnesium acetate, 0.1 M sodium cacodylate pH 6.5); D:** *JCSG+* **suite D1 (24 % PEG 1500, 20 % glycerol); E***: Cryos* **suite H1 (20 % PEG 4,000, 20 % glycerol, 0.08 M sodium acetate pH 4.6, 0.16 M ammonium sulfate); F:** *Classics* **suite H4 (30 % PEG 4,000, 0.2 M magnesium chloride, 0.1 M Tris/ HCl pH 8.5, 0.2 M magnesium chloride).**

After identification of these conditions, the gene encoding for a new ThiM fusion protein with a C-terminal His-tag (cleavable through TEV protease digestion) was generated. The gene was expressed, the derived protein purified using a Ni-NTA matrix and dialysed against buffer W. The protein was concentrated to a concentration of 20 mg/ml and centrifuged at 100,000 x g, at 4 °C for 1 h. The DLS measurements show a monodisperse solution after ultra-centrifugation at 100,000 x g with a hydrodynamic radius of 3.2 ± 0.3 nm (see Figure 23 B).

This monodisperse solution was applied for crystallisation experiments to 24-well CPL-130 plates (JenaBioscience, Germany) using the hanging drop vapour diffusion technique by varying PEG conditions around the initially obtained condition (20 % PEG 3,350, 0.2 M magnesium formate). Crystals grew in optimised conditions H5 from the *JCSG+* suite in the range from 18-22 % PEG 3,350, but they were barely separated and though not suitable for X-ray diffraction experiments (see Figure 25 A-E).
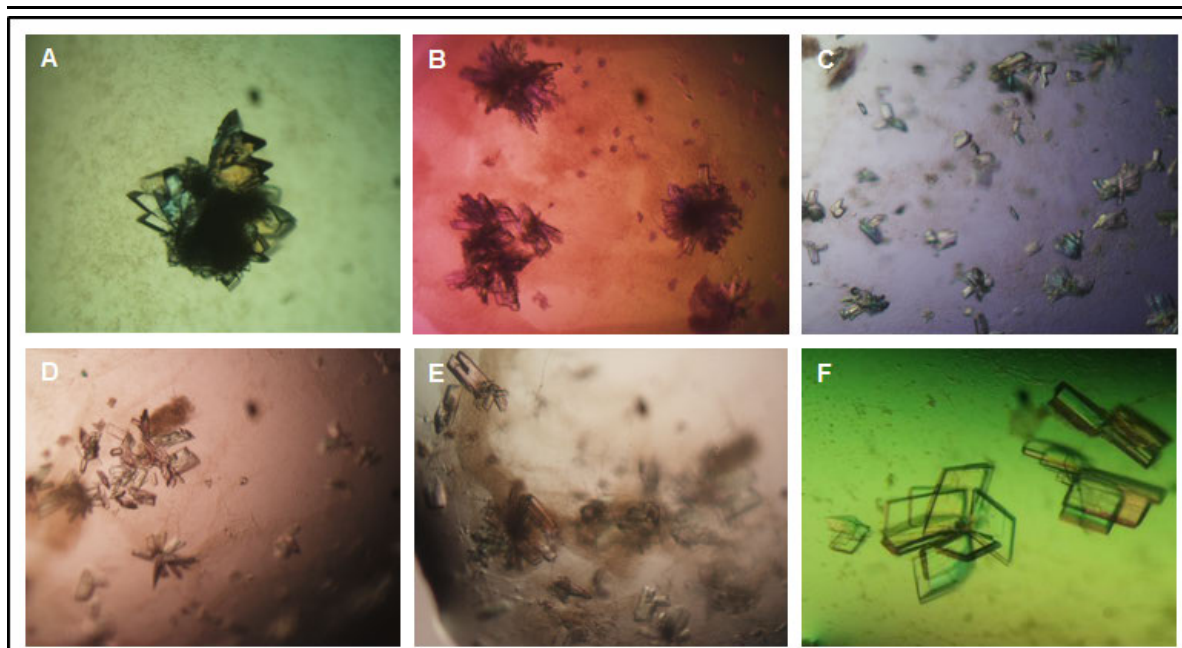
Figure 25: Optimisation of condition A5 from the *JCSG+* suite for ThiM His-tag fusion protein obtained by vapour diffusion in 24-well CPL-130 plates (JenaBioscience, Germany) within 4 d in the range from 18-24 % PEG 3,350. A: 18 % PEG 3,350, 0.2 M magnesium formate; B: 19 % PEG 3,350, 0.2 M magnesium formate; C: 20 % PEG 3,350, 0.2 M magnesium formate; D: 22 % PEG 3,350, 0.2 M magnesium formate; E: 24 % PEG 3,350, 0.2 M magnesium formate; F: 20 % PEG 3,350, 0.2 M magnesium formate, 5 % (v/v) isopropanol.

In order to obtain more X-ray suitable crystals, an alcohol screen was performed testing addition of 1-10 % of either ethanol or isopropanol to the already obtained conditions in the range from 18-28 % PEG 3,350 and 0.2 M magnesium formate. X-ray suitable crystals grew at 18 % PEG 3,350, 0.2 M magnesium formate and 5 % isopropanol to final dimensions of 0.3 x 0.2 x 0.02 mm after 5 d at 20 °C (see Figure 25 F). A single lamella shaped crystal was separated with microtools (Hampton Research, USA) and flash frozen for data collection in a nylon loop. The PEG 3,350 contained in the crystallisation condition was sufficient allowing cryo protection and no additional cryo-protectants were added prior to flash freezing.

4.4.2 Crystallisation in preparation for the Shenzou8 space project

To obtain increased crystal quality in order to collect high resolution data, crystals were grown in space, as under microgravity conditions no sedimentation and convection are present and higher crystal quality can be expected.

Counter diffusion experiments in capillaries in a microgravity environment were prepared by **RAPHAEL EBERLE** and **DOMINIK OBERTHÜR**. After return of the space shuttle, the micro crystals were prepared from agarose with microtools (Mitegen,

USA) (see Figure 26 A-C). A seedstock was prepared according to the manufacturer´s protocol and streakseeding from the microseedstock was carried out in a 24-well CPL-130 plate (JenaBioscience, Germany). After 8 d, an intergrown crystal appeared in the first droplet (see Figure 26 D), which was subsequently used to prepare a microseedstock. In 48-well MRC sitting drop plates (Molecular Dimensions, UK) three rows of the precipitants were prepared (18, 20 and 22 % PEG 3,350, 0.2 M magnesium formate and 5 % isopropanol). Crystals grew after 4 d to maximum dimensions of 0.3 x 0.1 x 0.1 mm (see Figure 26 E).
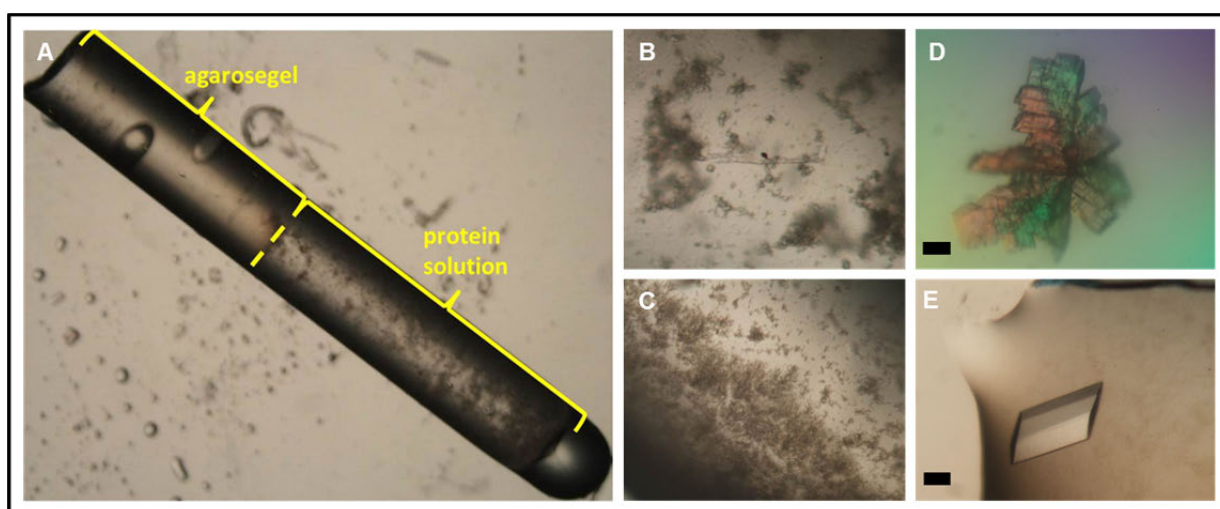
Figure 26: ThiM crystals grown in space for 3 d and seeding crystals. A: Capillary with crystals from space, sealed with agarose. B, C: Detailed view of crystals grown in space. D: Intergrown crystal, grown from a seedstock made from crystals seen in B and C obtained in a 24-well CPL-130 plate (JenaBioscience, Germany) with the hanging drop vapour diffusion technique at a protein concentration of 9.8 mg/ml. E: Crystal grown from a seedstock made from crystal seen in D in a 48-well MRC sitting drop plate (Molecular Dimensions, UK) with the vapour diffusion sitting drop technique at a protein concentration of 10 mg/ml. Figures A-C courtesy of DOMINIK OBERTHÜR. Scale bar: 100 µM.

4.4.3 Co-crystallisation and soaking

For co-crystallisation of ThiM with its natural substrates or putative substrate analogues, ThiM solutions at 10 mg/ml and 20 mg/ml concentration were used to identify new crystallisation conditions. The protein was mixed with 1 mM of THZ, 1mM of AMP-PCP and incubated on ice for 2 h. The reservoirs of pre-greased 24-well VDX plates (Hampton Research, USA) for hanging drop vapour diffusion were filled with 500 µl of stock solutions from the *Wizard Screens I-VI* (Emerald BioSystems, USA) and *Crystal Screens I* and *II* (Hampton Research). In total, 288 conditions were tested. 2 droplets, one with 1 µl of the 10 mg/ml solution and one with 1 µl of the 20 mg/ml solution were placed on a siliconised cover slide and mixed

with equal volumes of precipitant before sealing. After 3 d crystals were grown in six conditions (see Figure 27).
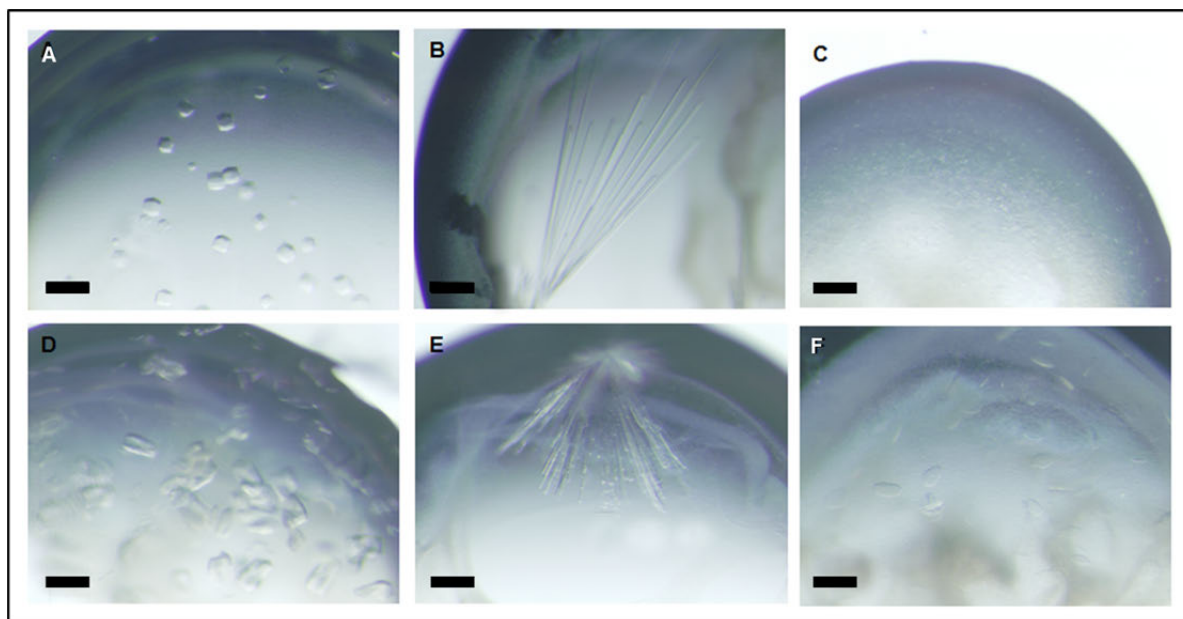
Figure 27: Initial crystals from a ThiM co-crystallisation screen obtained after 3d VDX plates (Hampton Research, USA) for hanging drop vapour diffusion. Scale bar: 100 µm. A: 20 mg/ml ThiM (precipitant: 1.6 M NaH_2PO_4/0.4 M K_2HPO_4 phosphate-citrate pH 4.2); B: 20 mg/ml ThiM (precipitant: 10 % (w/v) PEG 8,000, 0.1 M imidazole pH 8.0, 0.2 M Ca(OAc)$_2$); C: 20 mg/ml ThiM (precipitant: 1.26 M (NH4)2SO4, 0.1 M cacodylate pH 6.5; D: 20 mg/ml ThiM (precipitant: 20 % (w/v) PEG-1000, 0.1 M imidazole pH 8.0, 0.2 M Ca(OAc)$_2$; E: 20 mg/ml ThiM (precipitant: 20 % (w/v) PEG 3,350, 0.1 M BisTris propane 6.5, 200 mM sodium fluoride); F: 20 mg/ml ThiM (precipitant: 0.2 M ammonium sulfate, 0.1 M sodium acetate trihydrate pH 4.6, 30 % (w/v) PEG MME 2000).

Co-crystallisation was also carried out with the crystallisation condition of native by mixing 10 mg/ml with the same ligand concentrations as used in the *Crystal* and *Wizard Screens*. The protein was previously concentrated to a concentration of 10 mg/ml and precipitated overnight with an equal volume of 0.5 M magnesium formate at 4 °C. The solution was clarified (70,000 x g, 4 °C, 50 min) and subsequently concentrated to a concentration of 10 mg/ml. After incubation of the protein with its ligands for 2 h on ice, crystallisation trials were set up in VDX plates (Hampton Research, USA) for hanging drop vapour diffusion, varying the PEG 3,350 concentration in the range from 14-24 %. Precipitant also contained 5 % isopropanol and 0.1 M magnesium formate. After incubation at 20 °C, crystals appeared after 3 d (see Figure 28 A).
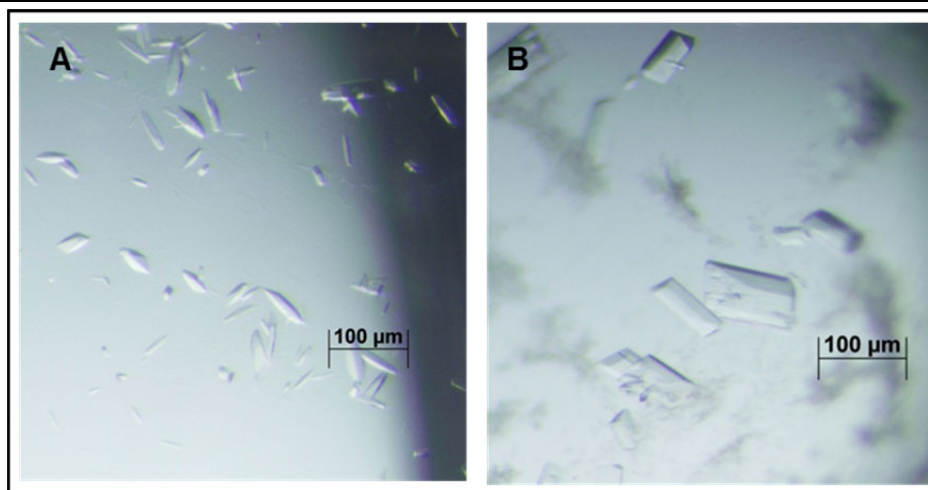
Figure 28 A: ThiM co-crystallised with 1mM THZ and 1mM AMP-PCP at a concentration of 10 mg/ml (precipitant: 16 % PEG 3,350, 0.1 M magnesium formate, 5 % isopropanol); B: Native ThiM crystal (precipitant: 15 % PEG 3350, 0.1 M magnesium formate, 5 % isopropanol) soaked with 10 mM THZ and 10mM AMP-PCP.

Crystals were cryo-protected with precipitant containing 10 °C glycerol and diffraction was recorded at A1 and F1 beamlines (CHESS, USA). Diffraction was recorded for the crystal shown in Figure 27 D to approximately 8 Å. All other conditions contained salt crystals. The crystallisation was further optimised in 24-well CPL-130 plates (JenaBioscience, Germany), but no X-ray suitable crystals were obtained.

As co-crystallisation did not yield X-ray suitable crystals, native ThiM crystals (vapour diffusion technique, 15 % PEG 3,350, 0.1 M magnesium formate, 5 % isopropanol, concentration:10 mg/ml) were transferred to a droplet containing the respective precipitant and 10 mM of THZ and AMP-PCP respectively. The crystal was incubated for 10 min and flash frozen in liquid nitrogen for data collection applying synchrotron radiation.

4.4.4 ThiM diffraction data analysis

4.4.4.1 ThiM native structure determination

Diffraction of a ThiM single lamella crystals as displayed in Figure 25 F, was recorded to 2.1 Å resolution at consortium beamline X13 (Hasylab/DESY, Germany). Data were indexed with *Denzo* and scaled with *Scalepack (*both from the *HKL-package* [121]) in the triclinic space group P1 with an overall R_{merge} of 7.6 % in the resolution range from 50-2.15 Å. A Matthews´ coefficient [137] of 2.3 $Å^3$ Da^{-1} with a corresponding solvent content of approximately 46 % indicated six molecules in the asymmetric unit.

Table 5: Data collection and refinement statistics for native ThiM

Data collection statistics[a]	
Beamline	Consortium Beamline X13, HASYLAB/DESY
Temperature [K]	100
Wavelength [Å]	0.81
Space group	P1
Unit cell parameters: a, b, c [Å]	62.02, 62.40, 107.82
α, β, γ [°]	92.25, 91.37, 101.48
Resolution range	50-2.15
Measured reflections	1271580
Unique reflections	84534
Completeness [%]	98.7 (97.8)
Multiplicity	3.6 (3.4)
Average I/σ(I)	13.4 (2.8)
R_{merge}[b]	7.6 (35.3)
Refinement statistics	
Resolution range	50-2.15
R_{work}/ R_{free} [%]	19.75/ 24.38
Asymmetric unit content:	
Protein atoms	11233
Water molecules	699
Rms bond-length deviation [Å]	0.007
Rms bond angle deviation [°]	1
Mean B factor [Å^2]	28.28
Ramachandran plot analysis:	
Most favoured regions [%]	93.4
Allowed regions [%]	6.5
Generously allowed regions [%]	0.1

[a]Values in parentheses are for the highest resolution shell.

[b]R_{merge}: $\sum_{hkl} \sum_i | I_i (hkl) - \langle I (hkl) \rangle | / \sum_{hkl}\sum_i I_i (hkl)$, where $\langle I (hkl) \rangle$ is the mean intensity of the observations $I_i (hkl)$ of reflection hkl.

Sequence alignment with the homologue structures from an NCBI/Blast [138] search query carried out with *Clustal W* [179] and *BOXSHADE* [180] showed a high degree of ThiM conservation (see Figure 29). A homology model for molecular replacement with *Bs*ThiK (pdb entry: 1C3Q, sequence identity: 38 %) was built with the homology modelling server *HOMER* [139].

Figure 29: Sequence alignment for ThiM derived from *S. aureus* with the most homologue structures from an NCBI/ Blast search. Alignment was carried out with *Clustal W* [140] and *BOXSHADE* [141]. Identical residues are shown in black and similar residues in grey. Secondary structure elements are marked below in a purple ribbon representation and were generated with *PDBsum* [142]. H= α-helix, S= β-sheet, dashed red line indicates disordered regions and red solid line indicates β-hairpins. Secondary structure elements are based on the solved structure seen in Figure 30. Red circles above the sequence indicate THZ binding residues, blue circles ATP binding residues based on the superimposition model shown in Figure 37.

Molecular replacement was carried out with *PHASER* [149] at a final Z score of 15.5 and a log-likelihood gain value of 849.7. Twinning analysis revealed two twin domains and therefore twin refinement was carried out. *COOT* [125] was used for model building and refinement with *Refmac5* from the *CCP4* [123] suite applying isotropic B-factor refinement. The starting model was refined to final R: 19.8 % and R$_{free}$: 24.4 %.
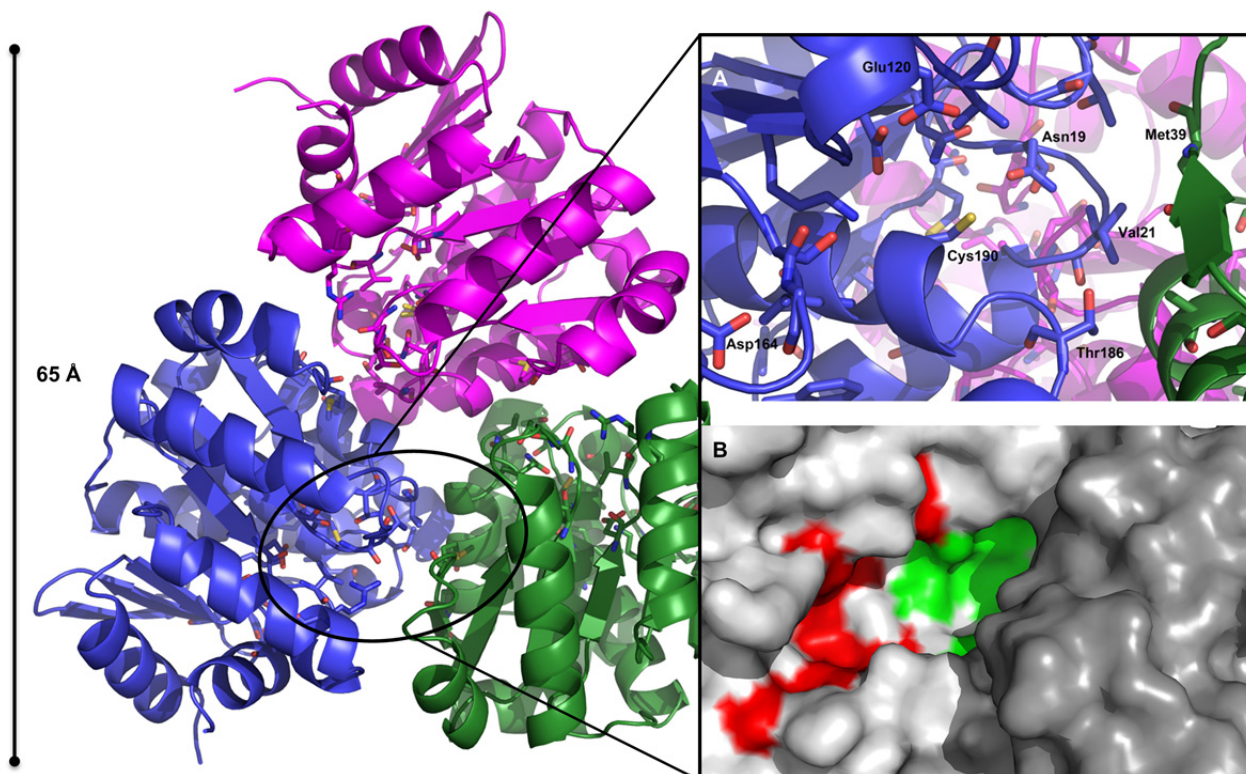
Figure 30: Ribbon representation of the *Sa*ThiM structure, which was solved to 2.15 Å resolution. The structure comprises three identical monomers, indicated by three different colours. The active site is located within the interface of two monomers. The active site residues are depicted in stick representation with carbon in the respective chain colour, nitrogen in blue, oxygen in red and sulphur in yellow. A: Detailed view of the active site pocket with the chains in ribbon representation and the active site residues in stick representation, using the same colour code as for the trimer. The labels indicate some of the active site residues. B: The active site pocket shown in A in surface representation. Green surface indicates active site residues coordinating THZ, red surface indicates the active site pocket for ATP. Dark grey and light grey differentiate between the two monomers previously shown in green and blue. Active site prediction was carried out via sequence and structure alignment of *Sa*ThiM and *Bs*Thik, which was co-crystallised with THZ-P and ATP (see Figure 29 and Figure 37). Figure was obtained using PyMOL (PyMOL Molecular Graphics System, Version 1.3, Schrödinger, LLC.).

The structure comprises three monomers building a trimer with three independent active sites located within the interface of two subunits and a total accessible surface area of approximately 18,000 Å^2 (calculated with *AREAMOL* from the *CCP4* [123] suite) (see Figure 30). In every monomer, nine β-sheets are flanked by five α- helices on each side. The first six β-sheets are parallel to each other, the last three in antiparallel orientation. A topology diagram of monomeric ThiM is shown in Figure 31. The structure consists of approximately 49 % α-helix and approximately 17 % β-sheet [144]. Viewed along the three-fold axis the trimer resembles a three-blade propeller (see Figure 30). The region between amino acid 126 in helix 8 and 140 in helix 9 in every monomer is disordered, due to high flexibility in this loop and could not be built in the electron density (see Figure 31 A, dashed red line) .
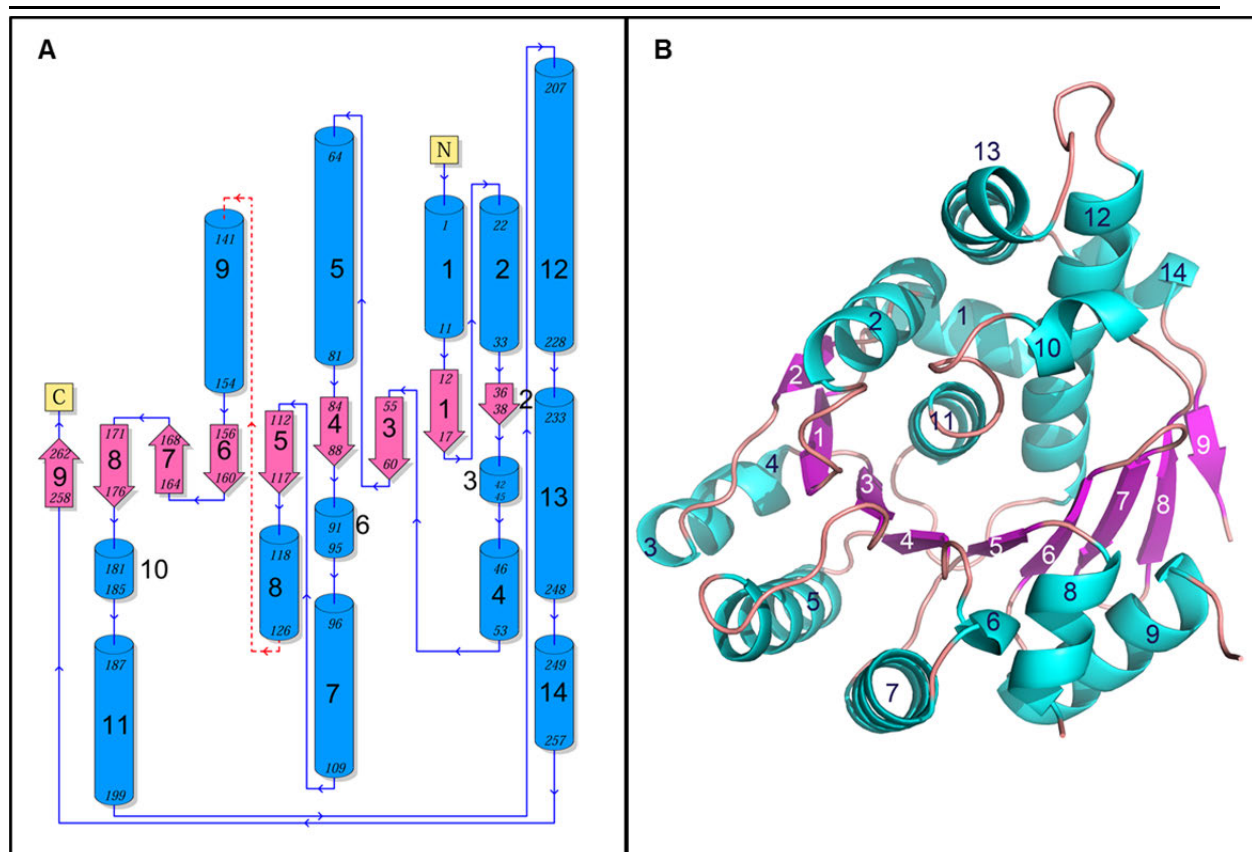
Figure 31: Topology and ribbon drawing of the subunit structure of ThiM. A: Topology diagram. The α-helices are represented by blue cylinders, the β-sheets as pink arrows, connecting loops in dark blue. The smaller numbers indicate the beginning and ending residue number of each secondary structural element. The figure was prepared with *PDBsum* [142]. B: In the ribbon drawing the α-helices are depicted as light blue coils, β-sheets are depicted in pink and loops are depicted in pale red. Numbers in dark blue designate the α-helices, white numbers designate β-sheets numbered from the N- to the C-terminus. Figure was obtained using PyMOL (PyMOL Molecular Graphics System, Version 1.3, Schrödinger, LLC.).

4.4.4.2 Structure determination of ThiM in complex with THZ

Diffraction of ThiM crystals soaked with 10 mM THZ and AMP-PCP respectively displayed in Figure 28 B was recorded to 3 Å resolution at beamline A1 (CHESS, USA). Data were indexed with *HKL-2000* [121] and scaled with *Scalepack* [121] in the triclinic space group P1 with an overall R_{merge} of 11.8 % in the resolution range from 50-3.05 Å. A Matthews´ coefficient [137] of 2.3 $Å^3$ Da^{-1} with a corresponding solvent content of approximately 47 % indicated 12 molecules in the asymmetric unit.
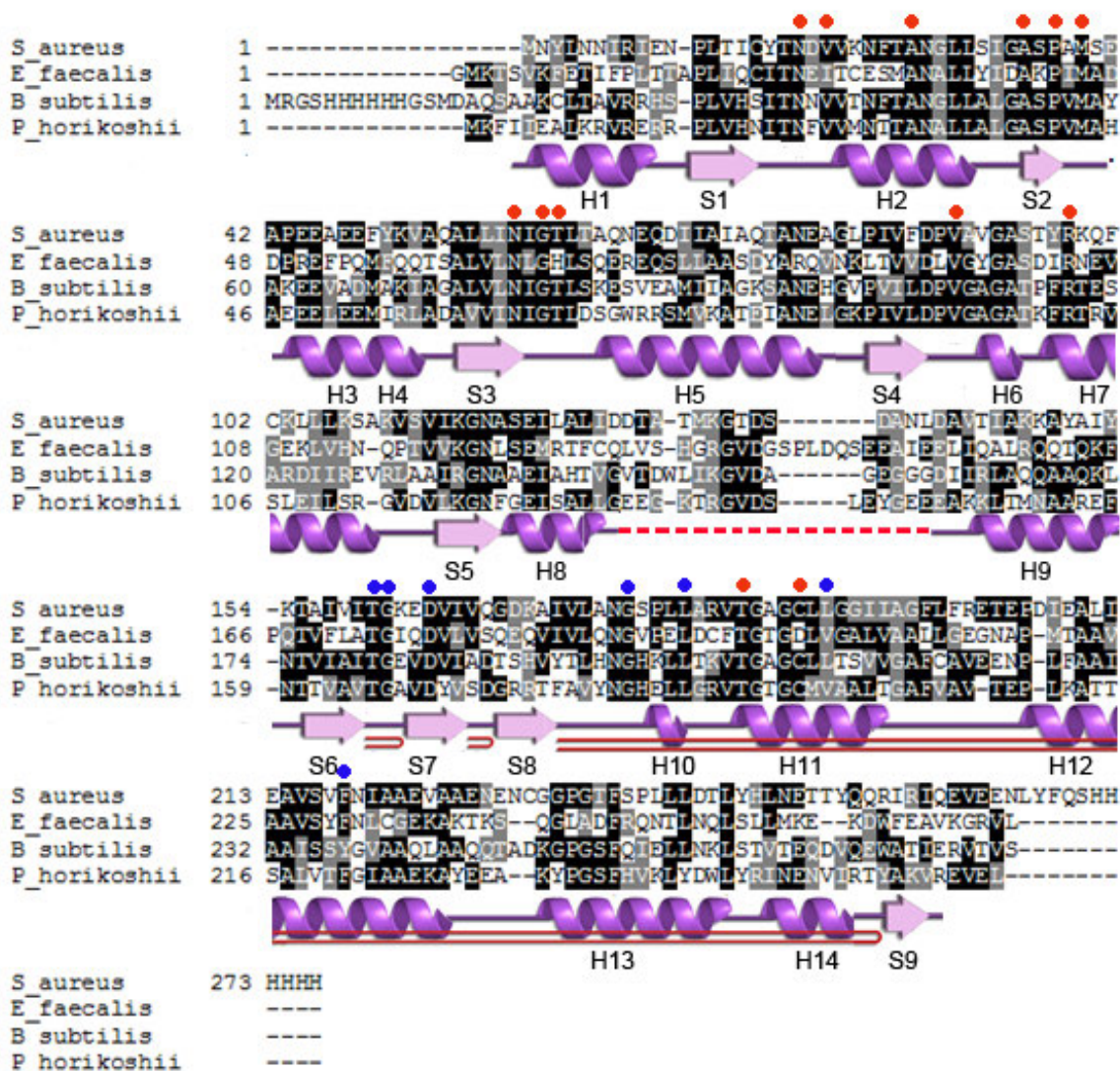
Molecular replacement was carried out with *PHASER* [149] with a final Z score of 51.2 and a log-likelihood gain value of 14262 using a single chain of the native ThiM structure described in chapter 4.4.4.1. Model building was carried out with *COOT* [125] and refinement with *Refmac5* from the *CCP4* [123] suite and *REFINE* [150] from the *PHENIX* suite [124] applying overall B-factor refinement. The starting model was refined to final R: 18.93 % and R_{free}: 24.55 %.

Table 6: Data collection and refinement statistics for ThiM in complex with THZ

Data collection statistics[a]

Beamline	CHESS Beamline A1
Temperature [K]	100
Wavelength [Å]	0.98
Space group	P1
Unit cell parameters: a, b, c [Å]	62.5, 106.3, 125.5
α, β, γ [°]	89.4, 99.4, 91.8
Resolution range	50-3.05 (3.1-3.05)
Measured reflections	1396539
Unique reflections	60692
Completeness [%]	97.4 (92.4)
Multiplicity	3.7 (3.4)
Average $I/\sigma(I)$	24.4 (8.5)
R_{merge}[b]	11.8 (28.5)

Refinement statistics

Resolution range	31.14-3.05 (3.15-3.05)
R_{work}/ R_{free} [%]	18.93/ 24.55 (25.61-34.48)

Asymmetric unit content:

Protein atoms	22671
Water molecules	66
Rms bond-length deviation [Å]	0.01
Rms bond angle deviation [°]	1.0
Mean B factor [Å^2]	29.74

Ramachandran plot analysis:

Most favoured regions [%]	92.3
Allowed regions [%]	7.2
Generously allowed regions [%]	0.2

[a]Values in parentheses are for the highest resolution shell.

[b]R_{merge}: $\sum_{hkl} \sum_i | I_i (hkl) - \langle I (hkl) \rangle | / \sum_{hkl} \sum_i I_i (hkl)$, where $\langle I (hkl) \rangle$ is the mean intensity of the observations $I_i (hkl)$ of reflection hkl.

The ThiM crystal was soaked with both THZ and AMP-PCP, but only THZ was built from the electron density. The active site is located at the interface between two monomers. The binding pocket is formed by the conserved residues: Cys190, Asn19, Val 21, Val22, Val90, Thr62, Met39,Gly61, Thr186, Pro37, whereas Met39 and Pro37 belong to one chain and the remaining amino acids to a second chain. Due to the resolution of 3 Å the ligand position varies slightly throughout the 12 chains, but a preferential orientation of THZ was observed with the methyl group pointing towards Thr186 and the thiazole sulphur pointing towards Asn19 (see Figure 32 B and Figure 33 A). Preferentially, the amide group of Met39 donates a hydrogen bond to the

nitrogen in the thiazolium ring and the sulphur of Cys190 is building a hydrogen bond to the hydroxyl group of THZ (see Figure 32).
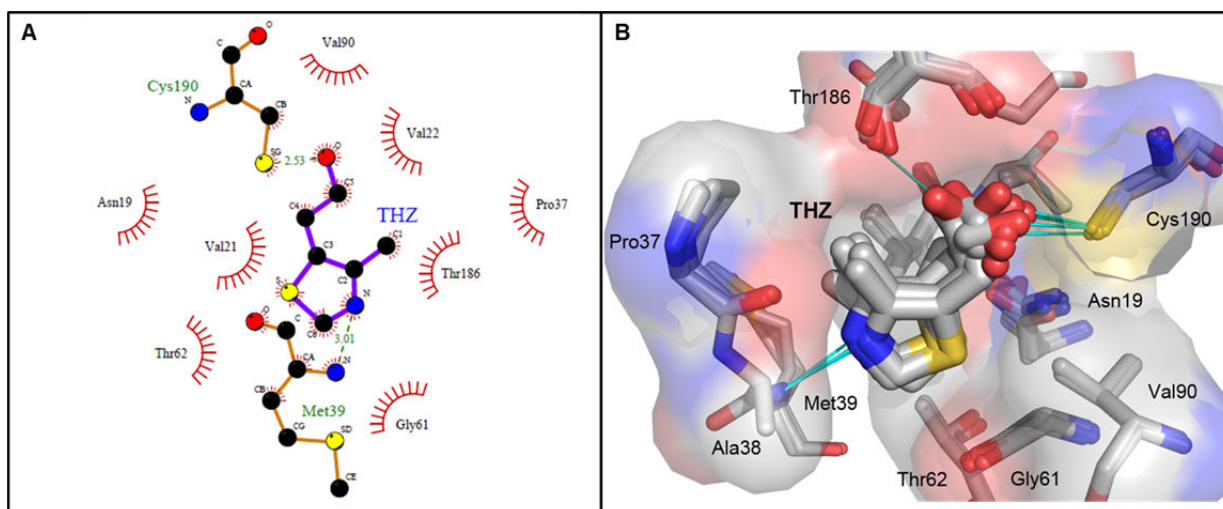
Figure 32: Binding pocket of ThiM for THZ. A: Schematic of the active site with hydrophobic contacts marked by an arc with spokes radiating in red and hydrogen bonds represented as dashed lines in green. Green numbers show hydrogen bond lengths. Carbons are depicted as black balls, oxygen as red balls, nitrogen as blue balls and sulphur as yellow balls. Labels designate the respective residues involved in interaction. Figure was prepared with LIGPLOT [151] B: Superimposition of the active site of all chains refined from the obtained complex data set (see Table 6). Active site residues and the ligand are depicted in sticks representation with carbons in grey oxygen in red, nitrogen in blue and sulphur in yellow. The surface generated for the active site residues highlights the limits of the binding pocket with blue for negative charge, red for positive charge and grey for uncharged residues. Light blue lines show hydrogen bonds. Labels designate the respective residues and the ligand. Figure was obtained using PyMOL (PyMOL Molecular Graphics System, Version 1.3, Schrödinger, LLC.).

The THZ position variation throughout the ThiM chains in *S. aureus* was more pronounced than in *B. subtilis* (compare Figure 33 A and B) due to the difference in resolution (resolution *S. aureus*: 3.05 Å and *B. subtilis*: 1.7 Å), but the overall orientation is relatively similar (see Figure 33 C). Although the resolution is relatively low, a complete electron density was identified for THZ in the ThiM binding site (see Figure 34 A). The omit map contoured at 3 σ confirms the presence of the ligand (see Figure 34 B).
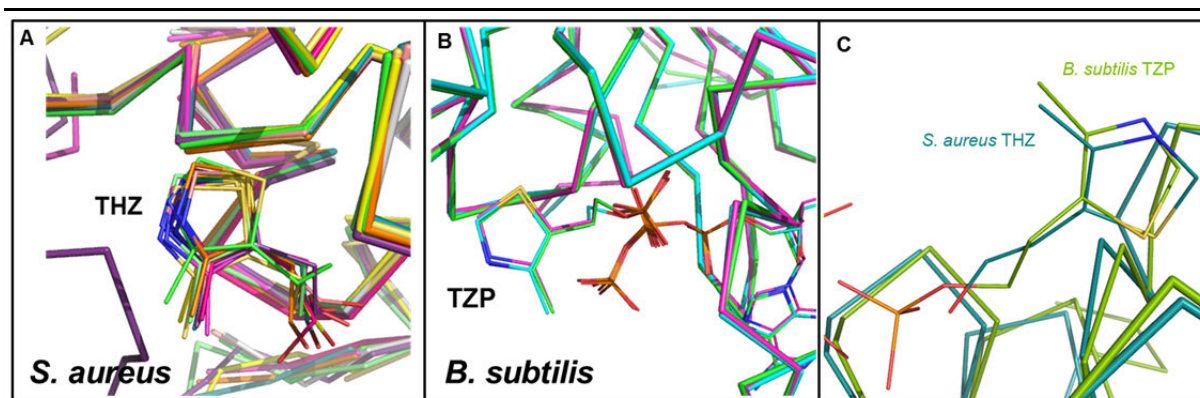
Figure 33: Comparison of THZ binding in *S. aureus* and *B. subtilis*. A: Superimposition in line representation of the THZ binding sites in *S. aureus* based on all refined chains of the ThiM (in complex with THZ) data set (see Table 6). Different colours indicate different chains, whereas oxygen atoms are depicted in red, carbon in the respective chain colour, nitrogen in blue, and sulphur in yellow. B: Superimposition in line representation of TZP (THZ) binding of all chains in pdb entry 1esq from *B. subtilis*. D: Comparison of the THZ binding site from *S. aureus* and *B. subtilis* in line representation. Colour codes for atoms in B-C are as described for A. Figures were obtained using PyMOL (PyMOL Molecular Graphics System, Version 1.3, Schrödinger, LLC.).
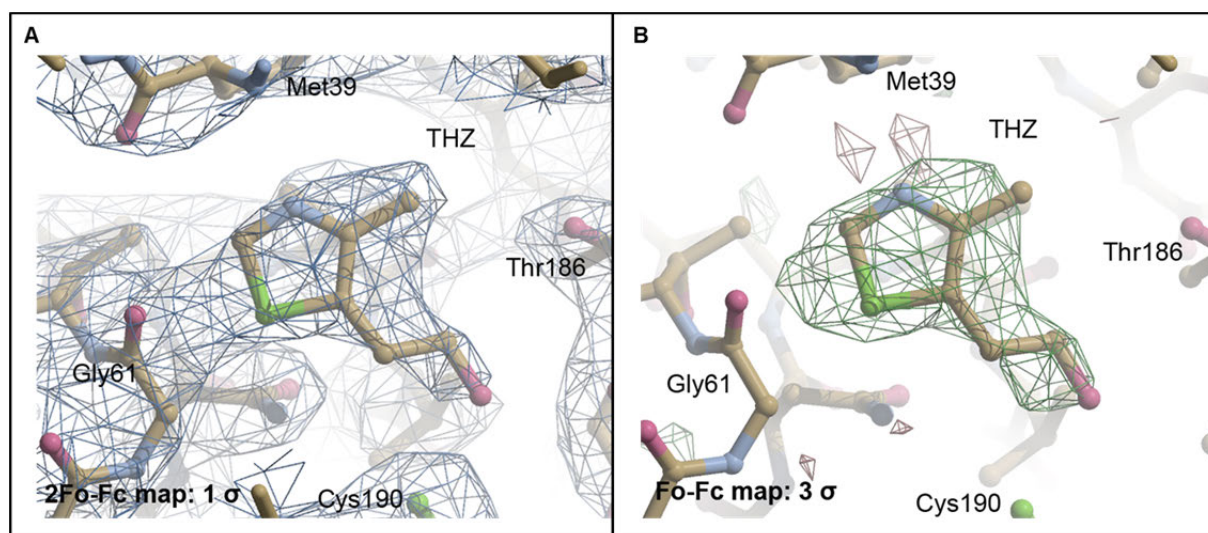
Figure 34: Electron density maps for the THZ binding site. A: 2FoFc map contoured at 1 σ for *S. aureus*. THZ and the amino acid chains are depicted in ball and stick representation, 2Fo-Fc map contoured at 1 σ in dark blue, whereas oxygen atoms are depicted in red, carbon in the respective chain colour, nitrogen in blue, and sulphur in green. Labels show ligand name and respective amino acids. B: Omit map for THZ binding contoured at 3 σ. The Fo-Fc map is depicted in dark green, colour code for the ligand, amino acids and labels are set as for A. Figures were generated with *COOT* [125].

As already observed in the native structure of ThiM (see chapter 4.4.4.1), the region between the amino acids 126 and 141 is very flexible and no electron density was detected for most chains (see Figure 35 A) within the data set. The same accounts for the flexible N-terminus (see Figure 35 B).
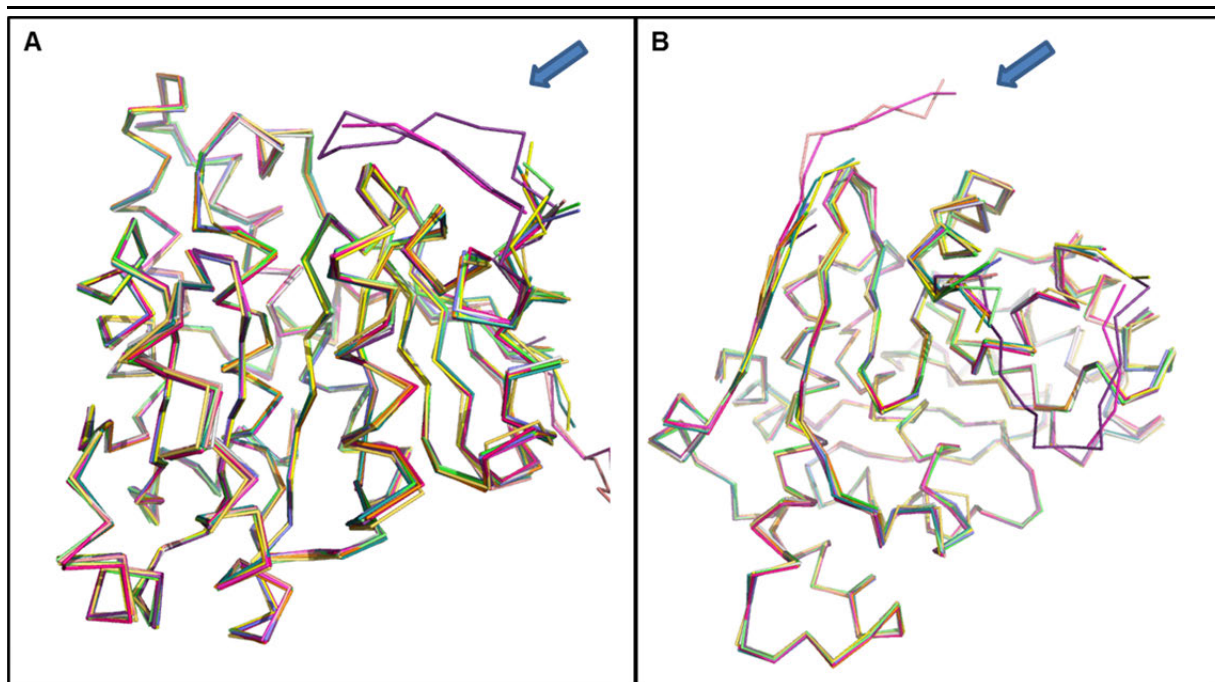
Figure 35: Superimposition of all refined chains of ThiM in complex with THZ in line representation. Different colours indicate different chains. The overall structure shows relatively small variations (rmsd between 0.299 and 0.348 Å). Arrows indicate incomplete regions due to flexibility in the region of amino acid 126 and 141 (A) and the N-terminus (B).

4.4.4.3 Structure determination of native ThiM from seeding experiments

Diffraction of a single ThiM crystal displayed in Figure 26 E was recorded to 1.9 Å resolution at the consortium beamline X13 (HASYLAB/DESY, Germany). Data were indexed with *XDS* [120] and after import to *CCP4* format with *COMBAT*, scaled with *Scala* (both CCP4 [123]-supported programmes) in the monoclinic space group P2$_1$ with an overall R$_{merge}$ of 7.8 % in the resolution range from 20-2.09 Å. A Matthews´ coefficient [137] of 2.3 Å^3 Da^{-1} with a corresponding solvent content of approximately 46 % indicated 6 molecules in the asymmetric unit.

Molecular replacement was carried out with *MOLREP* [143]. The best solution was obtained with a score of 72.9 % and an R-factor of 52.2 % for data in the resolution range from 19.99-2.09 Å. Model building was carried out with *COOT* [125] and refinement with *Refmac5* from the *CCP4* [123] suite applying isotropic B-factor refinement. The starting model was refined to final R: 19.98 % and R$_{free}$: 24.77 %.

Table 7: Data collection and refinement statistics for ThiM from seeding experiments.

Data collection statistics[a]	
Beamline	Consortium Beamline X13, HASYLAB/DESY
Temperature [K]	100
Wavelength [Å]	0.81
Space group	$P2_1$
Unit cell parameters: a, b, c [Å]	62.50, 103.52, 126.18
α, β, γ [°]	90.00, 99.48, 90.00
Resolution range	19.99-2.09
Measured reflections	726828
Unique reflections	93740
Completeness [%]	99.9 (100)
Multiplicity	7.8 (7.7)
Average I/σ(I)	17.3 (4.2)
R_{merge}[b]	7.8 (49.2)
Refinement statistics	
Resolution range	19.91-2.09
R_{work}/ R_{free} [%]	19.98/ 24.77
Asymmetric unit content:	
Protein atoms	11509
Water molecules	788
Rms bond-length deviation [Å]	0.01
Rms bond angle deviation [°]	1.3
Mean *B* factor [Å^2]	25.09
Ramachandran plot analysis:	
Most favoured regions [%]	91.8
Allowed regions [%]	7.5
Generously allowed regions [%]	0.4

[a]Values in parentheses are for the highest resolution shell.

[b]R_{merge}: $\sum_{hkl} \sum_i | I_i (hkl) - \langle I (hkl) \rangle | / \sum_{hkl} \sum_i I_i (hkl)$, where $\langle I (hkl) \rangle$ is the mean intensity of the observations $I_i (hkl)$ of reflection hkl.

The structure in the monoclinic space group is very similar to that observed in the triclinic structure (see Figure 30). Also, the oligomeric assembly is trimeric and unfortunately the flexible loop between the amino acids 126 and 140 could only be built incompletely.

4.4.5 ThiM SAXS structure

To verify the trimeric assembly in solution, SAXS measurements at the beamline X33 (Hasylab/EMBL, Germany) were carried out. ThiM was purified, dialysed against

buffer W overnight and centrifuged at 70,000 x g for 50 min at 4 °C. Dispersity was monitored by DLS. Four different dilutions were prepared in the range of 1.3-9.8 mg/ml. Dialysis buffer was used as a reference for the measurements.

The indirect transform package *GNOM* [127] was used to compute the experimental R_g of 2.84 ± 0.05 Å and a D_{max}-value of 90 ± 10 Å were calculated. *DAMMIF* [130] was used to calculate the *ab initio* envelope structure by imposition of P3 symmetry. The most probable model out of a eight reconstructions merged with *DAMAVER* [131] fits the experimental data with a discrepancy of $\chi = 0.4$. The scattering of the high resolution crystal structure was calculated with the program *CRYSOL*. The crystal structure yields a good fit ($\chi = 1.4$) to the experimental data, except for the region of 1.2- 1.4 $Å^{-1}$ (see Figure 36 A). This difference indicates a smaller crystal structure than the obtained SAXS *ab initio* model due to missing loops or a shrunk structure due to crystal packing forces. In case of the ThiM crystal structure, each monomer lacks a 10 amino acid loop in the region of the SAXS shape corners of the triangle structure, which could explain the discrepancy between the SAXS model and the crystal structure (see Figure 36 B).
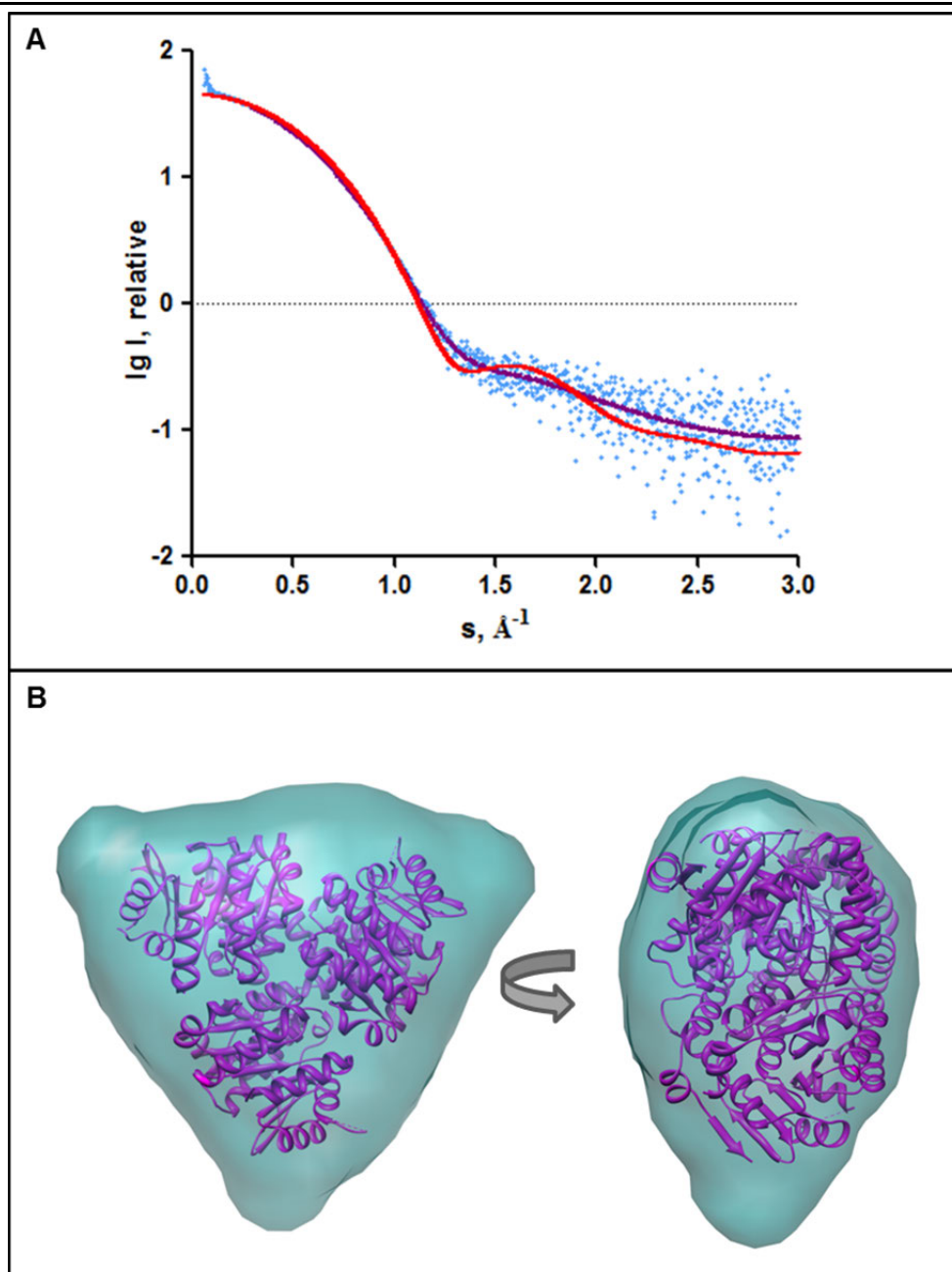
Figure 36: Processed solution scattering pattern and *ab initio* shape of ThiM obtained by SAXS. A:
Experimental data is displayed in blue with the theoretical scattering fit in red for crystallographic data
generated with *CRYSOL* [132] and the purple fit for the *DAMMIF* [130] *ab initio* model. B: Front and side
view of the trimeric ThiM *ab initio* shape in turquoise in superimposition with the crystal structure in a
purple ribbon representation. Figure was generated with CHIMERA [145].

4.5 Substrate-analogue search for ThiM

Based on the P1 crystal structure of ThiM with ThiK from *B. subtilis* co-crystallised
with THZ-P and ATP, the active site of *Sa*ThiM was identified. In the superimposition
model, the positions of the active site residues were very similar to the counterparts
of *B. subtilis* (see Figure 37). THZ binding is mediated by N19, V21, A27, A35, P37,
M39, N59, G61, T62, V90, R98, T86 and C190 and ATP binding by T160, G161,

D164, G178, L182, L192 and F218. The residues D88, K115 and E120 coordinate the ligands via water and magnesium ions (see Figure 37). The proposed mode of action based on the co-crystal structure of *Bs*ThiK with THZ-P and ATP imply an enhanced nucleophilicity of the THZ alcohol by the proton-relay system consisting of a magnesium bound water and its interaction with C190 in addition to the increased electrophilicity of the γ-phosphate of ATP by coordination of its oxygen with the magnesium ion and the hydrogen bonds between the amide protons of G189 and C190 and a second phosphate oxygen atom. The ADP leaving group is stabilised via its hydrogen bond with magnesium and an electrostatic interaction with K115 [152].
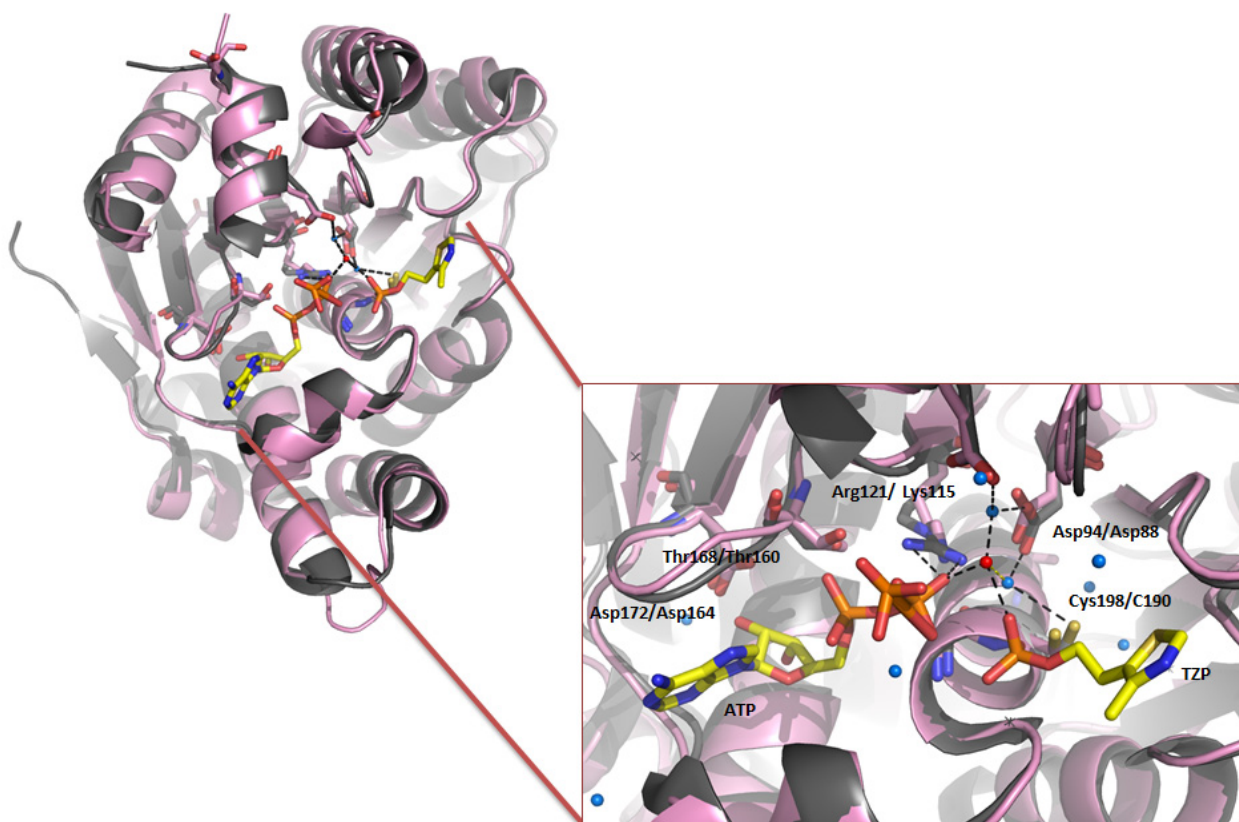
Figure 37: Superimposition model in ribbon representation of *Bs*ThiK (pdb entry 1ESQ) co-crystallised with THZ-P and ATP and *Sa*ThiM. The *Sa*ThiM structure is displayed in pink and the homologue structure from *B. subtilis* in grey. In the detailed view, active site residue labels are displayed as (*Bs*Thik/ *Sa*ThiM). Hydrogen bonds are represented as dashed lines, active site waters as blue balls and magnesium ions as red balls. The ligands and active site residues are depicted in stick representation with oxygen atoms in red, carbon in the respective chain colour, nitrogen in blue, and sulphur in yellow. Figure was obtained using PyMOL (PyMOL Molecular Graphics System, Version 1.3, Schrödinger, LLC.).

The energy minimisation calculation of the structure and docking was carried out by **BJÖRN WINDSHÜGEL,** European Screening Port (Hamburg, Germany). Search query constraints for docking of compounds from the ZINC library was i) phosphorylation possible at a hydroxyl moiety, ii) transfer of HMP-P onto nitrogen possible and iii)

replacement of sulphur in the ring structure (see Figure 38 A). The search yielded 78 hits, whereas 15 of the hits were selected for further characterisation after docking into the active site. For docking analyses *AutoDock* 4.2.3. [153] was used which calculation estimated the conservation of the hydrogen bond of the nitrogen at position 3 in the ring. Therefore, the superimposition of the new ring structures with docked thiazole was important. In a second approach, compounds were docked with GOLD [154] into the active site. The compounds for further characterisation were selected based on the positioning of the heterocycle within the active site from both docking approaches. Structures were based on imidazole, triazole, pyrazole and oxazole ring systems (see Figure 38 B-E)
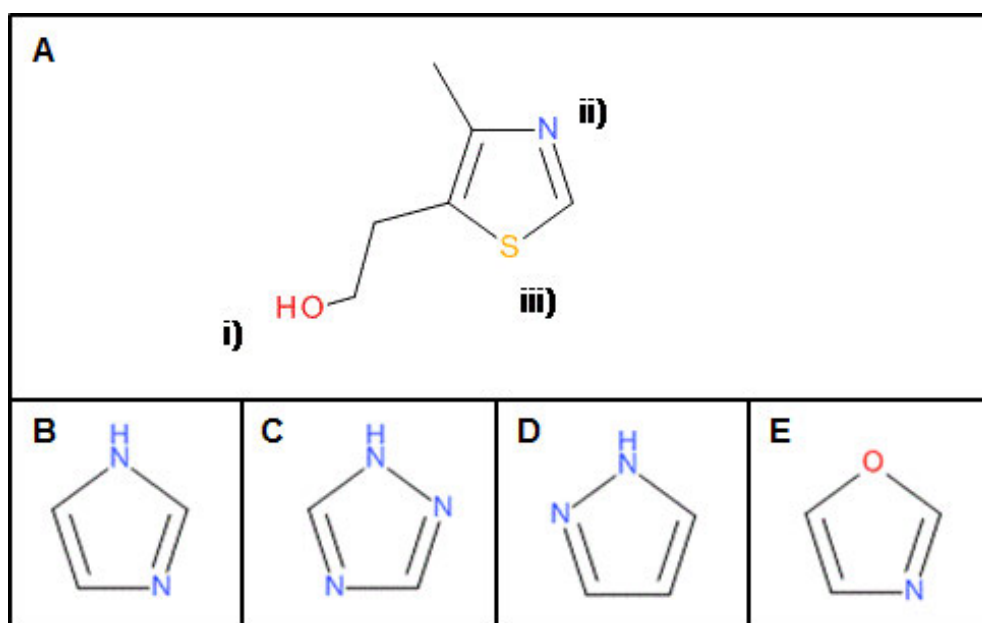
Figure 38: ThiM substrate THZ (A) and ring systems on which screened substrate analogues are based on. B: imidazole; C: triazole; D: pyrazole; E: oxazole. Figures were generated through Accelrys draw 4.0 (Accelrys Software Inc., USA).
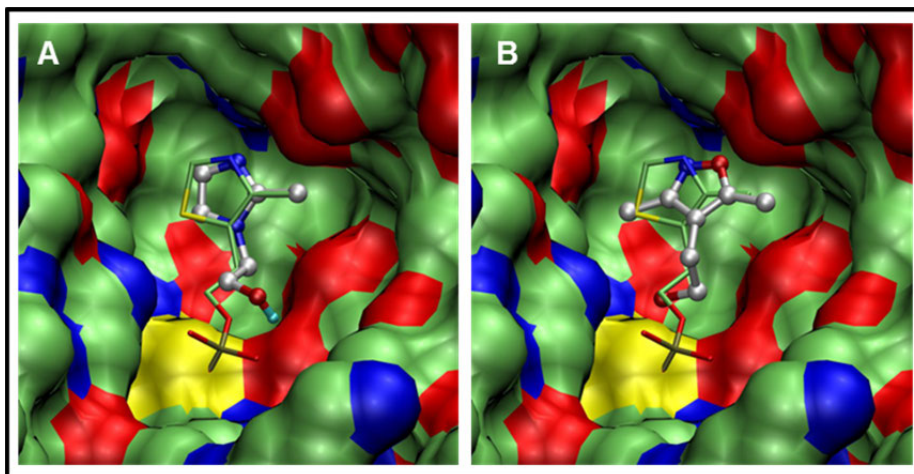
Figure 39: Examples for putative substrate analogues, docked into the active site of ThiM. The active site is represented as a surface with blue surface for nitrogen, red surface for oxygen, yellow surface for sulphur and green surface for carbon. The compounds are depicted in ball and stick representation and THP in line representation with the same colour code for the respective atoms as used for the surface. A: compound 2; B: compound 4. Figures: courtesy of Björn Windshügel.

Selected compounds were forwarded for activity testing and co-crystallisation experiments.

4.5.1 Activity tests for potential ThiM substrate-analogues

4.5.2 Preliminary activity test

ThiM amounts in the range of 0.125-1.00 µg were tested in three independent tests of a reaction volume of 100 µl, which was carried out in duplicates and incubated for 30 min or 15 min. The radioactively marked molecule was ^{14}C-ATP and the conversion of ^{14}C-ATP-^{14}C-ADP in the presence of THZ was measured. ThiM amounts were plotted against ATP conversion and evaluation was carried out using non-linear regression.
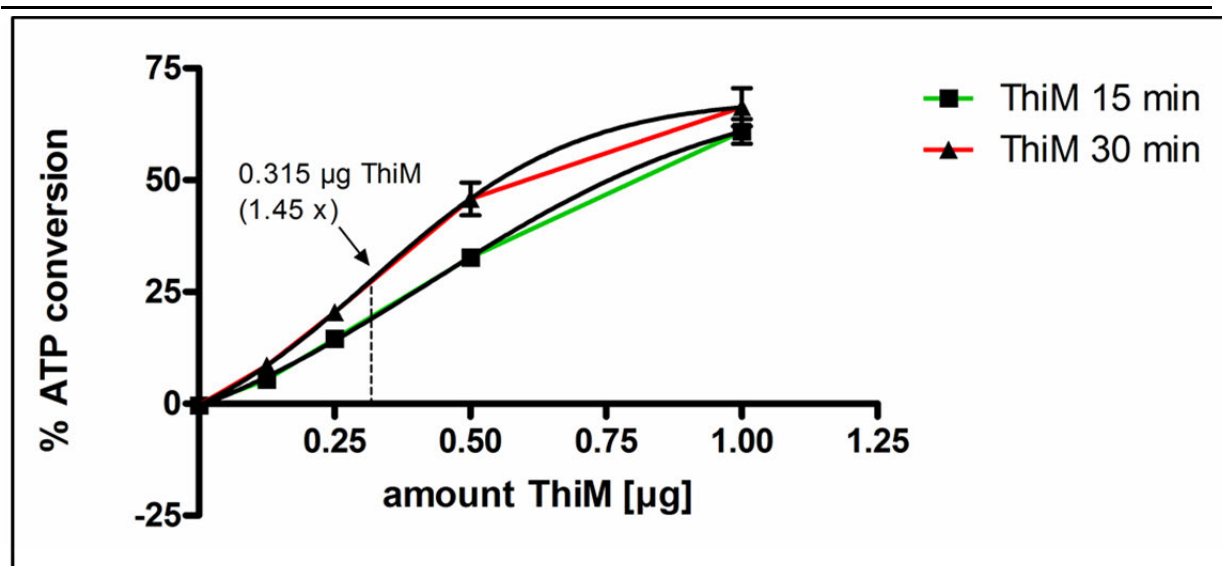
Figure 40: Preliminary test to determine ThiM amount for compound testing. Duplicates from three individual tests were included in the diagram. ThiM amount, where conversion rate almost doubled between 15 and 30 min incubation time was calculated from the non-linear regression curve. ATP-conversion was measured with ^{14}C-ATP. ATP conversion was equated with THZ phosphorylation. Error bars indicate SEM. Figure has been generated with GraphPad Prism 5 version 5.01 for Windows (GraphPad Software, La Jolla California USA, www.graphpad.com).

A 1.45 x increase in ATP conversion was observed using 0.315 µg ThiM, as calculated from the regression curve generated with GraphPad Prism (see Figure 40). Subsequently the standard assay for the characterisation of the compounds were carried out with the same quantity of *Sa*ThiM, however an incubation time of 15 min was chosen due to conversion level of 20 %. ATP-ADP conversion was observed with ^{14}C-ATP, but for further characterisation ^{33}P-ATP was used to detect phosphorylated products.

4.5.3 Competition between THZ and substrate-analogues

13 potential substrate analogues were tested in a ^{33}P-ATP test using the compounds alone and in competition to THZ. The radioactively labelled γ-phosphate group of ATP allowed us to see directly the phosphorylated product and not the conversion product ADP (like in case of the ^{14}C-ATP based tests). From three individual tests carried out in duplicates, the specific activity was calculated.
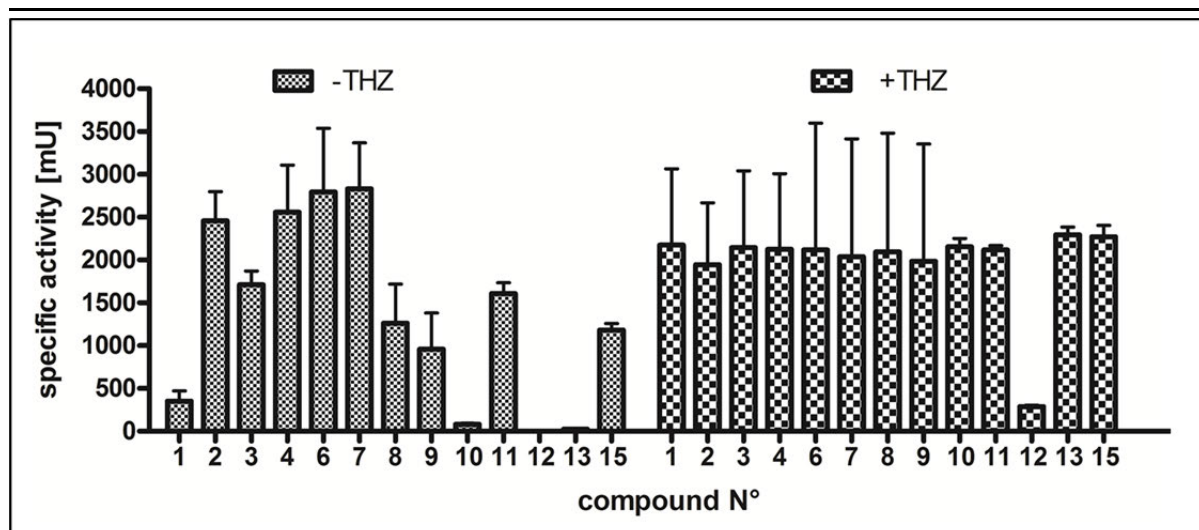
Figure 41: ThiM assay with possible substrate analogues alone and in competition to THZ. Columns with small squares represent the measurements of the compounds alone, with larger squares the measurements with both, the respective compound and THZ. Compounds are not consecutively numbered: compounds 5 and 14 could not be delivered. ATP-conversion was measured with ^{33}P-ATP. ATP conversion was equated with compound/THZ phosphorylation. Error bars indicate standard SEM. Figure was generated with GraphPad Prism 5 version 5.01 for Windows (GraphPad Software, La Jolla California USA, www.graphpad.com).

Compounds 1-11, 13 and 15, were accepted as substrates, because the phosphorylation product was detected. In the competitive measurements for these compounds, only the signal of THZ phosphorylation was detected, but no signal of the phosphorylated compound (see Figure 42). Compound 12 is the only compound which was not accepted as substrate by ThiM, but also THZ phosphorylation was significantly reduced when used in the competitive assay (see Figure 41).
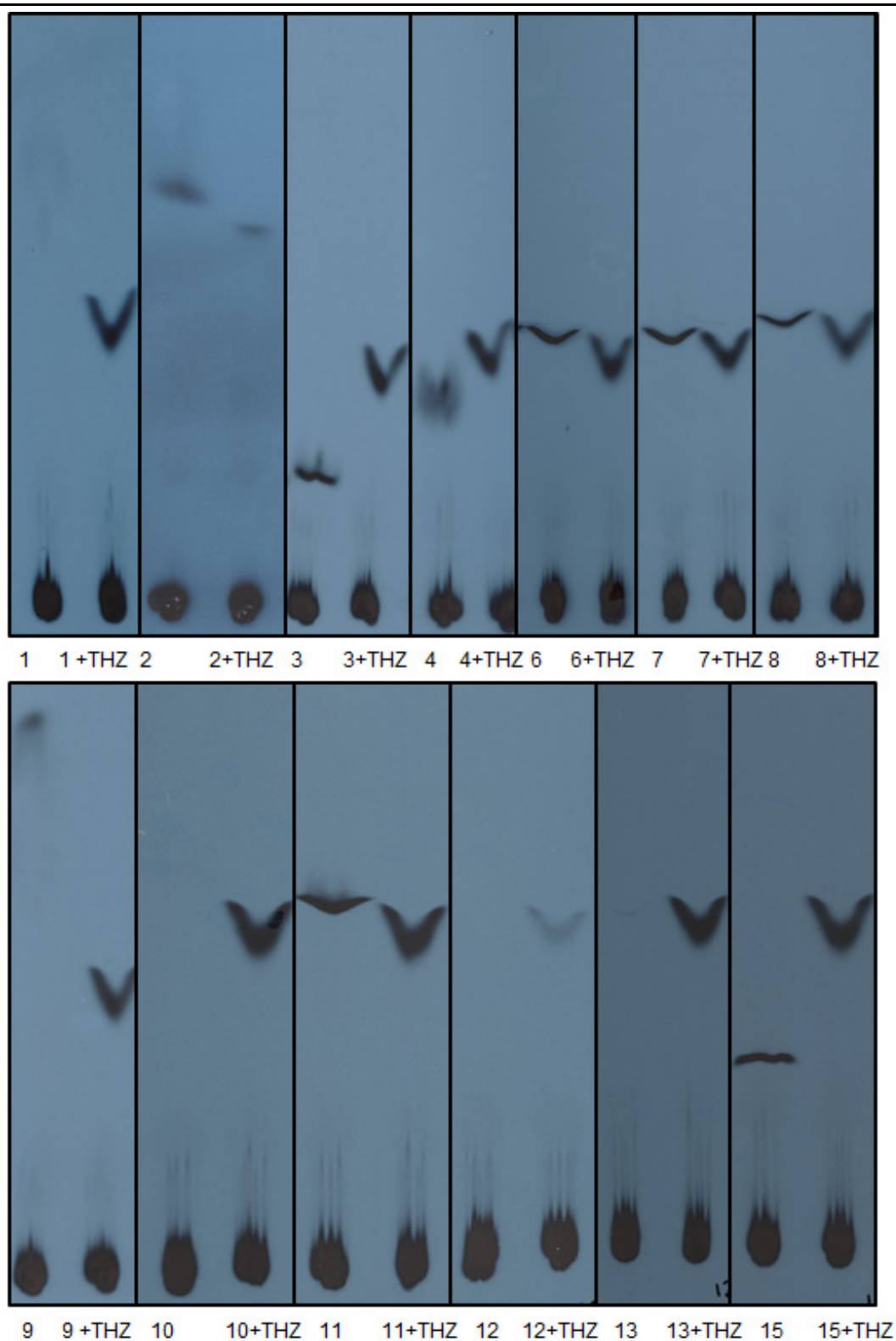
Figure 42: Autoradiograph of a ThiM assay with putative substrate analogues alone and in competition to THZ. Shown are X-ray sensitive films after 2 d exposure to radioactively marked compounds/ATP/THZ on TLC plates. Experiments were carried out with ^{33}P-ATP. The density on the bottom indicates unconsumed ^{33}P-ATP, the upper density of every box shows ^{33}P-phosphorylated compound (left side) and ^{33}P-phosphorylated THZ (right side).

4.5.4 K_M determination for substrate analogues

Substrate analogues with the highest specific activities (see Figure 41), namely compound 2, 4, 6 and 7, were chosen to determine the values for K_M and V_{max} which were subsequently used to calculate the turnover number (k_{cat}) and efficiency. Compound concentrations between 0.0625-4 mM were used and phosphorylated products and ATP spots were cut from a TLC plate. These spots were used to measure the radioactivity. ATP conversion was calculated and plotted against the substrate concentrations. The kinetic parameters were calculated from non-linear regression.
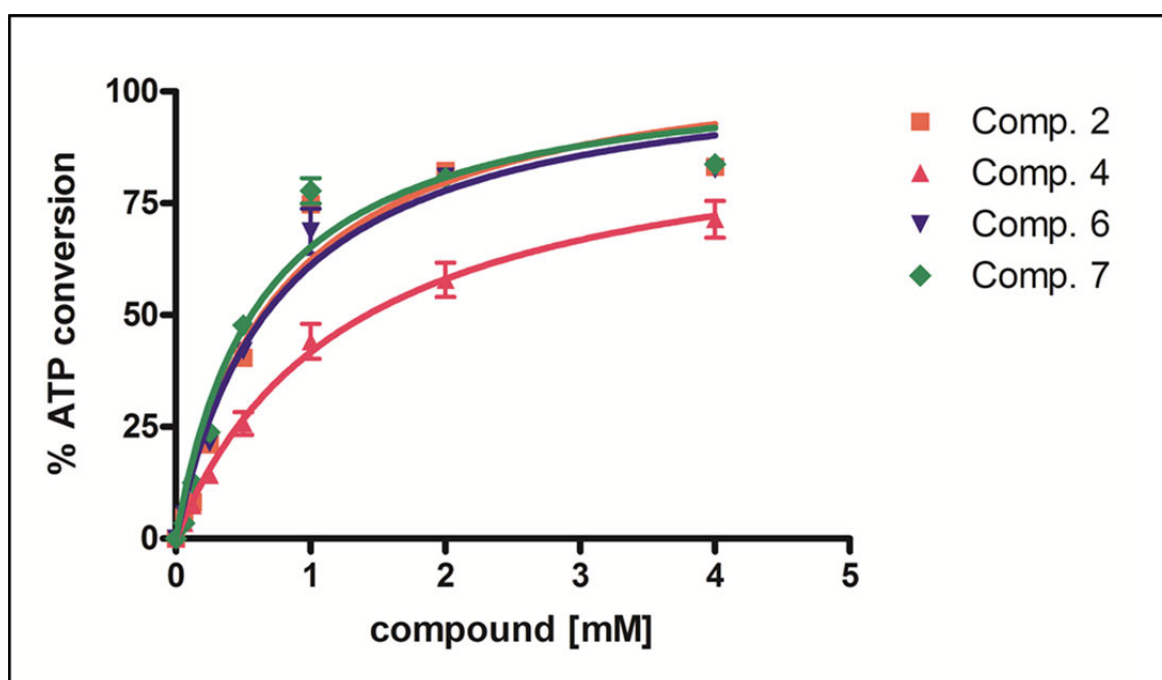
Figure 43: Michaelis-Menten diagram of selected THZ substrate analogues. From non-linear regression kinetic parameters have been determined. ATP-conversion was measured with ^{33}P-ATP. ATP conversion was equated with compound phosphorylation. orange squares show measurements for compound 2, pink triangles for compound 4, blue triangles for compound 6 and green rhombi for compound 7.Error bars indicate SEM. Figure was generated with GraphPad Prism 5 version 5.01 for Windows (GraphPad Software, La Jolla California USA, www.graphpad.com)

Table 8: Kinetic parameters for THZ [103] and substrate analogues.

Comp.	specific activity (nmol min^{-1} mg^{-1})	K_M [µM]	k_{cat} (min^{-1})	k_{cat}/K_M (M^{-1} s^{-1})
THZ	4880 ± 488	44 ± 5	137 ± 13	3.10
2	7418 ± 91	831 ± 169	218 ± 3	0. 26
4	5214 ± 598	1258 ± 388	153 ± 17	0.12
6	7297 ± 267	834 ± 147	215 ± 8	0.26
7	7264 ± 270	659 ± 64	214 ± 8	0.31

The specific activity of compound 4 is in the same range as the natural substrate THZ, in case of compounds 2, 6 and 7 the specific activities are 1.5 times higher than for THZ. Specific activities differ from those obtained in the competitive assay, as the competitive tests were not carried out at saturation conditions. In the Michaelis-Menten diagram it became obvious that saturation is not entirely reached at 4 mM. In comparison to THZ, the k_{cat} value of the compounds is within the same range however the efficiencies (k_{cat}/K_M) showed that the most efficient compound number 7 had only 1/10 of the natural substrate´s efficiency which is a result of the elevated K_M values of all tested compounds in comparison to the natural substrate Table 8.

4.5.5 K_i determination for a selected ThiM compound

After incubation of compound 12 using standard assay conditions this molecule showed a significant reduction of THZ phosphorylation at equimolar concentrations (see Figure 42). Therefore, the ThiM test was performed with increasing concentrations of THZ (2-800 µM) at three different compound 12 concentrations (10, 50 and 250 µM). The test was carried out with three different ThiM preparations in duplicates using ^{33}P-ATP for detection. Conversion of ATP was calculated and plotted in a Michaelis-Menten diagram. Non-linear regression served to calculate K_M^{app} for ThiM reaction without compound 12 and different compound 12 concentrations.
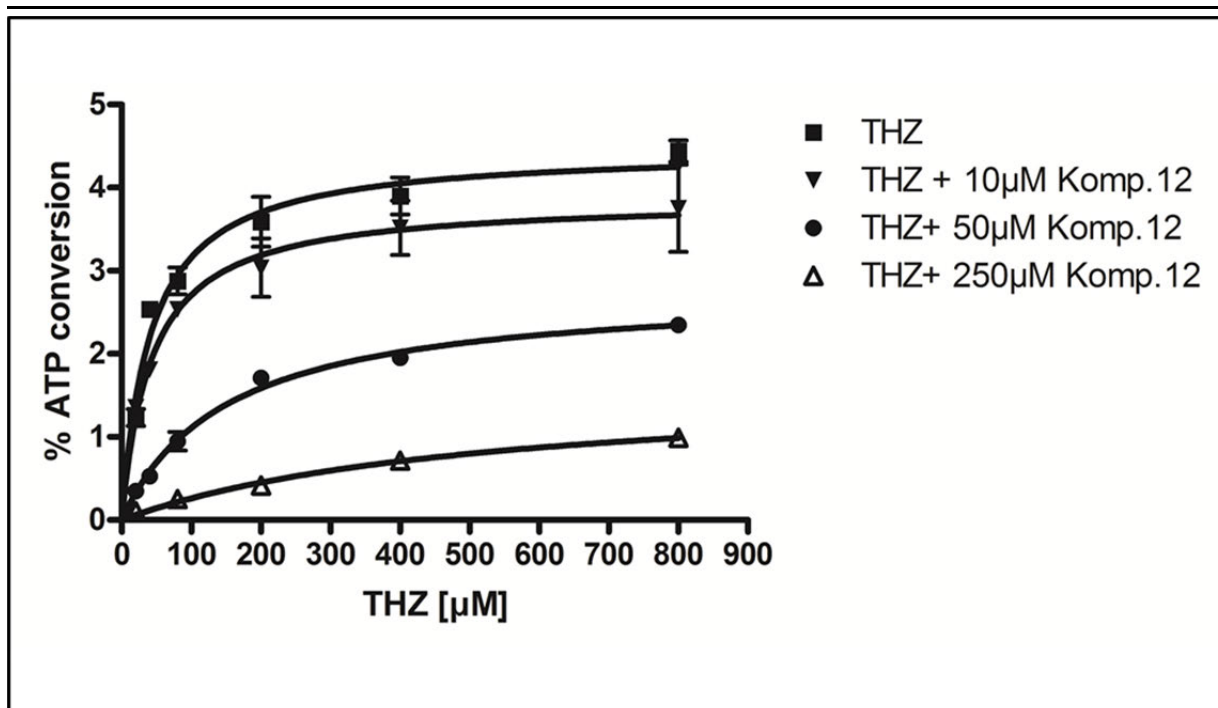
Figure 44: Michaelis-Menten diagram for K_i determination of compound 12. Non-linear regression was used to calculate kinetic parameters. Measurements were carried out in duplicates with ThiM from three individual preparations and increasing THZ concentrations at constant inhibitor concentrations. ATP-conversion was measured with ^{33}P-ATP. ATP conversion was equated with THZ phosphorylation. squares show measurements for THZ alone, triangles for THZ in the presence of 10 μM compound 12, filled circles for THZ in the presence of 50 μM compound 12 and empty circles for THZ in the presence of 250 μM compound 12. Error bars indicate SEM. Figure was generated with GraphPad Prism 5 version 5.01 for Windows (GraphPad Software, La Jolla California USA, www.graphpad.com)

The highest V_{max} was observed for the curve without compound 12. With increasing inhibitor concentrations K_M increases and V_{max} decreases. The K_M-value in the absence of compound 12 is 41 ± 3 μM, the K_M^{app}-value upon addition of 10 μM compound 12 was calculated to be 44 ± 13 μM, the respective values in the presence of for 50 μM and 250 μM were found to be 104 ± 32 μM and 526 ± 14 μM.

When applying linear regression of the K_M^{app} values at different concentrations of compound 12, the intercept with the Y-axis marks $-K_i$. The K_i-value is the dissociation constant for inhibitor binding and compound 12 reveals a value of 17 ± 4 μM (see Figure 45).
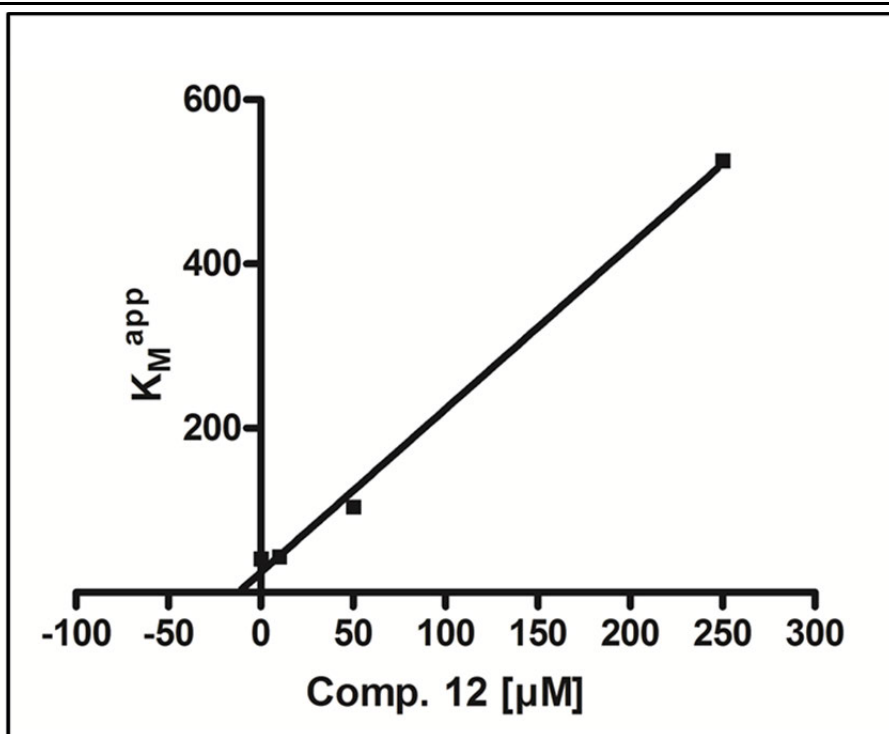
Figure 45: K_i determination by linear regression. Compound 12 concentration is plotted against K_M^{app} of measurements at different inhibitor concentrations calculated from Michaelis-Menten diagram shown in Figure 44. Figure was generated with GraphPad Prism 5 version 5.01 for Windows (GraphPad Software, La Jolla California USA, www.graphpad.com).

To determine the inhibition type, a Lineweaver-Burk plot as double reciprocal representation was used. Important is the intercept of the four graphs, from which the inhibition type was determined. In this case the intercept is (-0.004/0.229) which indicates a mixed inhibition type (see Figure 46).
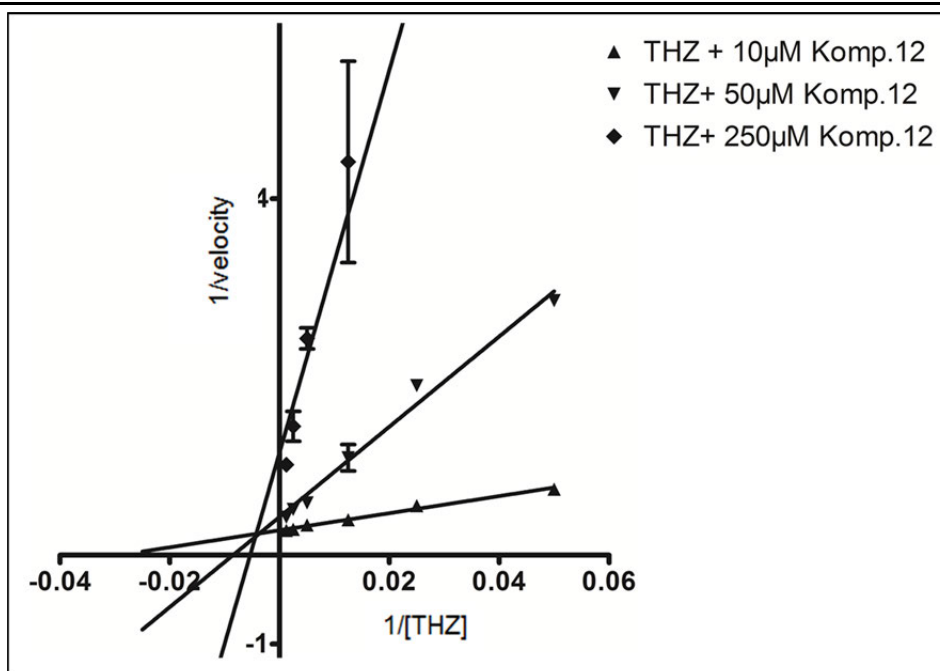
Figure 46: Lineweaver-Burk double reciprocal representation of different ThiM assay with increasing THZ concentrations in the presence of constant compound 12 concentration. Upwards pointing triangles show the measurements with THZ and 10 µM compound 12, downwards pointing triangles the measurements with THZ in the presence of 50 µM compound 12 and rhombi in the presence of 250 µM compound 12. Error bars indicate SEM. Transform and linear regression were calculated with GraphPad Prism 5 version 5.01 for Windows (GraphPad Software, La Jolla California USA, www.graphpad.com).

4.5.6 Docking studies of a selected compound

As the determined inhibition mode of compound 12 was mixed type, additional docking studies were carried out by BJÖRN WINDSHÜGEL using the ThiM trimer. Missing loops between helix 8 and 9 were modelled with *SYBYL-X 2.0* (Tripos Associates, USA) and *SCWRL* 3 [155] and docking was carried out with *AutoDock* 4.2.3. [153]. The docking analysis identified two binding sites outside of the active site of compound 12, which was indicated by an approximately 10 % decreased docking score in comparison to the scores observed for THZ docking. Figure 47A shows compound 12 binding close to the active site coordinated between helix 5, sheet 3 and helix 3. The active site of ATP is very close to that position, so that this position might be blocked upon compound 12 binding. Another binding site for compound 12 was predicted for the loop between helix 8 and 9, which could not be built from the electron density Figure 47B). Conformational changes throughout the whole chain could lead to ThiM inhibition.
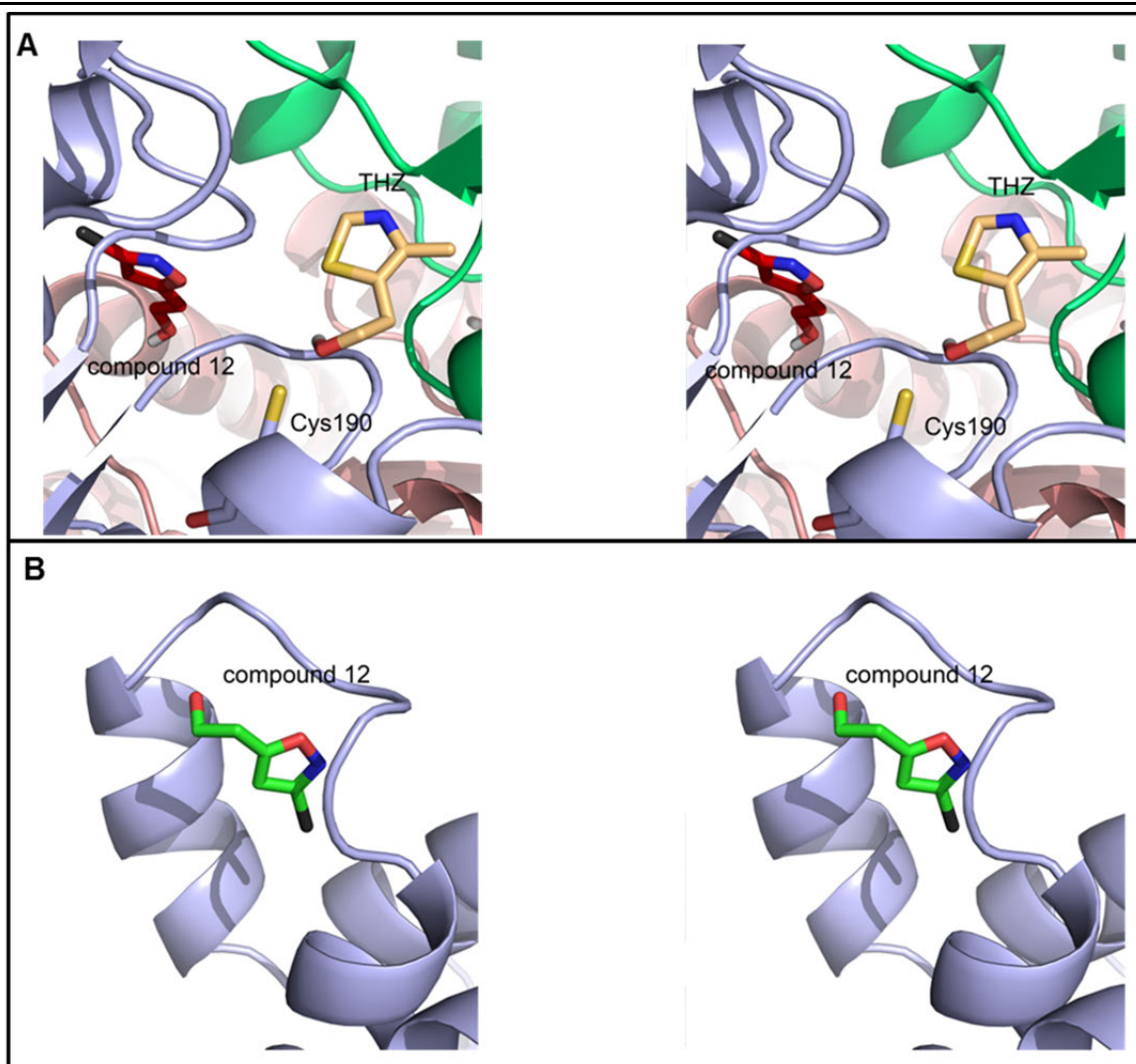
Figure 47: Stereo view (wall-eye) of docking analyses for compound 12 together with THZ into ThiM trimer. ThiM is depicted in ribbon representation with light blue, salmon and lime green differentiating the three monomers. The catalytic residue Cys190 is depicted in stick representation. The ligands compound 12 (A: red; B: green) and THZ (light orange) are depicted in stick representation with carbons in the respective residue colour, nitrogen in blue, sulphur in yellow, bromine in dark grey and oxygen in red. A: Compound 12 binds close to the active site. B: Compound 12 binds to an external loop. Docking was carried out with *AutoDock* 4.2.3. [153]. Figure was obtained using PyMOL (PyMOL Molecular Graphics System, Version 1.3, Schrödinger, LLC..).

4.6   Determination of binding epitopes with NMR spectroscopy

All NMR-experiments were carried out in cooperation with **MIRIAM KÖTZLER**. Epitope mapping of ligands by saturation transfer difference (STD)-experiments requires complete assignment of proton chemical shifts. Therefore, ^{1}H-NMR spectra of the ligands were recorded. The integral gives the number of protons giving rise to a certain resonance. Examples for 700 MHz ^{1}H-spectra of ligands are shown in Figure 48 (THZ) and in Figure 49 (non-hydrolysable ATP, AMP-PCP). In order to assign all resonances in the ^{1}H-spectra, additional NOESY spectra were recorded for

compounds 1, 2, 6, 7, 8 and 9 and an HMBC spectrum was recorded for compound 4.
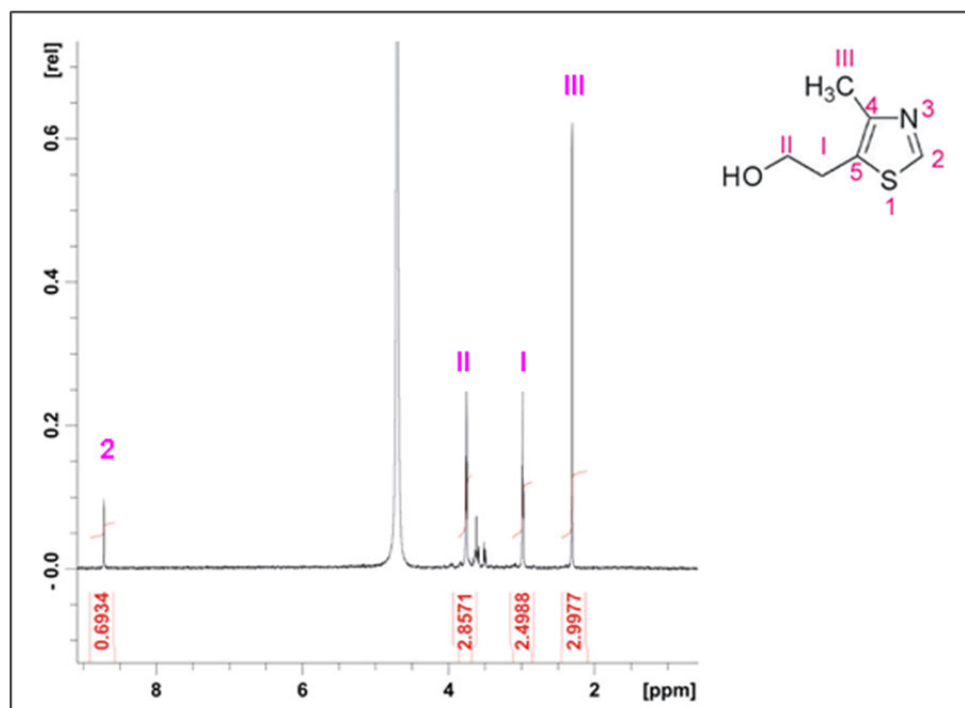
Figure 48: 700 MHz ¹H-NMR spectrum of 5mM THZ in tris-*d11*-D₂O, 300 K. Pink numbers assign the respective peaks from the spectrum to the respective hydrogen positions within THZ. The red numbers below the spectrum show the integrals of the respective peaks, giving a measure for the number of hydrogens at this position.
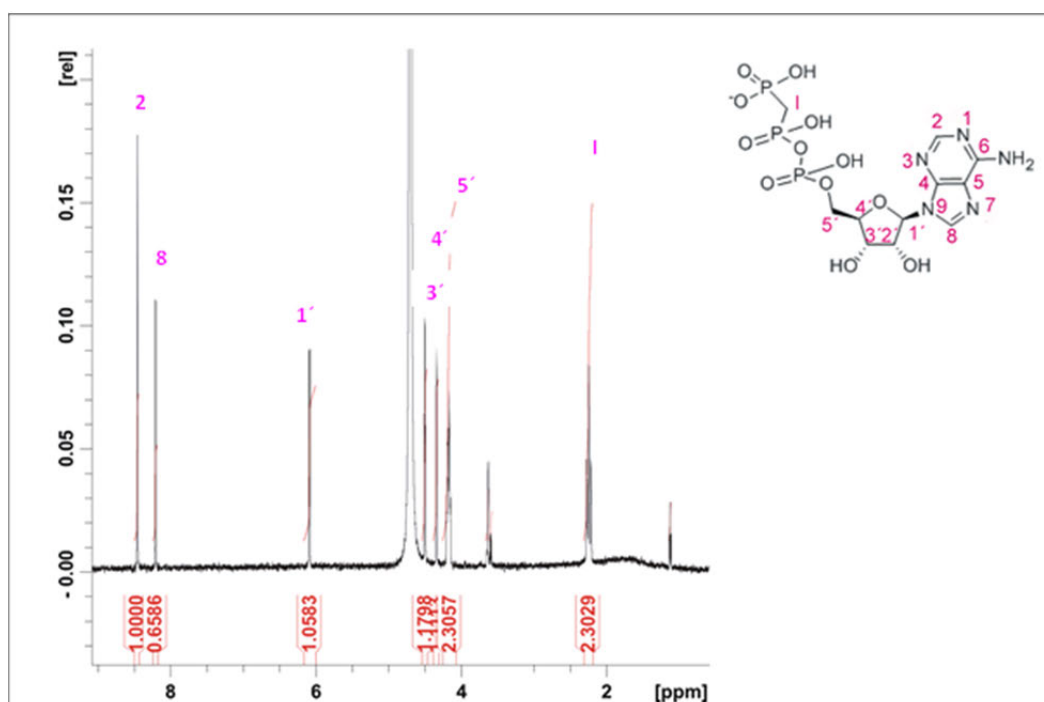
Figure 49: 700 MHz ¹H-NMR spectrum of 5 mM AMP-PCP in tris-*d11*-D₂O, 300 K. Pink numbers assign the respective peaks from the spectrum to the respective hydrogen positions within AMP-PCP. The red

numbers below the spectrum show the integrals of the respective peaks, giving a measure for the number of hydrogens at this position.
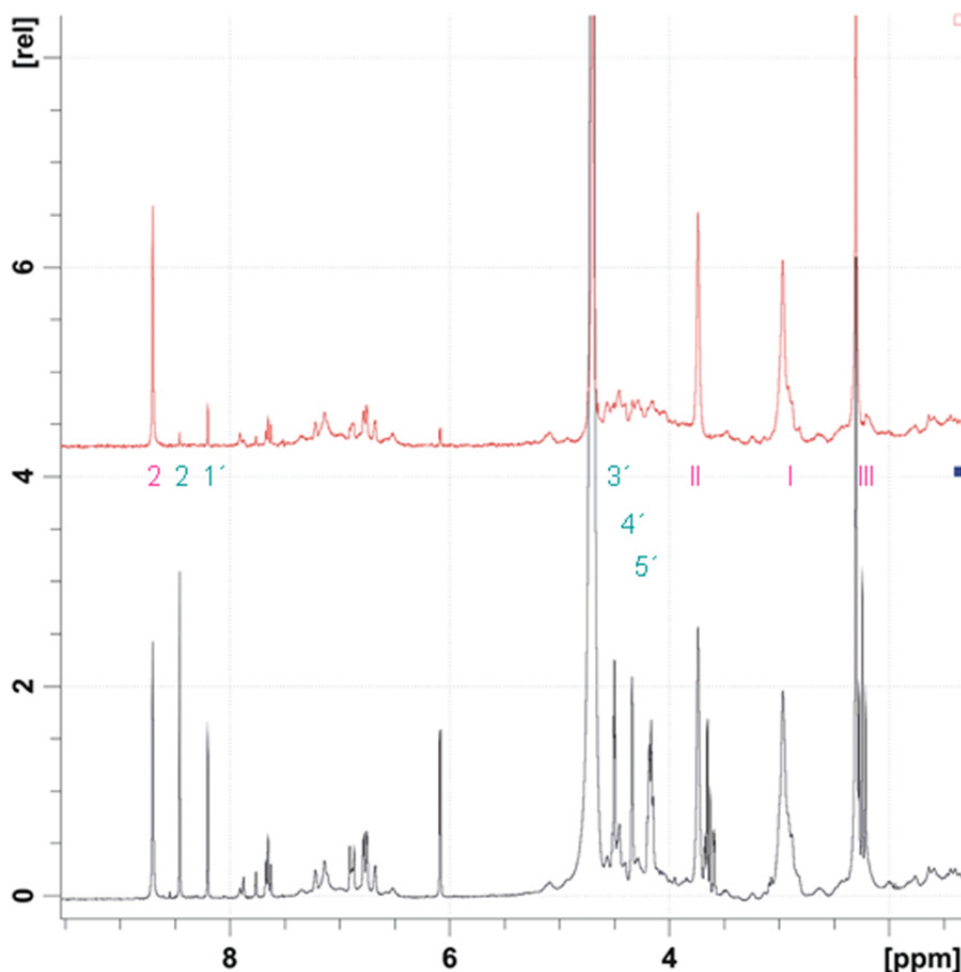
Figure 50: STD spectrum (red) and off-resonance spectrum (black) of *Sa*ThiM (40 µM), THZ (5 mM), AMP-PCP (5 mM). The spectra were recorded with suppression of the protein resonances by a T1rho relaxation filter. Peak assignment was done according to the [1]H- spectra of THZ and AMP-PCP (pink numbers= THZ, turquoise numbers= AMP-PCP).

The absolute STD effects were calculated from the signal intensities of STD- and off-resonance for the assigned peaks. As differing longitudinal relaxation behaviour of different protons may bias the size of STD effects, the determined absolute STD effects were corrected by their individual longitudinal relaxation time constants (T1) as determined by inversion recovery experiments [156]. The corrected absolute STD-effects were normalised to the signal with the highest absolute STD effect, yielding the corrected relative STD-effect. Because the size of the STD effect is proportional to the distance of the respective proton to the enzyme surface in the ligand/protein complex, the binding epitope can be depicted graphically from the STD effects (see

Figure 51). Tables with STD-effects for compounds in complex with ThiM with and without presence of AMP-PCP can be found in the appendix.
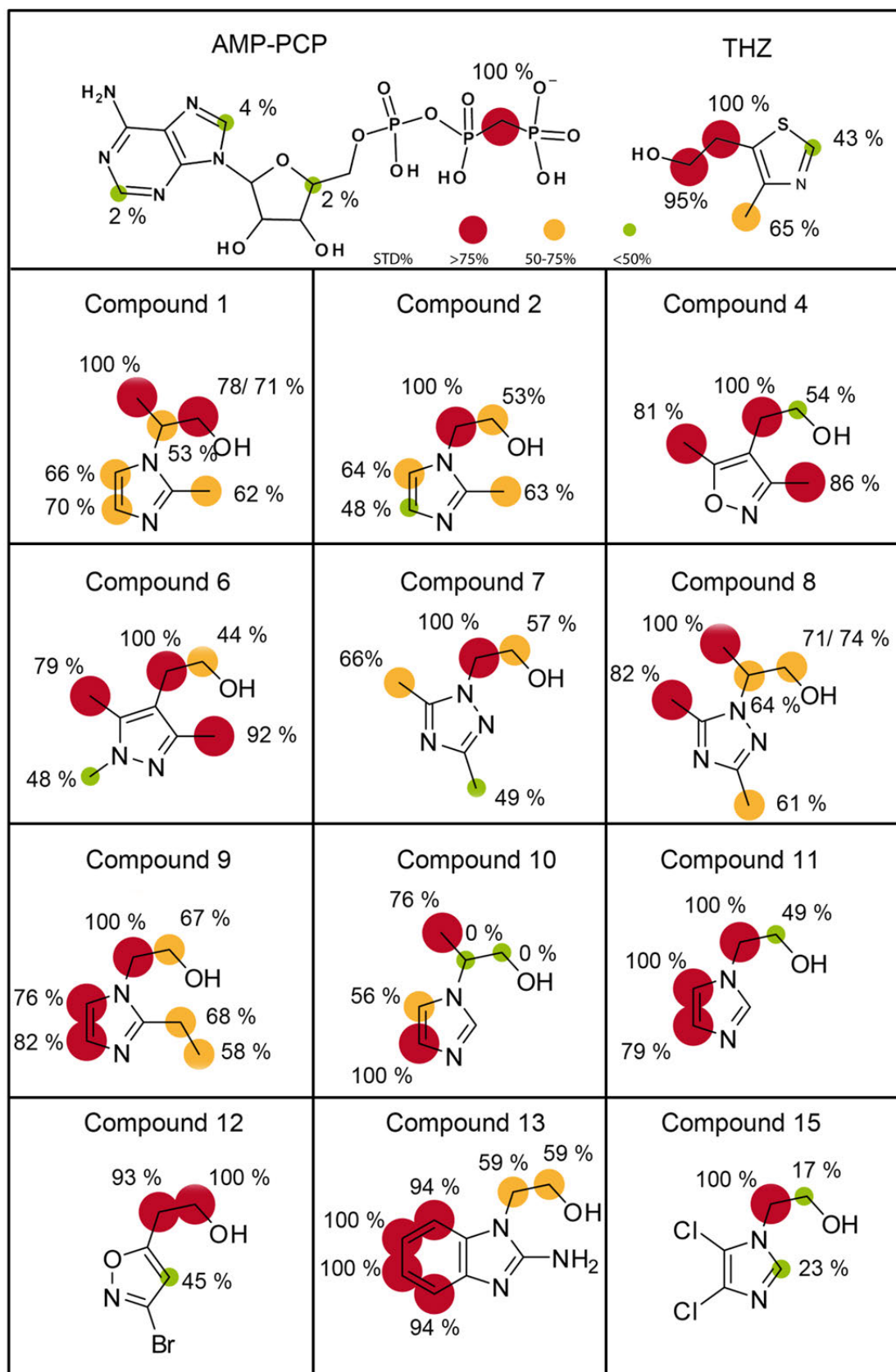
Figure 51: Binding epitopes for substrate analogues of ThiM, THZ and AMP-PCP. Colour code indicates >75 % STD= red, 50-75 % STD= yellow and <50 % STD= green. Numbers show relative STD %. Figures were generated through Accelrys draw 4.0 (Accelrys Software Inc., USA), ChemDraw 12 (PerkinElmer, USA) and Adobe Illustrator (Adobe Systems, USA).

The binding of THZ in the active site was characterised by the closest binding at the hydroxyethyl moiety (95 and 100 %), a moderate binding at the methyl moiety (65 %) and weak binding at the thiazole ring (43 %). The nitrogen atom within the thiazole ring has no STD percentage itself, because it is lacking the hydrogen for detection of STD percentage. However, from co-crystallisation experiments we already determined that the nitrogen atom within the heterocycle is the acceptor for a hydrogen bond with Met39 (see 4.4.4.2) (see Figure 51, top). Non-hydrolysable ATP (AMP-PCP) was present in all measurements to ensure the correct position in the active site. As no co-crystallisation structure with ATP analogue present in the active site was built from crystallographic data, the binding epitope of AMP-PCP could only be compared to the binding mode described by Campobasso *et al.* for *B. subtilis* [152]. In *B. subtilis* there are no hydrogen bonds between the adenine base and the protein and also the phosphate groups are solvent exposed and coordinated via water or magnesium ions in the active site. Only phosphates are in close proximity to the protein for saturation transfer. In the STD-NMR measurement of AMP-PCP, the methylene bridge between β and γ-phosphate allowed the determination of the binding epitope also in this region. It was shown that the closest binding occurs at the methylene bridge (100 %) between β and γ-phosphate, which would be important for phosphate transfer and also no significant saturation at the base or the ribose were determined as already described by Campobasso *et al*. [152]. The coordination of ATP within the active site via water and other ions is not quantifiable with STD-NMR, as saturation is transferred from the protein to the ligands. This was confirmed by our STD-measurements for the adenine base and ribose (see Figure 51, top).

Compound 2 showed the closest binding at the β-carbon of the hydroxyethyl moiety (100 %), but only moderate binding at the α-carbon (53 %). When comparing the binding epitope of compound 1 and 2 it becomes clear, that the closest binding switches from the β-carbon in compound 2 to the γ-carbon in compound 1. By addition of a hydroxypropyl moiety instead of a hydroxyethyl moiety, the orientation of the alkyl group seems to influence the relative orientation of the ligand to the protein surface. Additionally, compound 1 is a chiral molecule and diastereotopic protons can be seen in the [1]H-spectrum. As a racemat was measured, the binding epitope needs further characterisation.

Compound 4 shows a similar epitope at the hydroxyethyl moiety compared to the epitope observed for compound 2.

The same accounts for compounds 6 and 7, whereas the methylgroups in compound 6 are bound closer to the surface than the methyl group in in compound 7.

Compound 7 and 8 differ only in the addition of a hydroxypropyl moiety instead of a hydroxyethyl moiety, as it was already seen for compounds 1 and 2. Also here, the closest binding at the alkyl residue switches from the β-carbon to the γ-carbon. Again, the analysed compound was used as a racemat and the contribution of the enantiomers to the final epitope is not differentiable.

In comparison to compound 2, 4, 6 and 7, compound 9 has the most similar binding epitope at the hydroxyethyl moiety to THZ: the closest binding occurs at the β-carbon (100 %) and at the α-carbon (67 %). The saturation at the imidazole ring is with 76 and 82 % relatively high. Altogether, with close binding at the alkyl moiety, but also the moderate binding at both carbons of the additional ethyl residue could indicate, that the positioning within the active site is different to that one observed for THZ.

The binding epitope for compound 10 showed that no saturation occurred at the α- and β-carbon of the hydroxypropyl moiety, what makes the phosphate transfer to the hydroxyl group difficult. Also here, the molecule was chiral and an ultimate characterisation has to be carried out with only one enantiomer.

The binding at the hydroxyethyl of compound 11 is similar to the observed binding of compound 2, 4, 6, 7, and 9, but as already observed for compound 9 and 10, the saturation at the imidazole ring is very high in comparison to the natural substrate (100 and 79 % vs. 43 %). Additionally, in compound 10 and 11 besides the alkyl groups at the nitrogen of the heterocycle (position 1), no further hydrogen substitution is present, which could influence the positioning within the active site.

Compound 12 shows an optimal binding epitope at the hydroxyethyl moiety and also at the oxazole ring when compared to THZ. It has high saturation at both carbons of the hydroxyethyl moiety (100 and 93 %) and moderate (45 %) saturation at the oxazole ring.

Compound 13 obtains the highest saturation at the benzodiazole ring (94-100 %) and only moderate saturation at the hydroxyethyl moiety (59 %) and compound 15 obtained the highest saturation at the β-carbon of the hydroxyethyl group (100 %), but only very weak saturation (17 %) at the α-carbon (17 %) and the imidazole ring (23 %).

Taking into account the kinetic data (see chapter 3.3.17.3 and 3.3.17.4) for ThiM compounds, it was observed that the best binders: compound 2, 4, 6 and 7 (see Table 8) had in common a similar STD epitope at the hydroxyethyl moiety with the highest saturation at the β-carbon (100 %) and moderate saturation at the α-carbon (44-57 %). The highest efficiency was determined for compound 7 (0.31 see Table 8), which showed only moderate saturation at the attached methyl groups, but also the binding epitope of compound 2 showed this moderate binding at the methyl group and within the heterocycle, but efficiency (0.26 see Table 8) was reduced in comparison to compound 7 (0.31 see Table 8).

In summary, it was confirmed by applying STD-NMR spectroscopy analyses, that the best binders within the analysed compounds had a similar binding epitope at the hydroxyethyl moiety and moderate to strong binding at the methylgroups attached to the heterocycle. The lowest efficiency was determined for compound 4 (0.12 Table 8) which lacks the methylgroup at the opposite of the hydroxyethyl moiety compared to compound 6 with higher efficiency (0.26, see Table 8).

Compound 12 showed the most similar binding epitope in comparison to the natural substrate, although it lacks the methylgroup at the heterocycle, but from kinetic data it was shown that compound 12 is an inhibitor instead of a substrate analogue as no phosphorylated product was measured and also THZ phosphorylation was significantly reduced when compound 12 was present (see Figure 41). However, the Lineweaver-Burk representation of the K_i-value determination indicated that the observed inhibition type of compound 12 is a mixed inhibition type. These findings imply that the binding of the individual compounds may also occur at a different position than for THZ. The observed epitope for compound 12 determined by STD-NMR did not reflect the binding within the active site pocket for this compound.

Kinetics and the binding epitopes characterised by STD-NMR help to sort out compounds for further optimisation.

4.7   Structure of TPK

4.7.1   TPK crystallisation

The *S. aureus* TPK 6 x His-tag fusion protein was purified via a Ni-NTA matrix and dialysed against buffer W containing 300 mM sodium chloride. The solution was

concentrated to a concentration of 20 mg/ml and centrifuged at 70,000 x g, for 50 min, at 4 °C. Dispersity was monitored by DLS (see Figure 52).
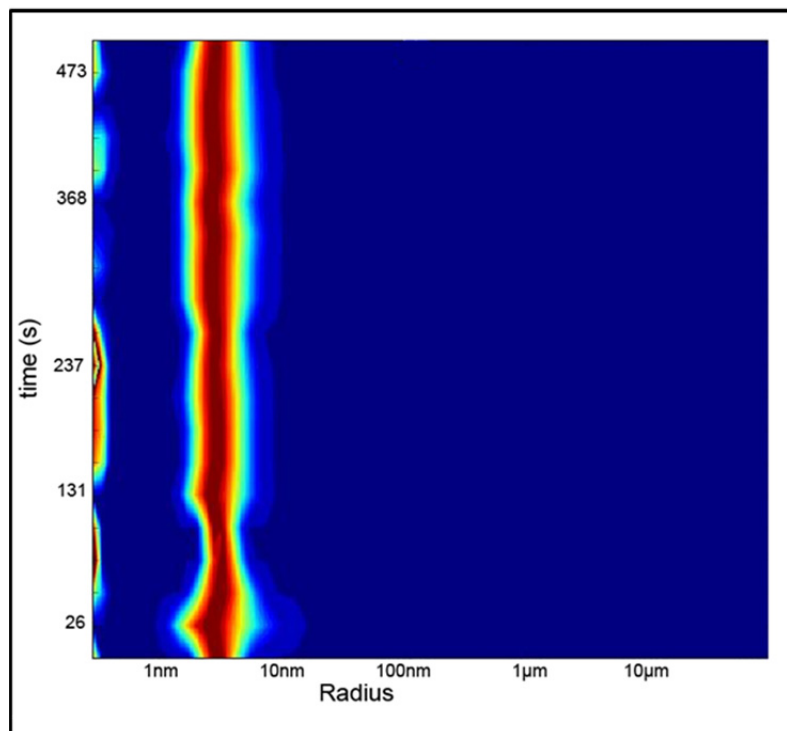
Figure 52: Heatmap of the DLS measurement for TPK after 50 min centrifugation at 70,000 x g and 4 °C. The colours of the heatmap indicate the relative intensity of the particle, with blue being zero and dark red being maximum. The particle size was plotted against the time of the measurement.

The DLS measurement shows a monomodal size distribution with a R_H-value of 2.9 ± 0.2 nm. For crystallisation, the protein solution was concentrated to a concentration of 25 mg/ml in a 10 K cutoff centrifugal filter device (Millipore, USA). In total, 384 conditions were tested applying the *Cryos, Classics, JCSG+* and *ComPAS* screening suites (all Qiagen, Germany). 300 nl of protein solution were mixed with 300 nl of precipitant solution by the pipetting robot Honeybee 961 (Genomic Solutions, USA) in 96-well sitting drop plates (NeXtal QIA1 µplates, Qiagen, Germany). The reservoir was filled with 55 µl of precipitant solution. After 10 d at 20 °C, initial crystals grew in eight conditions (Figure 53).
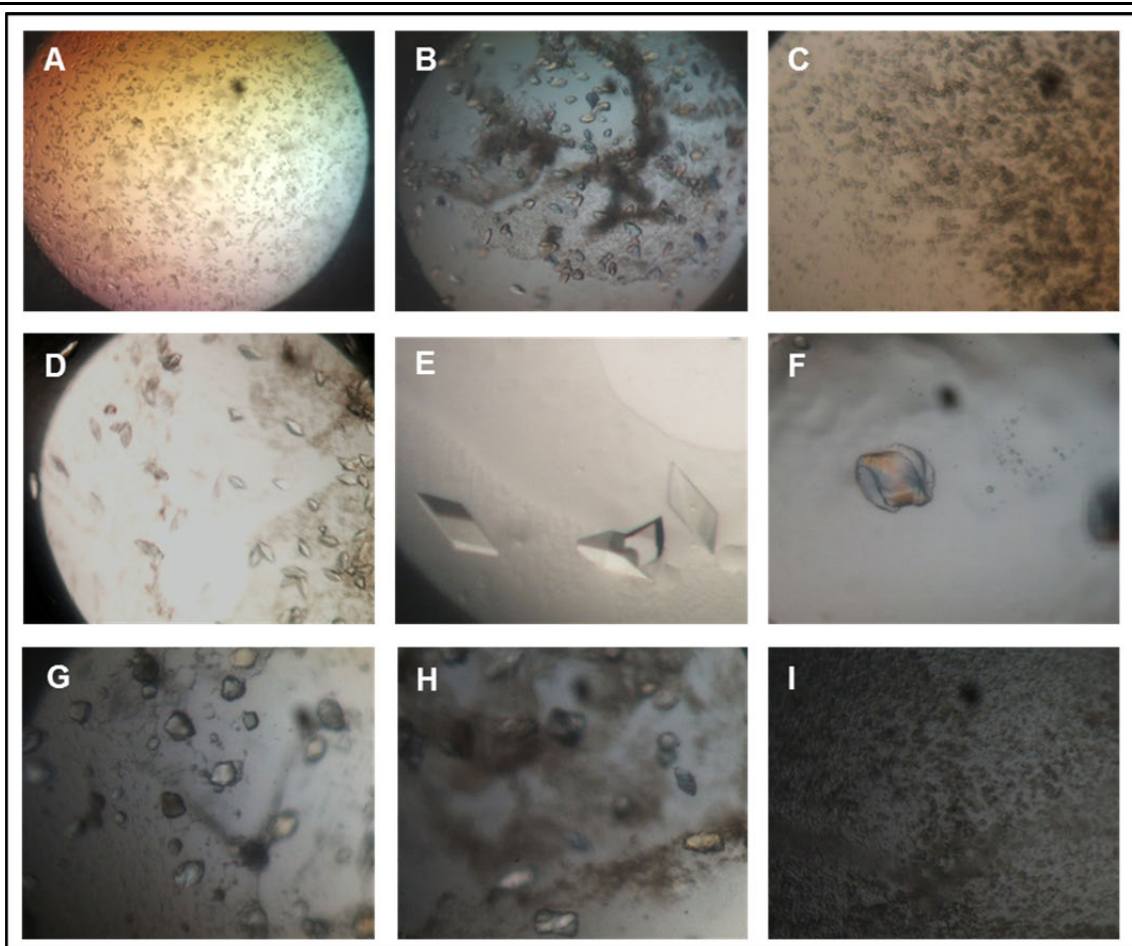
Figure 53: Initial TPK crystals grown after 10 d at 20 °C and a protein concentration of 25 mg/ml in NeXtal QIA1 µplates (Qiagen, Germany) applying the sitting drop vapour diffusion technique. A: *ComPAS* **suite E1 (0.1 M HEPES pH 7.5, 5 %(w/v) isopropanol); B :** *ComPAS* **suite B1 (0.2 M ammonium sulfate, 0.1 M MES pH 6.5, 22 %(w/v) PEG 8,000); C:** *JCSG+* **suite C1 (0.2 M sodium chloride, 0.1 M phosphate-citrate pH 4.2, 20 %(w/v) PEG 8,000); D:** *Classics suite* **F10 (0.2 M ammonium sulfate, 0.1 M sodium cacodylate pH 6.5, 30 %(w/v) PEG 8,000); E:** *Cryos* **suite F9 (0.04 M potassium phosphate, 16 %(w/v) PEG 8,000, 20 %(v/v) glycerol); F:** *JCSG+* **suite C2 (1 M lithium chloride, 0.1 M citric acid pH 4.0, 20 %(w/v) PEG 6,000); G:** *Cryos* **suite F10 (0.17 M ammonium sulfate, 0.085 M sodium cacodylate pH 6.5, 25.5 %(w/v) PEG 8,000, 20 %(v/v) glycerol); H: Detail view of G; I:** *JCSG+* **suite H7 (0.2 M ammonium sulfate, 0.1 M BIS-TRIS pH 5.5, 25 %(w/v) PEG 3,350).**

These conditions were optimised varying PEG and salt conditions around the initial concentration in 24-well hanging drop CPL-130 plates (JenaBioscience, Germany) by mixing 1 µl of previously centrifuged (70,000 x g, 4 °C, 50 min) protein solution and 1 µl of the respective precipitant solution, but no X-ray suitable crystals were obtained. Also protein concentration variation (15, 18, 20 mg/ml) was not successful to optimise crystals.

Freshly purified protein solution was concentrated to A_{280} of 6.6 (8.4 mg/ml) and centrifuged for 50 min at 100,000 x g and 4 °C. The clarified protein solution was applied for crystallisation screens, using the *Stura/ Footprint*, *Morpheus*, *PACT* (Molecular Dimensions, USA) and *JCSG+* (Qiagen, Germany) screening suites.

300 nl of protein solution were mixed with 300 nl of precipitant solution by the pipetting robot Honeybee 961 (Genomic Solutions, USA) in 96-well sitting drop plates (NeXtal QIA1 µplates, Qiagen, Germany). The reservoir was filled with 35 µl of precipitant solution.

Initial crystals grew after 10 d at four conditions which were further optimised in 24-well CPL-130 plates (JenaBioscience, Germany) applying the vapour diffusion technique and with the batch technique under oil. Protein was freshly purified and centrifuged at 100,000 x g for 50 min at 4 °C and PEG and salt concentrations were varied around the initial concentration in CPL-130 plates (JenaBioscience, Germany) mixing 1 µl of protein solution with 1 µl of precipitant solution for vapour diffusion. Two plates were prepared for optimisation, applying concentrations of A_{280}= 6.6 and 13.2. For crystallisation under oil, Terazaki (Nunc, Denmark) plates were moistened with paraffin oil and 2 µl droplets consisting of 1 µl of protein solution and 1 µl of precipitant solution were placed into the wells under the microscope. Two plates with different protein concentrations were used for crystallisation trials. A crystal grew applying a TPK concentration of 13 mg/ml after 11 d with 0.8 M tri-sodium citrate and 0.01 M sodium bromide under oil to maximum dimensions of 0.5 x 0.1 x 0.03 mm. The crystal was partially intergrown. (see Figure 54).

Figure 54: TPK crystal grown at a concentration of 13 mg/ml (precipitant 0.8 M tri-sodium citrate, 10 mM sodium bromide) after 11 d under oil in a Terazaki plate (Nunc, Denmark). Scale bar: 100 µM

4.7.2 TPK diffraction data analysis

For X-ray data collection, the crystal was protected in a precipitant solution containing 10 % glycerol. Microtools (Mitegen, USA) were used to remove smaller

crystals grown on the surface and crystal was mounted with a nylon loop. Diffraction of TPK was recorded to 2.78 Å resolution at consortium beamline X13 (Hasylab/DESY, Germany) (Figure 54). Data were indexed with *iMOSFLM* and scaled with *Scala* in the resolution range from 44-3.06 Å with an overall R_{merge} of 9 % in the tetragonal space group $P4_12_12$. A Matthews´ coefficient [137] of 2.02 $Å^3$ Da^{-1} with a corresponding solvent content of 39.1 % indicated 1 molecule in the asymmetric unit.

Table 9: Date collection and refinement statistics for *Sa*TPK

Data collection statistics[a]	
Beamline	Consortium Beamline X13, HASYLAB/DESY
Temperature [K]	100
Wavelength [Å]	0.81
Space group	$P4_12_12$
Unit cell parameters: a, b, c [Å]	87.87, 87.87, 53.53
Resolution range	43.96-3.06
Measured reflections	21728
Unique reflections	4266
Completeness [%]	99.6 (97.4)
Multiplicity	5.1 (3.8)
Average I/σ(I)	16.2 (4.2)
R_{merge}[b]	9.0 (38.5)
Refinement statistics	
Resolution range	43.96-3.06
R_{work}/ R_{free} [%]	24.17/30.07
Asymmetric unit content:	
Protein atoms	1411
Water molecules	8
Rms bond-length deviation [Å]	0.01
Rms bond angle deviation [°]	1.8
Mean *B* factor [$Å^2$]	44.75
Ramachandran plot analysis:	
Most favoured regions [%]	87
Allowed regions [%]	10.4
Generously allowed regions [%]	1.9

[a]Values in parentheses are for the highest resolution shell.

[b]R_{merge}: $\sum_{hkl} \sum_i | I_i (hkl) - \langle I (hkl) \rangle | / \sum_{hkl} \sum_i I_i (hkl)$, where $\langle I (hkl) \rangle$ is the mean intensity of the observations $I_i (hkl)$ of reflection hkl.

Sequence alignment with the most homologue structures from an NCBI/Blast [138] search query carried out with *Clustal W* [179] and *BOXSHADE* [180] is shown in Figure 55.

A homology for molecular replacement model with TPK from *Staphylococcus saprophyticus* (pdb entry: 3L8M, sequence identity: 49 %) was built with the homology modelling server SWISS-Model [157].
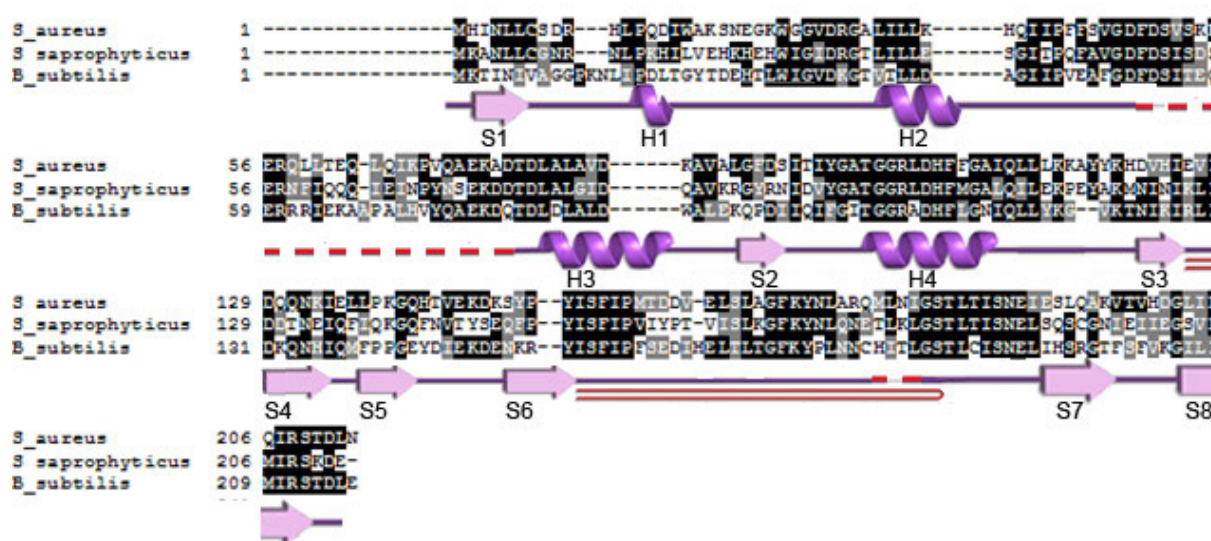
Figure 55: Sequence alignment for TPK derived from *S. aureus* with the most homologue structures from an NCBI/ Blast search. Alignment was carried out with *Clustal W* [140] and *BOXSHADE* [141]. Identical residues are shown in black and similar residues in grey. Secondary structure elements are marked below in a purple ribbon representation. H= α-helix, S= β-sheet, dashed red line indicates disordered regions and red solid line indicates β-hairpins. Secondary structure elements are based on the solved structure seen in Figure 57 and were generated with *PDBsum* [142].

Homology modelling showed a conservation of the β-sheet structure, but diversity in the N-terminal α-helix position (see Figure 56).
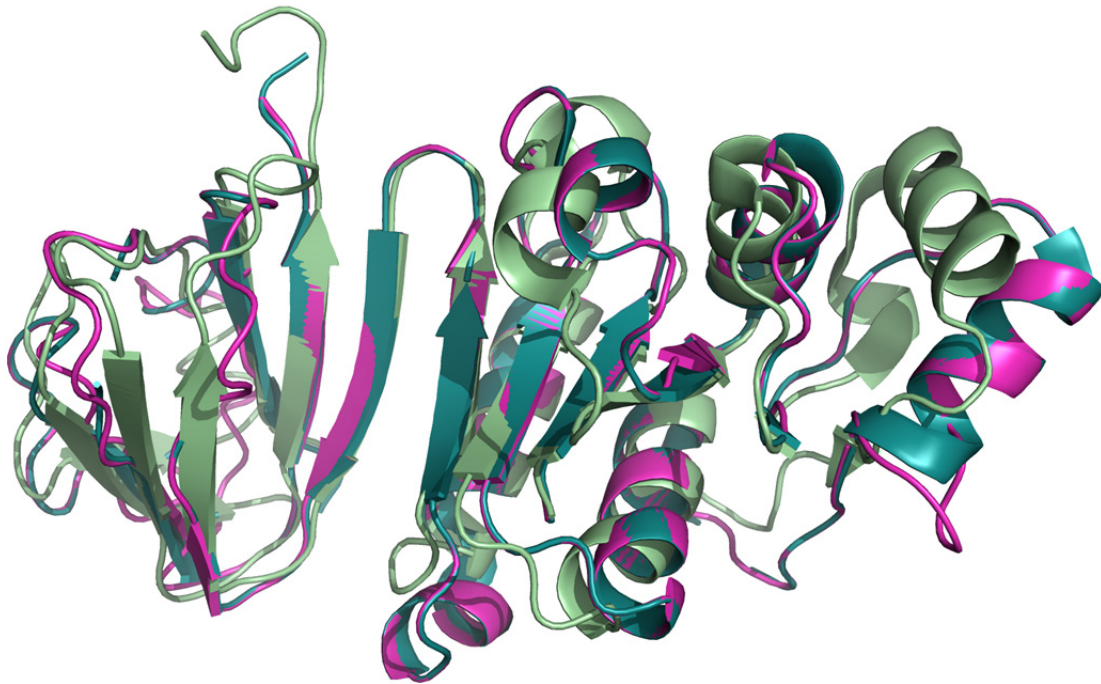
Figure 56: Superimposition in ribbon representation of *Sa*TPK homologue structures and homology model calculated by the SWISS-Model server [158-160]. Green: *Geobacillus thermodenitrificans* TPK (pdb entry: 3K94, identity: 41 %), turquoise: *Staphylococcus saprophyticus subsp. saprophyticus* TPK (pdb entry: 3L8M, identity: 49 %), pink: Homology model for *Staphylococcus aureus* TPK based on *S. saprophyticus* structure; Rmsd: 3K94 to 3L8M: 1.522. Figure was obtained using PyMOL (PyMOL Molecular Graphics System, Version 1.3, Schrödinger, LLC.).

Molecular replacement was carried out with *MOLREP* [143] resulting in a correlation coefficient of 30.6 % and an R-factor of 55.7 %. Model building was carried out with *COOT* [125] and refinement with *Refmac5* from the *CCP4* [123] suite applying overall B-factor refinement. The starting model was refined to final R: 24.2 % and R_{free}: 30.1 %.
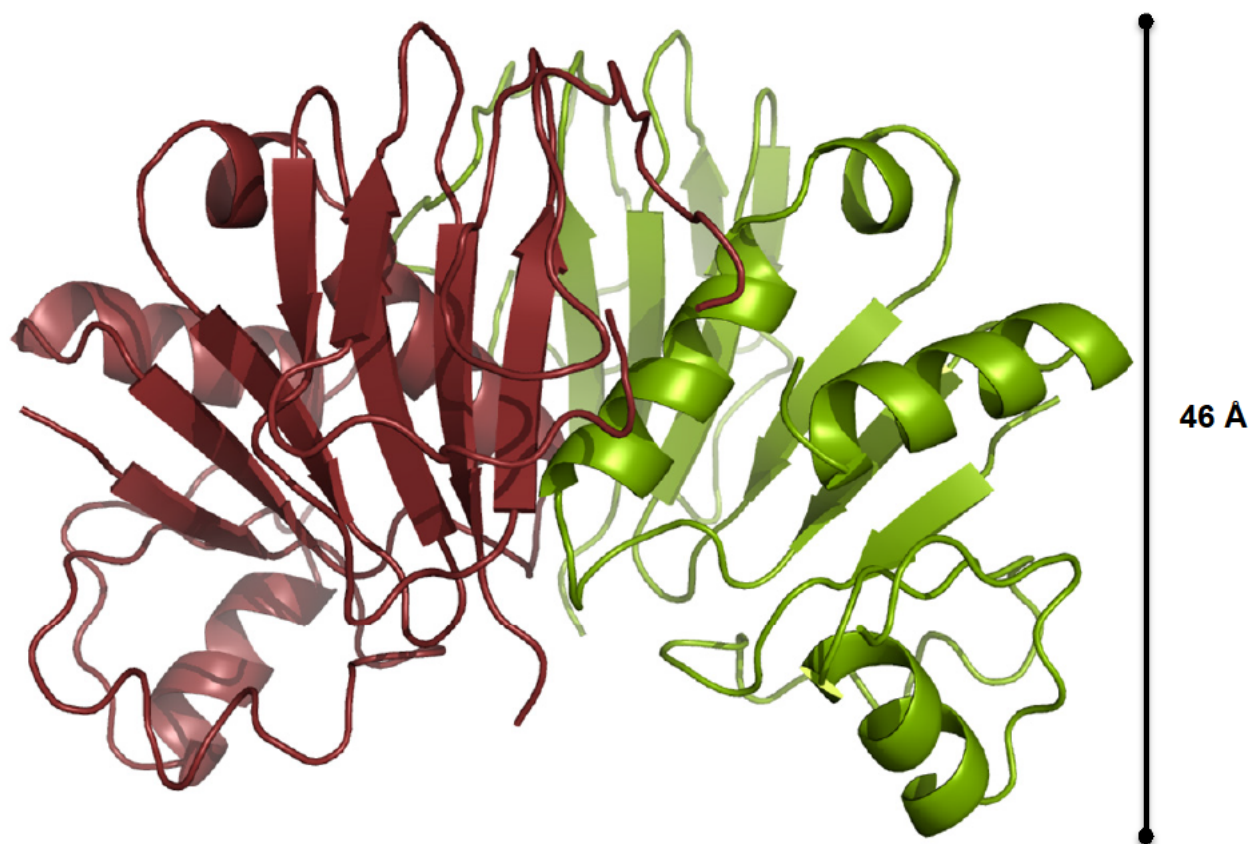
Figure 57: Ribbon representation of the *Sa*TPK structure, which was solved to 3.05 Å resolution. The structure comprises two identical monomers, indicated by two different colours. Figure was obtained using PyMOL (PyMOL Molecular Graphics System, Version 1.3, Schrödinger, LLC.).

The structure comprises two monomers building a dimer through crystallographic symmetry with two independent active sites and a total accessible surface area of approximately 17,500 $Å^2$ and a buried interface of approximately 3,000 $Å^2$ (calculated with PISA at European Bioinformatics Institute (http://www.ebi.ac.uk/pdbe/prot_int/pistart.html) [158-160]). Every monomer consists of eight β-sheets and three short α- helices. The first three β-sheets are parallel to each other and the last five are in antiparallel orientation. The structure consists of approximately 17 % α-helix and approximately 21 % β-sheet [144]. The region between amino acid 49 in helix 1 and amino acid 75 in helix 2 (see Figure 58 A) is disordered and due to high flexibility in this loop no electron density was identified.
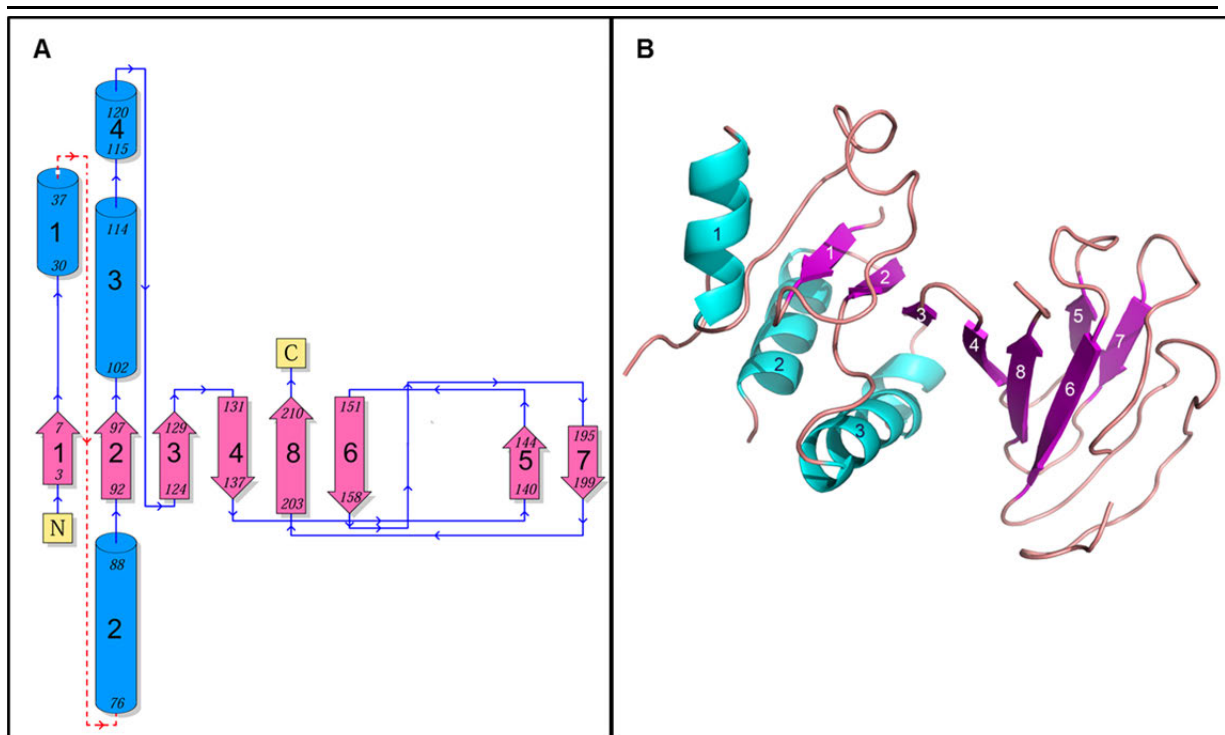
Figure 58: Topology and ribbon drawing of the subunit structure of TPK. A: Topology diagram. The α-helices are represented by blue cylinders and β-sheets by pink arrows. Connecting loops are depicted in dark blue, the dashed red line indicates a missing loop, which could not be seen in the electron density. The smaller numbers indicate the beginning and ending residue number of each secondary structural element. The figure was prepared with *PDBsum* [182]. B: In the ribbon drawing the α-helices are depicted as light blue coils, β-sheets are depicted in pink and loops are depicted in pale red. Numbers in dark blue designate the α-helices, white numbers designate β-sheets numbered from the N- to the C-terminus. Figure was obtained using PyMOL (PyMOL Molecular Graphics System, Version 1.3, Schrödinger, LLC.).

4.7.3 Further optimisation of TPK crystallisation: magnesium screen and His tag removal

Due to the relatively poor model quality of the obtained crystals structure, the homology modelling server *I-TASSER* (http://zhanglab.ccmb.med.umich.edu/I-TASSER/) [161, 162] was used to obtain further information from homologue structures to further optimise crystallisation.
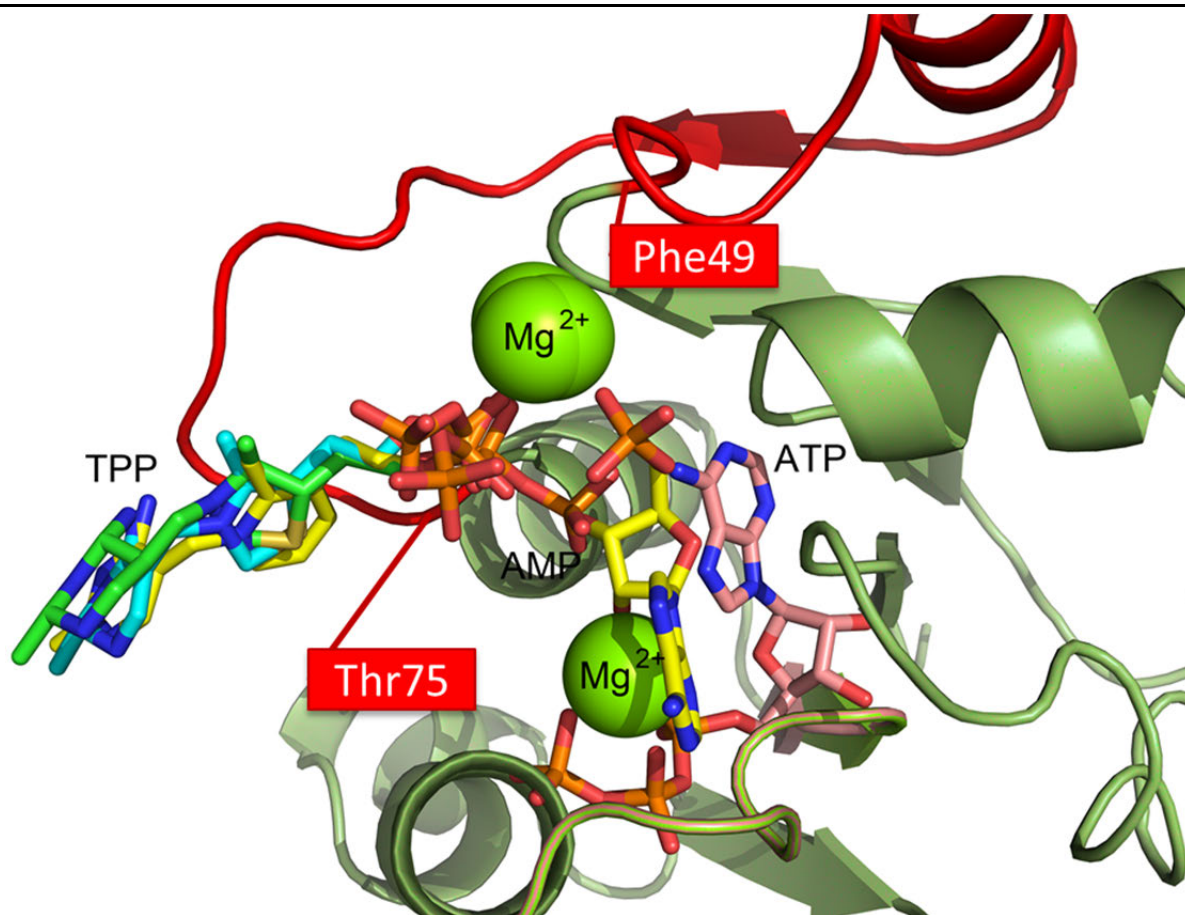
Figure 59: Ribbon representation of TPK homology models, calculated on the base of co-crystallised homologue structures and the _Sa_TPK sequence by the I-TASSER server [158-160]. The calculated consensus is depicted in dark green, the missing loop from the SaTPK structure in red with the respective beginning and ending residue and magnesium ions in light green. TPP, AMP and ATP are displayed in stick representation with oxygen atoms in red, carbon in the respective chain colour, nitrogen in blue and phosphorus in orange. Positions of ligands are based on coordinates of co-crystallised structures deposited in the pdb database. Figure was obtained using PyMOL (PyMOL Molecular Graphics System, Version 1.3, Schrödinger, LLC.).

Homology modelling revealed that the loop which was not visible in the electron density carries the substrate binding sites of ATP, magnesium and thiamin. Based on this knowledge, a magnesium screen by varying Mg^{2+} concentrations between 1-500 mM with different counter ions (sulfate, formate, chloride and acetate) was designed and included in the already known crystallisation condition (0.8 M sodium citrate, 10 mM sodium bromide) (the formulation can be found in the Appendix). Additionally, to stabilise TPK structure, the His-tag was removed by TEV protease cleavage. After purification, the recombinant TPK protein was dialysed against buffer W overnight. DTT was added to a final concentration of 5 mM and the TEV protease was added in a 1:100 ratio and incubated overnight at 4 °C. The next day, cleaved His-tags and the TEV protease were removed by Ni-NTA matrix. The flow through contained cleaved protein and was dialysed against buffer W containing 300 mM

sodium chloride overnight and concentrated to a A_{280} of 9.9 (7.8 mg/ml) and 18.6 (23.4 mg/ml) and centrifuged for 50 min at 100,000 x g and 4 °C.
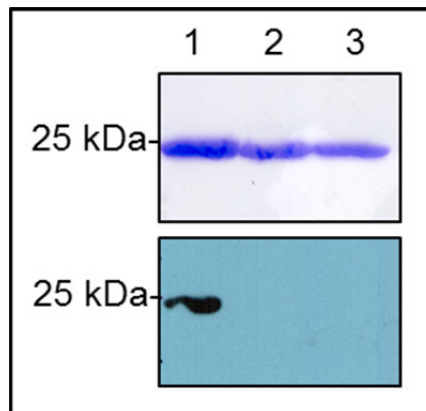
Figure 60: Stained SDS- gel (top) of TPK digestion and corresponding autoradiograph from a western blot incubated with α-His antibody (1:5000)). Lane 1 shows undigested protein, lane 2 digested protein and lane 3 digested and purified protein.

Figure 60 shows undigested, digested and purified protein (lane 1-3). In the corresponding western blot only the signal of undigested TPK was visible. Neither digested nor the purified proteins were detected by an α-His antibody.

After concentration, the protein was mixed with 3 mM thiamin and 0.5 mM AMP-PCP and incubated on ice for 1 h. Screening was pipetted by the Honeybee 961 (Genomic solutions, UK) pipetting robot in 96-well MRC sitting drop plates (Molecular Dimensions, UK) for vapour diffusion. Plates were incubated at 20 °C and 4 °C in RUMED 3001 (Rubarth, Germany) incubators and at 14 °C in a laboratory with air condition. The reservoir contained 55 µl precipitant solution and two droplets containing 500 nl or 700 nl precipitant which were mixed with 500 nl of protein solution respectively.
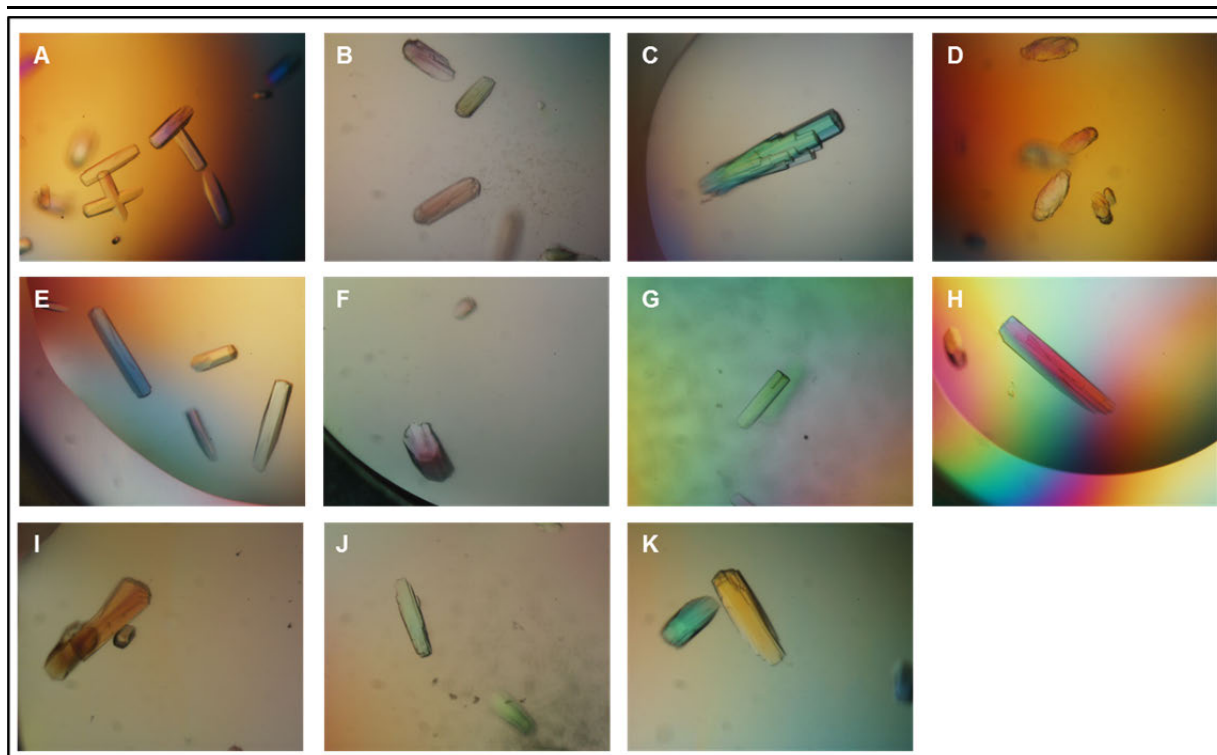
Figure 61: TPK co-crystals with thiamin and AMP-PCP grown after 4 d in a self-designed magnesium screen in MRC sitting drop plates (Molecular Dimensions, UK). All conditions contained 0.8 M sodium citrate and 10 mM sodium bromide, but individual magnesium concentrations. A:500 mM magnesium chloride, 20 °C, 23.4 mg/ml; B: 150 mM magnesium acetate, 20 °C, 7.8 mg/ml; C: 400mM magnesium chloride, 20 °C, 23.4 mg/ml; D:500 mM magnesium chloride, 14 °C, 23.4 mg/ml; E: 500mM magnesium chloride, 20 °C, 7.8 mg/ml; F: 200mM magnesium chloride, 20 °C, 7.8 mg/ml; G: 500 mM magnesium chloride, 4 °C, 7.8 mg/ml; H: 400 mM magnesium chloride, 20 °C, 23.4 mg/ml; I: 200 mM magnesium chloride, 20 °C, 7.8 mg/ml; J: 150 mM magnesium formate, 20 °C, 7.8 mg/ml; K: 500 mM magnesium chloride, 20 °C, 23.4 mg/ml.

In summary, most conditions obtained in the magnesium screen contained high concentrations of magnesium chloride and grew with both protein concentrations mainly at 20 °C.

For diffraction data collection, crystals were protected by adding glycerol to the droplets and mounted with micro mounts (JenaBioscience, Germany). The resolution range was from 8-3.1 Å for different crystals, whereas most spots were smeared and pattern did not show diffraction of a single crystal. The best diffraction was recorded from the crystal grown with 400 mM magnesium chloride at 4 °C and an initial protein concentration of 23.4 mg/ml. Even though diffraction spots were round, indexing was so far not possible and no data set was collected.

After that, all plates with TPK crystallisation trials were revised carefully and all conditions that have been found so far were optimised for hanging drop and with micro bridges for sitting drop vapour diffusion in CPL-130 plates (JenaBioscience, Germany).

TPK was purified and dialysed against buffer W. His-tag was cleaved by TEV protease overnight and protein was dialysed against 100 mM Tris/HCl, pH 8 with 400 mM magnesium chloride, concentrated to a concentration of 20 mg/ml and centrifuged at 100,000 x g at 4 °C for 50 min. A final concentration of 20 mg/ml (~800 μM) of SaTPK was mixed with 8 mM thiamin dissolved in protein buffer and 2 mM AMP-PCP also dissolved in protein buffer. Mixture was incubated for 1 h on ice and crystallisation trials were set up mixing 1 μl of protein solution with 1 μl of the respective precipitant for hanging and sitting drop vapour diffusion experiments. Crystals grew after 5 d (data not shown), but diffraction analysis at the consortium beamline X13 (Hasylab/DESY, Germany) showed only smeared spots to a maximum resolution of 4 Å, indicating intergrown crystals.

4.7.4 TPK SAXS analysis

To verify the dimeric assembly in solution, SAXS measurements at the beamline X33 (Hasylab/EMBL, Germany) were carried out. TPK was purified, dialysed against buffer W overnight and centrifuged at 100,000 x g for 50 min at 4 °C. Dispersity was monitored by DLS. Four different dilutions were prepared in the range of 0.8-7.5 mg/ml. Dialysis buffer was used as a reference for the measurements.

The indirect transform package $GNOM$ [127] was used to compute R_g from the entire scattering pattern, the pairwise distribution function p(r) and the size of the particle D_{max}. An experimental R_g-value of 2.34 $\pm$ 0.02 Å was calculated. $DAMMIF$ [130], $DAMMIN$ [129] and $GASBOR$ [163] were used to calculate the ab $initio$ envelope structure by imposition of P2 symmetry, whereas only the $GASBOR$ shape was in agreement with the scattering pattern (χ = 2.1) and was superimposed with the crystal structure (see Figure 62 B).
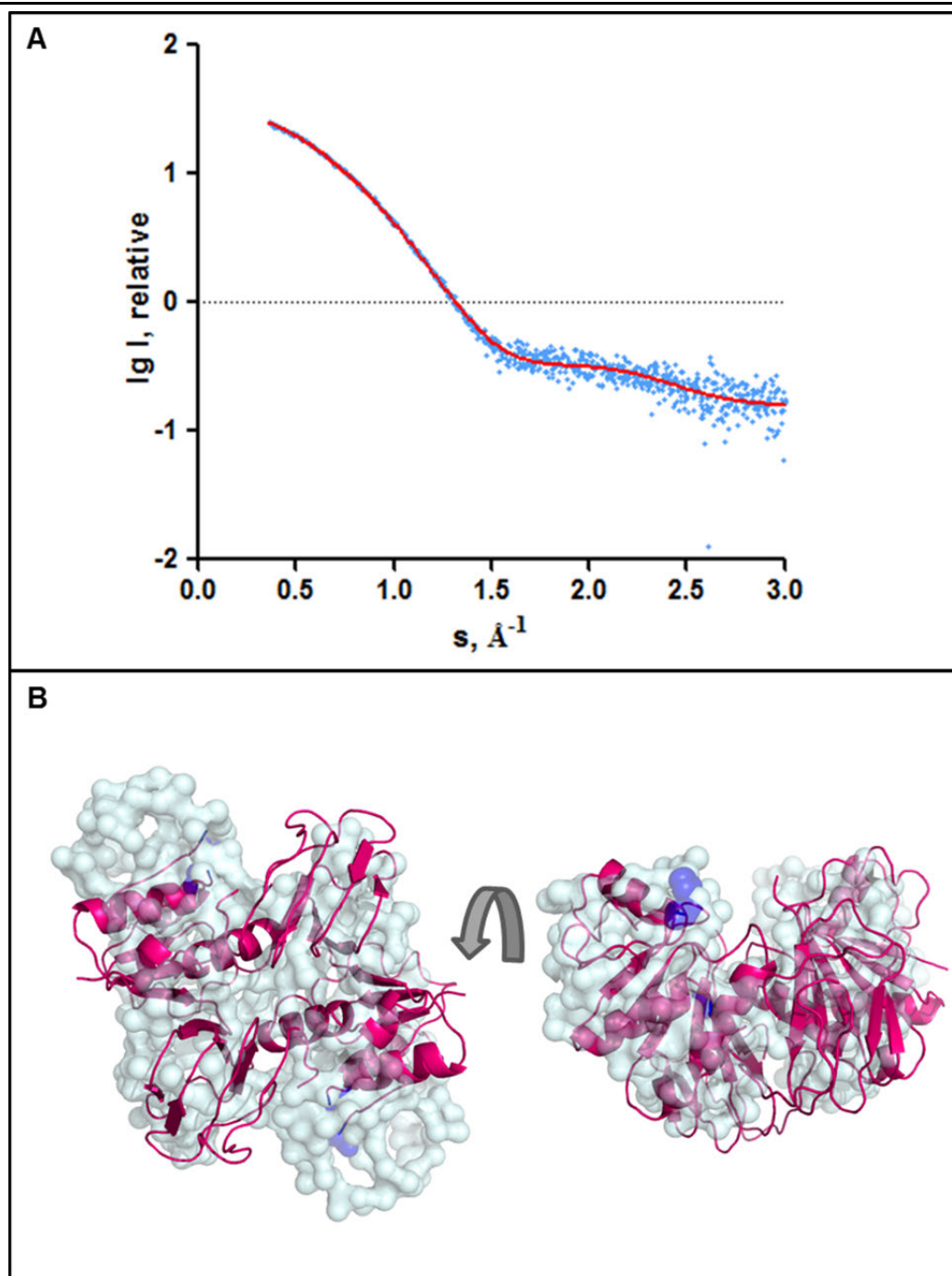
Figure 62: Processed solution scattering pattern and *ab initio* shape from dimeric TPK obtained by SAXS. A: Experimental data is displayed in blue with a red fit for the *GASBOR* [163] *ab initio* model. B: Front and side view of dimeric TPK *ab initio* shape in superimposition with the crystal structure in a pink ribbon representation and the beginning and ending residue of the missing loop in a blue sphere representation (Figure generated with PyMOL (PyMOL Molecular Graphics System, Version 1.3, Schrödinger, LLC.).

As already mentioned in chapter 4.4.4, the putative ligand binding site of TPK could not be built in the crystal structure, because in this region there was no electron density present. Each monomer lacks a loop of 26 amino acids between the positions 49 and 75. This was also reflected by the *ab initio* model obtained by SAXS (see Figure 63). The outer amino acids representing the beginning and the end of the

missing loop are represented as spheres in blue. The "empty" SAXS envelope indicates the position of this missing part in the crystal structure and explains the obtained discrepancy of $\chi = 2.1$. A final comparison between experimental data and the crystal structure by *CRYSOL* [132] can only be provided having a complete high resolution model.
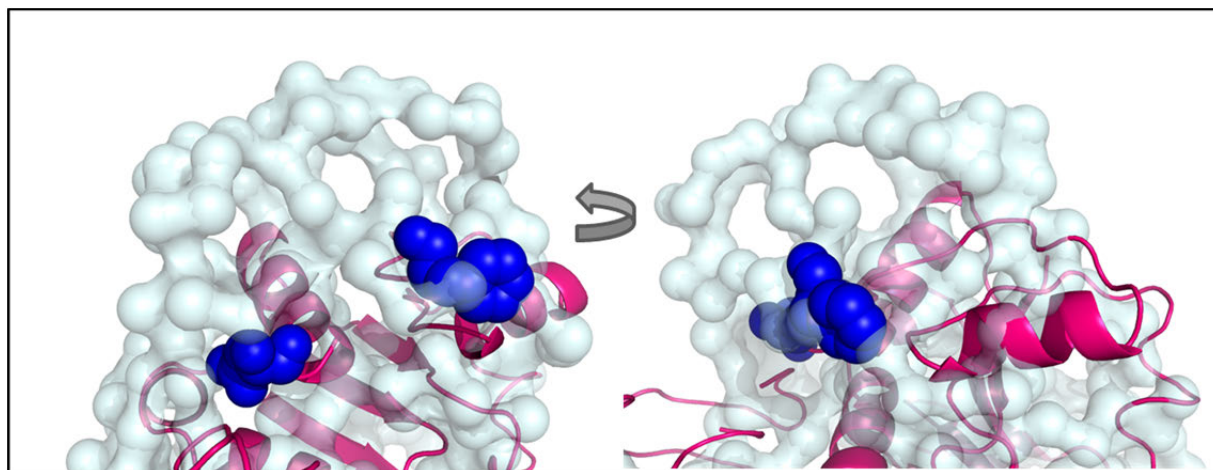
Figure 63: Detailed view of the TPK crystal structure (ribbon representation, pink) in superimposition with the *ab initio* SAXS model (light blue). Amino acids marking the borders of the missing loop are represented as spheres in blue. Figure was generated through PyMOL (PyMOL Molecular Graphics System, Version 1.3, Schrödinger, LLC.).

5 DISCUSSION

5.1 Exploiting the thiamin biosynthesis for pro-drug design

Thiamin is an important co-factor for a large variety of key enzymes in the carbohydrate and amino acid metabolism. In its active form TPP it catalyses decarboxylations and transketolations. Thiamin can be synthesised *de novo* by bacteria, fungi and some plants [6, 100], whereas humans have to cover their needs by dietary uptake. A lack of thiamin in humans leads to severe neurological impairment. Bioinformatics could show that proteins involved in vitamin biosyntheses are scored within the highest category as druggable [5]. The absence of such pathways in humans could prevent possible side effects. Drug discovery attempts interfering with other co-factor biosynthesis pathways were applied successfully [113, 164].

The vitamin B1 biosynthesis has been characterised biochemically including the complete identification of involved enzymes, activity analyses and regulation mechanism [103]. The 3D information of these enzymes was so far not analysed.

To obtain structural information for drug discovery approaches, the genes of the involved enzymes were cloned and expressed as His-tag fusion proteins with a TEV protease cleavage site for possible cleavage of the flexible affinity tag.

Test expression and purification showed, that ThiM, TenA and TPK eluted as a single band from the affinity column. ThiD with a C-terminal TEV-His site was completely insoluble. A new construct with the tag and the cleavage site at the N-terminus was soluble, but showed minor impurities after affinity chromatography. ThiE with a C-terminal TEV-His site was soluble, but showed two main bands in the elution fraction indicating an N-terminal processing of the protein. An N-terminal fusion protein showed a single main band, but a relatively high degree of impurity. The GTPase also showed impurities that indicate a systematic N-terminal processing of the protein. In summary, ThiM, TenA and TPK were directly used for crystallisation experiments, whereas ThiD, ThiE and the GTPase needed further optimisation.

It was shown that centrifugation at velocities >70,000 x g removed completely aggregated protein and monodisperse solutions monitored by DLS were applied for crystallisation and were also suitable for SAXS measurements. ThiM and TPK were initially used as His-tag fusion protein. A removal of the affinity tag was at first not performed. As TenA was already successfully applied for crystallisation as a Strep-

tag fusion protein and initial crystals were optimised, the His-tag fusion protein was not used for further experiments.

5.2 Structural characterisation of the thiamin biosynthesis in S. aureus

5.2.1 Structure analysis of native ThiM and in complex with THZ

ThiM was crystallised (precipitant: 20 % PEG 3,350 and 0.2 M magnesium formate) (condition A5 from the *JCSG+* suite (Qiagen, Germany)) applying the vapour diffusion sitting drop technique [165]. This condition was successfully optimised with the hanging drop technique varying the PEG 3,350 concentration and crystals grew more separated after addition of 5 % isopropanol to the precipitant composition (final precipitant: 20 % PEG 3,350, 0.2 M magnesium formate, 5 % isopropanol). Diffraction data was recorded at the consortium beamline X13 (Hasylab/ DESY, Germany) to 2.1 Å resolution. The data were indexed and subsequently scaled in the space group P1 in the resolution range from 50 to 2.15 Å. The phase information was obtained successfully, using a single chain of the homologue structure from *B. subtilis* as a search model. The final model was refined to R/R_{free}: 19.75/24.38 %, which is in a good range for protein structures and also the ratio of these values indicates that the model is not overfitted [166]. The surface loops from amino acid 126 in helix 8 and 140 in helix 9 were disordered and no electron density was obtained for this region, but for drug discovery this region is not relevant as the substrate binding region is located elsewhere. In the homologue structure from *B. subtilis,* two magnesium ions are located within the active site to catalyse the phosphorylation of THZ. In the structure from *S. aureus* no such ions were identified in the electron density although magnesium was present in high concentrations in the precipitant solution. The overall structure resembles a trimer, which was already described for *B. subtilis* [152] and SAXS measurements confirmed the trimeric state in solution.

The active site region was identified by superimposition of *Sa*ThiM with *Bs*Thik (rmsd: 1.08 Å) which was co-crystallised with TZP (THZ-P) and ATP. The residues forming the active site are highly conserved and also the positions in 3D-space matched very well when superimposed with the homologue structure from *B. subtilis*.

A native ThiM crystal was soaked with THZ and non-hydrolysable ATP (AMP-PCP) and diffraction data to 3 Å was recorded at beamline A1 (CHESS, USA). The data were scaled in the space group P1 in the resolution range from 31 to 3.05 Å. The

crystal was besides THZ soaked with AMP-PCP, but only electron density for THZ was identified in the active site. Although data at this resolution is not suitable to determine exact ligand positions, the electron density for THZ throughout the 12 chains in the asymmetric unit was clear and allowed the positioning of THZ in the active site with small deviations, but in a preferred orientation which matches the orientation predicted by superimposition with co-crystallised *B. subtilis* homologue [152]. Also in the complex structure with THZ the surface loops in the region from amino acid 126 in helix 8 to amino acid 140 in helix 9 were not present in the electron density for all chains.

5.2.2 Structure analysis of native ThiM from the Shenzou8 space mission

Crystallisation is the major bottleneck in the determination of protein structures. From crystallisation experiments in space, evidence came up for an increased crystal quality in order to obtain higher resolution data for crystals grown in a microgravity environment with decreased convection and sedimentation [167].

The ThiM micro crystals that were grown under microgravity conditions in space were used to prepare a seed stock for a hanging drop vapour diffusion experiment. The resulting crystal was intergrown and a second seedstock was prepared from this crystal. The resulting crystals differed significantly in morphology from the ThiM crystals that were obtained before. In comparison to previous crystals, the seeding crystals were single crystals and not lamella shaped.

Diffraction data was recorded at the consortium beamline X13 (Hasylab/ DESY, Germany) to 1.9 Å and data were indexed and scaled in the monoclinic space group $P2_1$ in the resolution range from 20 to 2.09 Å. The final structure was refined to R/R_{free} 19.91/ 24.77 %, which accounts for reliable model that is not overfitted [166].

Altogether, seeding led to different crystal morphology (lamella shaped vs. single crystal), a higher crystal symmetry (P1 vs. $P2_1$) and a slightly better resolution (2.15 vs. 2.09 Å). A similar trend was reviewed by McPherson for other projects [167]. If the increase in quality was the result of crystal seeds grown in space or the seeding technique itself is questionable. However, it is tempting to speculate that the seeds grown without gravity were the base for higher symmetry and order in the crystal.

5.2.3 Pro-drug screen for ThiM to treat infections caused by MRSA

Since complete genome sequencing is possible, bacteria specific biochemical pathways and nutrient transport systems can be identified. The inhibition of such pathways is most desirable to prevent toxic side-effects in humans [168, 169]. The knowledge about possible salvage-pathways and transport systems completes the idea of the ideal drug that damages the bacterium without harming its host.

Due to emerging resistance and relatively high number of fatal cases related to MRSA infection a new approach for anti-staphylococcal drug discovery was addressed.

A pro-drug should be identified, which is metabolised by the bacterium, but yields an inactive TPP. As a consequence, thiamin dependent enzymes would be non-functional and key reactions in the carbohydrate and amino acid metabolism could not be carried out. In a similar approach, the B6 vitamer syntheses have been investigated in order to design a pro-drug to target PLP-dependent enzymes. A new compound with an IC_{50} in the low micromolar range has been identified recently [113]

Co-factor transport systems have to be taken into account to assure that the non-functional co-factor cannot be replaced by uptake from the environment. For thiamin, no such transporters were identified and non-functional thiamin would not be substituted by thiamin from the host.

Like the thiamin biosynthesis, also other co-factor biosyntheses have been considered to be new drug targets for different pathogens. Among marketed new drugs, iclaprim (Arpida) targets the dihydrofolate reductase to inhibit synthesis of tetrahydrofolate (THF) [1]. This pathway has also been considered by Chhabra and colleagues [164] to treat MRSA infections.

In 2010, the structure of andenylo-succinate lyase PurB was reported. It catalyses reactions for purine supply and control of AMP/fumarate levels and is essential for *S. aureus* survival. Its dimeric interface was considered to be a drug target, as three subunits from two dimers forming a tetramer are required to build the active site [170].

Based on the structure of the vitamin K biosynthesising enzymes, a promising lead compound was screened which reduces mycobacterial growth [171].

The folate biosynthesis, more precisely the inhibition of the dihydropteroate synthase and dihydrofolate reductase, has been exploited as an antimalarial drug target since the 1940s [172].

In a study carried out by Gerdes *et al.* [173], genetic footprinting was used to identify putative targets for broad-spectrum antibiotic use. The selected genes are associated with pathways that are conserved among various bacteria, but totally absent in humans or the gene products are at least structurally unrelated to their human counterparts. In this respect the andenylate cofactor NAD, CoA and flavin adenine dinucleotide (FAD) syntheses have been studied also for anti-staphylococcal drug development. Only *Helicobacter pylori* seems to have a suitable target within the NAD biosynthesis pathway. This bacterium lacks the niacin salvage, whereas *S. aureus* is capable to scavenge this co-factor as well as cobalamin (vitamin B12). In contrast, the pantothenate kinase (PK) as the first enzyme of the pantothenate pathway is structurally different to eukaryotic PKs; thus, it suits well for antibiotic development [173].

The co-factor biosyntheses for pro-drug discovery are not widely investigated and such pathways are rather intended to be blocked. Inhibition involves the danger of rapid resistance development. However, Nitazoxanide is such an example to treat protozoal infections, with no resistant mutants to date [174]. Also the treatment of multi-drug resistant tuberculosis by pro-drugs has been considered [175].

For antiprotozoal drugs, the biosyntheses of vitamin B6 and vitamin B1 have been considered as a target [176]. In chemotherapy, the naturally occurring HMP-analogue bacimethrin (MeO-HMP) or synthetic CF_3-HMP have been tested and showed promising results [177, 178].

With the architecture of the active site of ThiM from *S. aureus*, which was predicted in this work by superimposition with the homologue structure from *B. subtilis* and confirmed by a complex structure with THZ in the active site, a lead structure search for pro-drug discovery was carried out. Thereby it was important to replace the sulphur in the thiazole ring of THZ, because the 3d orbitals stabilise the ylid group, which is the chemical structure to catalyse thiamin assisted reactions. It was reported that derivatives having an oxazolium or imidazolium ring are less reactive than the thiazolium compound [82, 84, 85]. In contrast, the nitrogen in the heterocycle for HMP transfer and a hydroxyl group had to be maintained to ensure the synthesis of a complete derivative and a phosphorylation site for final pyrophosphorylation.

Putative substrate analogues were screened from the ZINC library and docked into the active site. 13 compounds were obtained and analysed alone and in competition to the natural substrate. In the test system without the natural substrate, it was shown that 12 out of 13 compounds were accepted as substrates except for compound 12. The highest specific activities were in the same range as for the natural substrate, but when THZ was present no turnover of the substrate analogues was observed. Compounds 2, 4, 6 and 7 with the highest specific activities were further analysed and compared to THZ. The specific activities were in the same range for compound 4 (5214 ± 598 nmol min^{-1} mg^{-1}) and approximately 1.5 times higher for compound 2 (7418 ± 91 nmol min^{-1} mg^{-1}), 6 (7297 ± 267 nmol min^{-1} mg^{-1}) and 7 (7264 ± 270 nmol min^{-1} mg^{-1}) in comparison to the natural substrate (4880 ± 488 nmol min^{-1} mg^{-1} [103]). The K_M values of the compounds in comparison to THZ (44 ± 5 µM [103]) were approximately 20 times higher for compounds 2 (831 ± 169 µM) and 6 (834 ± 147 µM) and even approximately 30 times higher for compound 4 (1258 ± 388 µM). This correlates with a reduced affinity for the substrate analogues and reflects the results of the competitive assay, that if the natural substrate is present no more turnover of compounds was observed. The highest efficiency, which was observed for compound 7 (0.31) was also only one tenth of the THZ efficiency (3.1). Altogether it was a success to identify compounds which were accepted as substrates for ThiM, but in the future, these lead structures have to be optimised towards a better binding and turnover. With regard to the type of heterocycle that could be used for further optimisation of the compounds, no preferred chemical structure was identified, as the compounds with the highest specific activities are on the base of imidazole, oxazole, pyrazole and triazole.

Compound 12 differed from all other tested compounds as it inhibited the phosphorylation of the natural substrate when the inhibitor was present and also no phosphorylated product was identified when used exclusively. Instead of a substrate analogue, an inhibitor was found. Further analyses revealed that the affinity for the inhibitor is higher than for THZ (K_i of compound 12 (17 ± 4 µM) and K_M of THZ (44 ± 5 µM [103]). This explains the decreased THZ turnover when present in equimolar ratio. The inhibition type found was a mixed inhibition type indicated by different apparent V_{max} for different inhibitor concentrations and an intercept of the graphs corresponding to different inhibitor concentrations in the double reciprocal representation. Additionally, docking studies were performed, to localise putative

binding sites for compound 12. Interestingly, one of these binding sites is located very close to the ATP binding pocket. This finding suggests, that upon compound 12 binding the ATP binding site is blocked. Another putative binding site was located within the surface loop between helix 8 and 9. Although conformational changes throughout the chain could lead to a decreased substrate affinity this binding site appears to be less likely. The binding mode has to be further analysed with co-crystallisation experiments.

Complementarily, the binding epitopes of all compounds were analysed by STD-NMR measurements. STD-NMR was already used successfully to screen noro virus- and HIV entry inhibitors [179, 180].

Regarding the ThiM substrate analogues, it was shown that the compounds with the highest specific activities share the highest saturation at the β-carbon and a moderate saturation at the α-carbon of the hydroxyethyl group. Also a methylgroup attached to the heterocycle in direct neighbourhood to the hydroxyethyl group with moderate saturation seemed to be favourable. However, combining activity and NMR data, a hydroxypropyl group correlated with reduced affinity. This could also be observed when the heterocycle obtains high saturation. In this case the hydroxyl group seems to be in an unfavourable position for phosphate transfer.

The STD NMR determined binding epitopes of the ligands indicate a very similar binding mode as that of the lead structure. The binding studies provide structure activity relationships and demonstrate the utility of this approach.

5.3 Structure analysis of TPK and outlook

For further pro-drug optimisation, the determination of other enzymes within the thiamin biosynthesis pathway is very important, as the drugs which were developed for the active site of ThiM also have to be accepted by other enzymes involved in the processing of ThiM products. TPK catalyses the last step in the thiamin biosynthesis and pyrophosphorylates thiamin.

TPK was crystallised under oil (precipitant: 0.8 M sodium citrate and 10 mM sodium bromide) and the resulting crystal diffracted to 2.78 Å. The dataset was indexed and scaled in the tetragonal space group $P4_12_12$ in the resolution range from 44 to 3.06 Å. The phase information was obtained successfully, using a single chain of the homologue structure from *S. saprophyticus* as a search model. The final model was refined to R/R$_{free}$: 24.2/30.1 %, which indicates, that some optimisation has to be

done for future crystallisation. The resulting structure is a dimer, which could also be confirmed by SAXS, showing that the dimeric assembly is not a crystallographic artefact.

The putative ligand binding loop for thiamin, ATP and magnesium predicted by bioinformatics on the base of homologue structures, was not visible in the electron density and could not be built. Analysing the diffraction quality of TPK crystals with different magnesium concentrations, thiamin and AMP-PCP to stabilise the loop revealed that the best diffraction quality was obtained at high magnesium concentrations (>400 mM) and relatively low temperature (14/4 °C vs. 20 °C before). Therefore, the protein was directly dialysed against high magnesium concentrations after elution from affinity chromatography column. Additionally, the His-tag was successfully cleaved off and the protein was also stabilised by its substrates thiamin and AMP-PCP. Diffraction of these optimised crystals indicated that the crystal was not a single crystal, but consisted of very thin layers grown together.

Further crystal optimisation need to be carried out in the future using different divalent cations and different non-hydrolysable ATP analogues applying different crystallisation techniques.

5.4 Outlook for pro-drug discovery experiments

With the 3D-structure of ThiM, initial substrate analogues were analysed. 3D-structures of ThiM in complex with these substrates would provide a deeper insight into binding mode and the modified mode of action. This would allow more detailed conclusions about differences in affinity and activity. Taking into account the interactions of the binding pocket with the compounds and restraints from the co-crystal structure-activity relationship, specific chemical modifications at the compounds could be carried out.

With additional information on protein structures of the thiamin biosynthesis pathway, such as TPK, new compounds can be identified and subsequently optimised. With activity tests and binding epitope determination via STD-NMR spectroscopy in comparison to the natural substrate carried out with TPK, such compounds could be modified.

5.5 Structure analysis of TenA and functional characterisation of the oligomeric state

TenA is a bifunctional enzyme that catalyses the deamination of aminopyrimidine and also the cleavage of thiamin in the co-factor salvage pathway. For drug discovery it is was not selected due to its salvage function. However, using the 3D information and additional mutagenic studies the relationship between oligomeric state and protein stability was investigated.

TenA was crystallised (precipitant: 0.2 M sodium acetate 0.1 M Tris/HCl pH 8.5 and 26 % PEG 4,000) [136] applying the hanging drop vapour diffusion technique and the crystal diffracted to 2.69 Å. The data set was indexed and scaled in the orthorhombic space group $P2_12_12_1$ in the resolution range from 30 to 2.69 Å. The phase information was obtained successfully, using a single chain of the homologue structure from *S. epidermidis* as a search model. The final model was refined to R/R_{free}: 21.31/25.88 %, indicating a good structure solution [166]. The resulting structure is a tetramer, which was also confirmed as the oligomeric state in solution by SAXS.

To study the relationship between oligomerisation and biological function, single amino acids at the interfaces of the TenA tetramer were mutated to disrupt the oligomeric state of the WT. The interface was studied and the amino acids D111, K115, E76 and K49 were chosen for mutagenesis studies. Amino acids 111, 115, 76 and 49 were exchanged against alanine, amino acid 49 against serine. Surprisingly, the mutations D111A and K115A already led to the monomerisation of the protein as seen by size exclusion chromatography. The mutant in its monomeric form had 30 % more hydrophobic amino acids exposed to the solvent that were buried within the interfaces in case of the WT and therefore solubility was reduced. Further DLS and SAXS analyses were not possible due to solubility limitations during concentration of the protein.

Monomeric TenA was compared with the tetrameric WT in terms of activity (thiamin cleavage), folding stability and protease stability. Activity analysis revealed no major differences between the two species. Specific activity of the WT is slightly smaller than for the mutant, but both values are in the same range (mutant: 2.25 ± 0.17 mM, WT: 1.40 ± 0.19 mM) the same accounts for the turnover number k_{cat} (mutant: 6.8 ± 0.11 ms^{-1}, WT: 4.07 ± 0.07 ms^{-1}) and the efficiency (mutant: 3.04 ± 0.05 M^{-1}s^{-1},

WT: 2.92 ± 0.05 M^{-1}s^{-1}). This comparison shows that the activity is not affected by monomerisation of the protein.

Analyses with CD spectroscopy showed that both protein species were stable and folded during 15 d incubated at RT. Unfolding of the WT after 14 d is probably due to a contamination.

The protease stability test demonstrated major differences between both species. The WT protein was not affected by trypsin digestion and remained stable during the whole time course of digestion. In contrast, the mutant was partially digested after 0.5 h and the WT protein remained undigested after 52 h. Also during subtilisin digestion a difference between both protein species was observed. In contrast to trypsin digestion the WT protein is also digested, but not in the same extent as the mutant. After 52 h, undigested WT protein is only slightly reduced, whereas mutant protein is almost completely digested.

Exotoxin proteases are expressed during the exponential growth of bacteria in *S. aureus* infection [181]. Secreted into the host tissue, they degrade proteins to acquire nutrients. These proteases are expressed as zymogens to ensure inactivity during their passage through the cytoplasm or when misdirected instead of secretion [182]. Additionally, cysteine protease inhibitors are expressed to prevent degradation of cytoplasmic proteins [183]. In contrast, no serine protease inhibitors were identified in *S. aureus*. The serine protease-like proteins A and B (SplA and B) showed proteolytic activity, but do not carry pro-peptides. Only the signal sequence directs the protease to the extracellular compartment and assures its inactive state [182].

As part of the degradome in *S. aureus*, the caseinolytic proteins (Clp) protease complexes in analogy to the eukaryotic 26 S proteasome are expressed. They consist of Hsp100/Clp proteins belonging to the AAA+ superfamily and a proteolytic domain. They catalyse the unfolding and degradation of specific proteins and play a key role in the regulation of various cellular processes [184]. The Clp family is very well characterized for *E. coli* and most staphylococcal relatives are annotated by similarity [185]. ClpP and ClpQ are the proteolytic domains in this proteasome-like complex, whereas ClpP is a serine protease and ClpQ a threonine protease [186, 187]. The other members of this family provide the ATPase domains for the multienzyme complex.

The findings suggest that the assembly of multiple enzyme copies of TenA did not affect activity and substrate specificity, but could prevent cytoplasmic proteins from autolysis and increases their half-life time within the cell.

6 SUMMARY- ZUSAMMENFASSUNG

6.1 Summary

Vitamin B1 (thiamin) in its active form TPP is an important co-factor for a large variety of key enzymes in the carbohydrate and amino acid metabolism. Humans have to acquire this co-factor by dietary uptake, whereas most bacteria, fungi and plants are able to synthesise this co-factor *de novo*. Alarming statistics of fatal cases and resistance spread related to nosocomial infections with the pathogen *Staphylococcus aureus* require the identification of novel drug targets. In this context, the thiamin biosynthesis has been identified as a suitable target, as it is absent in humans and thus the risk of side effects is decreased and the potential drug could specifically poison the pathogen.

The genes of the six thiamin-synthesising enzymes were cloned and expressed successfully in *E. coli*. ThiM, TPK and TenA, were crystallised and the structure was solved applying synchrotron radiation. The oligomeric state observed in the crystal structure was confirmed in solution by small angle X-ray scattering (SAXS).

For drug discovery, the major focus was on the active site of ThiM, one of the first thiamin synthesising enzymes in this pathway. Bioinformatics tools were applied to identify the active site and the positioning of the substrate was verified by co-crystallisation experiments.

With the help of the active site architecture, substrate analogues were identified and analysed in terms of activity. Together with the binding epitopes for these compounds obtained by saturation transfer difference (STD)-NMR, a base for further optimisation was provided. Also the TPK structure could lead towards the discovery of an anti-staphylococcal drug.

Moreover, the relationship between the oligomeric state of TenA, an enzyme involved in thiamin salvage, and proteolytic stability were shown. Analysing the crystal structure of tetrameric TenA, interface residues were selected for *site-directed* mutagenesis to monomerise the wildtype (WT) protein. The mutant was successfully expressed and was compared to the WT protein in terms of activity, folding stability and protease stability. Regarding activity and folding stability, no major differences have been observed, whereas the WT protein was significantly more stable against digestion with serine proteases. This would suggest that *S. aureus* might be able to

protect TenA from intracellular proteases and proteases secreted during infection through stabilising oligomerisation of the protein.

6.2 Zusammenfassung

Vitamin B1 (Thiamin) in seiner aktiven Form TPP ist ein wichtiger Co-Faktor für viele Schlüsselenzyme des Kohlenhydrat- und Aminosäurestoffwechsels. Menschen sind darauf angewiesen ihren Bedarf über die Nahrung zu decken, wohingegen die meisten Bakterien, Pilze und Pflanzen in der Lage sind Thiamin *de novo* zu synthetisieren. Alarmierende Todesstatistiken und die zunehmende Verbreitung von Resistenzen im Zusammenhang mit nosokomialen Infektionen durch das Bakterium *Staphylococcus aureus* erfordern die Identifikation und Analyse neuartiger Angriffsziele für Antibiotika. In diesem Zusammenhang wurde die Vitamin B1 Biosynthese als geeignetes Ziel ermittelt, da sie im Menschen nicht existiert und dadurch unerwünschte Nebenwirkungen ausgeschlossen werden können, indem der Wirkstoff spezifisch den Krankheitserreger angreift.

Die Gene der sechs thiamin-synthetisierenden Enzyme konnten kloniert und erfolgreich in *E. coli* exprimiert werden. Die Enzyme ThiM, TPK und TenA wurden kristallisiert und die Struktur dieser Proteine konnte durch die Bestrahlung der Kristalle mit Synchrotronstrahlung gelöst werden. Der in der Kristallstruktur bestimmte Oligomerisierungsgrad wurde für diese Proteine mittels Röntgenkleinwinkelbeugung (SAXS) auch in Lösung bestätigt.

Für die Wirkstoffentwicklung lag der Schwerpunkt auf dem aktiven Zentrum von ThiM, eines der ersten Enzyme, die am Aufbau von Thiamin beteiligt sind. Mittels bioinformatischer Methoden wurde das aktive Zentrum lokalisiert und die Positionierung des Substrats konnte durch eine Co-Kristallstruktur bestätigt werden.

Auf Basis der Architektur des aktiven Zentrums wurden Substratanaloga identifiziert und hinsichtlich ihrer Aktivität analysiert. Zusammen mit den Bindungsepitopen, die durch Saturation Transfer Difference (STD)-NMR bestimmt wurden, konnte die Grundlage für die weitere Optimierung dieser Komponenten geschaffen werden. Auch die Einbeziehung der Kristallstruktur von TPK in den Optimierungsprozess könnte in Zukunft zur Entwicklung eines Wirkstoffs gegen Staphylokokken führen.

Darüber hinaus wurde der Zusammenhang zwischen dem Oligomerisierungsgrad von TenA, einem Thiamin-spaltendem Enzym und der Proteasestabilität dieses Enzyms gezeigt. Durch die Untersuchung der Kristallstruktur von tetramerem

Wildtyp-TenA wurden Aminosäuren in den Grenzflächen des Tetramers ausgewählt und mittels ortsgerichteter Mutagenese gegen andere Aminosäuren ausgetauscht, die zur Bildung eines Monomers führten. Das mutierte Gen wurde erfolgreich exprimiert und in Hinblick auf Aktivität, Stabilität der Faltung und Proteasestabilität mit dem Wildtypprotein verglichen. Bezüglich der Aktivität und der Stabilität der Proteinfaltung konnten keine Unterschiede zwischen Wildtyp und Mutante festgestellt werden. Allerdings konnte gezeigt werden, dass das Wildtypprotein eine deutlich erhöhte Stabilität gegenüber dem Verdau mit Serinproteasen aufwies. Das deutet darauf hin, dass *S. aureus* seine Proteine vor intrazellulären Proteasen und solchen Proteasen, die während der Infektion sekretiert werden durch den Aufbau von Oligomeren schützen könnte.

7 REFERENCES

1. Boucher, H.W., G.H. Talbot, J.S. Bradley, J.E. Edwards, D. Gilbert, L.B. Rice*, et al.*, *Bad bugs, no drugs: no ESKAPE! An update from the Infectious Diseases Society of America.* Clin Infect Dis, 2009. **48**(1): p. 1-12.

2. Robert Koch Institut, *Auftrenten und Verbreitung von MRSA in Deutschland 2008.* Epidemiologisches Bulletin, 2009. **17**.

3. World Health Organization/ Europe *Strategischer Aktionsplan zur Bekämpfung von Antibiotikaresistenzen.* 2011. 1-11 DOI: EUR/RC61/14 + EUR/RC61/Conf.Doc./7; Date accessed: 03/19/2012

4. Deutsche Gesellschaft für Krankenhaus Hygiene (DGKH) *Krank im Krankenhaus.* 2007. http://www.dgkh.de/pdfdata/krank_im_krankenhaus2007.pdf; Date accessed: mai 9, 2012

5. Hajduk, P.J., J.R. Huth, and C. Tse, *Predicting protein druggability.* Drug discovery today, 2005. **10**(23-24): p. 1675-1682.

6. Kluytmans, J., A. van Belkum, and H. Verbrugh, *Nasal carriage of Staphylococcus aureus: epidemiology, underlying mechanisms, and associated risks.* Clin Microbiol Rev, 1997. **10**(3): p. 505-20.

7. Kuehnert, M.J., H.A. Hill, B.A. Kupronis, J.I. Tokars, S.L. Solomon, and D.B. Jernigan, *Methicillin-resistant-Staphylococcus aureus hospitalizations, United States.* Emerg Infect Dis, 2005. **11**(6): p. 868-72.

8. Klevens, R.M., M.A. Morrison, J. Nadle, S. Petit, K. Gershman, S. Ray*, et al.*, *Invasive methicillin-resistant Staphylococcus aureus infections in the United States.* Jama, 2007. **298**(15): p. 1763-71.

9. Diefenbeck, M., T. Mückley, and G. Hofmann, *Multiresistente Erreger im Krankenhaus.* Trauma und Berufskrankheit, 2008. **10**: p. 133-137.

10. Jarvis, W.R., *The epidemiology of colonization.* Infection control and hospital epidemiology, 1996: p. 47-52.

11. Lowy, F.D., *Staphylococcus aureus infections.* N Engl J Med, 1998. **339**(8): p. 520-32.

12. Altemeier, W.A. and B.G. MacMillan, *The dynamics of incections in burns.* Res Burns, 1962. **9**(203-12).

13. Barber, M. and M. Rozwadowska-Dowzenko, *Infection by penicillin-resistant staphylococci.* Lancet, 1948. **2**(6530): p. 641-4.

14. Williams, R.E., *Epidemic staphylococci.* Lancet, 1959. **1**(7065): p. 190-5.

15. Hancock, R.E.W. and D. Knowles, *Are we approaching the ende of the antibiotic era?* Curr Opin Microbiol, 1998. **1**(5): p. 493-94.

16. Parker, M.T., *Staphylococci endemic in hospitals.* Sci Basis Med Annu Rev, 1966: p. 157-73.

17. Benner, E.J. and F.H. Kayser, *Growing clinical significance of methcillin-resistant Staphylococcus aureus.* Lancet, 1968. **2**(7571): p. 741-4.

18. Jessen, O., K. Rosendal, P. Bulow, V. Faber, and K.R. Eriksen, *Changing staphylococci and staphylococcal infections. A ten-year study of bacteria and cases of bacteremia.* N Engl J Med, 1969. **281**(12): p. 627-35.

19. Pal, S.C. and B.G. Ray, *Methicillin-Resistant Staphylococci.* J Indian Med Assoc, 1964. **42**: p. 512-7.

20. Parker, M.T. and J.H. Hewitt, *Methicillin resistance in Staphylococcus aureus.* Lancet, 1970. **1**(7651): p. 800-4.

21. Rountree, P.M. and M.A. Beard, *Hospital strains of Staphylococcus aureus, with particular reference to methicillin-resistant strains.* Med J Aust, 1968. **2**(26): p. 1163-8.

22. Zechovsky, N., *[Resistance of staphylococcus to methicillin].* Nouv Presse Med, 1974. **3**(8): p. 433-7.

23. Levine, D.P., R.D. Cushing, J. Jui, and W.J. Brown, *Community-acquired methicillin-resistant Staphylococcus aureus endocarditis in the Detroit Medical Center.* Ann Intern Med, 1982. **97**(3): p. 330-8.

24. Saravolatz, L.D., D.J. Pohlod, and L.M. Arking, *Community-acquired methicillin-resistant Staphylococcus aureus infections: a new source for nosocomial outbreaks.* Ann Intern Med, 1982. **97**(3): p. 325-9.

25. Dufour, P., Y. Gillet, M. Bes, G. Lina, F. Vandenesch, D. Floret*, et al.*, *Community-acquired methicillin-resistant Staphylococcus aureus infections in France: emergence of a single clone that produces Panton-Valentine leukocidin.* Clin Infect Dis, 2002. **35**(7): p. 819-24.

26. Amaral, M.M., L.R. Coelho, R.P. Flores, R.R. Souza, M.C. Silva-Carvalho, L.A. Teixeira*, et al.*, *The predominant variant of the Brazilian epidemic clonal complex of methicillin-resistant Staphylococcus aureus has an enhanced ability to produce biofilm and to adhere to and invade airway epithelial cells.* J Infect Dis, 2005. **192**(5): p. 801-10.

27. Klein, E., D.L. Smith, and R. Laxminarayan, *Community-associated methicillin-resistant Staphylococcus aureus in outpatients, United States, 1999–2006.* Emerging infectious diseases, 2009. **15**(12): p. 1925.

28. Rice, L.B., *Federal funding for the study of antimicrobial resistance in nosocomial pathogens: no ESKAPE.* J Infect Dis, 2008. **197**(8): p. 1079-81.

29. Hidron, A.I., J.R. Edwards, J. Patel, T.C. Horan, D.M. Sievert, D.A. Pollock*, et al.*, *NHSN annual update: antimicrobial-resistant pathogens associated with healthcare-associated infections: annual summary of data reported to the National Healthcare Safety Network at the Centers for Disease Control and Prevention, 2006-2007.* Infect Control Hosp Epidemiol, 2008. **29**(11): p. 996-1011.

30. Richards, M.J., J.R. Edwards, D.H. Culver, and R.P. Gaynes, *Nosocomial infections in medical intensive care units in the United States.* Critical care medicine, 1999. **27**(5): p. 887.

31. Richards, M.J., J.R. Edwards, D.H. Culver, and R.P. Gaynes, *Nosocomial infections in pediatric intensive care units in the United States.* Pediatrics, 1999. **103**(4): p. e39-e39.

32. Wisplinghoff, H., T. Bischoff, S.M. Tallent, H. Seifert, R.P. Wenzel, and M.B. Edmond, *Nosocomial bloodstream infections in US hospitals: analysis of 24,179 cases from a prospective nationwide surveillance study.* Clinical Infectious Diseases, 2004. **39**(3): p. 309-317.

33. Boyd, E.F. and D.L. Hartl, *Recent horizontal transmission of plasmids between natural populations of Escherichia coli and Salmonella enterica.* J Bacteriol, 1997. **179**(5): p. 1622-7.

34. Schofield, P.R., A.H. Gibson, W.F. Dudman, and J.M. Watson, *Evidence for genetic exchange and recombination of Rhizobium symbiotic plasmids in a soil population.* Appl Environ Microbiol, 1987. **53**(12): p. 2942-7.

35. Valdes, A.M. and D. Pinero, *Phylogenetic Estimation of Plasmid Exchange in Bacteria.* Evolution, 1992. **46**(3): p. 641-656.

36. Wimmerstedt, A. and G. Kahlmeter, *Associated antimicrobial resistance in Escherichia coli, Pseudomonas aeruginosa, Staphylococcus aureus, Streptococcus pneumoniae and Streptococcus pyogenes.* Clin Microbiol Infect, 2008. **14**(4): p. 315-21.

37. Grundmann, H., M. Aires-de-Sousa, J. Boyce, and E. Tiemersma, *Emergence and resurgence of meticillin-resistant Staphylococcus aureus as a public-health threat.* Lancet, 2006. **368**(9538): p. 874-85.

38. Pinho, M.G., H. de Lencastre, and A. Tomasz, *An acquired and a native penicillin-binding protein cooperate in building the cell wall of drug-resistant staphylococci.* Proc Natl Acad Sci U S A, 2001. **98**(19): p. 10886-91.

39. European Antimicrobial Resistance Surveillance Network, *Susceptibility of Staphylococcus aureus isolates to Methicillin in participating countries*, 2005-2010, European Center for Disease Prevention and Control.

40. Mehta, A., V.D. Rosenthal, Y. Mehta, M. Chakravarthy, S.K. Todi, N. Sen*, et al.*, *Device-associated nosocomial infection rates in intensive care units of seven Indian*

cities. Findings of the International Nosocomial Infection Control Consortium (INICC). J Hosp Infect, 2007. **67**(2): p. 168-74.

41. Hsu, L.Y., T.Y. Tan, R. Jureen, T.H. Koh, P. Krishnan, R. Tzer-Pin Lin*, et al.*, *Antimicrobial drug resistance in Singapore hospitals.* Emerg Infect Dis, 2007. **13**(12): p. 1944-7.

42. Borg, M.A., B.D. Cookson, P. Zarb, and E.A. Scicluna, *Antibiotic Resistance Surveillance and Control in the Mediterranean region: report of the ARMed Consensus Conference.* J Infect Dev Ctries, 2009. **3**(9): p. 654-9.

43. Reynolds, P., *Structure, biochemistry and mechanism of action of glycopeptide antibiotics.* European Journal of Clinical Microbiology & Infectious Diseases, 1989. **8**(11): p. 943-950.

44. Klein, E., D.L. Smith, and R. Laxminarayan, *Hospitalizations and deaths caused by methicillin-resistant Staphylococcus aureus, United States, 1999–2005.* Emerging infectious diseases, 2007. **13**(12): p. 1840.

45. Lopez, S., C. Hackbarth, G. Romano, J. Trias, D. Jabes, and B.P. Goldstein, *In vitro antistaphylococcal activity of dalbavancin, a novel glycopeptide.* Journal of Antimicrobial Chemotherapy, 2005. **55**(suppl 2): p. ii21-ii24.

46. Candiani, G., M. Abbondi, M. Borgonovi, G. Romanò, and F. Parenti, *In-vitro and in-vivo antibacterial activity of BI 397, a new semi-synthetic glycopeptide antibiotic.* Journal of Antimicrobial Chemotherapy, 1999. **44**(2): p. 179-192.

47. Malabarba, A., T. Nicas, and R. Ciabatti, *Glycopeptide resistance in multiple antibiotic-resistant Gram-positive bacteria: a current challenge for novel semi-synthetic glycopeptide derivatives.* European journal of medicinal chemistry, 1997. **32**(6): p. 459-478.

48. Malabarba, A., R. Ciabatti, R. Scotti, B.P. Goldstein, P. Ferrari, M. Kurz*, et al.*, *New semisynthetic glycopeptides MDL 63,246 and MDL 63,042, and other amide derivatives of antibiotic A-40,926 active against highly glycopeptide-resistant VanA enterococci.* The Journal of antibiotics, 1995. **48**(8): p. 869.

49. Zhanel, G.G., F. Schweizer, and J.A. Karlowsky, *Oritavancin: Mechanism of Action.* Clinical Infectious Diseases, 2012. **54**(suppl 3): p. S214-S219.

50. Pace, J.L., K. Krause, D. Johnston, D. Debabov, T. Wu, L. Farrington*, et al.*, *In vitro activity of TD-6424 against Staphylococcus aureus.* Antimicrobial agents and chemotherapy, 2003. **47**(11): p. 3602-3604.

51. European Medicines Agency *Epar summary for the public, Vibativ, telavancin*. 2011. http://www.ema.europa.eu/docs/en_GB/document_library/EPAR_-_Summary_for_the_public/human/001240/WC500115429.pdf; Date accessed: 08/22/2012

52. Fowler, V.G., Jr., H.W. Boucher, G.R. Corey, E. Abrutyn, A.W. Karchmer, M.E. Rupp*, et al.*, *Daptomycin versus standard therapy for bacteremia and endocarditis caused by Staphylococcus aureus.* N Engl J Med, 2006. **355**(7): p. 653-65.

53. Arbeit, R.D., D. Maki, F.P. Tally, E. Campanaro, and B.I. Eisenstein, *The safety and efficacy of daptomycin for the treatment of complicated skin and skin-structure infections.* Clin Infect Dis, 2004. **38**(12): p. 1673-81.

54. Enoch, D.A., J.M. Bygott, M.L. Daly, and J.A. Karas, *Daptomycin.* J Infect, 2007. **55**(3): p. 205-13.

55. Ge, Y., D. Biek, G.H. Talbot, and D.F. Sahm, *In vitro profiling of ceftaroline against a collection of recent bacterial clinical isolates from across the United States.* Antimicrobial agents and chemotherapy, 2008. **52**(9): p. 3398-3407.

56. European Medicines Agency *Summary of opinion (initial authorisation), Zinforo, Ceftaroline fosamil*. 2012. http://www.ema.europa.eu/docs/en_GB/document_library/Summary_of_opinion_-_Initial_authorisation/human/002252/WC500129089.pdf; Date accessed: 08/22/2012

57. Apodaca, A.A. and R.M. Rakita, *Linezolid-induced lactic acidosis.* N Engl J Med, 2003. **348**(1): p. 86-7.

58. Stevens, D.L., D. Herr, H. Lampiris, J.L. Hunt, D.H. Batts, and B. Hafkin, *Linezolid versus vancomycin for the treatment of methicillin-resistant Staphylococcus aureus infections.* Clin Infect Dis, 2002. **34**(11): p. 1481-90.

59. Yan, K., L. Madden, A.E. Choudhry, C.S. Voigt, R.A. Copeland, and R.R. Gontarek, *Biochemical characterization of the interactions of the novel pleuromutilin derivative retapamulin with bacterial ribosomes.* Antimicrobial agents and chemotherapy, 2006. **50**(11): p. 3875-3881.

60. Moellering, R.C., Jr., *Current treatment options for community-acquired methicillin-resistant Staphylococcus aureus infection.* Clin Infect Dis, 2008. **46**(7): p. 1032-7.

61. Markowitz, N., E.L. Quinn, and L.D. Saravolatz, *Trimethoprim-sulfamethoxazole compared with vancomycin for the treatment of Staphylococcus aureus infection.* Ann Intern Med, 1992. **117**(5): p. 390-8.

62. Proctor, R.A., *Role of folate antagonists in the treatment of methicillin-resistant Staphylococcus aureus infection.* Clin Infect Dis, 2008. **46**(4): p. 584-93.

63. Robert Koch Institut *Auftreten und Verbreitung von MRSA in Deutschland 2010.* Epidemiologisches Bulletin, 2011. **26**; Date accessed:

64. Riedel, D.J., E. Weekes, and G.N. Forrest, *Addition of rifampin to standard therapy for treatment of native valve infective endocarditis caused by Staphylococcus aureus.* Antimicrob Agents Chemother, 2008. **52**(7): p. 2463-7.

65. Shepard, T., A. Fantel, P. Mirkes, J. Greenaway, E. Faustman-Watts, M. Campbell*, et al.*, *Teratology testing: I. Development and status of short-term prescreens. II. Biotransformation of teratogens as studied in whole embryo culture.* Progress in clinical and biological research, 1983. **135**: p. 147.

66. Stevens, D.L., Y. Ma, D.B. Salmi, E. McIndoo, R.J. Wallace, and A.E. Bryant, *Impact of antibiotics on expression of virulence-associated exotoxin genes in methicillin-sensitive and methicillin-resistant Staphylococcus aureus.* J Infect Dis, 2007. **195**(2): p. 202-11.

67. Bastos, M.C.F., B.G. Coutinho, and M.L.V. Coelho, *Lysostaphin: a Staphylococcal bacteriolysin with potential clinical applications.* Pharmaceuticals, 2010. **3**(4): p. 1139-1161.

68. Wu, J.A., C. Kusuma, J.J. Mond, and J.F. Kokai-Kun, *Lysostaphin disrupts Staphylococcus aureus and Staphylococcus epidermidis biofilms on artificial surfaces.* Antimicrobial agents and chemotherapy, 2003. **47**(11): p. 3407-3414.

69. Dajcs, J.J., E.B.H. Hume, J.M. Moreau, A.R. Caballero, B.M. Cannon, and R.J. O'Callaghan, *Lysostaphin treatment of methicillin-resistant Staphylococcus aureus keratitis in the rabbit.* Investigative ophthalmology & visual science, 2000. **41**(6): p. 1432-1437.

70. Hayon, J., C. Figliolini, A. Combes, J.L. Trouillet, N. Kassis, M.C. Dombret*, et al.*, *Role of serial routine microbiologic culture results in the initial management of ventilator-associated pneumonia.* American journal of respiratory and critical care medicine, 2002. **165**(1): p. 41-46.

71. Álvarez-Lerma, F., B. Alvarez, P. Luque, F. Ruiz, J.M. Dominguez-Roldan, E. Quintana*, et al.*, *Empiric broad-spectrum antibiotic therapy of nosocomial pneumonia in the intensive care unit: a prospective observational study.* Crit Care, 2006. **10**(3): p. R78.

72. Fritsche, T.R., H.S. Sader, and R.N. Jones, *Comparative activity and spectrum of broad-spectrum β-lactams (cefepime, ceftazidime, ceftriaxone, piperacillin/tazobactam) tested against 12,295 staphylococci and streptococci: report from the SENTRY antimicrobial surveillance program (North America: 2001-2002).* Diagnostic microbiology and infectious disease, 2003. **47**(2): p. 435-440.

73. Bryson, H.M. and R. Brogden, *Piperacillin/tazobactam. A review of its antibacterial activity, pharmacokinetic properties and therapeutic potential.* Drugs, 1994. **47**(3): p. 506.

74. Dean, C.R., M.A. Visalli, S.J. Projan, P.E. Sum, and P.A. Bradford, *Efflux-mediated resistance to tigecycline (GAR-936) in Pseudomonas aeruginosa PAO1.* Antimicrobial agents and chemotherapy, 2003. **47**(3): p. 972-978.

75. Bonitus, J., *De paralyseos quadam specie quam indigenae beriberi vocant.* 3 ed. De Medicina Indorum, cap. I. 1630, Lugdum, Batavia.

76. Eijkman, C., *Eine Beri Beri-ähnliche Krankheit der Hühner.* Virchows Archiv, 1897. **148**(3): p. 523-532.

77. Eijkman, C., *Anti-neuritis vitamin and beriberi. Nobel prize paper. 1929].* Nederlands tijdschrift voor geneeskunde, 1990. **134**(34): p. 1654.

78. Williams, R. and J. Cline, *Synthesis of vitamin B1.* Journal of the American Chemical Society, 1936. **58**(8): p. 1504-1505.

79. Friedrich, W., *Vitamins.* 1988, Berlin, New York: Walter de Gruyter.

80. Grey, E.C., *The pre-Beriberi Condition. With special reference to its existence in Japan.* Journal of Hygiene, 1928. **27**(03): p. 257-267.

81. Peters, R.A., *Pyruvic acid oxidation in brain: Vitamin B(1) and the pyruvate oxidase in pigeon's brain.* Biochem J, 1936. **30**(12): p. 2206-18.

82. Breslow, R., *On the mechanism of thiamine action. IV. 1 Evidence from studies on model systems.* Journal of the American Chemical Society, 1958. **80**(14): p. 3719-3726.

83. Hogg, J.L., *Consideration of a new catalytic role for the thiazolium sulfur atom of the coenzyme thiamine pyrophosphate.* Bioorganic Chemistry, 1981. **10**(3): p. 233-242.

84. Haake, P. and W.B. Miller, *A Comparison of Thiazoles and Oxazoles.* Journal of the American Chemical Society, 1963. **85**(24): p. 4044-4045.

85. Hafferl, W., R. Lundin, and L.L. Ingraham, *Activated Hydrogens in Compounds Related to Thiamine*.* Biochemistry, 1963. **2**(6): p. 1298-1305.

86. Oae, S. and Y. Yano, *3d-orbital resonance in divalent sulphide—XIII: The E2 reaction of p-substituted β-phenylmercapto chlorides and the corresponding oxygen analogues.* Tetrahedron, 1968. **24**(17): p. 5721-5729.

87. Uneyama, K., W. Tagaki, I. Minamida, and S. Oae, *3d-orbital resonance in divalent sulphides—IX: A study on the mechanism of the base catalysed decarboxylation of α-mercaptocarboxylic acids.* Tetrahedron, 1968. **24**(15): p. 5271-5281.

88. Oae, S., W. Tagaki, K. Uneyama, and I. Minamida, *3d-orbital resonance in divalent sulphide—X: The effects of α-aryl and α-alkylmercapto groups on the rate of decarboxylation of α-substituted carboxylic acids.* Tetrahedron, 1968. **24**(15): p. 5283-5291.

89. Haake, P. and J.M. Duclos, *Thiazolium ions and related heteroaromatic systems. IV. Product identification, kinetics, and equilibria in ring-opening of thiazolium ions.* Tetrahedron Letters, 1970. **11**(6): p. 461-464.

90. Krampitz, L., *Catalytic functions of thiamin diphosphate.* Annual review of biochemistry, 1969. **38**(1): p. 213-240.

91. Schellenberger, A., *Struktur und Wirkungsweise des aktiven Zentrums der Hefe-Pyruvat-Decarboxylase.* Angewandte Chemie, 1967. **79**(23): p. 1050-1061.

92. Erixon, K.M., C.L. Dabalos, and F.J. Leeper, *Synthesis and biological evaluation of pyrophosphate mimics of thiamine pyrophosphate based on a triazole scaffold.* Org. Biomol. Chem., 2008. **6**(19): p. 3561-3572.

93. Iwata, H., *Possible role of thiamine in the nervous system.* Trends in Pharmacological Sciences, 1982. **3**: p. 171-173.

94. Bettendorff, L. and P. Wins, *Thiamin diphosphate in biological chemistry: new aspects of thiamin metabolism, especially triphosphate derivatives acting other than as cofactors.* FEBS Journal, 2009. **276**(11): p. 2917-2925.

95. Usmanov, R. and G. Kochetov, *Interaction of baker's yeast transketolase with substrates.* Biochem. Int, 1982. **5**: p. 727-734.

96. Langlais, P.J. and S.X. Zhang, *Cortical and subcortical white matter damage without Wernicke's encephalopathy after recovery from thiamine deficiency in the rat.* Alcoholism: Clinical and Experimental Research, 1997. **21**(3): p. 434-443.

97. Navarro, D., C. Zwingmann, and R.F. Butterworth, *Region-selective alterations of glucose oxidation and amino acid synthesis in the thiamine-deficient rat brain: a re-evaluation using 1H/13C nuclear magnetic resonance spectroscopy.* Journal of neurochemistry, 2008. **106**(2): p. 603-612.

98. Karuppagounder, S.S., H. Xu, Q. Shi, L.H. Chen, S. Pedrini, D. Pechman*, et al.*, *Thiamine deficiency induces oxidative stress and exacerbates the plaque pathology in Alzheimer's mouse model.* Neurobiology of aging, 2009. **30**(10): p. 1587-1600.

99. Begley, T.P., D.M. Downs, S.E. Ealick, F.W. McLafferty, A.P.G.M. Van Loon, S. Taylor*, et al.*, *Thiamin biosynthesis in prokaryotes.* Archives of microbiology, 1999. **171**(5): p. 293-300.

100. Downs, D.M., *Understanding microbial metabolism.* Annu. Rev. Microbiol., 2006. **60**: p. 533-559.

101. Hollenbach, A.D., K.A. Dickson, and M.W. Washabaugh, *Overexpression, purification, and characterization of the periplasmic space thiamin-binding protein of the thiamin traffic ATPase in Escherichia coli.* Protein expression and purification, 2002. **25**(3): p. 508-518.

102. Rodionov, D.A., A.G. Vitreschak, A.A. Mironov, and M.S. Gelfand, *Comparative genomics of thiamin biosynthesis in procaryotes.* Journal of Biological chemistry, 2002. **277**(50): p. 48949-48959.

103. Müller, I.B., B. Bergmann, M.R. Groves, I. Couto, L. Amaral, T.P. Begley*, et al.*, *The vitamin B1 metabolism of Staphylococcus aureus is controlled at enzymatic and transcriptional levels.* PLoS One, 2009. **4**(11): p. e7656.

104. Webb, E. and D. Downs, *Characterization of thiL, encoding thiamin-monophosphate kinase, in Salmonella typhimurium.* Journal of Biological chemistry, 1997. **272**(25): p. 15702-15707.

105. Jenkins, A.H., G. Schyns, S. Potot, G. Sun, and T.P. Begley, *A new thiamin salvage pathway.* Nature chemical biology, 2007. **3**(8): p. 492-497.

106. Toms, A.V., A.L. Haas, J.H. Park, T.P. Begley, and S.E. Ealick, *Structural characterization of the regulatory proteins TenA and TenI from Bacillus subtilis and identification of TenA as a thiaminase II.* Biochemistry, 2005. **44**(7): p. 2319-2329.

107. Soriano, E.V., K.R. Rajashankar, J.W. Hanes, S. Bale, T.P. Begley, and S.E. Ealick, *Structural similarities between thiamin-binding protein and thiaminase-I suggest a common ancestor.* Biochemistry, 2008. **47**(5): p. 1346-1357.

108. Chiu, H.J., J.J. Reddick, T.P. Begley, and S.E. Ealick, *Crystal structure of thiamin phosphate synthase from Bacillus subtilis at 1.25 Å resolution.* Biochemistry, 1999. **38**(20): p. 6460-6470.

109. Mironov, A.S., I. Gusarov, R. Rafikov, L.E. Lopez, K. Shatalin, R.A. Kreneva*, et al.*, *Sensing small molecules by nascent RNA: a mechanism to control transcription in bacteria.* Cell, 2002. **111**(5): p. 747-756.

110. Winkler, W., A. Nahvi, and R.R. Breaker, *Thiamine derivatives bind messenger RNAs directly to regulate bacterial gene expression.* Nature, 2002. **419**(6910): p. 952-956.

111. Zhang, Y., S.V. Taylor, H.J. Chiu, and T.P. Begley, *Characterization of the Bacillus subtilis thiC operon involved in thiamine biosynthesis.* Journal of bacteriology, 1997. **179**(9): p. 3030-3035.

112. Blundell, T.L., *Structure-based drug design.* Nature, 1996. **384**(6604 Suppl): p. 23.

113. Müller, I.B., F. Wu, B. Bergmann, J. Knockel, R.D. Walter, H. Gehring*, et al.*, *Poisoning pyridoxal 5-phosphate-dependent enzymes: a new strategy to target the malaria parasite Plasmodium falciparum.* PLoS One, 2009. **4**(2): p. e4406.

114. Bradford, M.M., *A rapid and sensitive method for the quantitation of microgram quantities of protein utilizing the principle of protein-dye binding.* Analytical biochemistry, 1976. **72**(1-2): p. 248-254.

115. Yang, J.T., *Calculation of protein conformation from circular dichroism.* Methods Enzymol., 1986. **130**: p. 208-269.

116. DNA: http://www.dna.ac.uk/.

117. Popov, A.N. and G.P. Bourenkov, *Choice of data-collection parameters based on statistic modelling.* Acta Crystallographica Section D: Biological Crystallography, 2003. **59**(7): p. 1145-1153.

118. Bourenkov, G.P. and A.N. Popov, *A quantitative approach to data-collection strategies.* Acta Crystallographica Section D: Biological Crystallography, 2005. **62**(1): p. 58-64.

119. Leslie, A., *Jnt CCP4/ESF-EACBM Newsl.* Protein Crystallogr, 1992. **26**: p. 27-33.

120. Kabsch, W., *Xds.* Acta Crystallographica Section D: Biological Crystallography, 2010. **66**(2): p. 125-132.

121. Otwinowski, Z. and W. Minor, *Processing of X-ray diffraction data.* Methods in enzymology, 1997. **276**: p. 307-326.

122. Evans, P., *Scaling and assessment of data quality.* Acta Crystallographica Section D: Biological Crystallography, 2005. **62**(1): p. 72-82.

123. Bailey, S., *The CCP4 suite: programs for protein crystallography.* Acta Crystallogr. D, 1994. **50**: p. 760-763.

124. Adams, P.D., R.W. Grosse-Kunstleve, L.W. Hung, T.R. Ioerger, A.J. McCoy, N.W. Moriarty*, et al.*, *PHENIX: building new software for automated crystallographic structure determination.* Acta Crystallographica Section D: Biological Crystallography, 2002. **58**(11): p. 1948-1954.

125. Emsley, P. and K. Cowtan, *Coot: model-building tools for molecular graphics.* Acta Crystallographica Section D: Biological Crystallography, 2004. **60**(12): p. 2126-2132.

126. Guinier, A., *La diffraction des rayons X aux tres petits angles; application a l'etude de phenomenes ultramicroscopiques.* Ann. Phys., 1939. **12**: p. 161-237.

127. Svergun, D., *Determination of the regularization parameter in indirect-transform methods using perceptual criteria.* Journal of Applied Crystallography, 1992. **25**(4): p. 495-503.

128. Konarev, P.V., V.V. Volkov, A.V. Sokolova, M.H.J. Koch, and D.I. Svergun, *PRIMUS: a Windows PC-based system for small-angle scattering data analysis.* Journal of Applied Crystallography, 2003. **36**(5): p. 1277-1282.

129. Svergun, D., *Restoring low resolution structure of biological macromolecules from solution scattering using simulated annealing.* Biophysical journal, 1999. **76**(6): p. 2879.

130. Franke, D. and D.I. Svergun, *DAMMIF, a program for rapid ab-initio shape determination in small-angle scattering.* Journal of Applied Crystallography, 2009. **42**(2): p. 342-346.

131. Volkov, V.V. and D.I. Svergun, *Uniqueness of ab initio shape determination in small-angle scattering.* Journal of Applied Crystallography, 2003. **36**(3): p. 860-864.

132. Svergun, D., C. Barberato, and M. Koch, *CRYSOL-a program to evaluate X-ray solution scattering of biological macromolecules from atomic coordinates.* Journal of Applied Crystallography, 1995. **28**(6): p. 768-773.

133. Petoukhov, M.V. and D.I. Svergun, *Global rigid body modeling of macromolecular complexes against small-angle scattering data.* Biophysical journal, 2005. **89**(2): p. 1237-1250.

134. Mayer, M. and B. Meyer, *Characterization of ligand binding by saturation transfer difference NMR spectroscopy.* Angewandte Chemie International Edition, 1999. **38**(12): p. 1784-1788.

135. ExPASy: http://web.expasy.org/protparam/.

136. Begum, A., J. Drebes, M. Perbandt, C. Wrenger, and C. Betzel, *Purification, crystallization and preliminary X-ray diffraction analysis of the thiaminase type II from Staphylococcus aureus.* Acta Crystallographica Section F: Structural Biology and Crystallization Communications, 2010. **67**(1): p. 51-53.

137. Matthews, B.W., *Solvent content of protein crystals.* J. Mol. Biol., 1968. **33**: p. 491-497.

138. BLAST: http://blast.ncbi.nlm.nih.gov/Blast.cgi.

139. Tosatto, S.C.E., *HOMER*: http://protein.bio.unipd.it/homer/.

140. Larkin, M., G. Blackshields, N. Brown, R. Chenna, P. McGettigan, H. McWilliam*, et al.*, *Clustal W and Clustal X version 2.0.* Bioinformatics, 2007. **23**(21): p. 2947-2948.

141. BOXSHADE: http://www.ch.embnet.org/software/BOX_form.html.

142. Laskowski, R.A., E.G. Hutchinson, A.D. Michie, A.C. Wallace, M.L. Jones, and J.M. Thornton, *PDBsum: a Web-based database of summaries and analyses of all PDB structures.* Trends in Biochemical Sciences, 1997. **22**(12): p. 488-490.

143. Vagin, A. and A. Teplyakov, *MOLREP: an automated program for molecular replacement.* Journal of Applied Crystallography, 1997. **30**(6): p. 1022-1025.

144. Heinig, M. and D. Frishman, *STRIDE: a web server for secondary structure assignment from known atomic coordinates of proteins.* Nucleic acids research, 2004. **32**(suppl 2): p. W500-W502.

145. Pettersen, E.F., T.D. Goddard, C.C. Huang, G.S. Couch, D.M. Greenblatt, E.C. Meng*, et al.*, *UCSF Chimera—a visualization system for exploratory research and analysis.* Journal of computational chemistry, 2004. **25**(13): p. 1605-1612.

146. Jo, S., M. Vargyas, J. Vasko-Szedlar, B. Roux, and W. Im, *PBEQ-Solver for online visualization of electrostatic potential of biomolecules.* Nucleic acids research, 2008. **36**(suppl 2): p. W270-W275.

147. Im, W., D. Beglov, and B. Roux, *Continuum solvation model: computation of electrostatic forces from numerical solutions to the Poisson-Boltzmann equation.* Computer Physics Communications, 1998. **111**(1): p. 59-75.

148. Reynolds, C., D. Damerell, and S. Jones, *ProtorP: a protein–protein interaction analysis server.* Bioinformatics, 2009. **25**(3): p. 413-414.

149. McCoy, A.J., R.W. Grosse-Kunstleve, P.D. Adams, M.D. Winn, L.C. Storoni, and R.J. Read, *Phaser crystallographic software.* Journal of Applied Crystallography, 2007. **40**(4): p. 658-674.

150. Afonine, P.V., R.W. Grosse-Kunstleve, and P.D. Adams *The Phenix refinement framework.* CCP4 Newsletter No. 42, 2005. http://www.ccp4.ac.uk/newsletters/newsletter42/content.html . Date accessed: 08/16/2012

151. Wallace, A.C., R.A. Laskowski, and J.M. Thornton, *LIGPLOT: a program to generate schematic diagrams of protein-ligand interactions.* Protein Engineering, 1995. **8**(2): p. 127-134.

152. Campobasso, N., I.I. Mathews, T.P. Begley, and S.E. Ealick, *Crystal structure of 4-methyl-5-β-hydroxyethylthiazole kinase from Bacillus subtilis at 1.5 Å resolution.* Biochemistry, 2000. **39**(27): p. 7868-7877.

153. Morris, G.M., R. Huey, W. Lindstrom, M.F. Sanner, R.K. Belew, D.S. Goodsell*, et al.*, *AutoDock4 and AutoDockTools4: Automated docking with selective receptor flexibility.* Journal of computational chemistry, 2009. **30**(16): p. 2785-2791.

154. Jones, G., P. Willett, R.C. Glen, A.R. Leach, and R. Taylor, *Development and validation of a genetic algorithm for flexible docking1.* Journal of molecular biology, 1997. **267**(3): p. 727-748.

155. Canutescu, A.A., A.A. Shelenkov, and R.L. Dunbrack Jr, *A graph-theory algorithm for rapid protein side-chain prediction.* Protein science, 2003. **12**(9): p. 2001-2014.

156. Yan, J., A.D. Kline, H. Mo, M.J. Shapiro, and E.R. Zartler, *The effect of relaxation on the epitope mapping by saturation transfer difference NMR.* Journal of Magnetic Resonance, 2003. **163**(2): p. 270-276.

157. Arnold, K., L. Bordoli, J. Kopp, and T. Schwede, *The SWISS-MODEL workspace: a web-based environment for protein structure homology modelling.* Bioinformatics, 2006. **22**(2): p. 195-201.

158. Krissinel, E. and K. Henrick, *Detection of protein assemblies in crystals.* Computational Life Sciences, 2005: p. 163-174.

159. Krissinel, E. and K. Henrick, *Inference of macromolecular assemblies from crystalline state.* Journal of molecular biology, 2007. **372**(3): p. 774-797.

160. Krissinel, E., *Crystal contacts as nature's docking solutions.* Journal of computational chemistry, 2010. **31**(1): p. 133-143.

161. Zhang, Y., *Template-based modeling and free modeling by I-TASSER in CASP7.* Proteins: Structure, Function, and Bioinformatics, 2007. **69**(S8): p. 108-117.

162. Roy, A., A. Kucukural, and Y. Zhang, *I-TASSER: a unified platform for automated protein structure and function prediction.* Nature protocols, 2010. **5**(4): p. 725-738.

163. Svergun, D.I., M.V. Petoukhov, and M.H.J. Koch, *Determination of domain structure of proteins from X-ray solution scattering.* Biophysical journal, 2001. **80**(6): p. 2946-2953.

164. Chhabra, S., O. Dolezal, B.M. Collins, J. Newman, J.S. Simpson, I.G. Macreadie*, et al., Structure of S. aureus HPPK and the discovery of a new substrate site inhibitor.* PLoS One. **7**(1): p. e29444.

165. Drebes, J., M. Perbandt, C. Wrenger, and C. Betzel, *Purification, crystallization and preliminary X-ray diffraction analysis of ThiM from Staphylococcus aureus.* Acta Crystallogr Sect F Struct Biol Cryst Commun, 2011. **67**(Pt 4): p. 479-81.

166. Tickle, I.J., R.A. Laskowski, and D.S. Moss, *Rfree and the Rfree ratio. I. Derivation of expected values of cross-validation residuals used in macromolecular least-squares refinement.* Acta Crystallographica Section D: Biological Crystallography, 1998. **54**(4): p. 547-557.

167. McPherson, A., *Effects of a microgravity environment on the crystallization of biological macromolecules.* Microgravity science and technology, 1993. **6**(2): p. 101.

168. Galperin, M.Y. and E.V. Koonin, *Searching for drug targets in microbial genomes.* Curr Opin Biotechnol, 1999. **10**(6): p. 571-8.

169. Galperin, M.Y., R.L. Tatusov, and E.V. Koonin, *Comparing microbial genomes: how the gene set determines the lifestyle.* Organization of the Prokaryotic Genome, ed. R.L. Charlebois. 1999, Washington: ASM Press.

170. Fyfe, P.K., A. Dawson, M.T. Hutchison, S. Cameron, and W.N. Hunter, *Structure of Staphylococcus aureus adenylosuccinate lyase (PurB) and assessment of its potential as a target for structure-based inhibitor discovery.* Acta Crystallographica Section D: Biological Crystallography, 2010. **66**(8): p. 881-888.

171. Kurosu, M. and D.C. Crick, *MenA is a promising drug target for developing novel lead molecules to combat Mycobacterium tuberculosis.* Med Chem, 2009. **5**(2): p. 197-207.

172. Hyde, J.E., *Exploring the folate pathway in Plasmodium falciparum.* Acta tropica, 2005. **94**(3): p. 191-206.

173. Gerdes, S.Y., M.D. Scholle, M. D'Souza, A. Bernal, M.V. Baev, M. Farrell*, et al., From genetic footprinting to antimicrobial drug targets: examples in cofactor biosynthetic pathways.* J Bacteriol, 2002. **184**(16): p. 4555-72.

174. Bobak, D.A., *Use of nitazoxanide for gastrointestinal tract infections: treatment of protozoan parasitic infection and beyond.* Current infectious disease reports, 2006. **8**(2): p. 91-95.

175. Dover, L.G. and G.D. Coxon, *Current status and research strategies in tuberculosis drug development.* J Med Chem. **54**(18): p. 6157-65.

176. Wrenger, C., J. Knöckel, R. Walter, and I. Müller, *Vitamin B1 and B6 in the malaria parasite: requisite or dispensable?* Brazilian Journal of Medical and Biological Research, 2008. **41**(2): p. 82-88.

177. Zilles, J.L., L.R. Croal, and D.M. Downs, *Action of the thiamine antagonist bacimethrin on thiamine biosynthesis.* Journal of bacteriology, 2000. **182**(19): p. 5606-5610.

178. Lawhorn, B.G., S.Y. Gerdes, and T.P. Begley, *A genetic screen for the identification of thiamin metabolic genes.* Journal of Biological chemistry, 2004. **279**(42): p. 43555-43559.

179. Neffe, A.T., M. Bilang, and B. Meyer, *Synthesis and optimization of peptidomimetics as HIV entry inhibitors against the receptor protein CD4 using STD NMR and ligand docking.* Org. Biomol. Chem., 2006. **4**(17): p. 3259-3267.

180. Rademacher, C., J. Guiard, P.I. Kitov, B. Fiege, K.P. Dalton, F. Parra*, et al.*, *Targeting Norovirus Infection—Multivalent Entry Inhibitor Design Based on NMR Experiments.* Chemistry-A European Journal, 2011. **17**(27): p. 7442-7453.

181. Todar, K., *Todar's online textbook of bacteriology.* 2006: Kenneth Todar, University of Wisconsin-Madison Department of Bacteriology.

182. Popowicz, G.M., G. Dubin, J. Stec-Niemczyk, A. Czarny, A. Dubin, J. Potempa*, et al.*, *Functional and Structural Characterization of Spl Proteases from Staphylococcus aureus.* Journal of molecular biology, 2006. **358**(1): p. 270-279.

183. Rzychon, M., A. Sabat, K. Kosowska, J. Potempa, and A. Dubin, *Staphostatins: an expanding new group of proteinase inhibitors with a unique specificity for the regulation of staphopains, Staphylococcus spp. cysteine proteinases.* Molecular microbiology, 2003. **49**(4): p. 1051-1066.

184. Zhang, J., F. Ye, L. Lan, H. Jiang, C. Luo, and C.G. Yang, *Structural Switching of Staphylococcus aureus Clp Protease.* Journal of Biological chemistry, 2011. **286**(43): p. 37590-37601.

185. Consortium, U., *Reorganizing the protein space at the Universal Protein Resource (UniProt).* Nucleic Acids Res, 2012. **40**: p. D71-D75.

186. Maurizi, M.R., W.P. Clark, Y. Katayama, S. Rudikoff, J. Pumphrey, B. Bowers*, et al.*, *Sequence and structure of Clp P, the proteolytic component of the ATP-dependent Clp protease of Escherichia coli.* Journal of Biological chemistry, 1990. **265**(21): p. 12536-12545.

187. Bochtler, M., L. Ditzel, M. Groll, and R. Huber, *Crystal structure of heat shock locus V (HslV) from Escherichia coli.* Proceedings of the National Academy of Sciences, 1997. **94**(12): p. 6070.

8 RISK AND SAFETY STATEMENTS

8.1 Chemicals used (GHS classification)

Compound	CAS-No.	Supplier	GHS hazard	Hazard Statements	Precautionary Statements
Acetic acid	64-19-7	Chem-solute	**GHS02 GHS05**	H226, H314	P280, P305+351+338, P310
Acrylamide 30%	79-06-1	Carl Roth	**GHS06 GHS08**	H301, H312, H316, H317, H319, H332, H340, H350, H361f, H372	P201, P280, P301+310, P305+351+338, P308+313
ATP	34369-07-8	Sigma	-	-	-
Agarose	9012-36-6	Serva	-	-	-
$(NH_4)_2SO_4$	7283-20-2	Carl Roth	-	-	-
NH_4NO_3	6484-52-2	Applichem	**GHS03**	H272	P210
Ampicillin	69-52-3	Carl Roth	**GHS08**	H334, H317	P280, P261, P302+P352, P342+P311
AMP-PCP	7414-56-4	Sigma	**GHS06**	H301, H311, H315, H319, H331, H335	P261, P280, P301+P310, P305+P351+P338
APS	7727-54-0	Carl Roth	**GHS03 GHS07 GHS08**	H272, H302, H315, H317, H319, H334; H335	P280, P305+351+338, P302+352, P304+341, P342+311
Bromphenol blue	115-39-9	Applichem	-	-	-
$CaCl_2$	10043-52-4	Merck	**GHS07**	H319	P305+351+338
$Ca(H_3CCOO)_2$	114460-21-8	Sigma	-	H315, H319, H335	P261, P305+P351+P338
Citric acid	77-92-9	Sigma	**GHS05**	H318	P305+351+338, P311
Coomassie Brilliant Blue R250	6104-59-2	Serva	-	-	-
CHES	9005-64-5	Sigma	-	H319	P305+P351+P338
DTT	578517	Applichem	**GHS07**	H302, H315, H319, H335	P302+352, P305+351+338

Compound	CAS-No.	Supplier	GHS hazard	Hazard Statements	Precautionary Statements
EDTA	60-00-4	Sigma	GHS07	H319	P305+351+338
Ethanol	64-17-5	Carl Roth	GHS02	H225	P210
Ethidium bromide	1239-45-8	Sigma	GHS06, GHS08	H302, H330, H341	P260, P281, P284, P310
Glycerol	56-81-5	Sigma	-	-	-
Guanidinhydrochlorid	50-01-1	Applichem	GHS07	H302, H315, H319	P305+P351+P388, P302+P352
Hepes	7365-45-9	Sigma Aldrich	-	-	-
Hydrochloric acid >25 %	7647-01-0	Merck	GHS05, GHS07	H314, H335	P261, P280, P310, P305+351+338
Imidazole	288-32-4	Carl Roth	GHS05, GHS06, GHS08	H301; H314; H361	P260, P281, P303+P361+P353, P301+P330+P331, P305+P351+P338, P308+P313
Isopropanol	67-63-0	Carl Roth	GHS02, GHS07	H225, H319, H336.	P210, P233, P305+351+338
KCl	7447-40-7	Carl Roth	-	-	-
LiCl	7447-41-8	Merck	GHS07	H302; H315, H319, H335	P302+352, P305+351+338
Li_2SO_4	10102-25-7	Merck	GHS07	H302	-
$Mg(HCOO)_2$	6150-82-9	Fluka	-	-	-
$MgCl_2$	7786-30-3	Carl Roth	-	-	-
MgOAc	16674-78-5	Merck	-	-	-
$MgSO_4$	7487-88-9	Merck	-	-	-
Methanol	67-56-1	Carl Roth	GHS02, GHS06, GHS08	H225, H301, H311, H331, H370	P210, P280, P233, P302+P352, P309, P310
MPD	107-41-5	Carl Roth	GHS07	H315, H319	-
2-Mercaptoethanol	60-24-2	Fisher Scientific	GHS06, GHS09	H302, H411, H315, H335, H311, H319	P280, P312, P302+P350, P261, P273, P301+P312, P305+P351+P338

Compound	CAS-No.	Supplier	GHS hazard	Hazard Statements	Precautionary Statements
NaOAc	127-09-3	Applichem	-	-	-
NaBr	7647-15-6	Merck	-	-	-
(CH$_3$)$_2$AsO$_2$Na)	124-65-2	Sigma	GHS09, GHS06	H301, H331, H410	P261, P273, P301+P310, P311, P501
NaCl	7647-14-5	Carl Roth	-	-	-
NaH$_2$PO$_4$	10049-21-5	Applichem	-	-	-
NaOH	1310-73-2	Merck	GHS05	H314	P280, P310, P305+351+338
Na$_3$ citrate	6132-04-3	Sigma	-	-	-
Ni(II)SO$_4$	10101-97-0	Applichem	GHS08, GHS09, GHS07	H332, H315, H334, H317, H341, H350i, H360D, H372 H410	P280, P273, P201, P342+P311, P308+P313, P302+P352
Paraffin	8002-74-2	Applichem	-	-	-
PEG 10000	25322-68-3	Merck	-	-	-
PEG 1500	25322-68-3	Fluka	-	-	-
PEG 2000 MME	25322-68-3	Fluka	-	-	-
PEG 300	25322-68-3	Applichem	-	-	-
PEG 3350	25322-68-3	Sigma	-	-	-
PEG 400	25322-68-3	Sigma	-	-	-
PEG 4000	25322-68-3	Merck	-	-	-
PEG 6000	25322-68-3	Merck	-	-	-
PEG 8000	25322-68-3	Sigma	-	-	-
PMSF	329-98-6	Applichem	GHS06, GHS05	H301, H314	P280, P305+P351+P338, P310
SDS	151-21-3	Sigma	GHS02 GHS06	H228, H302, H311, H315, H319, H335	P210, P261, P280, P312, P305+351+338
Sodium citrate	1545832	Sigma	-	-	-
Sodium tartrate	868-18-8	Applichem	-	-	-

Compound	CAS-No.	Supplier	GHS hazard	Hazard Statements	Precautionary Statements
TEMED	110-18-9	Merck	**GHS02 GHS05 GHS07**	H225, H302, H314, H332	P261, P280, P305+351+338
tert-Butanol	75-65-0	AppliChem	**GHS02 GHS07**	H225, H319, H332, H335	P210, P305+351+338, P403+233
Tris	1185-53-1	Fluka	**GHS07**	H315, H319, H335	P261, P305+351+338
Tween 20	9005-64-5	Carl Roth	-	-	-
Yeast Extract	8013-01-2	Serva	-	-	-

8.2 Commercial Protein Screens and Kits

Name	Supplier	Risk label	Risk phrases	Safety phrases
PCT	Hampton	-	-	-
Floppy Choppy	Jena Bio Science	**C, Xn, Xi**	R35, R41, R42, R36/37/38	S22, S26, S45, S24/25, S36/37/39:
Macrosol	Molecular Dimensions	**T, N**	R10, R45, R46, R60, R61, R25, R36/37/38, R48/20/22, R51/53	S20, S26, S45, S53, S61, S36/37/39
Morpheus	Molecular Dimensions	**T, N**	R10, R45, R46, R60, R61, R63, R23/25, R36/37/38, R48/20/22, R51/53	S20, S26, S45, S53, S61, S36/37/39
PACT premier	Molecular Dimensions	**T**	R23/25, R52/53	S20, S36, S45, S61
Stura / Footprint	Molecular Dimensions	**T, N**	R10, R45, R46, R60, R61, R25, R36/37/38, R48/20/22, R51/53	S20, S26, S45, S53, S61, S36/37/39
AmSO4 Suite	Qiagen	**T+, N**	R10, R25, R26, R45, R46, R60, R61, R48/23/25, R51/53	S45, S53, S61, S36/37.

Name	Supplier	Risk label	Risk phrases	Safety phrases
Classic Suite	Qiagen	**T, N**	R10, R45, R46, R60, R61, R23/25, R36/37/38, R48/20/22, R51/53	S20, S26, S45, S53, S36/37/39. ,
ComPAS Suite	Qiagen	**T**	R10, R45, R23/24/25, R36/38, R39/23/24/25, R51/53	S13, S26, S45, S53, S61, S36/37/39.
Cryos Suite	Qiagen	**T, N**	R10, R45, R46, R60, R61, R23/25, R36/37/38, R48/20/22, R51/53	S20, S26, S45, S53, S61, S36/37/39.
JCSG+ Suite	Qiagen	**T, N**	R10, R21, R41, R45, R23/25, R37/38, R51/53	S13, S20, S26, S45, S53, S36/37/39
Pure Link PCR Purification Kit	Invitrogen	**Xn**	R22, R36/38	S28, S24/25
peqGOLD Plasmid Mini Kit	peqlab	**-**	-	-

8.3 GHS and risk symbols and information about hazard-, risk-, safety- and precaution-statements

Figure 64: GHS pictograms (source: http://www.unece.org/trans/danger/publi/ghs/pictograms.html).

GHS Hazard Statements	
H 225	Highly flammable liquid and vapour
H 226	Flammable liquid and vapour
H 228	Flammable solid
H 272	May intensify fire; oxidizer
H 301	Toxic if swallowed
H 302	Harmful if swallowed
H 311	Toxic in contact with skin
H 312	Harmful in contact with skin
H 314	Causes severe skin burns and eye damage
H 315	Causes skin irritation
H 316	Causes mild skin irritation
H 317	May cause an allergic skin reaction
H 318	Causes serious eye damage
H 319	Causes serious eye irritation
H 330	Fatal if inhaled
H 331	Toxic if inhaled
H 332	Harmful if inhaled
H 334	May cause allergy or asthma symptoms or breathing difficulties if inhaled
H 335	May cause respiratory irritation
H 336	May cause drowsiness or dizziness
H 340	May cause genetic defects
H 341	Suspected of causing genetic defects
H 350	May cause cancer
H 350i	May cause cancer by inhalation

GHS Hazard Statements	
H 360	May damage fertility or the unborn child
H 360D	May damage the unborn child
H 361	Suspected of damaging fertility or the unborn child
H361f	Suspected of damaging fertility
H 370	Causes damage to organs
H 372	Causes damage to organs through prolonged or repeated exposure
H 410	Very toxic to aquatic life with long lasting effects
H 411	Toxic to aquatic life with long lasting effects

GHS Precautionary Statements	
P201	Obtain special instructions before use
P210	Keep away from heat/sparks/open flames/hot surfaces – No smoking
P233	Keep container tightly closed
P260	Do not breathe dust/fume/gas/mist/vapors/spray
P261	Avoid breathing dust/fume/gas/mist/vapors/spray
P264	Wash … thoroughly after handling
P273	Avoid release to the environment
P281	Use personal protective equipment as required
P280	Wear protective gloves/protective clothing/eye protection/face protection
P284	Wear respiratory protection
P309	IF exposed or you feel unwell
P310	Immediately call a POISON CENTER or doctor/physician
P311	Call a POISON CENTER or doctor/physician

P312	Call a POISON CENTER or doctor/physician if you feel unwell
P321	Specific treatment (see respective MSDS)
P362	Take off contaminated clothing and wash before reuse
P501	Dispose of contents/container to …
P301+310	IF SWALLOWED: Immediately call a POISON CENTER or doctor/physician
P301+P312	IF SWALLOWED: Call a POISON CENTER or doctor/physician if you feel unwell
P301+P330+P331	IF SWALLOWED: Rinse mouth. Do NOT induce vomiting
P302+P352	IF ON SKIN: Wash with soap and water
P303+P361+P353	IF ON SKIN (or hair): Remove/Take off immediately all contaminated clothing. Rinse skin with water/shower
P304+341	IF INHALED: If breathing is difficult, remove victim to fresh air and keep at rest in a position comfortable for breathing
P305+351+338	IF IN EYES: Rinse cautiously with water for several minutes. Remove contact lenses if present and easy to do – continue rinsing
P308+313	IF exposed or concerned: Get medical advice/attention
P332+313	If skin irritation occurs: Get medical advice/attention
P342+311	Call a POISON CENTER or doctor/physician
P403+233	Store in a well-ventilated place. Keep container tightly closed

O Oxidising   C Corrosive   T Toxic
                              T+ Very toxic   Xi Irritant
                                               Xn Harmful   N Hazardous
                                                             to the
                                                             environment

Figure 65 Hazard symbols for formulations and respective risk labels (Source: http://de.wikipedia.org/wiki/Gefahrensymbol).

Risk Statements	
R8	Contact with combustible material
R10	May cause fire
R20	Flammable
R21	Harmful by inhalation
R22	Harmful in contact with skin
R25	Harmful if swallowed
R35	Toxic if swallowed
R36	Causes severe burns
R38	Irritating to eyesIrritating to skin
R41	Risk of serious damage to eyes
R42	May cause sensitisation by inhalation
R43	May cause sensitisation by skin contact
R45	May cause cancer
R46	May cause heritable genetic damage
R60	May impair fertility
R61	May cause harm to the unborn child
R39/23/24/25	Toxic: danger of very serious irreversible effects through inhalation, in contact with skin and if swallowed
R36/37/38	Irritating to eyes, respiratory system and skin
R23/24/25	Toxic by inhalation, in contact with skin and if swallowed
R20/21/22	Harmful by inhalation, in contact with skin and if swallowed
R48/20/22	Harmful: danger of serious damage to health by prolonged exposure through inhalation and if swallowed
R23/25	Toxic by inhalation and if swallowed
R36/38	Irritating to eyes and skin

Risk Statements	
R51/53	Toxic to aquatic organisms, may cause long-term adverse effects in the aquatic environment
R37/38	Irritating to respiratory system and skin

Safetey Statements	
S20	When using do not eat or drink. Do not breathe dust
S22	In case of contact with eyes, rinse immediately with plenty of water and seek medical advice
S26	In case of accident or if you feel unwell seek medical advice immediately (show the label where possible).
S28	After contact with skin, wash immediately with plenty of ... (*to be specified by the manufacturer*)
S45	If swallowed, seek medical advice immediately and show this container or label
S46	Avoid exposure - obtain special instructions before use
S53	Avoid release to the environment
S61	Refer to special instructions/safety data sheet
S24/25	Avoid contact with skin and eyes
S36/37	Wear suitable protective clothing and gloves
S36/37/39	Wear suitable protective clothing, gloves and eye/face protection

9 APPENDIX

Table 10: Peak assignment and STD-effects of ThiM substrate analogues measured with and without AMP-PCP. ThiM concentration was 40µM, compound and AMP-PCP concentration 5mM in in Tris-*d11*-D$_2$O, 300 K. Whereas δ: chemical shift, J: coupling constant, T1: relaxation time, STD % (abs., corr.): STD-effect corrected by T1, STD % (rel., corr.): STD-effect corrected by T1 and normalised to strongest signal.

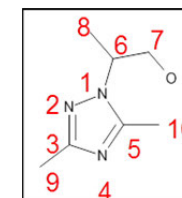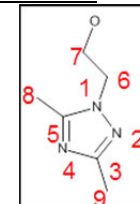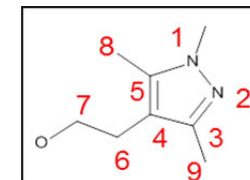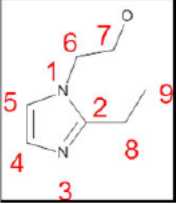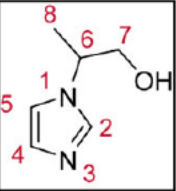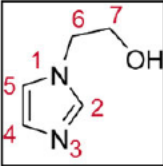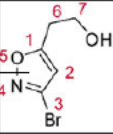|	δ [ppm]	multiplicity	J (H,H) [Hz]	integral	assignment	T1 [s]	STD % (abs.) w/o AMP-PCP	STD % (abs.) w. AMP-PCP	STD% (abs., corr.) w/o AMP-PCP	STD% (rel., corr.) w/o AMP-PCP	STD% (abs., corr.) w. AMP-PCP	STD% (rel., corr.) w. AMP-PCP	
compound 1	7.308	s		1	5	3.8	0.0411823	0.0662	0.010837446	94.39%	0.0174	65.78%	
	7.141	s		1	4	5.5	0.0560356	0.1014	0.01018829	88.73%	0.0184	69.63%	
	4.468	m		1	6	3.3	0.03789037	0.0466	0.011481931	100.00%	0.0141	53.31%	
	3.807	dd	12.2, 3.5	1	7a	1.3	-0.00092551	0.0269	-0.000711932	-6.20%	0.0207	78.20%	
	3.692	dd	8.9, 12	1	7b	1.3	0.00456909	0.0245	0.003514685	30.61%	0.0189	71.22%	
	2.482	s		3	9	2.5	0.0133443	0.0413	0.005337718	46.49%	0.0165	62.46%	
	1.376	d	6.8	3	8	1.2	0.01288126	0.0318	0.010734383	93.49%	0.0265	100.00%	

compound 2	δ [ppm]	multiplicity	J (H,H) [Hz]	integral	assignment	T1 [s]	STD % (abs.) w/o AMP-PCP	STD % (abs.) w. AMP-PCP	STD% (abs., corr.) w/o AMP-PCP	STD% (rel., corr.) w/o AMP-PCP	STD% (abs., corr.) w. AMP-PCP	STD% (rel., corr.) w. AMP-PCP	
	7.215	s		1	5	5	0.07402006	0.1093	0.014804013	79.94%	0.0219	64.10%	
	7.102	s		1	4	5.8	0.07338601	0.0956	0.012652761	68.33%	0.0165	48.33%	
	4.123	t	4.7	2	6	1.6	0.02962958	0.0546	0.018518485	100.00%	0.0341	100.00%	
	3.854	t	4.7	2	7	1.7	0.01566448	0.0306	0.0092144	49.76%	0.0180	52.76%	
	2.466	s		3	8	2.8	0.02891908	0.0598	0.010328242	55.77%	0.0214	62.68%	

compound 4	δ [ppm]	multiplicity	J (H,H) [Hz]	integral	assignment	T1 [s]	STD % (abs.) w/o AMP-PCP	STD % (abs.) w. AMP-PCP	STD% (abs., corr.) w/o AMP-PCP	STD% (rel., corr.) w/o AMP-PCP	STD% (abs., corr.) w. AMP-PCP	STD% (rel., corr.) w. AMP-PCP	
	3.634	t	6.3	2	7	1.8	0.00841901	0.0087	0.00467723	44.48%	0.0048	44.05%	
	2.541	t	6.4	2	6	1.3	0.01312389	0.0142	0.0100953	96.00%	0.0109	100.00%	
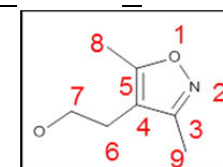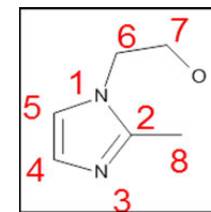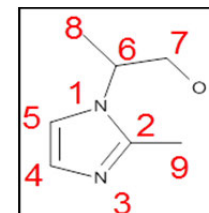
|	δ [ppm]	multiplicity	J (H,H) [Hz]	integral	assignment	T1 [s]	STD % (abs.) w/o AMP-PCP	STD % (abs.) w. AMP-PCP	STD% (abs., corr.) w/o AMP-PCP	STD% (rel., corr.) w/o AMP-PCP	STD% (abs., corr.) w. AMP-PCP	STD% (rel., corr.) w. AMP-PCP
	2.28	s		3	8	2.7	0.02839306	0.0238	0.01051595	100.00%	0.0088	80.64%
	2.166	s		3	9	2.6	0.02519588	0.0245	0.009690725	92.15%	0.0094	86.41%
compound 6	δ [ppm]	multiplicity	J (H,H) [Hz]	integral	assignment	T1 [s]	STD % (abs.) w/o AMP-PCP	STD % (abs.) w. AMP-PCP	STD% (abs., corr.) w/o AMP-PCP	STD% (rel., corr.) w/o AMP-PCP	STD% (abs., corr.) w. AMP-PCP	STD% (rel., corr.) w. AMP-PCP
	3.602	s		3	1	1.9	0.01219332	0.0247	0.006417535	56.88%	0.0130	48.39%
	3.562	t	6.8	2	7	1.2	0.00801556	0.0175	0.006679635	59.20%	0.0146	54.19%
	2.548	t	6.8	2	6	0.99	0.01081537	0.0266	0.010924611	96.82%	0.0269	100.00%
	2.126	s		3	8	1.9	0.01783366	0.0403	0.009386135	83.19%	0.0212	78.87%
	2.08	s		3	9	2	0.02256624	0.0497	0.011283121	100.00%	0.0248	92.31%
compound 7	δ [ppm]	multiplicity	J (H,H) [Hz]	integral	assignment	T1 [s]	STD % (abs.) w/o AMP-PCP	STD % (abs.) w. AMP-PCP	STD% (abs., corr.) w/o AMP-PCP	STD% (rel., corr.) w/o AMP-PCP	STD% (abs., corr.) w. AMP-PCP	STD% (rel., corr.) w. AMP-PCP
	4.125	t	4.9	2	6	1.1	0.01476202	0.0202	0.013420015	100.00%	0.0183	100.00%
	3.853	t	4.9	2	7	1.2	0.00740418	0.0123	0.006170152	45.98%	0.0102	55.73%
	2.359	s		3	8	2.1	0.0096541	0.0252	0.004597192	34.26%	0.0120	65.55%
	2.222	s		3	9	2	0.01112788	0.0181	0.005563938	41.46%	0.0091	49.37%
compound 8	δ [ppm]	multiplicity	J (H,H) [Hz]	integral	assignment	T1 [s]	STD % (abs.) w/o AMP-PCP	STD % (abs.) w. AMP-PCP	STD% (abs., corr.) w/o AMP-PCP	STD% (rel., corr.) w/o AMP-PCP	STD% (abs., corr.) w. AMP-PCP	STD% (rel., corr.) w. AMP-PCP
	4.457	m		1	6	2.9	0.02154864	0.0274	0.007430566	100.00%	0.0094	63.76%
	3.76	dd	12, 4.1	1	7a	0.9	0.00350987	0.0094	0.00389986	52.48%	0.0105	70.93%
	3.702	dd	12, 9.8	1	7b	0.94	0.00293707	0.0102	0.003124537	42.05%	0.0109	73.51%
	2.363	s		3	10	1.8	0.00779322	0.0219	0.004329569	58.27%	0.0121	82.11%
	2.229	s		3	9	1.8	0.00828336	0.0162	0.004601867	61.93%	0.0090	60.78%
	1.302	d	6.8	3	8	1.1	0.00671016	0.0163	0.006100144	82.10%	0.0148	100.00%

δ [ppm]	multiplicity	J (H,H) [Hz]	integral	assignment	T1 [s]	STD % (abs.) w/o AMP-PCP	STD % (abs.) w. AMP-PCP	STD% (abs., corr.) w/o AMP-PCP	STD% (rel., corr.) w/o AMP-PCP	STD% (abs., corr.) w. AMP-PCP	STD% (rel., corr.) w. AMP-PCP
7.212	s		1	5	4.6	0.06070399	0.0832	0.013196519	68.83%	0.0181	75.51%
7.11	s		1	4	6.3	0.09408869	0.1230	0.014934713	77.89%	0.0195	81.52%
4.128	t	4.9	2	6	1.3	0.02492584	0.0311	0.019173726	100.00%	0.0239	100.00%
3.852	t	4.9	2	7	1.4	0.01362596	0.0223	0.009732827	50.76%	0.0159	66.52%
2.829	q	7.6	2	8	2.5	0.01720746	0.0402	0.006882982	35.90%	0.0161	67.22%
1.253	t	7.5	3	9	2.9	0.01845787	0.0403	0.006364782	33.20%	0.0139	58.05%

compound 10	δ [ppm]	multiplicity	J (H,H) [Hz]	integral	assignment	T1 [s]	STD % (abs.) w/o AMP-PCP	STD % (abs.) w. AMP-PCP	STD% (abs., corr.) w/o AMP-PCP	STD% (rel., corr.) w/o AMP-PCP	STD% (abs., corr.) w. AMP-PCP	STD% (rel., corr.) w. AMP-PCP
	7.298	s		1	5	4	0.025828784	0.005659023	0.0065	75.76%	0.00566	55.98%
	7.107	s		1	4	2.3	0.019171803	0.010109013	0.0083	97.80%	0.01011	100.00%
	4.459-4.412	m		1	6	3.2	0.025262081	-0.000971527	0.0079	92.63%	-0.00097	-9.61%
	3.834	dd	12.2, 4.1	1	7a	1.4	0.005758712	-0.000631331	0.0041	48.26%	-0.00063	-6.25%
	3.74	dd	12.2, 8.0	1	7b	1.4	0.003594378	-0.000568602	0.0026	30.12%	-0.00057	-5.62%
	1.463	d	7.0	3	8	1.2	0.010227378	0.00771028	0.0085	100.00%	0.00771	76.27%

compound 11	δ [ppm]	multiplicity	J (H,H) [Hz]	integral	assignment	T1 [s]	STD % (abs.) w/o AMP-PCP	STD % (abs.) w. AMP-PCP	STD% (abs., corr.) w/o AMP-PCP	STD% (rel., corr.) w/o AMP-PCP	STD% (abs., corr.) w. AMP-PCP	STD% (rel., corr.) w. AMP-PCP
	7.237	s		1	5	5.6	0.043276442	0.04019597	0.0077	100.00%	0.00718	100.00%
	7.086	s		1	4	3.9	0.024918605	0.022246661	0.0064	82.68%	0.00570	79.47%
	4.185	t	5.2	2	6	2	0.013210488	0.014316297	0.0066	85.47%	0.00716	99.73%
	3.887	t	5.2	2	7	1.8	0.007411106	0.006273025	0.0041	53.28%	0.00349	48.55%

compound 12	δ [ppm]	multiplicity	J (H,H) [Hz]	integral	assignment	T1 [s]	STD % (abs.) w/o AMP-PCP	STD % (abs.) w. AMP-PCP	STD% (abs., corr.) w/o AMP-PCP	STD% (rel., corr.) w/o AMP-PCP	STD% (abs., corr.) w. AMP-PCP	STD% (rel., corr.) w. AMP-PCP
	6.488	s	6.3	1	2	8.2	0.469410973	0.369089194	0.0572	54.69%	0.04501	44.74%

δ [ppm]	multiplicity	J (H,H) [Hz]	integral	assignment	T1 [s]	STD % (abs.) w/o AMP-PCP	STD % (abs.) w. AMP-PCP	STD% (abs., corr.) w/o AMP-PCP	STD% (rel., corr.) w/o AMP-PCP	STD% (abs., corr.) w. AMP-PCP	STD% (rel., corr.) w. AMP-PCP
3.914	t	6.1	2	6	1.7	0.170267135	0.158317833	0.1002	95.69%	0.09313	92.56%
3.061	t	6.1	2	7	1.8	0.188397204	0.18110231	0.1047	100.00%	0.10061	100.00%

compound 13	δ [ppm]	multiplicity	J (H,H) [Hz]	integral	assignment	T1 [s]	STD % (abs.) w/o AMP-PCP	STD % (abs.) w. AMP-PCP	STD% (abs., corr.) w/o AMP-PCP	STD% (rel., corr.) w/o AMP-PCP	STD% (abs., corr.) w. AMP-PCP	STD% (rel., corr.) w. AMP-PCP
	7.391-7.363	m		2	8, 11	2.9	0.109029758	0.104025709	0.0376	88.85%	0.03587	93.55%
	7.155-7.108	m		2	9, 10	2.7	0.114247464	0.103532893	0.0423	100.00%	0.03835	100.00%
	4.119	t	5.2	2	6	0.77	0.021322312	0.017417136	0.0277	65.44%	0.02262	58.99%
	3.856	t	5.2	2	7	0.95	0.02251092	0.021415127	0.0237	56.00%	0.02254	58.79%

compound 15	δ [ppm]	multiplicity	J (H,H) [Hz]	integral	assignment	T1 [s]	STD % (abs.) w/o AMP-PCP	STD % (abs.) w. AMP-PCP	STD% (abs., corr.) w/o AMP-PCP	STD% (rel., corr.) w/o AMP-PCP	STD% (abs., corr.) w. AMP-PCP	STD% (rel., corr.) w. AMP-PCP
	7.696	s		1	2	5.8	0.084661004	0.104025709	0.0146	80.78%	0.01794	22.52%
	4.173	t	5.3	2	6	1.3	0.02349029	0.103532893	0.0181	100.00%	0.07964	100.00%
	3.872	t	5.3	2	7	1.3	0.021190306	0.017417136	0.0163	90.21%	0.01340	16.82%
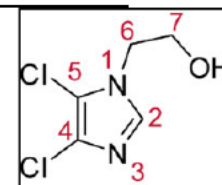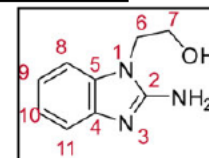
Table 11: Formulation of the magnesium screen designed to optimise TPK crystallisation (see chapter 4.7.3) based on the findings from the homology modelling server I-Tasser. Precipitant: 10 mM sodium bromide, 0.8 M sodium citrate.

		1	2	3	4	5	6	7	8	9	10	11	12
A	Precipitant with Mgsulphate	1 mM	5 mM	10 mM	50 mM	100 mM	150 mM	200 mM	250 mM	300 mM	350 mM	400 mM	500 mM
B	Precipitant with Mgformate	1 mM	5 mM	10 mM	50 mM	100 mM	150 mM	200 mM					
C	Precipitant with Mgchloride	1 mM	5 mM	10 mM	50 mM	100 mM	150 mM	200 mM	250 mM	300 mM	350 mM	400 mM	500 mM
D	Precipitant with Mgacetate	1 mM	5 mM	10 mM	50 mM	100 mM	150 mM	200 mM	250 mM	300 mM	350 mM	400 mM	500 mM

10 ACKNOWLEDGEMENTS

Ich danke meinem Doktorvater Prof. Dr. Dr. Christian Betzel für die Betreuung und die Begutachtung meiner Arbeit und für diverse Chancen auf Konferenzen und bei Auslandsaufenthalten ein wenig über den Tellerrand hinauszuschauen. Außerdem danke ich Prof. Dr. Carsten Wrenger für die Unterstützung und das tolle Thema, sowie für die vielen fruchtbaren Diskussionen und die Organisation der Aufenthalte in den USA und Brasilien.

Dr. Markus Perbandt danke ich als Mitglied in meinem PhD advisory committee für die vielen Anregungen zu meiner Arbeit und für die tolle Organisation des Programms der LEXI-Graduiertenschule „Hamburg School for Structure and Dynamics in Infection".

Ganz herzlich möchte ich auch Prof. Dr. Peter Heisig für die Anfertigung eines Zweitgutachtes und den Disputationsgutachtern Prof. Dr. Andrew Torda und Dr. Thomas Hackl danken.

Großer Dank gilt auch der Joachim Herz Stiftung als Teil der Hamburger Landesexzellenzinitiative (LEXI) für die finanzielle Unterstützung über die Graduiertenschule „Hamburg School for Structure and Dynamics in Infection" und dem DAAD für die Finanzierung der Auslandsaufenthalte.

Außerdem danke ich meinen Kollegen in den Laboren an der Uni Hamburg, am DESY und im BNI, allen voran Raphael Eberle für die vielen erheiternden Stunden und die Hilfe innerhalb und außerhalb des Labors. Dr. Dominik Oberthür und Dr. Ahmed Akrem haben mir besonders bei der Einführung in die Kristallisation und Strukturlösung geholfen, sowie mich an der Beamline unterstützt. Miriam Kötzler danke ich für ihre Zeit bei der Auswertung der NMR Experimente und die netten Abende in der Kneipe.

Im BNI gilt mein Dank v.a. Sabine Butzloff für die Hilfe wenn ich doch wieder schnell ins nächste Labor musste, Bärbel Bergmann für die Hilfe bei der Durchführung der Aktivitätstests und Dr. Ingrid Müller für die Unterstützung bei der Planung und Auswertung der Aktivitätstests und die netten Abende danach.

Außerdem danke ich Dr. Alexey Kikhney für die Hilfe bei der Durchführung und Auswertung der SAXS Experimente, Dr. Björn Windshügel für die nette Zusammenarbeit bei der Substratanaloga-Suche, Prof. Dr. Steven Ealick für die Möglichkeit in sein Labor hineinzuschnuppern und Dr. Jolita Seckute für die Hilfe im Baker Lab. Ferner danke ich Dr. Klaus Weber für die Einblicke in den Klinikalltag mit MRSA Patienten und deren Behandlung.

Ich danke allen meinen Freunden und meiner WG, die mich während der gesamten Zeit unterstützt und aufgefangen haben und besonders Leif Ludwig und Anett Köhler für ihr Korrekturlesen. Mein besonderer Dank gilt meiner Familie dabei besonders meinen Eltern Karin Drebes und Alain Pioche und meinem Bruder Andi Drebes für die liebevolle Unterstützung in Schieflagen. Meinem Freund Karsten Knorr danke ich für seine vielen guten Ratschläge, seine liebe Unterstützung und seine Geduld.

Danke euch allen!!!!

11 CURRICULUM VITAE

entfällt aus datenschutzrechtlichen Gründen

entfällt aus datenschutzrechtlichen Gründen